

ISTC Project No. K-1265

Experimental study of the processes at the corium melt retention in the reactor pressure vessel (INVECOR)

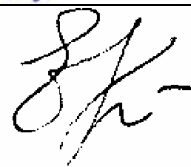
**Final Project Technical Report
on the work performed from 01.05.2006 to 30.04.2010**

Affiliated State Enterprise "Institute of Atomic Energy" of the Republican State-Owned Enterprise "National Nuclear Center" of the Republic of Kazakhstan (IAE NNC RK)

Project Manager **Vladimir S. Zhdanov**
Candidate of Science



Director **Ergazy A. Kenzhin**
Candidate of Physical & Mathematical Sciences



November 2009

This work is supported financially by International Science and Technology Center (ISTC) and performed under the contract to the International Science and Technology Center (ISTC),
Moscow

Title of the Project: Experimental study of the processes at the corium melt retention in the reactor pressure vessel (INVECOR)

Commencement Date: 01.05.2006 г.

Duration: 48 month

Project Manager: Zhdanov Vladimir Semenovich

Phone number: +7 72251 23125

Fax: +7 72251 23125

E-mail address: zhdv@nnc.kz

Leading Institute: Affiliated State Enterprise "Institute of Atomic Energy" of the Republican State-Owned Enterprise "National Nuclear Center" of the Republic of Kazakhstan
071100, East-Kazakhstan region, Kurchatov-city, 10,
Krasnoarmeyskaya St.
Republic of Kazakhstan
Tel.:+7 72251 23125
iae@nnc.kz

Participating Institutes: No

Foreign Collaborators: Hervé Chalaye
Commissariat à l'Énergie Atomique (CEA)
CEA Saclay DEN/DSNI Batiment 121
Gif sur Yvette Cedex, Ile de France
91191, France
+33 1 69 08 16 81
herve.chalaye@cea.fr

Christophe Journeau
Commissariat à l'Énergie Atomique (CEA)
CEA Cadarache DEN/DTN/STRI/LMA Bâtiment 708
St Paul lez Durance, Provence-Alpes-Côte d'Azur
13108, France
+33 4 42 25 41 21
christophe.journeau@cea.fr

Eberhard Altstadt
Forschungszentrum Rossendorf
Bautzner Landstrasse (B6) 128
Dresden, Saxony
01328 Dresden, Germany
+49-351-260-2276
e.altstadt@fz-rossendorf.de

Alexei Miassoedov
Forschungszentrum Karlsruhe GmbH
Hermann-von-Helmholtz-Platz 1
Karlsruhe
76021, Germany
+49 7247 82 22 53
alexei.miassoedov@iket.fzk.de

Th. Walter Tromm
Forschungszentrum Karlsruhe GmbH
Hermann-von-Helmholtz-Platz 1
Karlsruhe
76021, Germany
+49 7247 82 55 09
walter.tromm@nuklear.fzk.de

Francesco Oriolo
DIMNP – Pisa University
Via Diotisalvi, 2
Pisa
56126, Italy
+39 050 836652
f.oriolo@ing.unipi.it

Florian FICHOT
Institut de Radioprotection et de Sureté Nucléaire
IRSN/DPAM/SEMCA – BP 3
St Paul lez Durance
13115, France
+33 442199519
florian.fichot@irsn.fr

Key words:

Experimental modeling; Prototype corium; Graphite; Protective coating; reactor pressure vessel; Molten pool; Decay heat; Corrosion; Thermal insulation; Physical-chemical processes; Plasmatrons; Electrode nozzle; Calibration large-scale experiment; Integral test.

List of content

- 1. Brief description of the Working Plan: Project objectives, expected results, Technical Approach 5
- 2. Brief Description of the Test Facilities 8
 - 2.1 Induction Electric-melting Furnace** 8
 - 2.2 Decay Heat Simulator** 11
 - 2.3 Experimental section** 14
 - 2.4 The small-scale test facility** 28
- 3. Calibration tests 30
 - 3.1 Testing of the electric melting furnace** 30
 - 3.1.1 First large-scale calibration test 31
 - 3.1.2 Second large-scale calibration test 32
 - 3.2 Testing of coaxial plasmatrons** 34
 - 3.2.1 Testing of single plasmatrons without immersion into corium 34
 - 3.2.2 Testing of the device of five plasmatrons without immersion in the corium 42
 - 3.2.3 Testing of single plasmatrons with immersion in the corium components 50
- 4. Integral tests 70
 - 4.1 First integral test INVECOR-1.3** 70
 - 4.2 Second integral test INVECOR-2** 74
 - 4.3 Third integral test INVECOR-3** 79
 - 4.4 Fourth integral test INVECOR-4** 84
 - 4.5 Post-test calculations** 88
- 5. Results 94
 - 5.1 Investigations after the calibration tests** 94
 - 5.2 Investigation after the integral test INVECOR-1.3** 96
 - 5.3 Investigation after the integral test INVECOR-2** 103
 - 5.4 Investigation after the integral test INVECOR-3** 115
 - 5.5 Investigations after integral test INVECOR-1.4** 121
 - 5.6 Analysis of the data resulted from the integral tests INVECOR** 131
- 6. Conclusion 135
- 7. Comments 136

1. Brief description of the Working Plan: Project objectives, expected results, Technical Approach

1.1 Overall Project objective

The overall objective of the Project is to improve the safety assessment of LWR corium in-vessel retention (IVR) under severe accident conditions.

Specific objective of the project is the experimental simulation of the thermal and physicochemical processes at the retention of the prototype molten corium pool on the water-cooled lower head of the reactor pressure vessel (RPV) for estimation of:

- influence of scale, shape of the interface and other 2-D effects on the corrosion processes, which determine the final thickness of the RPV wall;
- influence of the metal-oxide stratified molten pool structure on the possibility of corium in-vessel retention;
- quantitative characteristics of processes at IVR, which are necessary for the development and verification of models involved in IVR justifying.

The LAVA –B test facility constructed in the Institute of Atomic Energy of NNC RK in the course of the international COTELS and IVR-AM programs implementation (in cooperation with NUPEC Company, Japan) was used for achievement of the Project purposes.

1.2 Expected Results and Their Application

The Project concerns the category of applied researches. The main results of the Project will be the large-scale experimental data on the structure of molten pool on the RPV model and on RPV steel corrosion depending on the prototypic corium composition and heat load distribution on the reactor vessel. The resultant data may be used for the development of models describing melt behavior at the in-vessel accident phase, verification of the appropriate calculation computer codes in justification of IVR concept for existing and newly-developed projects.

The technique for producing corium melt and the methodology of tests on corium/RPV steel interaction can be improved owing to the involvement of foreign collaborators (CEA, Cadarache) in calculated validation of the electrical melt furnace modes and large-scale test conditions. The collaborators' thermodynamic and physicochemical computer codes will make it possible to interpret small-scale test results in order to use in LAVA-B facility considering the EMF structure.

Engineering developments ensuring melt and retention of corium melt may be used in practice of similar studies and in industry on melting of reactive and radioactive materials.

1.3 Scope of Activities

As per the scope of the Project, 4 tasks are expected for implementation. All tasks are assigned for achievement of the Project objective – to obtain experimental data on IVR processes.

Task 1 Modernization of test facilities and optimization of melting process and simulation of decay heat.

Task 2 Calculation support of experiments

Task 3 Large-scale experiments

Task 4 Post-test analysis

Each task is phased according to the investigation lines..

1.4 Technical Approach and Methodology

The technical approach and methodology involve modeling of basic processes in the reactor pressure vessel model specific for IVR conditions.

Induction heating through the "hot crucible" method is applied to obtaining of the prototype corium melt. With achievement of the required melt temperature, the corium produced is

discharged from the electric melting furnace into the experimental section from height about 1.7 m. The experimental section is placed in the test facility pressure vessel, that is a cylindrical sealed vessel about 5 m³ in volume made of stainless steel. The internal surface of the pressure vessel is insulated to reduce heat losses.

The corium components/carbon interaction during their heating-up is limited using the method of zirconium melt coating on the crucible internal surface with further zirconium carbiding. The similar method is used at protection of electrode nozzles external surface of the device simulating decay heat in corium.

The reactor pressure vessel model is made of VVER RPV steel with the scale about 1:12. The model's size and configuration are determined by the possible maximum corium volume produced in the existing electric melting furnace of the LAVA-B facility, as well as by the preset conditions of thermal and physicochemical interaction between corium and steel. In this context, thickness of the wall may not reflect the scale of the RPV model diameter. Thus, the requirement for filling the whole hemi-elliptical part of the RPV model with discharged corium is kept, and on condition of partial corium displacement by electrodes of the simulating decay heat device, the cylindrical model section should be partly filled up.

The decay heat in the reactor pressure vessel model is simulated by means of the electrode heater immersed into the melt via heating-up of each electrode by an electric arch due to the electrode nozzle coaxial structure.

The following concepts are to be tested during the implementation of the integral large-scale experiments:

- 1) Retention of prototypic oxide corium melt C-30 in the reactor pressure vessel model within not less than 2 hours with simulation of decay heat in corium.
- 2) Retention of prototypic oxide-metallic corium melt in the reactor pressure vessel model within not less than 1 hour with simulation of decay heat in corium and existence of reactor pressure vessel external cooling with further stopping of cooling water supply for organization of reactor pressure vessel wall penetration according to the "focusing effect" interaction model.
- 3) Retention of prototype oxide-metallic corium in the reactor pressure vessel model within not less than 1,5 hour with simulation of decay heat in corium and existence of reactor pressure vessel external cooling with further stopping of cooling water supply for organization of reactor pressure vessel wall penetration according to the MASCA interaction model.

The difference in engineering realization of the experiments under scenarios 2 and 3 is in different depth of electrodes immersion in the corium pool and/or in change of the shape of external nozzles of coaxial electrodes of the decay heat simulating device.

To measure profiles of heat fluxes, the reactor pressure vessel model is equipped with the set of thermocouples built in the wall at different depth from the external surface and in various zones along the height and azimuth (in the lowest point of the model, in the hemi-elliptical zone, in the cylindrical zone, and also in the cylindrical zone not filled with corium).

The deformation of the reactor pressure vessel model wall is measured in chosen points using the displacement gauges installed in the clearance between the reactor pressure vessel model external wall and the technological base

The cooling water is supplied from below into the gap between the reactor pressure vessel model and the technological base, and discharged from the upper zone. Heating and the flow rate of the cooling water is measured by appropriate gauges. The water flow rate is controlled to ensure the specified test conditions.

The small-scale tests are performed in the test facility with induction heating equipped with appropriate instrumentations for measuring temperature, pressure inside the working chamber and with the gas sampling system during the experiment.

After each experiment, the post-test analysis is executed including the operations as follows

- Removal of fragmented corium and analysis of its grain-size composition debris;

- Longitudinal cutting of the reactor pressure model with solidified melt (or without melt if no strong coupling between corium and the RPV model wall, - in this case the debris ingot is cut separately from RPV model);
- Investigation of section plane;
- Measurement of reactor pressure model wall corrosion/penetration depth;
- Fabrication of powder from the fragmented corium and corium ingot;
- Fabrication of metallographic specimen from RPV model wall samples;
- Fabrication of specimen from corium/vessel steel interaction area;
- Element analysis of powder specimen;
- Phase X-ray analysis of powder specimen;
- Density measurement of powder specimen and ingot specimen;
- Measurement of specific electrical resistance of powder samples and ingot samples;
- Re-melting of corium samples in the small-scale facility and subsequent phase and element analysis of the resulting compositions.

Note: In the course of the activity implementation the Project Working Plan was revised in respect of the experimental technique improvement. The changes were not concerned to the primary objective of the Project and were aimed at improving the quality of the integrated large-scale tests performance.

2. Brief Description of the Test Facilities

The Institute of Atomic Energy of the National Nuclear center of the Republic of Kazakhstan has available the "Lava-B" Test Facility designed for the performance of the out-of-pile experiments on simulating the processes accompanying the melt-of-core severe accident. The installation makes it possible to melt up to 60 kg of the light water reactor core materials mixture with subsequent discharge of the corium produced into the experimental section. In the course of the tests the thermo- and hydraulic parameters of interaction of corium with core, RPV material or concrete, depending on the specific test conditions, are studied. Decay heat of the fuel is simulated by means of different electrical systems as well as accident localization by means of modeling of the standard reactor facility systems.

The "Lava-B" Test Facility involves two main functional parts:

- Electric melting furnace (EMF) for producing corium melt of the required temperature;
- Melt receiver (MR) housing the experimental section for simulating interaction of corium and core, concrete or RPV lower head model.

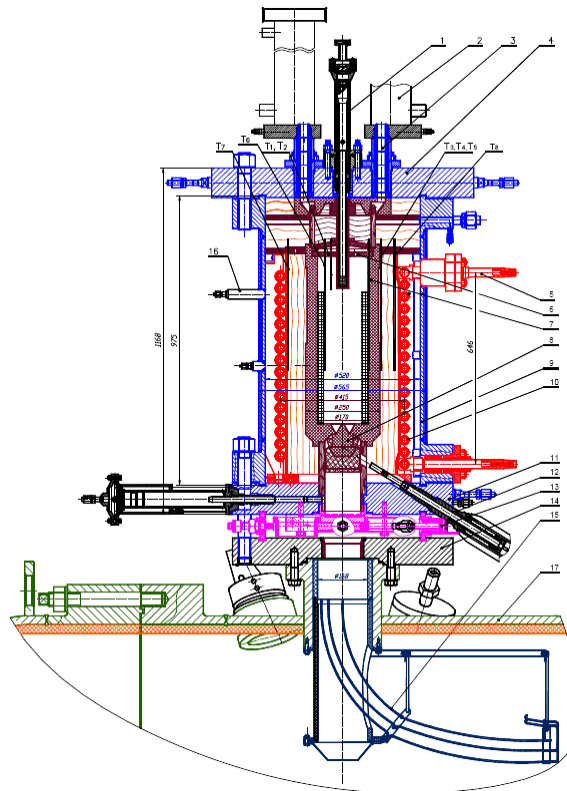
2.1 Induction Electric-melting Furnace

The induction EMF is supplied with an electric generator of 2400 Hz with maximum capacity up to 165 kW. The core materials mix is loaded into the graphite crucible. To prevent burden components/carbon interaction, there were used different ways of shielding:

- Sheet metal tantalum with preliminary or simultaneous (with burden heating) carbodization of the surface;
- Refractory carbide coating on the internal crucible surface;
- Zirconium melt coating as a fine film with its further carbidization;
- Tungsten inserts.

The EMF crucible is insulated with graphite felt. The crucible is fixed from top and bottom with bearing sleeves made of carbon plastic. The melt is discharged from the EMF to the MR through the hole of 50 mm, that is produced in the crucible bottom after the plug breaking with a special pneumatic mechanism. In the EMF bottom there is a lock valve for closing of the MR from EMF cavity after melt discharge. The EMF allows to producing up to 60 kg of melt at temperature to 3000°C. The EMF construction diagram is depicted in Fig. 1.

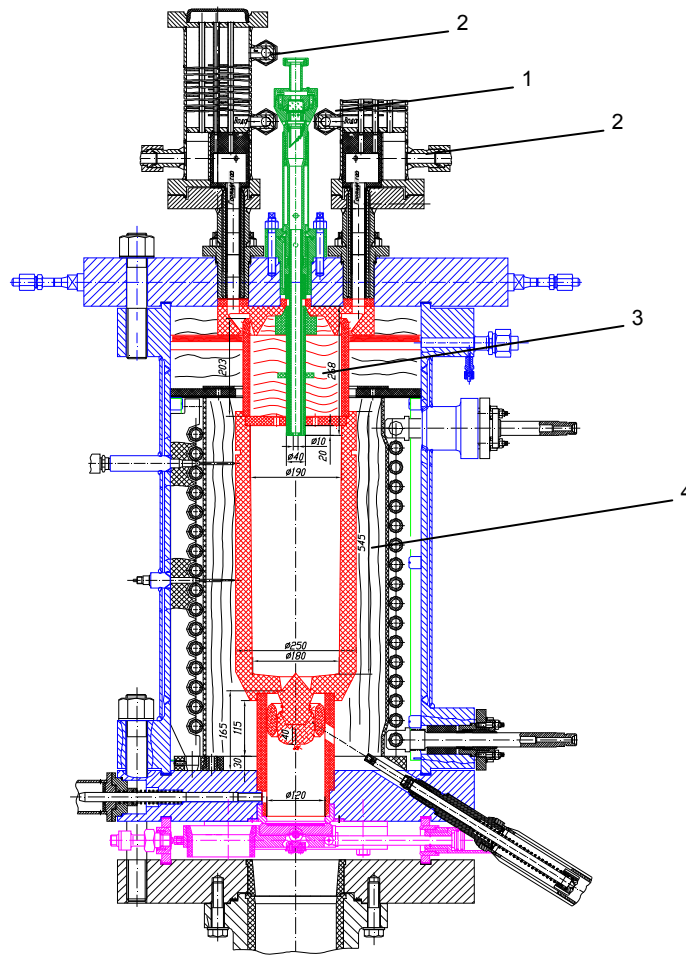
To realize the project mission, the protective zirconium carbide-based coating on the internal melting crucible wall was decided to use. With this end in view the supporting experiments on testing the technique for coating of a large-scale crucible were carried out. Considering the tests results some changes in crucible size and shape were made.



1 – infrared pyrometer; 2 – heat exchanger; 3 – water-cooled channel for gas release; 4, 11 – copper flanges; 5 – current feed-through; 6 – crucible cover; 7 – crucible; 8 – crucible plug; 9 – EMF housing; 10 – inductor; 12 – plug breaking mechanism; 13 – lock valve; 14 – MR housing; 15 – plug trap

Figure 1 - EMF construction diagram prior to the modernization

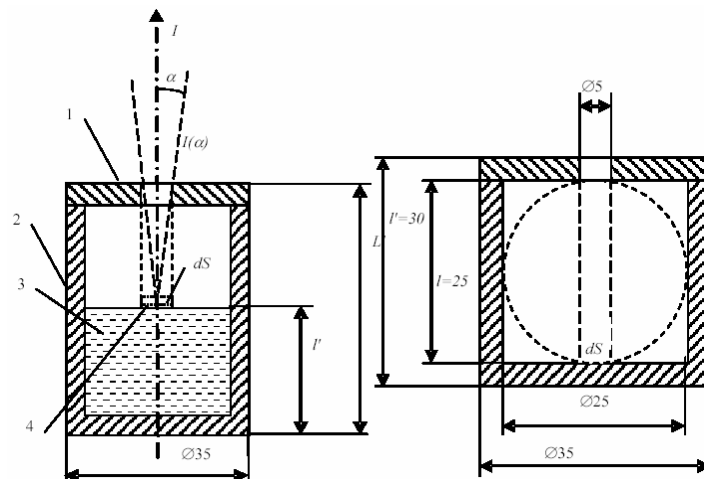
In order to reduce errors in measuring corium temperature during heating and melting with the use of infrared pyrometer, caused by non-isothermality of the tube model of the absolutely black body, the pyrometer sight unit on the melt surface in the melting crucible was changed. The crucible height was reduced for the purpose of its more uniform warming in the inductor area. For compensation of the crucible capacity, there was reduced the thickness of the lateral wall with consideration of the use of high-quality graphite of R4340 type. For better zirconium melt spreading along the crucible elevation when applying protective coating, the internal crucible cavity was made in the form of a cone with slight reduction of the internal diameter from the top to the crucible bottom. Fig. 2 represents the constructive diagram of the EMF after the modernization.



1 –infrared pyrometer; 2 – heat exchanger; 3 – pyrometer sight unit; 4 – crucible.

Figure 2 – The constructive diagram of the EMF after the modernization

In the planned tests INVECOR there was decided to transfer to the absolutely black body model "large cavity with small aperture" that will make it possible, in executors' judgment, to reduce essentially the error of the model due to uneven heating up of the internal crucible cavity between the lid and load. The calculations below confirm the assumption.



a) Scheme of measurement

b) Geometrical ratios of the chosen model

1 – crucible lid with aperture; 2 – crucible; 3 – melt; 4 – sighting area (projection of aperture in a lid on a melt surface with area dS); I – intensity of radiation in a normal direction; $I(\alpha)$ – intensity of radiation within an angle 2α .

Figure 3 – Calculation model

Effective factor of absolute black body model radiation ε_{eff} was defined by Guffe method:

$$\varepsilon_{\text{neff}} = \frac{1 + (1 - \varepsilon_m) \cdot (f/F' - f_c/F_0)}{1 - (1 - \varepsilon_m) \cdot (1 - f/F')}$$

where ε_m – normal integrated factor of radiation of a cavity material ;

f – aperture area in a cavity;

f_c – area of the spherical segment which is cut out by the aperture on imagined sphere, which diameter is equal to the cavity's depth;

F_0 – area of the surface of imagined sphere;

F' – total area of a cavity equal to the area of all internal surface of model F, taking into account the aperture area.

The calculations demonstrated that for the chosen crucible size and aperture diameter in its lid the cavity emissivity over the melt for two wave lengths (0,7 microns and 1,5 microns), characteristic for the applied pyrometers, make more than 0,99 for all existing types of graphite.

Due to the fact that the chosen measurement scheme involves heating the corium components in the melting volume at the open gas drainage system from the electric melting furnace, we calculated hydraulic resistance of the heat exchanger circuit to measure pressure inside the crucible during the corium heating/melting. The estimated assessment showed that the loss of pressure of the gas mixture in the drainage gas system would not exceed 0.04 MPa.

2.2 Decay Heat Simulator

To realize the Project mission, the technological equipment manufactured earlier for the experiments on corium melt retention in the vessel with simulation of decay heat in fission fragments by means of the heater consisting of coaxial plasmatrons immersed in the corium melt on the reactor lower head model was used.

In tests IVR-AM in the corium discharged to the reactor vessel lower head model, decay heat was simulated. The method of direct current transmission through the corium from the three-phase AC network, the method of electric arc heating of each of the three coaxial electrodes, and also the combination of these two methods were used.

Maximum electric power delivered to the corium in the reactor vessel lower head model, may reach 75 kW.

There were provided irrigation of the lower head model (LHM) lateral surface, LHM immersion into the pool with running water and irrigation of corium surface.

The lower head model was equipped with the thermocouples for measuring temperature field on the wall thickness and with the LHM wall displacement/strain gages.

To reduce load impact on the electrodes at the time of corium discharge to the MR, the intermediate trap at a height of near 40 cm over the LHM internal surface was installed. The MR diagram used for tests IVR-AM is demonstrated in Fig. 4.

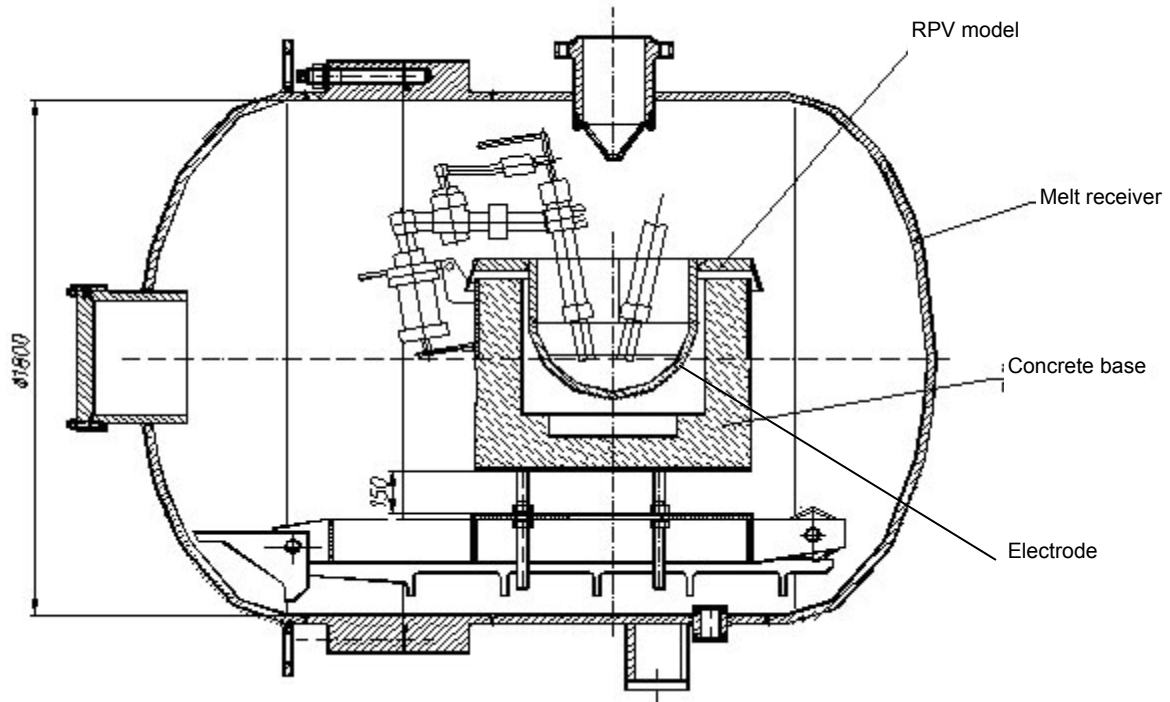
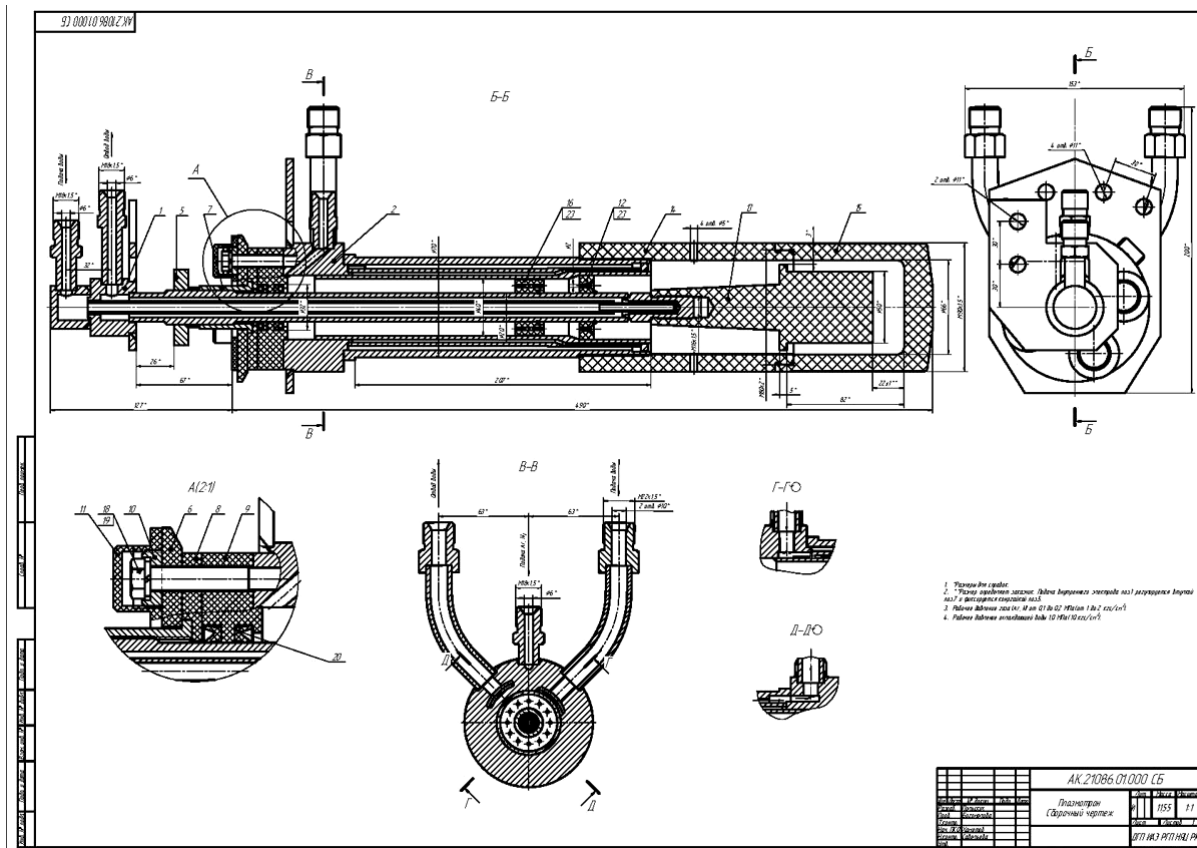


Figure 4 – The MR used in the IVR-AM tests

In the course of the resulted data analysis it was found that heating of the corium by the method of electric current passing through the corium, first of all, creates material uncertainties in analytic description of the heating process due to non-uniformity of corium electrical resistance on the pool volume and strong dependence of the parameter on temperature. Secondly, the efficiency of such heating is very low due to significant loss of energy in the supply lines. Considering the above, during the preparation of the tests within the project schedule, it was decided to simulate decay heat in the corium pool only at the expense of coaxial plasmatrons heating. At that, number of plasmatrons was increased from 3 available to 5, and the coaxial plasmatrons construction itself was modified in order to increase the power of the single plasmatrone and to enlarge the duration of uninterrupted work (see. Fig. 5). To provide electric supply of the additional plasmatrons, the additional equipment was purchased and assembled.



- 1 – electrode internal; 2 – electrode external; 5 – check nut; 6 – flange; 7 – control sleeve; 8 – washer;
- 9 – sleeve; 10 – locking pin; 11 – cap; 12 – spacing sleeve; 13 – internal nozzle; 14 – graphite sleeve;
- 15 – external nozzle; 16 – sleeve; 23 – closing ring.

Figure 4 – The coaxial plasmatrone diagram

For increase in efficiency of heat exchange between the plasmatrone surface and corium, the plasmatrone diameter was increased from 70 to 90 mm. More uniform warming up of the corium pool was able to reach at the expense of the semielliptical lower head model that is typical for VVER reactor design (see Fig. 6).

In the context of the changes described above, the water- and gas supply systems of the experimental facility were improved, and also the test facility IMS was finished.

Total capacity of the device for simulating decay heat after its improvement reaches 90 kW.

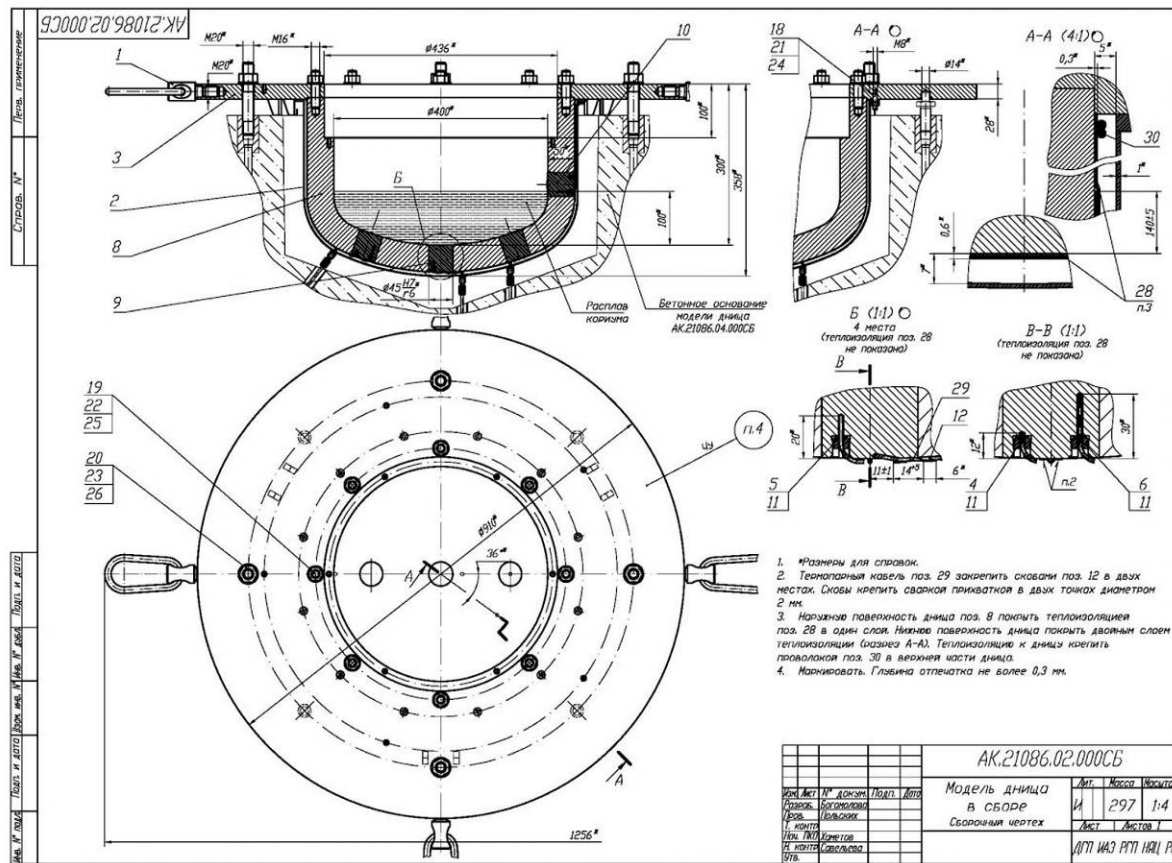


Figure 5 – RPV lower head model

2.3 Experimental section

For correct modeling of the processes at the corium melt retention in the reactor pressure vessel, the pre-test calculation of the RPV model was made based upon the design and parameters of the decay heat simulator. The objectives of the calculations were:

- Characterization of the molten pool, thermal and stress-strained state of the lower head model.
- Optimization of melt heating conditions and delivery of recommendations for electrodes arrangement and model geometry.

Calculation Methodology:

- ✓ Variants calculation of molten pool thermal-hydrodynamics with different model geometries and electrodes arrangement using the DYMELT code:
 - The problems of melt hydrodynamics with consideration for melt/crystallization and thermal conductivity in the solid wall were solved simultaneously;
 - 3-dimensional array (1/10 part of the lower head model – sector 36°)
 - Quasi-steady condition (pseudo-viscosity method)
 - Laminar convection regime (Navier - Stokes system of equations)
- ✓ ANSYS-based calculation of the model heat condition.

The problem was calculated with the assumption of the convection stream-line. The indirect confirmation of the fact that this approach is right is that the stable steady-state stream-line convection was resulted from the calculations. The calculators consider that the existence of numerical instabilities is the sign of the fact that under the given conditions transition to the turbulent regime is taken place, and we need either to use the turbulence models or to proceed

to DNS - to numerical simulation of turbulence by solution of the complete non-stationary system of Navier-Stokes equations with the use of very fine detailed grids and small time steps. That was not observed in our case; therefore we consider that the laminar approach is correct. In the basic calculations the heat-hydrodynamics of the melting pool with consideration of melting/crystallization and temperature condition of the wall was calculated together (by means of the DYMELT code). However, in some calculations, to study the influence of the wall thickness, heat insulation, and etc., the temperature state of the vessel was determined independently of the heat-hydrodynamics of the molten pool by means of the ANSYS code on the basis of heat flux data on the corium/wall boundary. These heat flux data were obtained from the joint calculations. The stress-strained condition will be tested after selection of the final model design.

Basic RPV model (Figure 7)

Model characteristics:

- Semi-elliptical lower head;
- Inner diameter – 400 mm;
- Wall thickness – 90 mm;
- Number of heaters – 5;
- Minimum distance from lower heater face to model inside – 10 mm;
- Distance between heater and model axes – 120 mm;
- Heater diameter – 90 mm;
- Height of heater active region – 45 mm;
- Height of the heater lower passive region – 10 mm;
- Distance from the top heater active region point to corium surface – 5 mm;
- Corium surface - heat shield distance – 25 mm;
- Power of one heater – 18 kW, total power - 90 kW;
- Corium mass - 64 kg

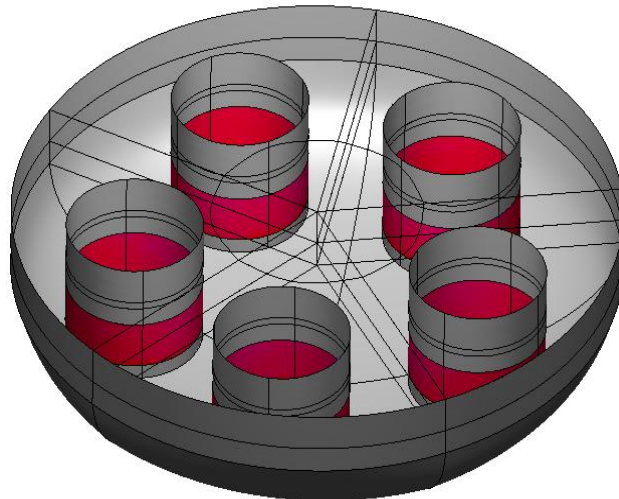


Figure 7 – Diagram of basic model

It should be noted that in the given design the heaters with large active surface area are failed in use (that is bad for their efficiency/life) because of the bottom rounding. But the lateral model dimension remains too great – non-optimum shape of the desired melting pool in the limitation of electrical power or, in other words, poor relationship of power and surface area of the melting pool heat transfer.

In the picture the geometry of the calculated region is shown in isometrics. Red-colored zones - active elements of the heaters (i.e. energy release region).

Boundary conditions

- Outer water-cooled surface of the lower head model - 100°C;
- Heat removal with irradiation occurs from the upper corium surface through transparent gas to the thermal screen and to the lateral model surface;
- The thermal screen is ideal (heat flux from its upper surface is zero);
- The uniform heat flux is specified on the heat-emitting surface of heaters;
- The remaining surface of heaters is insulated;
- There is no heat leakage upwards the heaters.

Boundary conditions are somewhat conservative, i.e., they underrate heat transfer (that is about the shield and deficiency of heat sink on the heaters). I.e. in reality the melting pool will be less, and wall temperature will be lower.

Thermal parameters

- Solidus temperature 2150° C (corium C-30);
- Corium liquidus temperature 2300°C;
- Thermal conductivity of solid/liquid corium 3.3 W/m·K;
- Thermal conductivity of steel 30 W/m·K;
- Thermal conductivity of corium and steel is independent of temperature;
- Corium emissivity factor, internal surface of the model and thermal screen – 0,8;

It should be mentioned that the dependence of thermal conductivity factor on temperature is not used, since we have no sufficiently reliable data on this dependence, but the value itself corresponds to the averaged data resulted from the RASPLAV Project.

Calculation data of basic model

Figure 8 shows the doubled calculated sector - $2 \cdot e' = 72$ degrees. The lower melt surface is green-colored, and upper – transparent. These two surfaces are connected on the edge of the figure. Arrows show value and direction of melt velocity in the point from which they start. Their crossing of the upper melt surface does not mean that the melt overflows through its own boundary, but only the fact that the speed in the point is sufficiently great.

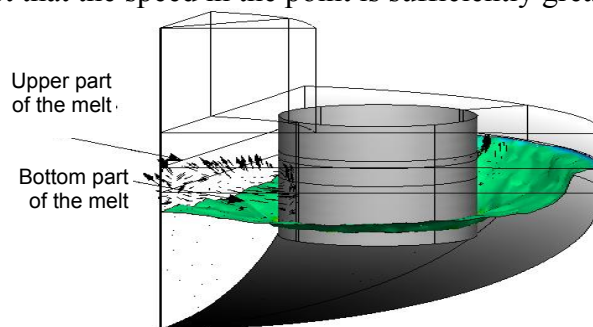


Figure 8 - Melt pool shape

The results of the calculation are shown in Figures 9 ... 11.

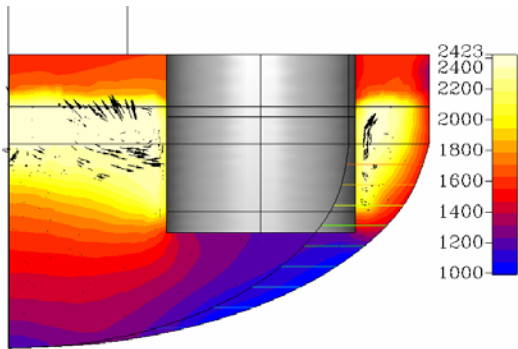


Figure 9 - Temperature field of corium in the section through the electrode axis

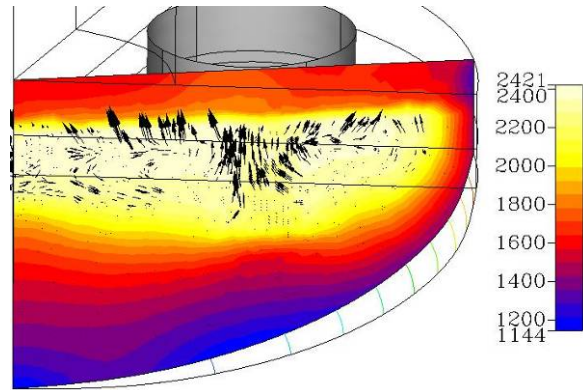


Figure 10 - Temperature field of corium in the section turned for 18°

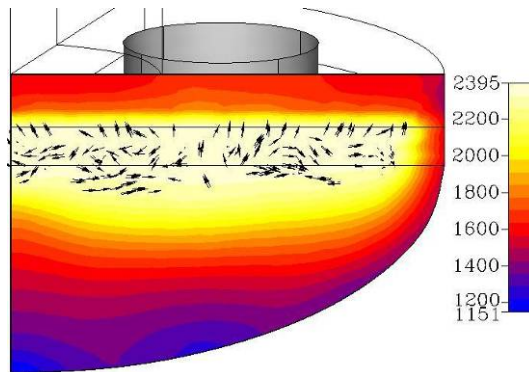


Figure 11 - Temperature field of corium in the section between the heaters

Bottom corium crust in various sections is shown in figures 12 ... 14.

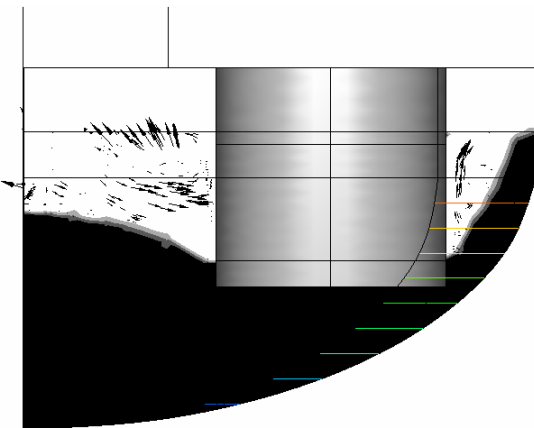


Figure 12 - Thickness of crust in the section through the heater axis

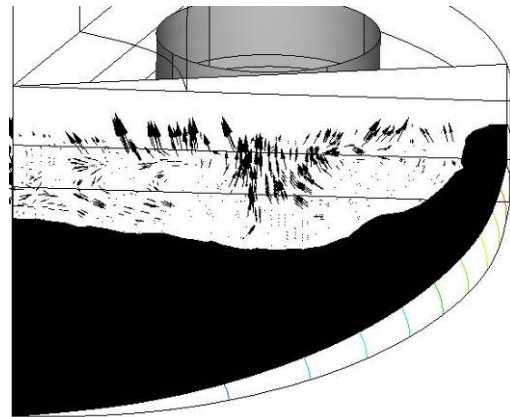


Figure 13 - Thickness of crust in the section turned for 18°

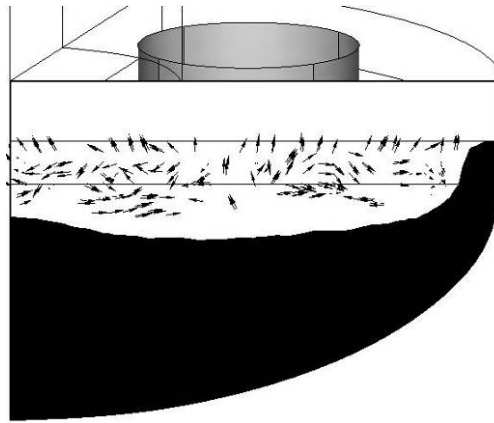


Figure 14 - Thickness of crust in the section between the heaters

The temperature field on the internal surface of the RPV model is shown in Figure 15. Apparently from figure, the temperature does not exceed 700°C. Hence, for creation of conditions for chemical interaction between corium and steel it is necessary the external thermal insulation of the RPV model.

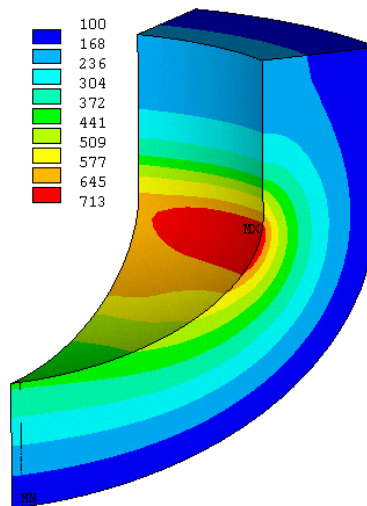


Figure 15 - Temperature field in the RPV model

Calculation with external insulation

- Only temperature state of the wall free of adjoin hydrodynamic problem was calculated.
- Heat flux distribution on the internal surface, received during combined calculation without heat insulation was used as the boundary condition.
- Heat insulation - ax symmetrical zone on the external lower head model surface (see also next slide)
- Thermal insulation is perfect

Results of calculation are shown in Figure 16.

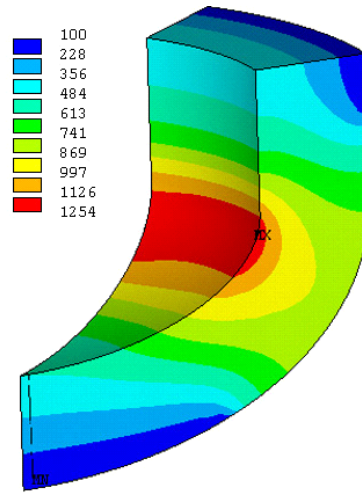


Figure 16 - Temperature field in the lower head model with partial thermal insulation

This figure illustrates, that it is possible to increase essentially temperature of an internal surface of model using thermal insulation (up to ~1200°C).

Main results from the calculation of the basic model

- Heating of the lower head model is impossible;
- The molten pool is small, considerable mass of the solidified corium is located under the pool. The elliptical part of the lower head model is "does not work" in fact.
- Temperature of the internal surface of the model, in the absence of the external insulation, does not exceed ~700°C.
- The most thickness of the model and the resulting heat flow along the wall leads to the need to insulate the most part of the surface. The maximum temperature of the internal surface of the model is about 1200°C.
- When we reduce the wall thickness, then the smaller area is insulated, but the molten pool becomes substantially less.

Effect of thermal insulation of the external surface of RPV model

The calculations are fulfilled for the RPV model $D_{inner}=400$ mm, 5 electrodes, power $N=90$ kW, $M_{melt}=60$ kg, thermal screen apart 25 mm from the melt surface. Thermal flux distribution along the internal surface of the model is gained by the results of thermal-hydraulics calculations of the melt. The case of lack of the heat insulation and the model wall thickness 90 mm is shown in Figure 17.

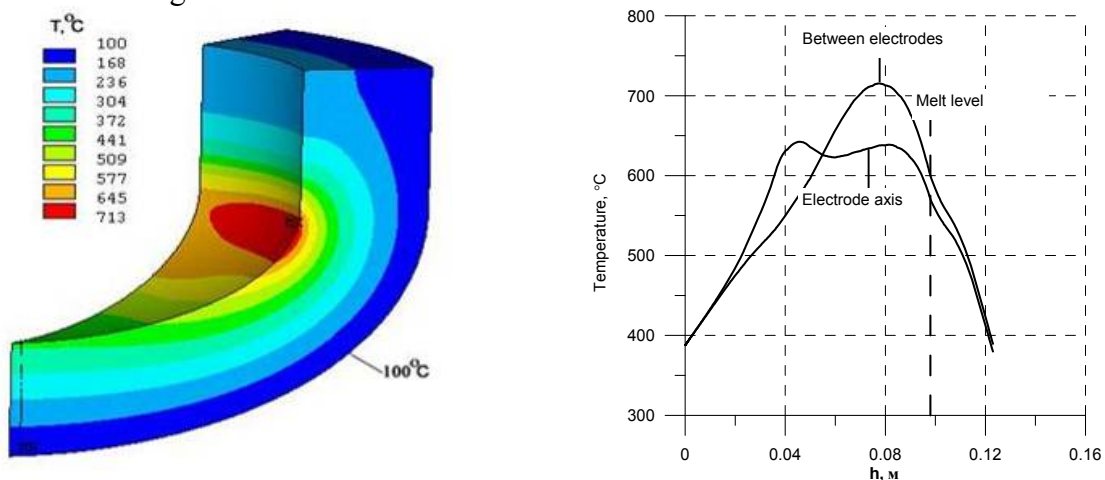


Figure 17 – Distribution of temperature on the internal surface of model without heat insulation

The results of the RPV model calculations with different variants of external heat insulation are given in Figures 18 ... 23.

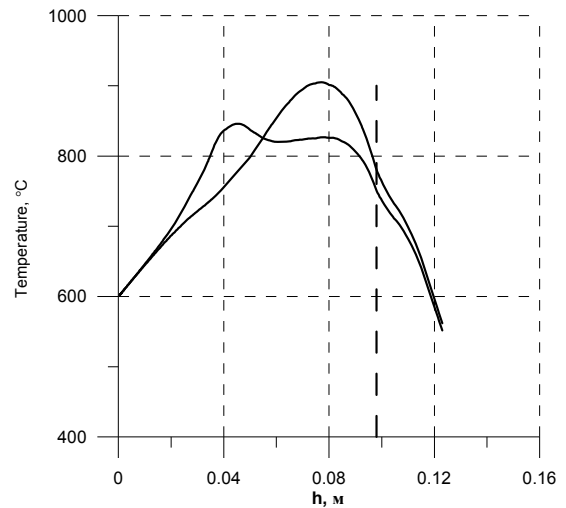
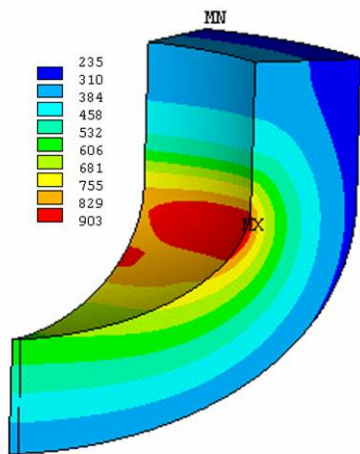


Figure 18 – Distribution of temperature on the internal surface of model with thermal insulation $\lambda/\delta=400$

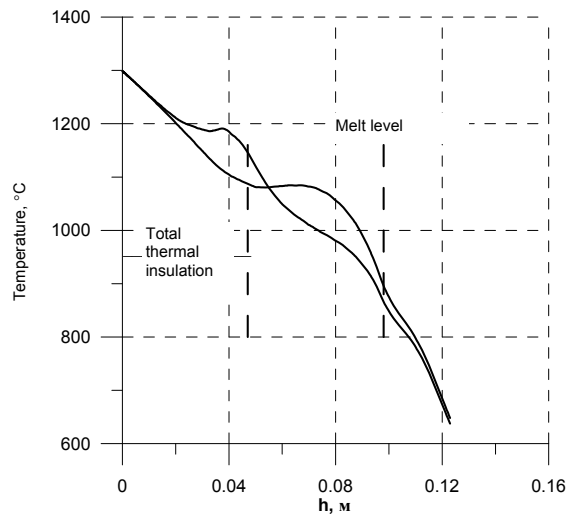
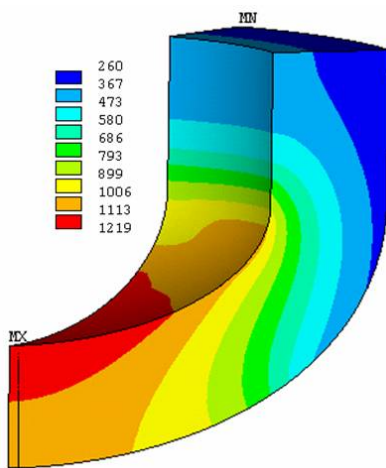


Figure 19 – Total thermal insulation on the surface up to h=44 mm Remaining insulation - $\lambda/\delta=400$

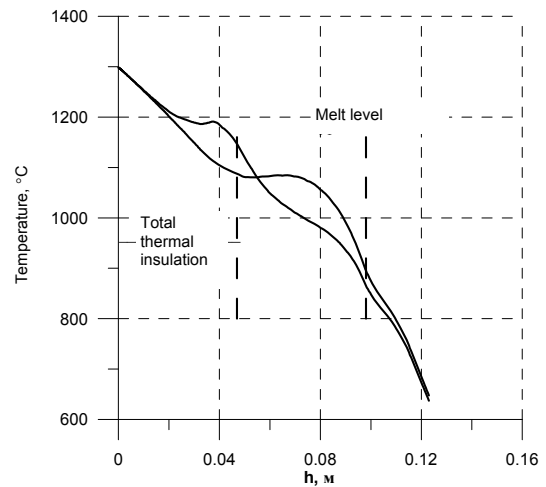
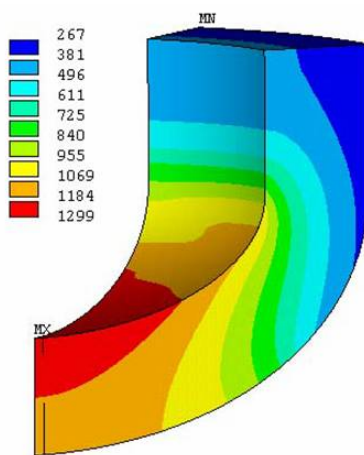


Figure 20 – Total thermal insulation on the surface up to h=47 mm Remaining insulation - $\lambda/\delta=400$

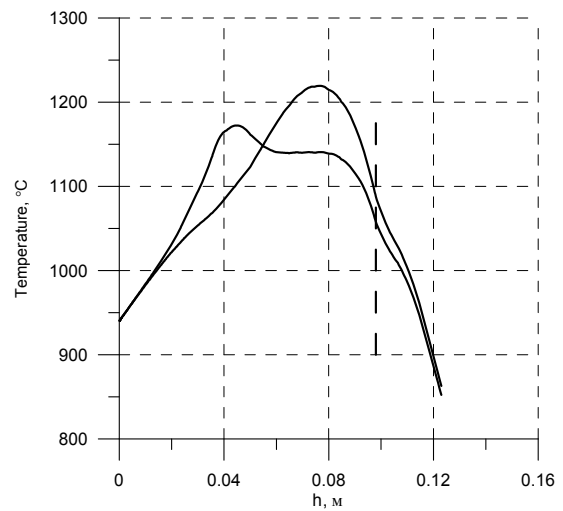
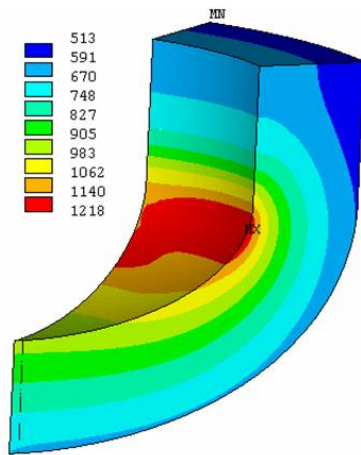


Figure 21 – Thermal insulation, $\lambda/\delta = 150$

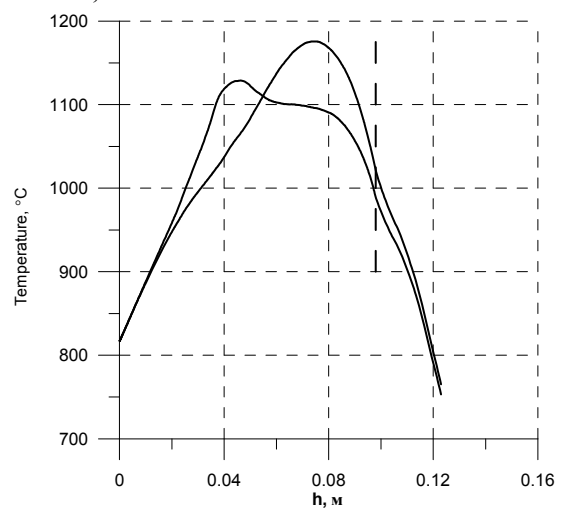
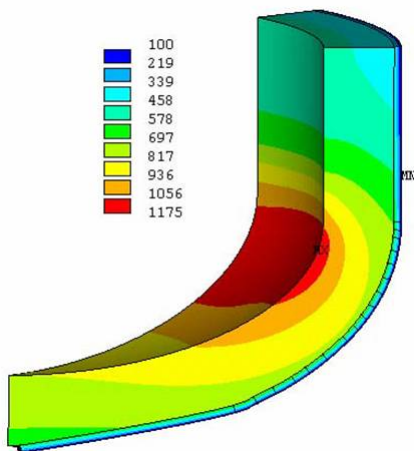


Figure 22 – Thermal insulation, $\lambda/\delta = 200$

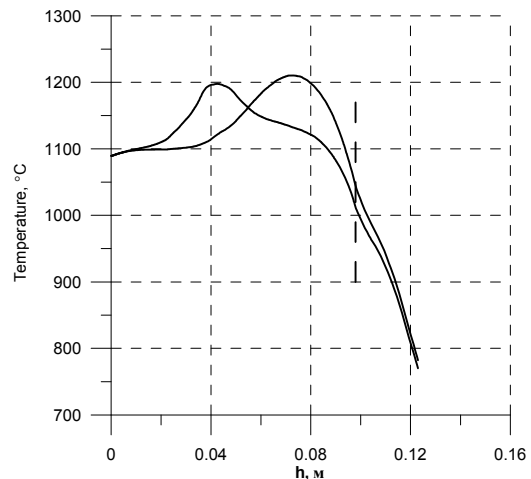
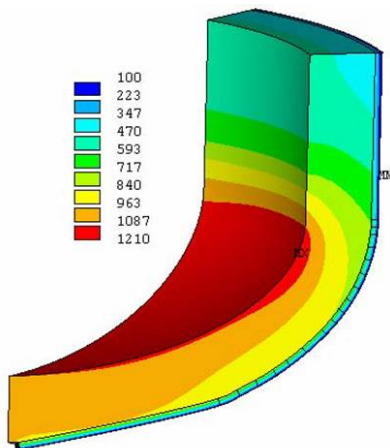


Figure 23 – Thermal insulation $\lambda/\delta = 100$ along the length from the centre 120 mm, thermal insulation $\lambda/\delta=200$ on the remaining surface

Based upon the above calculations we may conclude as follows:

- 1) The choice and allocation of thermal insulation on the external surface of the model can influence the magnitude and distribution of temperature on the interior surface of the RPV model via.
- 2) Thickness of thermal insulation depends on its thermal conductivity: the higher thermal conductivity, the thicker thermal insulation.

- 3) The thinner the wall of the RPV model, the thicker thermal insulation.
- 4) We may achieve uniform allocation of temperature on the interior surface through non-uniform distribution of thermal insulation (along the height of the model), including, the "complete" heat insulation on a part of the external surface of the model.
- 5) The assurance of insignificant contact thermal resistance between the model and thermal insulation, and between the thermal insulation and the shell (on the part of water cooling) is needed.
- 6) Computational accuracy of the optimal heat insulation depends on the accuracy of thermal-hydraulics calculations of the melt which, in turn, depends essentially on:

- the accuracy of the energy release field nearby the electrodes;
- the position and emissivity of the screen (screens) over the melt surface.

Thereby, preliminary calculation of the temperature fields in the reactor pressure vessel model at existing power of the heater, corium mass and the experimental facility size demonstrated that during the experiments the temperature in the "corium/steel" interaction area does not exceed 500 °C, and corium proportion in the liquid phase does not exceed 50% (if there is external cooling of the model with continuous water flow) and that is obviously insufficient for modeling of the physical-chemical processes at corium melt retention in the vessel. The problem was solved through the insulation of the external surface of the RPV model. The optimal insulation material was chosen on the basis of the results from the supporting tests.

Experiments on determination of the insulation thermal conductivity

In the course of Tests K-1, K-2, K-3 и K-4, carried out in the VCG-135 test facility, the thermal conductivity of candidate materials intended for creating the thermal insulating layer between the external wall of the "Lava-B" facility vessel model and water flow cooling the LHM was determined.

As the thermal insulation the fiber-glass and graphite cloths were tested.

Water-cooled calorimetric assemble used in these experiments (see also the diagram in Figure 24) was equipped with three thermocouples for measuring temperature of the external and internal surface of the steel sleeve, as well as to measure external wall temperature of the cooled cylinder.

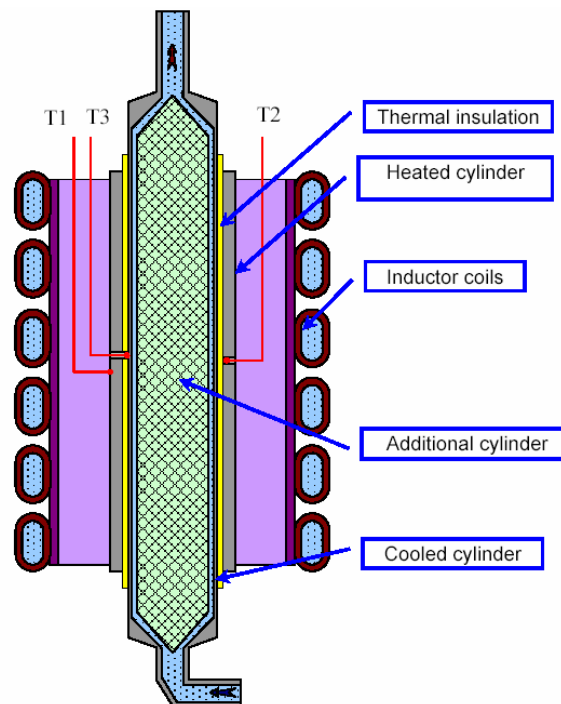


Fig. 24 – Diagram of the experimental device

Heating element of the system is the steel bushing that is heated by means of the eddy currents generated from running of the test facility induction coil. The heat removal from the system is performed through water cooling of the internal cylinder wall. When supplying voltage to the inductor and when heating the steel sleeve, a temperature differential must be generated between the sleeve and the water-cooled cylinder.

It was supposed that with the known power, spent for heating up of the device, and the measured temperature drop on the external and internal surface of heat insulation, the thermal conductivity of the candidate materials is found from the following relations:

$$Q = \frac{2\pi\lambda \cdot l}{\ln(d_{out}/d_{in})} (T_{in} - T_{out}),$$

where Q – power, spent on heating of the device;

λ – desired thermal conductivity of the material;

d_{in}, T_{in} – accordingly the diameter and temperature of the internal surface of the heat insulation;

d_{out}, T_{out} – accordingly the diameter and temperature of the external surface of the heat insulation.

Some parameters of the device are included in Table 1.

Table 1 – Parameters of the device for measuring heat flux

№	Parameter	Value
1.	Height of the inductor, mm	100
2.	Inner diameter of the inductor, mm	90
3.	Frequency of the high-frequency oscillator, kHz	66
4.	Size of the steel sleeve $d_{in} \times d_{ex} \times h$,	40×46×100
5.	Displacer diameter, mm	26
6.	Size of the cooled cylinder $d_{in} \times d_{ex} \times h$,	36×39×150
7.	Inlet water temperature, °C	15-20
8.	External heat insulation	«Supersil»
9.	Thickness of the tested insulation, mm	0,35

Thermohydraulic parameters of the calorimetric assemble are represented in Table 2.

Table 2 - Thermohydraulic parameters of the experimental assembly

№	Parameter	Value
1	Calorimeter open flow area S_p , mm ²	486,7
2	Size of the cylinder $d_{in} \times d_{ex} \times h$,	40×46×100
3	Water flow rate Q , l/s	0,208
4	Diameter of the inductor D , mm	95

Because of the large water flow rate through the calorimeter, the temperature differential between the inlet and outlet of water was not measured by the thermocouples (CC). The average water temperature, measured on the cooling inlet header (sensor TSP) was 16°C.

In the course of each of the carried out experiments were realized 3 (three) regimes with achievement of stabilization of the device thermal parameters at the condition of maintaining the fixed level of the power, supplied to the assembling:

- regime 1, the power supplied to the device was 0.5...0.7 kW;
- regime 2, the power supplied to the device was about 1.5 kW;
- regime 3, the power supplied to the device was 3.5...3.7 kW;

The measured values of the thermocouples indications of the device under condition 3 and power, supplied to the device, are included in the table below (Table 3).

Table 3 – Test parameters

№	T1, (oC)	T2, (oC)	T3, (oC)	Power, kW
K-2	680	630	300	3.35
K-3	670	620	290	3.55
K-4	670	640	570	3.65

The experimental data obtained were processed according to the above procedure. According to the measured differential in the temperature and power, supplied to the device, the thermal conductivity factors of the materials being investigated were determined. The thermal conductivity factors of different steels are known, they are represented in various reference books. Together with the determination of the thermal conductivity of the materials being investigated, the thermal conductivity of the steel bushing was calculated for evaluating the correctness of the procedure

Electromagnetic analysis of the VCG-135 testing bench (the calculations are described in the section dedicated to the analysis of the parameters of the process for electrode nozzles coating) demonstrated that the energy release field created by the testing bench inductor, has high altitude non-uniformity. Thus, energy release in the central part of the steel bushing of the device exceeds energy release in the vicinity of bushing ends one and a half times. The device thermocouples are installed on the level of its height center; therefore the values of the power supplied to the device, used in relationship (1), were one and a half increased when calculating the thermal conductivity factors.

It is obtained that the heat fluxes resulted from the experiments under regime 3 composed 460...480 kW/m². These fluxes are somewhat less than heat fluxes on the LHM external wall and equal to about 780 kW/m². However, making analysis of thermocouple T3 indications, which under regimes 2 and 3 of the experiments compose 200...300°C, we may assume that the cooling water velocities are insufficient, and the film boiling of underheated water occurs in the vicinity of hot wall. In continuation of the experiments, the liquid flow rate nearby the wall can be increased by the arrangement of the displacer of larger diameter in the water-cooled cylinder for the exception of water boiling, for more stable cooling of the construction

The calculated thermal conductivity factors of steel, fiberglass fabric and graphite cloth under regimes 2 and 3 are tabled below (see also Table 4).

Table 4 Thermal conductivity of used materials

№	2 shelf			3 (maximum) shelf		
	λ steel, W/(m K)	λ heat insulation W/(m K)	λ/δ	λ steel, W/(m K)	λ heat insulation, W/(m K)	λ/δ
K-2	26.7	0.18	514	22.4	0.21	600
K-3	14.2	0.23	657	23.7	0.22	629
K-4	11.7	2.63	7514	40.6	1.56	4457

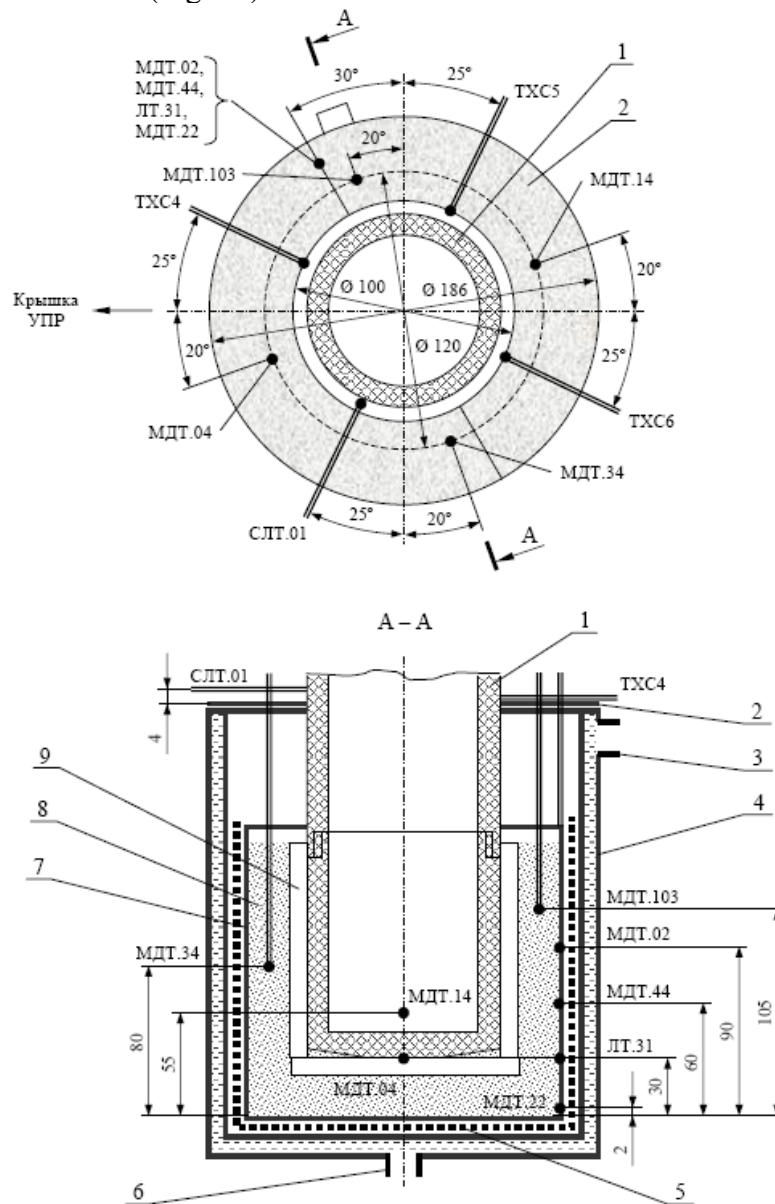
Making analysis of the experimental data we may say that Test K-2 was the most successful. In this test the thermal conductivity factors of steel and heat insulation under the second and third regimes have insignificant differences. Moreover the calculated steel thermal conductivity is in good correlation with the data presented in the reference books. The data obtained under regime 3 of Test K-3 coincide with those obtained from Test K-2.

On the basis of the experimental data we may say that the thermal conductivity values of fiberglass fabric lie over the range 0.18...0.23 W/(m K).

Test K-4 carried out to study the thermal conductivity factors of graphite cloth was less successful: the thermal conductivity values both steel and graphite cloth under regimes 2 and 3 have significant differences. This, possibly, is resulted from poor closing of thermocouples or mounting of the device. That is seen from the behavior of thermocouple T3, its indications began sharply to rise on ~ 450 second of the experiment, and in consequence the significant temperature differential of the heat insulation, fixed under regime 1 and at the initial stage of

regime 2, subsequently became comparable with a temperature differential of the thickness of the steel bushing.

The insulation efficiency was experimentally tested in the large-scale tests (TOP series) with heating of 12 kg prototype corium C-30 through the coaxial plasmatrone in the cell specially designed and manufactured (Fig. 25).



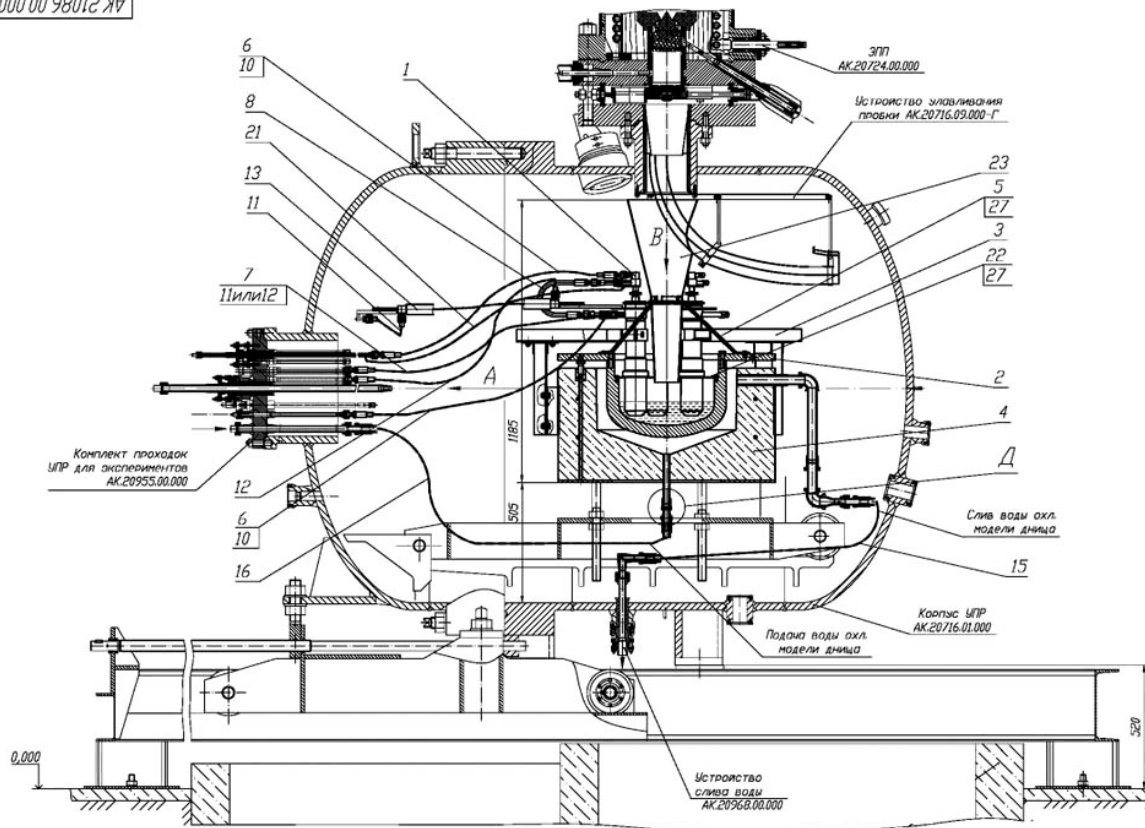
- 1 – composite graphite nozzle of the outer electrode; 2 – protective shield; 3 –cooling water outlet;
- 4 – cooling water jacket; 5 – glass fiber cloth; 6 – cooling water inlet; 7 – internal vessel; 8 – uranium dioxide pellets and zirconium dioxide power mixture; 9 – metallic zirconium.

Note: 1 – distance for the thermocouple of ch.p. СЛТ.01 is given from the shield top, 2 – distance for other thermocouples is given from the bottom of the internal vessel.

Fig. 25 – Experimental cell for TOP tests

The constructional diagram of the MR with the vessel model and the decay heat simulator installed in it is represented in Fig. 26.

AK.21086.00.0000СБ



1 –plasmatrons; 2 – flange of the vessel model; 3 – mechanism for fixing the block of plasmatrons; 4 – concrete base; 22 – thermal shield; 23 – director cone for melt discharge;

Fig. 26 – Constructional diagram of the "Lava-B" MR for performance of INCOVER tests

In consideration of the high cost of the products made of VVER vessel steel as well as the need to licensing the export/import of these products, it was decided to manufacture the vessel models from the ordinary carbon steel and the vessel steel samples are pressed in the most stressed areas of the model wall.

The preparation of the vessel models is illustrated in Figures 27a...27f.



a) Blank of the vessel model



b) Blanks of the vessel steel samples

Fig. 27 – Components of the experimental device



c) View of the vessel steel samples from the outside of the vessel model



d) View of the vessel steel samples from the inside of the vessel model



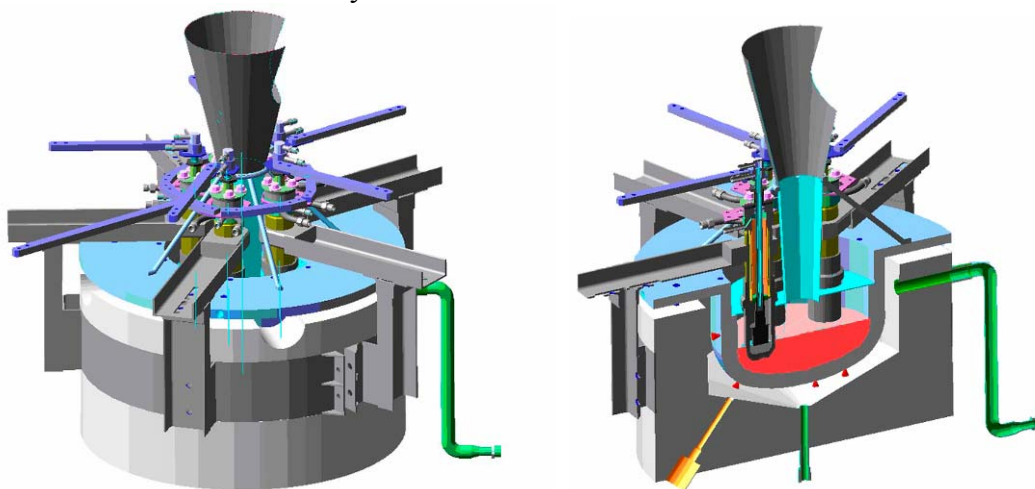
e) Steel shield of the insulation



f) Copper parts of the coaxial plasmatrons

Fig. 27 (cont'd) – Components of the experimental device

Figure 28 shows the appearance of the experimental section with the decay heat simulator and its location in the "Lava-B" facility.

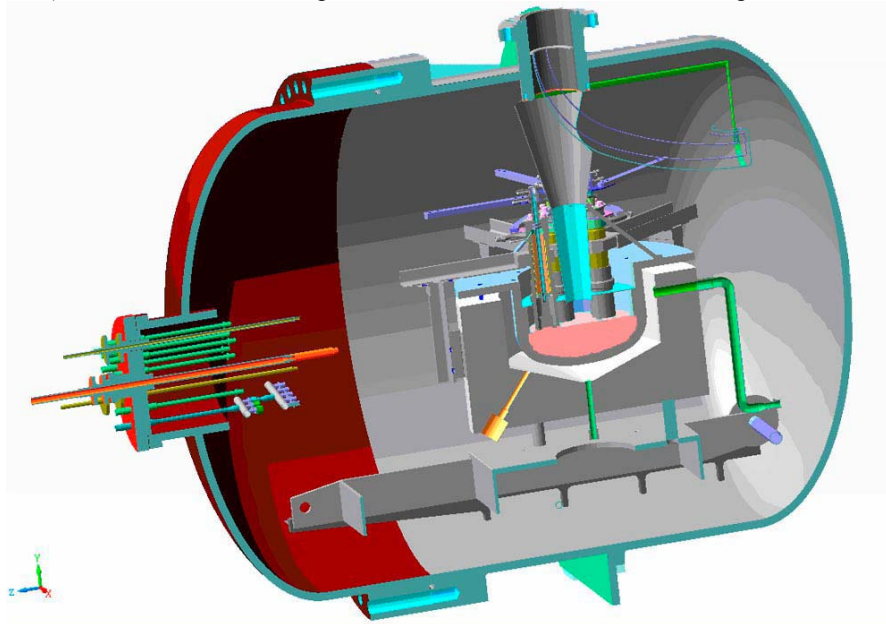


a) Ready-assembled experimental section

Figure 28 – General view of the experimental section for the integral tests



b) Concrete base of the experimental section with holders for the plasmatrons



c) Experimental section in the "Lava-B" pressure vessel

Figure 28 (cont'd) – General view of the experimental section for the integral tests

2.4 The small-scale test facility

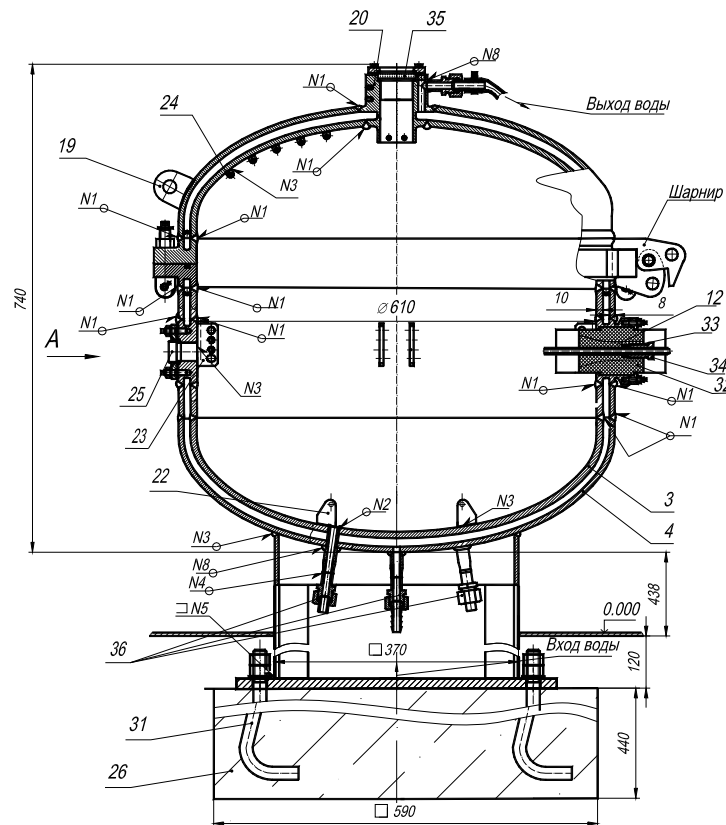
Preliminary tests on investigation of the EMF materials, the efficiency of the protective materials to prevent corium components/carbon interaction and on investigation of corium components interaction between themselves at their heating up to the melting point were performed in the small-scale induction VCG-135 test facility.

The technique for applying protective coating on the external surface of the coaxial plasmatrone working part being in contact with corium during the integral tests was tested in the VCG-135 test facility.

The VCG-135 working chamber enables one to put up to 150 g core materials mixture in the crucible. The heating up is conducted with the inductor powered from the generator of 66 kHz frequency. Maximum electric power of the generator is 60 kW.

The working chamber housing with the water-cooled wall withstands pressure inside the chamber up to 0,6 MPa.

The diagram of the VCG-135 working chamber is represented in Fig. 29. Fig.30 shows the appearance of the test facility with the generator and with the parameter registration system.



3 – internal shell of the pressure vessel; 4 – external shell of the pressure vessel; 12 – inductor current lead; 20 – optical window; 22 – experimental assembly clip; 23 – electrode holders; 26 – base.

Figure 29 – Working chamber of VCG-135



Figure 30 – Appearance of the test facility for the small-scale experiments

After the design, assembling and experimental work the operating characteristics of the "Lava-B" test facility was improved considerably, that enabled to perform the large-scale tests on investigation of the processes at retention of the prototype corium melt in the RPV model with heat fluxes through the model steel wall in the range 300...400 kW/m²V. The temperature at the "corium/steel" interaction boundary complied with the conditions of physico-chemical interaction of the test materials.

3. Calibration tests

To checkout the constructive solutions and to adjust the operating conditions of the vital functional parts of the "Lava-B" facility, different supporting experiments enabling to optimize the equipment for the performance of the large-scale integral tests, were carried out.

3.1 Testing of the electric melting furnace

The vital part of the "Lava-B" test facility is the induction electric melting furnace (EMF) designed for heating up/melting of 60 kg prototype corium and discharging of the melt produced in the experimental section. The primary experimental tasks for the above unit consist in correct choice of the technique for loading corium components in the melting crucible, checking of the heating mode (heating rate and power supplied to the inductor), determining of the "ready to discharge" melt moment, testing of the plug breaking device for opening the orifice in the crucible bottom. Another important task is the integrated testing of the EMF parameter measuring system (corium temperature and in-crucible pressure).

To realize the above tasks, there were performed two large-scale calibration tests. On the preparation of the tests the internal surface of the graphite crucibles was covered with the protective layer made of zirconium carbide avoiding chemical interaction of corium components and carbon "evaporating" from the graphite wall in the course of the EMF heating through the "hot crucible" method.

For the performance of the calibration tests the components were loaded in ratio given in Table 5 that corresponded to the composition C-30.

Table 5 – EMF crucible loading for the large-scale calibration tests

Материал	UO ₂	Zr	ZrO ₂	Total
Масса, г	45720	8815	5580	60115

The metallic zirconium was loaded in the form of a sheet covering the internal cavity of the graphite crucible, rods of about 30 mm diameter, length to 400 mm; uranium dioxide had the form of the BN-350 pellets (5,5 mm diameter and 10...12 mm length); zirconium oxide was of the form of fine-dispersed powder and was put in the cavity between the uranium dioxide pellets. Several melt loading steps are shown in Fig. 31.

The internal cavity of the EMF was pre-vacuumized and filled with argon. The repeated exhaust and argon-filling was performed at the initial stage of the EMF heating and maintenance at temperature about 400 °C.

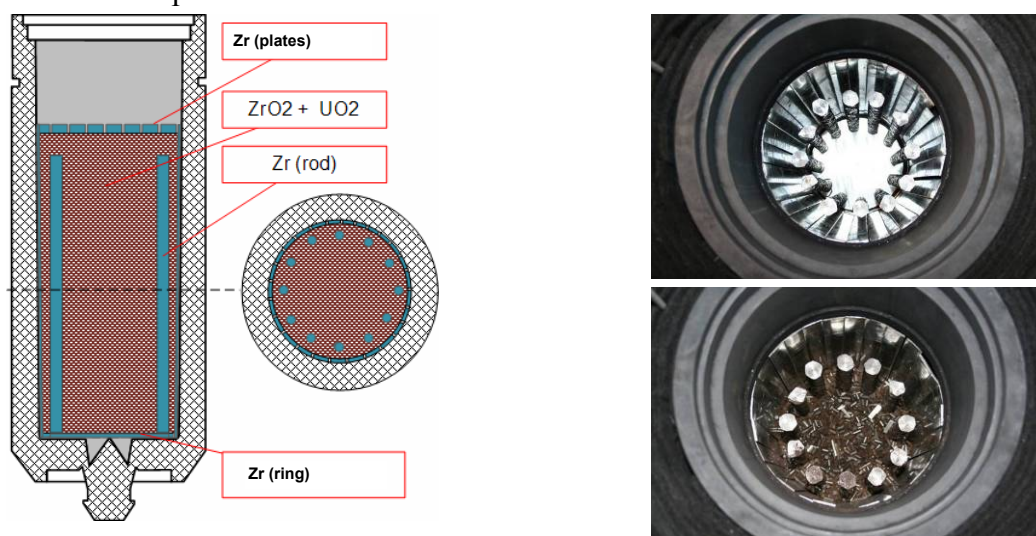


Figure 31 – Loading of the melting crucible before the large-scale test

The melting volume temperature was controlled through observation of the thermocouples indications installed on the lateral external wall of the graphite crucible and in the thermal

insulation layer enclosing the crucible. The temperature measurement for heating up corium components was performed by means of the infrared two-wave pyrometer of spectral ratio. At the initial heating stage (approximately to 2200 °C) the pyrometer’s indications were compared with thermocouple BP5/20 indications, installed inside the crucible in the field of pyrometer sighting.

3.1.1 First large-scale calibration test

The corium components heating diagram in the course of the first calibration test is represented in Fig. 32. Peak heating temperature was (according to the pyrometer’s indications) about 2600°C. Peak temperature reaching time was about 1 hour 20 minutes.

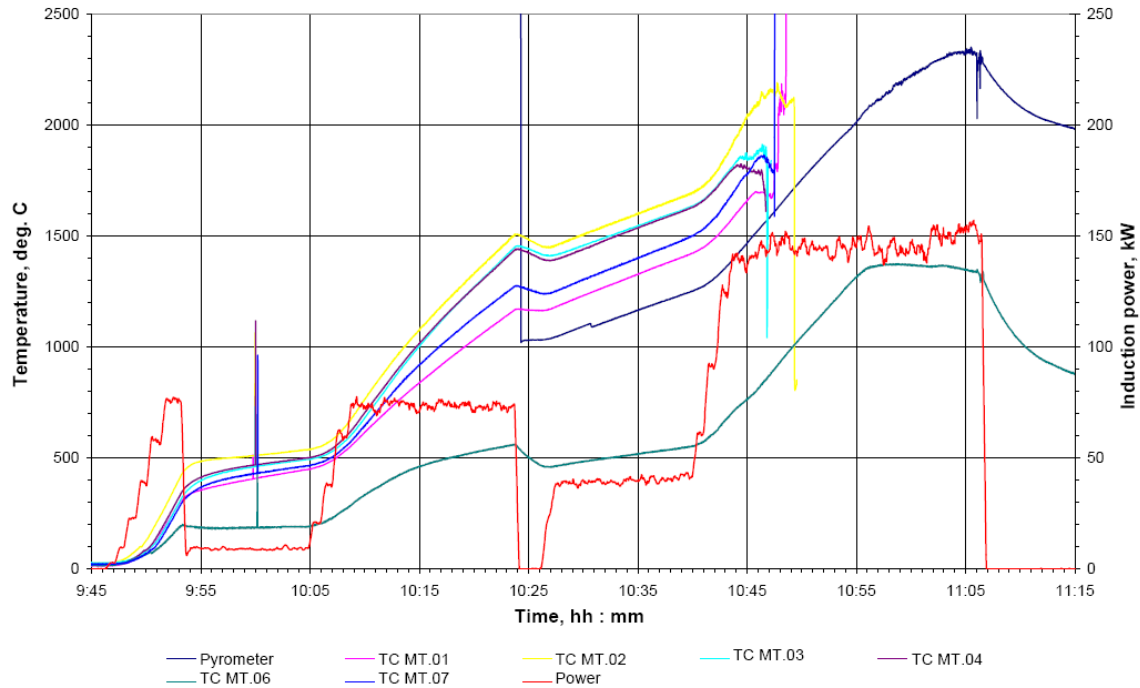


Figure 32 – The diagram of corium heating in the first calibration test

Unfortunately, the test was stopped in the fault in the inductor power supply system, and the power supplied was insufficient to reach complete melting of the components loaded and, consequently, to discharge the melt into the experimental section. In addition, as it was founded in the course the EMF disassembling after the test, the heating rate was too fast that resulted in emission of a part of the molten components (mostly, metallic zirconium) through the holes in the upper crucible lid to the side of the EMF gas drainage system. The result of the melting crucible disassemble is demonstrated in Fig. 33.

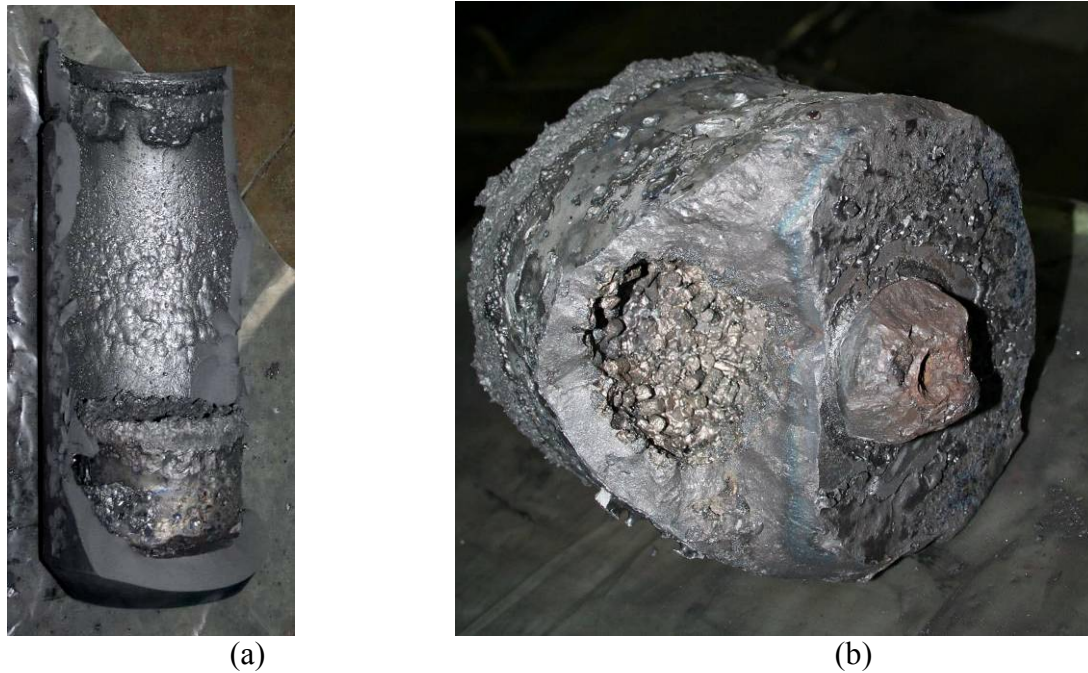


Figure 33 – Internal cavity of the crucible (a) and corium ingot (b) after the first calibration test

As we see in the figure there is no erosion of the internal wall of the graphite crucible that confirms the protective coating reliability and correctness of initial location of the components in loading. Mass of the solidified corium ingot was about 40 kg. The ingot was cut in the diametrical plane (see Fig. 34) and investigated in different points by the X-ray diffractometer method.



Figure 34 – Longitudinal section of the corium ingot

Main phases of the ingot material – a series of solid solutions: $U_{0.95}Zr_{0.05}O_2 \div U_{0.8}Zr_{0.2}O_2$. Low-zirconium in the solid solutions is explained both with emission of zirconium melt from the crucible through the drainage system and insufficient power given for loading during its heating up in the EMF.

In the sequel the ingot fragments were used for additional loading to the experimental section (further to the discharged corium melt) in the subsequent integral tests.

3.1.2 Second large-scale calibration test

During the preparation of the second calibration test there were performed preparatory operations similar to the first calibration test. In addition, the backup supply system was connected in case of an unexpected incident in the electric supply network, and the diagram of the initial loading heating up was specified with consideration of the drawbacks found in the previous experiments (see Fig. 35).

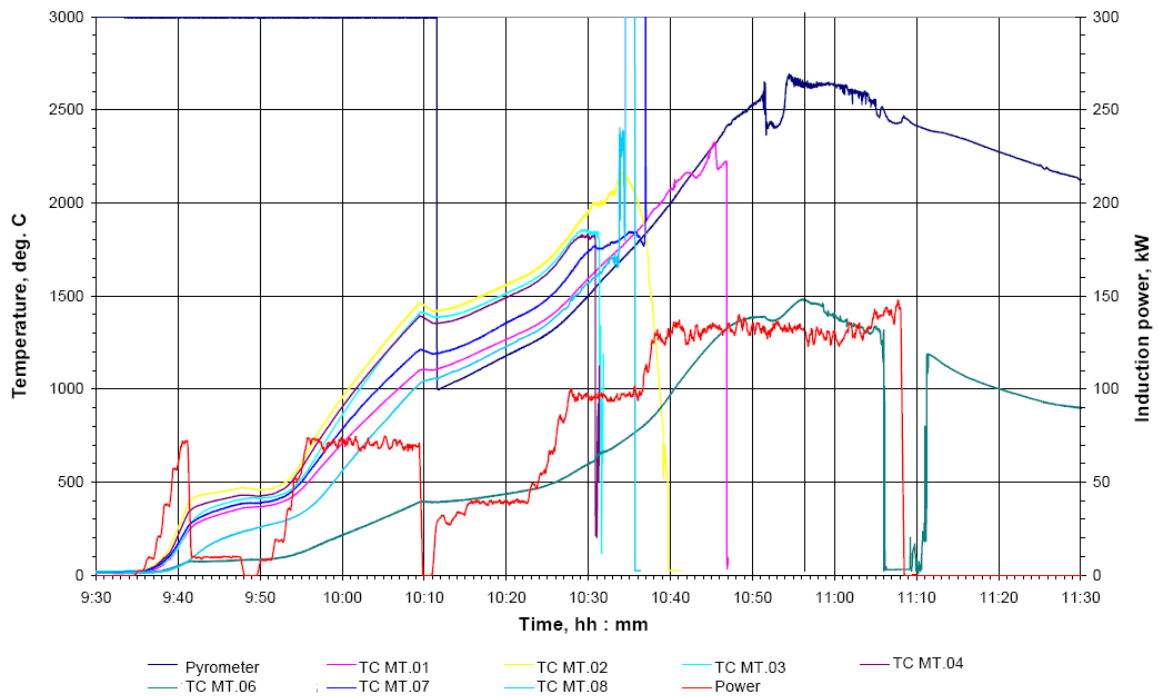


Figure 35 – Diagram of corium heating up in the second calibration test

In the second test the maximum corium temperature (2650 °C) in the melting volume reached in an hour and a half, but owing to faults in the plug breaking mechanism the melt was not discharged into the experimental section. We should remember that in heating up of the corium in the graphite crucible about two thirds energy of the inductor releases in the EMF graphite components owing to high graphite specific heat. Therefore, (when the orifice in the crucible bottom is closed) the crucible energy was continued to transmit to the corium. That resulted in the emission of practically whole melt from the melting volume to the upper drainage system. In the second test, before the attempt to drain the melt into the vessel model, 10 minutes before the start-up of the plug breaking mechanism, the device for modeling decay heat was actuated for preheating up of the model and to reduce the energy absorbed from the melt. As a consequence of 5 plasmatrons operation the model wall temperature increased up to 300 °C (see Fig. 36).

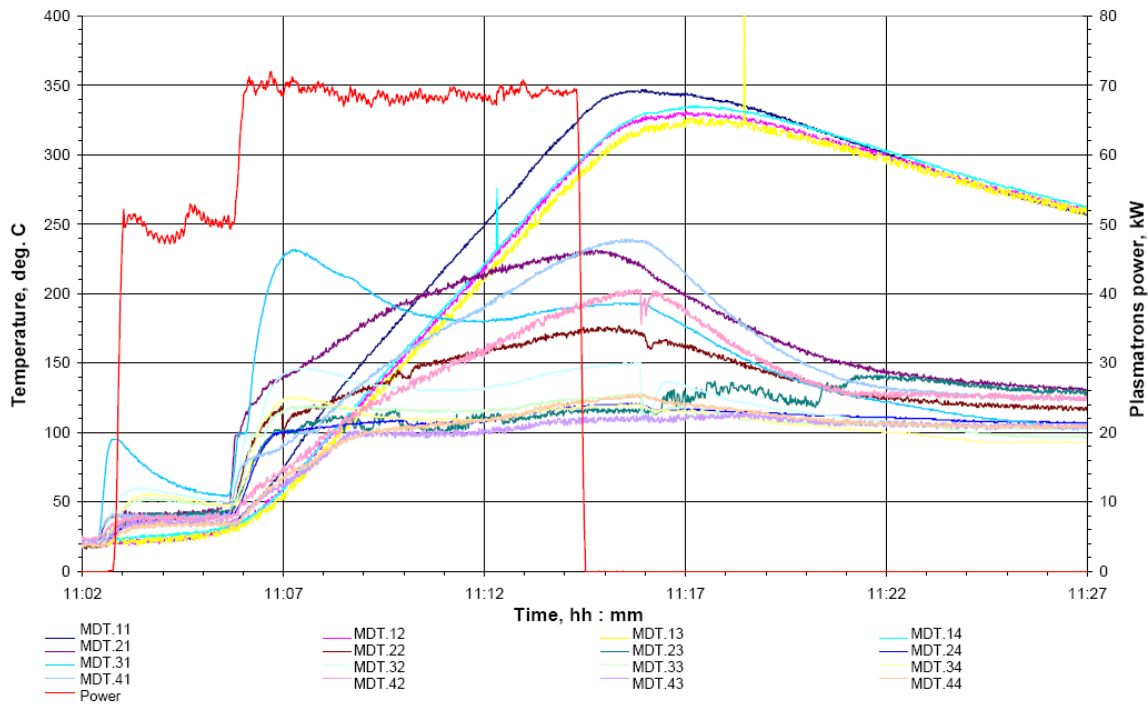


Figure 36 – Temperature of the vessel model wall in the second calibration test

Despite the large-scale calibration tests failure, their basis was used for the development of the corium heating/melting diagram in the EMF, as well as all "Lava-B" systems were adjusted for their reliable performance during the subsequent large-scale calibration tests.

3.2 Testing of coaxial plasmatrons

3.2.1 Testing of single plasmatrons without immersion into corium

Testing of the plasmatrons to specify geometry of the graphite nozzles and their life-time

Purpose of the test:

- definition of dependence of the plasmatrons power versus the distance between nozzles of the external and internal electrodes;
- definition of degradation rate of the composite graphite nozzle of the external electrode with outside diameter 90 mm and the graphite nozzle of the internal electrode with the working part diameter 46 mm at temperature ~2200°C in argon-gas medium;

Test conditions:

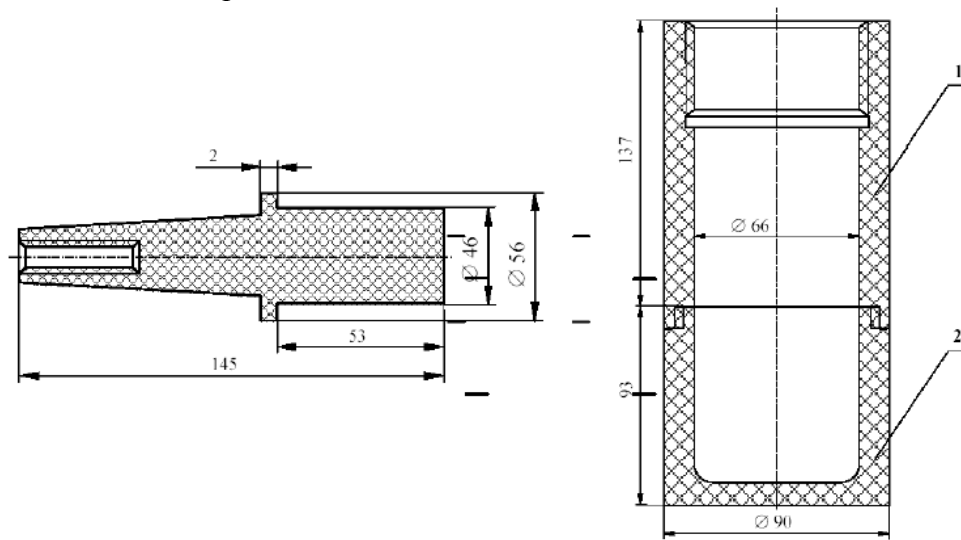
- maximum value of the plasmatrons operating current A up to 320
- value of voltage on the plasmatrons arc, V up to 70
- value of voltage of the plasmatrons "no-load running", V up to 140
- water flow rate through the plasmatrons cooling path, kg/s up to 0,2
- argon-gas flow rate supplied to the inter-electrode space, kg/s up to 0,001
- nitrogen flow rate supplied to the inter-electrode space, kg/s up to 0,0008

The work was conducted using one plasmatrone. The plasmatrone was installed on RPV model under an angle approximately 15° from vertical. The RPV model was disposed inside the MR. The cylindrical graphite nozzle of the internal electrode, shown in Figure 37a, and the composite graphite nozzle of the external electrode, given in Figure 37b, were fixed on the plasmatrone.

The ignition of the arc was performed by the special oscillator at supply of argon in the inter-electrode space with the subsequent change of argon-gas for nitrogen.

Six starting-ups of the plasmatrons were fulfilled. In the experiments the distance between the

end face of the internal nozzle and the external nozzle bottom from the inside was varied as follows: at the first start-up - 25 mm, second - 20 mm, third - 15 mm, fourth- 10 mm, fifth- 5 mm and at the sixth start-up - 30 mm.



a) Cylindrical graphite nozzle of the internal electrode with flat face

b) Composite graphite nozzle of the external electrode

Figure 37 – Graphite nozzles of the coaxial plasmatrons

Figure 38 depicts the change of the plasmatrons power depending on the distance between the bottom of the external electrode nozzle and the end face of the internal electrode. Maximum, minimum and mean plasmatrons powers are given in the figure. It is visible from the diagram that, from the distance 5 mm between the nozzles and up to 15 mm, the mean plasmatrons power is practically constant, and from the distance 15 mm between the electrodes nozzles the value of plasmatrons power increases with growth of the distance between the nozzles.

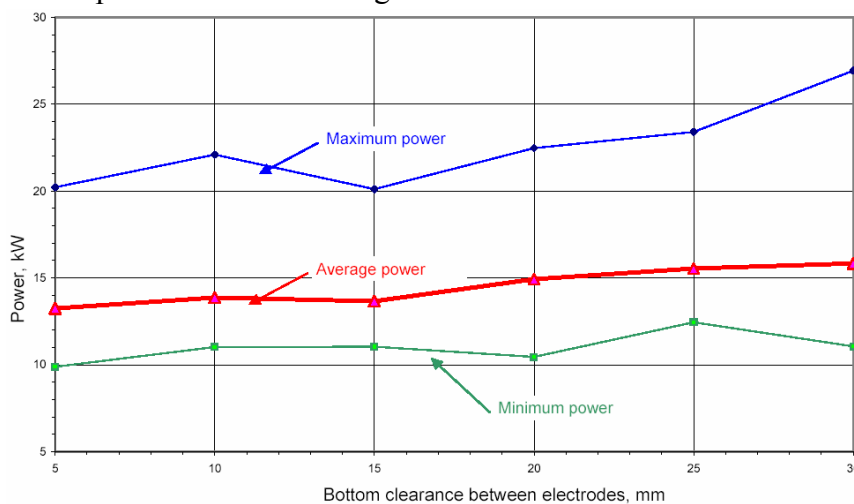


Figure 38 – Dependence of plasmatrons power on the distance between the electrodes

The plasmatrons was started-up for testing its life-time. As nozzles of the electrodes there were used the nozzles from the earlier experiments with clearance variation.

The operating time of the plasmatrons was 120 minutes. Parameters of the plasmatrons are given in Figures 39, 40. Temperature curves of the electrode external nozzle along the nozzle altitude are given in Figure 41.

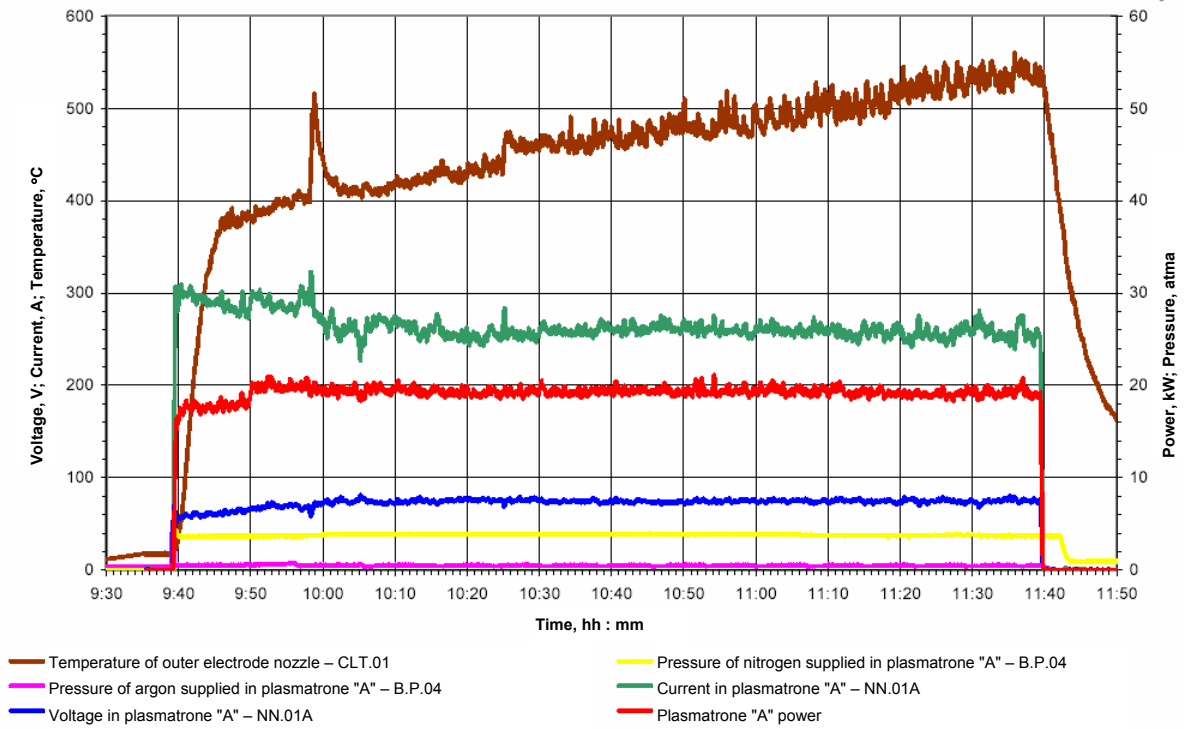


Figure 39 – Plasmatrone parameters on testing life-time

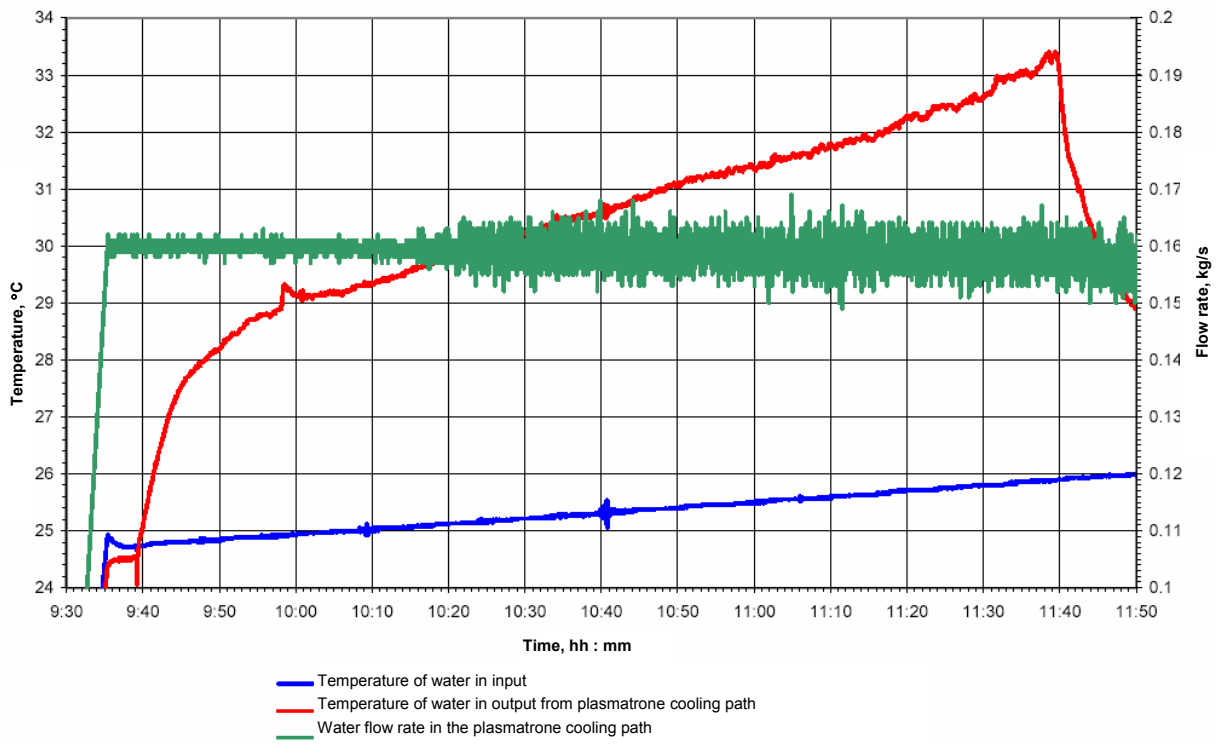


Figure 40 – Variation of cooling water parameters during the experiment

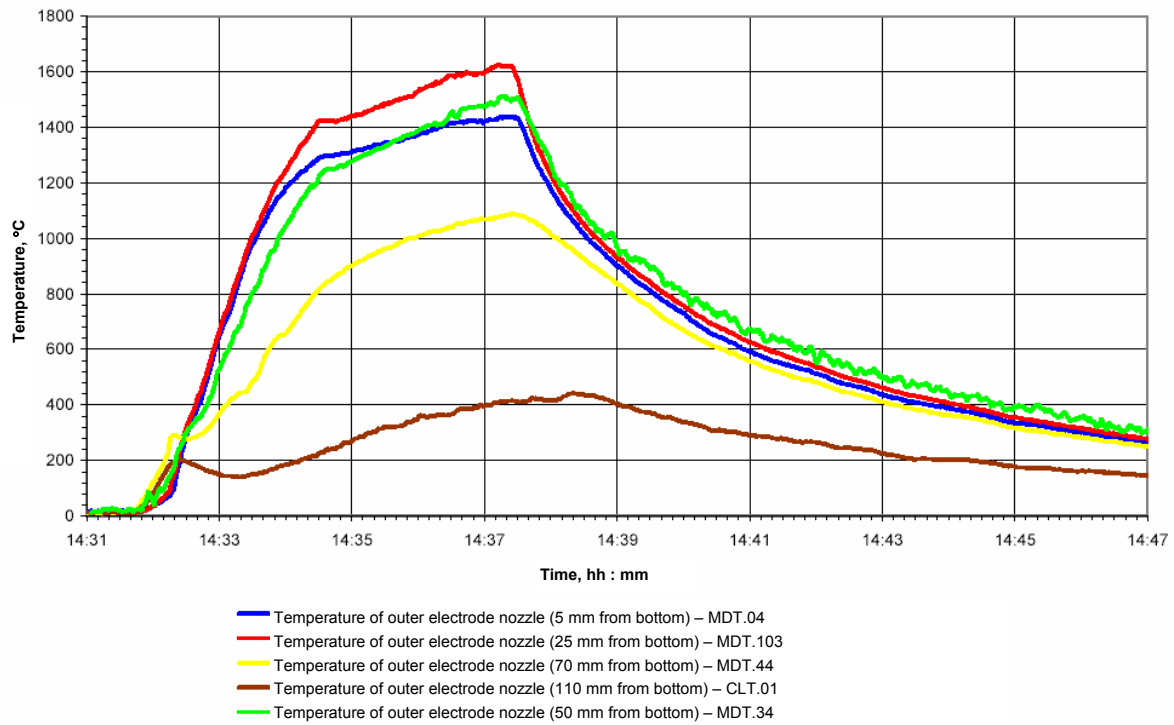


Figure 41 – Temperature of the electrode external nozzle

The plasmatrone parameters of the above group of tests are included in Table 6.

Table 6 – Values of the plasmatrone testing parameters

Parameter	Value						Life-time
	1 test	2 test	3 test	4 test	5 test	6 test	
Test							
Time of plasmatrons operation, mm : ss	3:33	5:34	3:49	3:43	3:25	6:0	120:0
Mean voltage of electrical arc, V	58,6	56,2	52,3	52,9	49,8	60,7	73
Mean current of electrical arc, A	264,7	265,6	261,4	261,8	266,9	262	264,2
Mean power of plasmatrons, kW	15,5	14,9	13,7	13,8	13,3	15,9	19,2
Maximum heating of water in the plasmatrons cooled channel, degree C	1,07	2,21	1,55	1,57	1,48	2,48	7,49
Maximum temperature of the graphite nozzle of the external electrode at the distance of 110 mm from the lower end, degree C	270	337	240	193	189	252	560
Weight of the graphite nozzle of the external electrode, g							
- before test	261	–	–	–	–	–	234,36
- after test	–	–	–	–	–	234,36	129,87
Distance from the bottom internal electrode nozzle to the bottom of the external electrode nozzle, mm							
- before test	25	20	15	10	5	30	28
- after test (minimum)	25	20	15	10	8	33	53
Burn-up rate of the graphite nozzle of the internal electrode, g/min						1.022	0.871

Conclusion

Decrease of the distance between the nozzles of the external and internal electrodes causes shifting of the arc from the lateral surface to the end face of the internal electrode nozzle.

Decrease of the distance between the nozzles of the external and internal electrodes less than 18 mm causes the plasmatrone power loss.

Average rate of the graphite nozzle erosion of the external electrode during the test was 0.6 g/min.

Average rate of the graphite nozzle erosion of the internal electrode during the test was 0.9 g/min.

Testing of a single plasmatrons to specify operating conditions of the device for modeling decay heat

Purpose of the experiments

- 1) Checking of reliability of arc burning depending on composition of the gas environment in the inter-electrode space and in the "Lava-B" MR;
- 2) Checking of reliability of arc burning depending on pressure of the gas environment in the inter-electrode space and in the "Lava-B" MR;
- 3) Search of ways for increasing electric power of individual plasmatrone.

Experiments on estimation of pressure influence in the MR on plasmatrone operation

1) Argon with the flow rate of 0,001 kg/s was supplied into the inter-electrode space. The gas pressure in the MR increased stage by stage with pitch 1 atm. The electric arc in the plasmatrone was interrupted on increasing gas pressure in the MR up to 6,8 atm.

2) Ignition of plasmatrone with argon (argon flow rate $\sim 0,001$ kg/s), then nitrogen was supplied in the inter-electrode space (nitrogen flow rate $\sim 0,001$ kg/s). Pressure in the pressure vessel increased stage by stage with pitch 0,2 atm. The electric arc in the plasmatrone was interrupted on reaching gas pressure in the MR 1,93 atm.

3) Attempt of the arch ignition was made at MR pressure $P = 1,8$ atm with the subsequent pressure loss up to 1 atm with pitch 0,2 atm. At pressure in the MR equal to 1,8 atm the arc burns unstably and dies away fast (~ 40 s), the arc burns steadily at lower pressure. When more low pressure of environment then more stable burning of the electric arc.

Experiments on studying of nitrogen influence on plasmatrone power

1) On preparation of the experiments the nozzle with diameter of critical section equal to $d_{N_2} = 0,8$ mm was located in the nitrogen supply path. In the nitrogen supply path the flow nozzle with diameter of critical section $d_{Ar} = 0,7$ mm was installed. To increase the arc power in the electrical feed circuit of the plasmatrons, the reactor was stopped and the rectifiers were brought out the maximum current (400 – 420 A). Three of four apertures for gas exhaust from the graphite nozzle of the external electrode were plugged for increasing pressure in the inter-electrode space.

2) The experiments with variation of nitrogen pressure in the facility pressure vessel from atmospheric 3,6 atm. With such gas pressure the plasmatrone arc quenching was taken place in the vessel.

The experimental data obtained at argon pressure before the flow nozzle $P \approx 9$ atma (argon flow rate $\sim 0,001$ kg/s) and nitrogen pressure before the flow nozzle changing from 1,5 to 11,0 atma with pitch $\sim 1,0$ atma are represented in Figure 42. Gas pressure in the inter-electrode space did not exceed 1,15 atma.

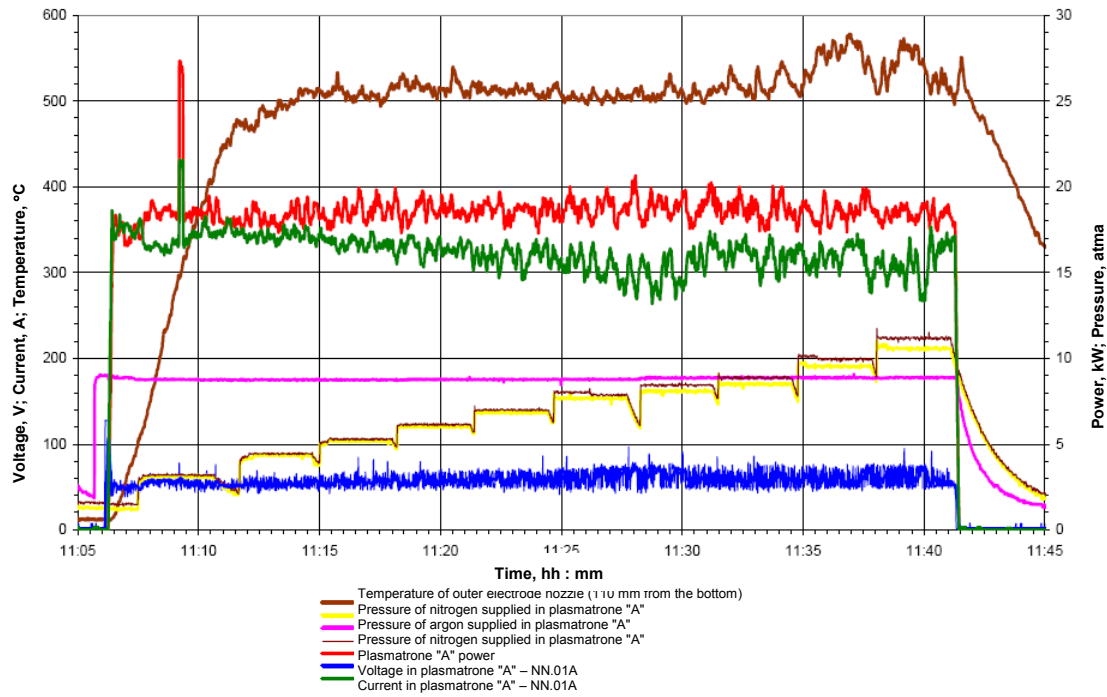


Figure 42 – Variation of plasmatrons parameters (test 1)

Figure 43 gives the experimental data obtained at argon pressure before the flow nozzle $P \approx 13$ atma (argon flow rate $\sim 0,0015$ kg/s) and nitrogen pressure before the nozzle over the range 1,6 – 14,0 atma with pitch $\sim 1,0$ atma. The gas pressure in the inter-electrode space did not exceed 1,25 atma.

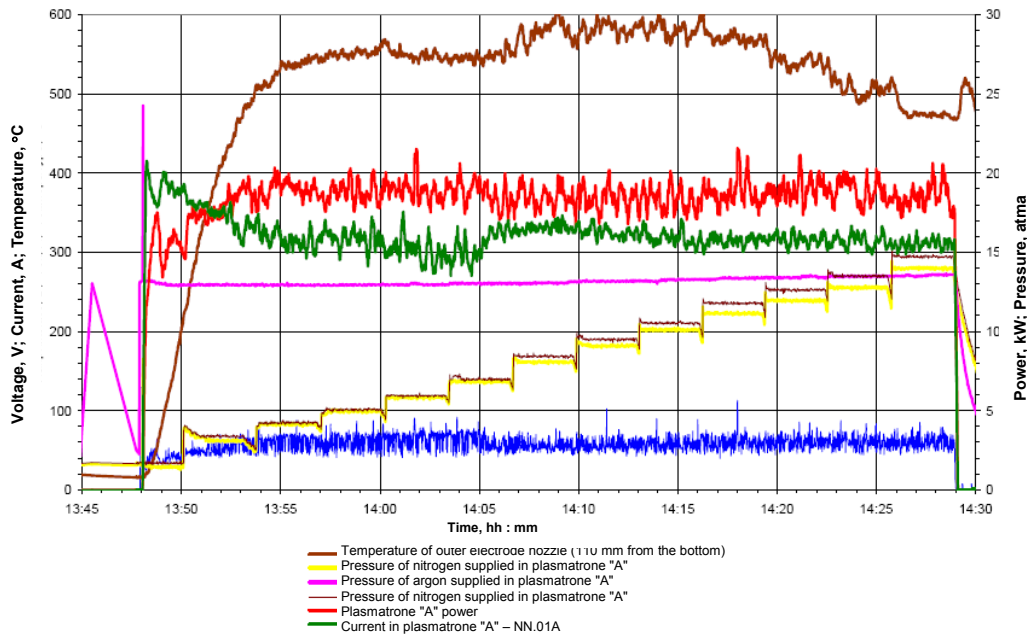


Figure 43 - Variation of plasmatrons parameters (test 2)

On comparing these tests we may note that the average value of the plasmatrons power is $\sim 18,5$ kW, and starting from some value of the nitrogen/ argon pressure relation before the flow-nozzles, the plasmatrons power is practically constant.

In terms of the experimental data resulted from the two first tests, there were chosen the values of gas pressure before the flow-nozzles at which the plasmatrons power was the most stable $P_{N_2} = 9,0$ atma, $P_{Ar} = 14$ atma. The third test was performed at nitrogen and argon pressure before the flow-nozzles which were 9,3 – 10,3 atma and 13 – 14 atma, accordingly. During the experiment the gas pressure increased in the power vessel. Figure 44 shows the plasmatrons

parameters variation during the experiment.

Temperature reduction of the plasmatrons nozzle surface in the course of cold nitrogen supply to the pressure vessel is shown in Figure 44. Then, at the steady-state level of pressure in the vessel, the plasmatrons nozzle temperature increased. There was a spontaneous interruption of plasma arc burning at pressure 3,3 atm.

The pressure in the vessel was decreased up to 2,9 atm for reliable ignition of the electric arc in the plasmatrons. Another test was conducted with reduction of gas pressure before the flow nozzles supplying gas to the inter-electrode space from 7 to 3,6 atm (for nitrogen) and from 12,8 to 11,0 atm (for argon). By the end of this experiment the plasmatrons operation was practically in argon atmosphere in the inter-electrode space, therefore the plasmatrons power was decreased from 19 to 14 kW. At the end of the experiment, on supplying nitrogen to the inter-electrode space, the electric arc in the plasmatrons was gone out.

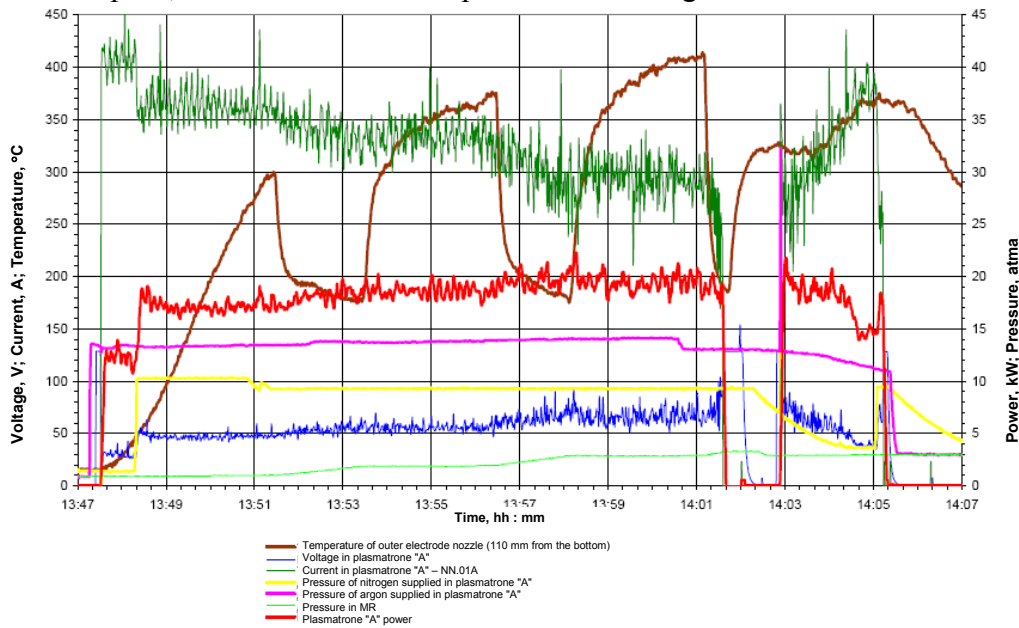


Figure 44 – Variation of plasmatrons parameters (tests 3 and 4)

The definition of nitrogen flow rate influence on the plasmatrons parameters was continued in the fifth experiment. The apertures for gas exhaust in the graphite nozzle of the external electrode had diameter $\varnothing 1,0$ mm. In the argon feed path the nozzle with diameter of critical section $\varnothing 0,7$ mm was located. In the nitrogen feed path the needle which effective area $\varphi F = 5,667 \times 10^{-8} \text{ mm}^2$ was located.

The first stage supposed the ignition of the arc with argon (argon flow rate $\sim 0,001$ kg/s) and then to perform step addition of nitrogen (P = 4; 7; 10; 13; 16; 19; 22; 26 atm.) for recording the plasmatrons electric characteristics at various composition of gas mix supplied to the inter-electrode space.

The maximum pressure difference between the cavity of the pressure vessel and inter-electrode space was $0,54 \text{ kg/cm}^2$. The test results are shown in Figure 45.

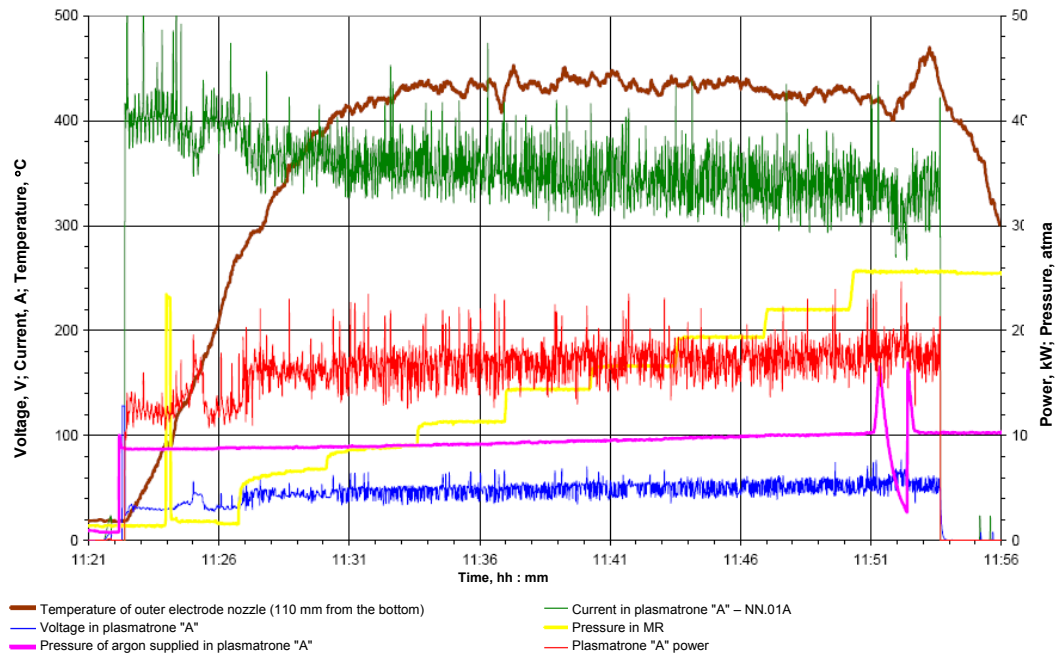


Figure 45 – Variation of plasmatrone parameters (test 5)

At the second stage (experiment 6 the arc ignition was made with argon, then there was a transition to the mix argon + nitrogen in the ratio 87/13 %. Further the pressure in the pressure vessel was increased step by step with pitch 1 atm for the purpose to define pressure of arc failure. The pressure in the cavity of the pressure vessel increased with approximate rate 1 atm per 2,5 minutes. At pressure in the vessel 5,2 atm the electric arc was extinguished. The test results are shown in Figure 46.

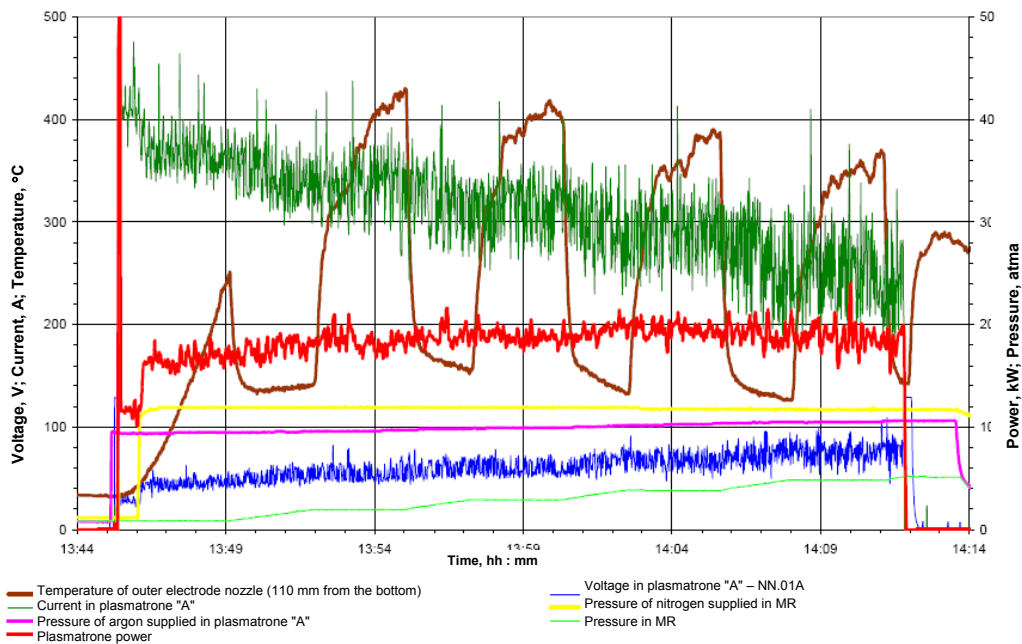


Figure 46 – Variation of plasmatrone parameters (test 6)

Figure 47 illustrates the processed data resulted from the above experiments. The designation of power i refers to i experiment ($i = 1, 2, 3, 4, 5, 6$).

The analysis of the processed experimental data show, but even at ~13 % nitrogen content in the gas mix the plasmatrone power becomes practically constant. Consequently, to increase the plasmatrone power it takes us only to add to the argon flow rate some nitrogen equals to ~15 % of the argon flow rate and the plasmatrone power would increase from 11...12 kW to

17...20 kW.

The approximating curve which allows us to calculate the average power of plasmatrons (N) depending on the relative content of nitrogen (p) in the gas mixture looks like as follows:

$$N = 10,791 \cdot p - 318,88 \cdot p^2 + 596,14 \cdot p^3 - 419,53 \cdot p^4.$$

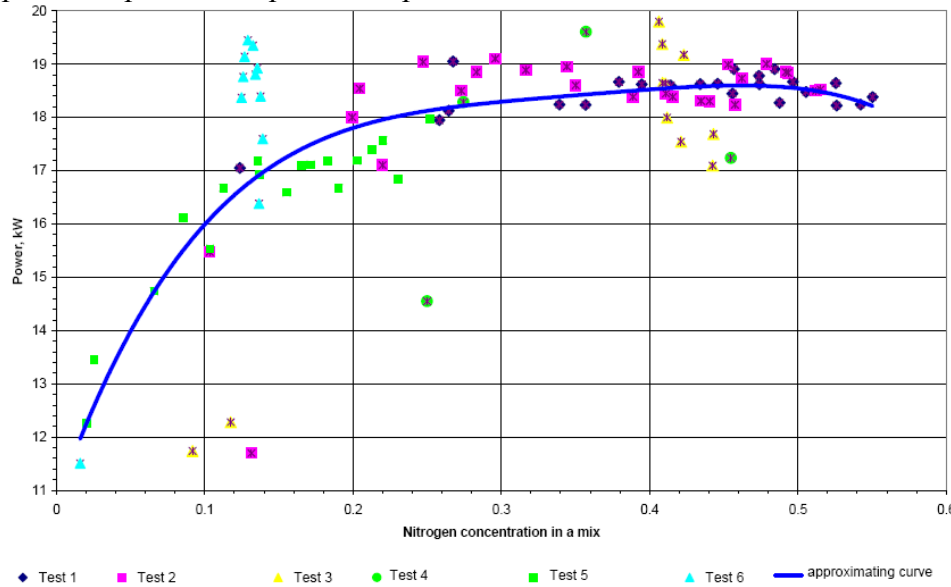


Figure 47 – Influence of the nitrogen concentration in the gas mixture on plasmatrons power

Conclusion

Increase of the gas pressure in the inter-electrode space raises risk of arc failure.

Maximum permissible gas pressure in the MR on running of the plasmatrons with argon is 6,8 atm, on running with nitrogen – 1,9 atm. Maximum permissible gas pressure in the MR on running of the plasmatrons with the mix of argon (87 %) and nitrogen (13 %), is 5,2 atm. The greatest working pressure at which arc burning is possible reaches on supplying argon to the inter-electrode space of the plasmatrons, but thus the arc power is the least. The maximum power of the arc reaches at nitrogen supplying to the inter-electrode space of plasmatrons, but thus the gas pressure in the pressure vessel at which occurs arc failure is the least. Making a compromise the use of the argon and nitrogen mix in the ratio ~4:1 is acceptable.

3.2.2 Testing of the device of five plasmatrons without immersion in the corium

The comprehensive testing of the device for simulating corium heat decay on the basis of five plasmatrons was performed. At first the plasmatrons were started one at a time and then a group of plasmatrons was tested. The tests were carried out under atmospheric pressure and with open MR of the "LAVA-B" test facility. Figure 48 illustrates variation of the plasmatrons pressure and temperature of the plasmatrons "A" graphite nozzle at distance 50 mm from the end during the test.

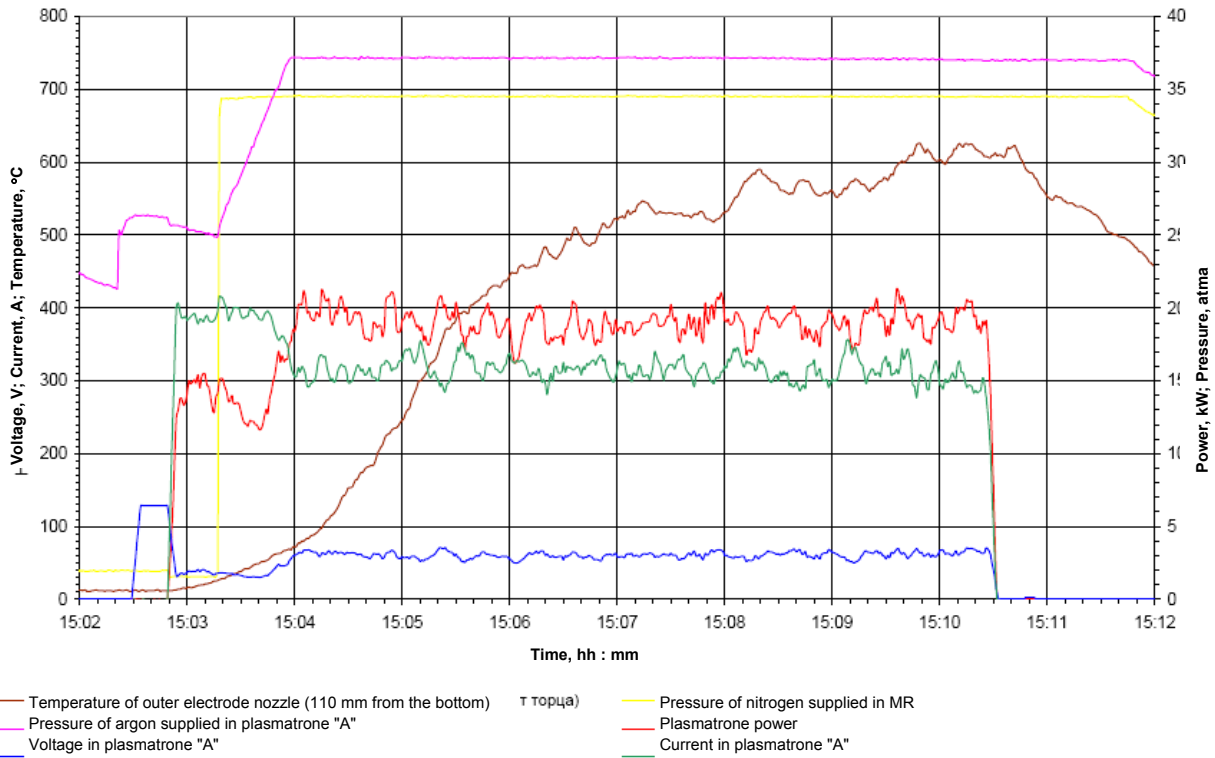


Figure 48 – Plasmatrons power and temperature of graphite nozzle of plasmatrons "A"

Figure 49 shows the plasmatrons power variation during starting up of the group of five plasmatrons. The start up of five plasmatrons was performed during ~50 seconds. The interval between plasmatrons starts was less than 15 seconds. Running time of the five plasmatrons was equal to ~2,5 minutes.

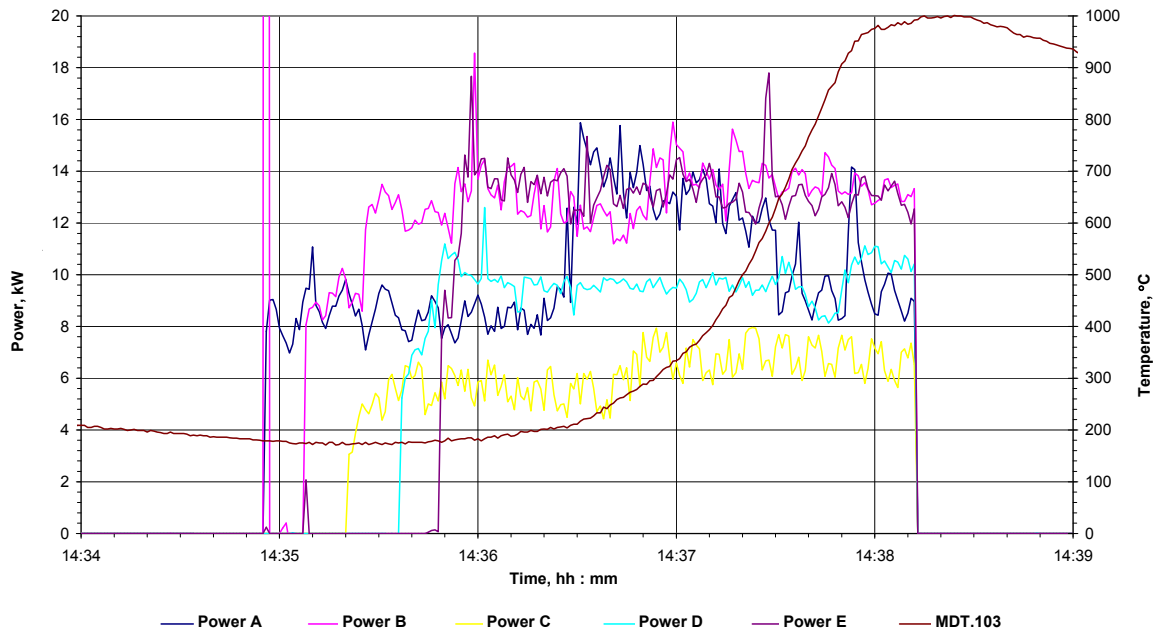


Figure 49 – Testing of group of five plasmatrons

The startup of the five plasmatrons was tested with the use of argon for supplying to the inter-electrode space. Total argon flow rate in the plasmatrons inter-electrode space was ~0,6 g/s.

Maximum plasmatrons power was as follows:

- plasmatrone "A" 16 kW;
- plasmatrone "B" 16 kW;

- plasmatrone "C" 16 kW *);
- plasmatrone "D" 11 kW;
- plasmatrone "E" 14 kW

*) – In the startup the plasmatrons "C" current was not registered by the DAS although according to the indicating gages it was about 300 A. The plasmatrons "C" pressure registered by DAS was ~2 times lower than on other plasmatrons. According to the indicating gages the plasmatrons "C" pressure was the same as on other plasmatrons. Therefore, considering the above, the plasmatrons "C" power in the table increases twice.

Maximum power of the group of five plasmatrons was 73 kW.

The temperature of the plasmatrons "A" graphite nozzle at a distance 50 mm from the end reached 1000 °C at the end of the test. The temperature of the plasmatrons "A" graphite nozzle at a distance 110 mm from the end reached 635 °C at the test end.

Water flow rate for cooling plasmatrons was from 0,066 to 0,079 kg/s. Water flow rate for cooling the electric cable was equal to ~0,175 kg/s. Variation of water temperature at inlet and outlet of the plasmatrons cooling paths and electric cable is given in Figure 50. Maximum heating of water in one of the cooling paths was 7,5 °C

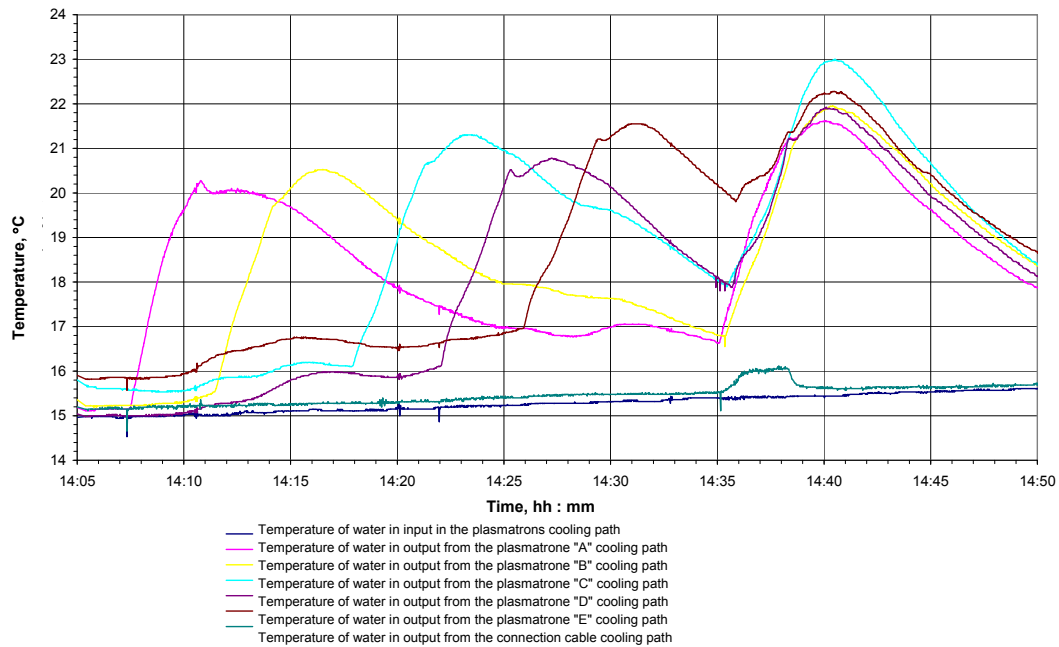


Figure 50 – Water temperature in the cooling paths

In the course of the test the vessel model bottom was covered with asbestos of thickness 3 mm. Figures 51...54 illustrate the temperature curve of the vessel model during the test.

The check points of the first thermocouple group (Figure 51) were located on the lateral surface of the vessel model in the point of plasmatrons "A" location. The second thermocouple group, seen in Figure 52, was located on the vessel model bottom under the end face of the plasmatrons "A". The third thermocouple group, seen in Figure 53, was located at the bottom in the vessel model center. The fourth thermocouple group, see Figure 54, was located at the vessel model bottom between the plasmatrons "C" and "D".

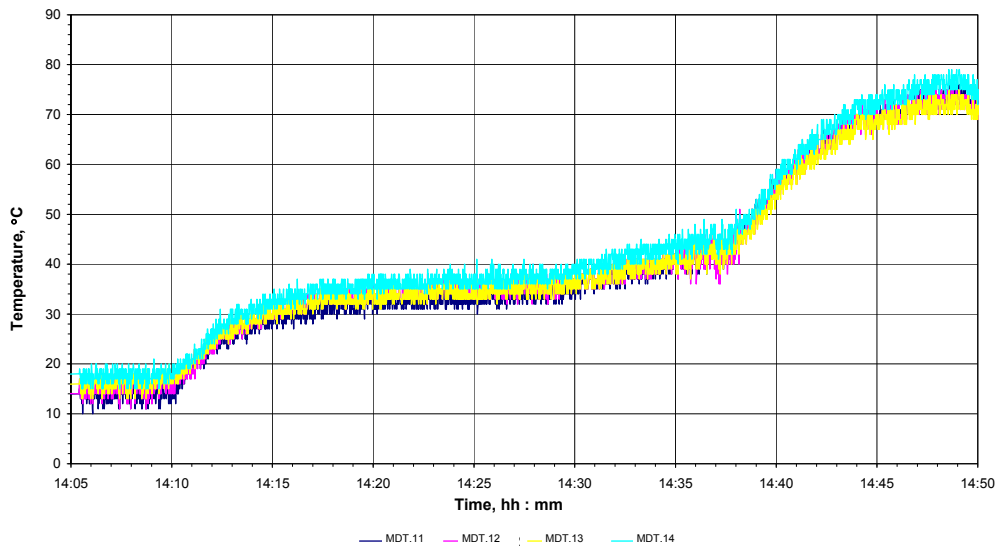


Figure 51 – Data of the first group of thermocouples

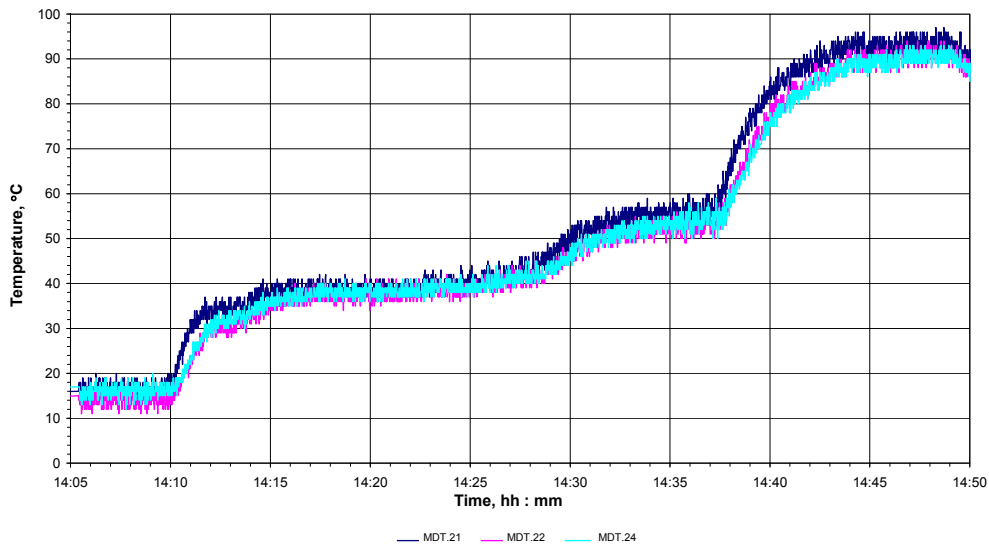


Figure 52 – Data of the second group of thermocouples

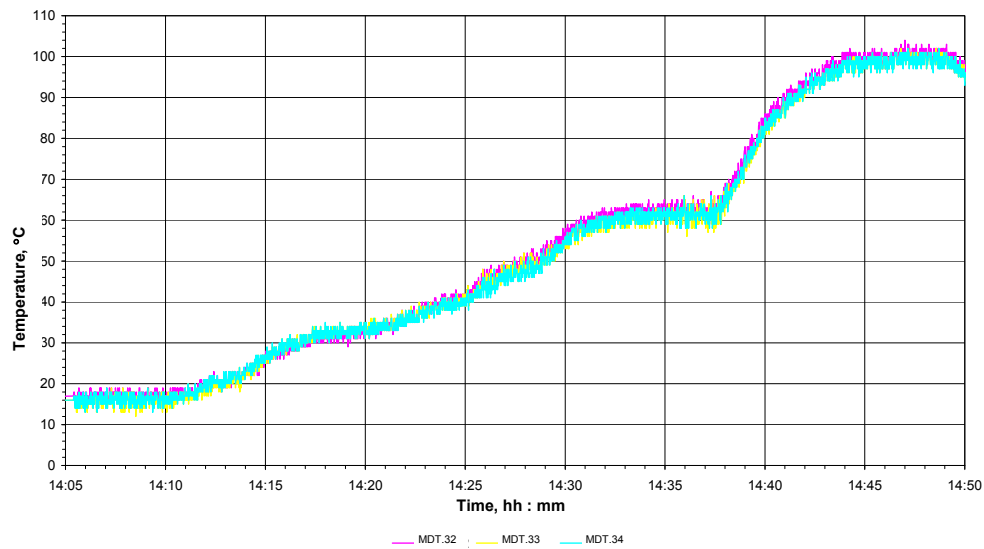


Figure 53 – Data of the third group of thermocouples

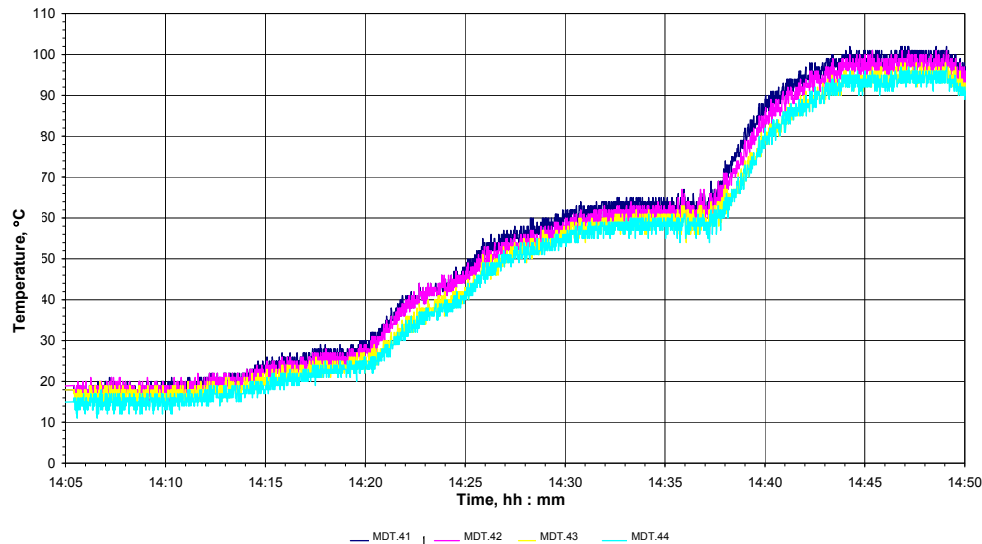


Figure 54 – Data of the fourth group of thermocouples

The initial temperature of RPV model wall was 13 ... 17 °C. It is visible in the plot that the thermocouples located at the bottom of RPV model show approximately identical temperature during the experiment, but on the lateral surface the temperature was lower by ~17 °C. Heating on the lateral surface of the RPV model was approximately by ~40 % less that indirectly specifies that the places of electric arc burning in the plasmatrons were in the bottom part of plasmatrons nozzles. After actuation of the plasmatrons the temperature of the RPV model increased due to return heat exchange from the hot plasmatrons surfaces. After completion of the experiment the average temperature of the RPV model bottom, for 10 minutes, increased from 60 to 95 °C, and of the lateral wall - from 43 to 75 °C.

Six experiments were executed using the group of five plasmatrons. The tests were performed on supplying the gas mixture of argon and nitrogen in the inter-electrode space of the plasmatrons with total flow rate ~1 g/s. The gas mix was composed of 70 - 74% of argon and 30 - 26% of nitrogen. The water flow rate for plasmatrons cooling during the experiments was 0,067...0,079 kg/s.

Duration of the test with the group of five plasmatrons was 30 ... 45 seconds.

Total running time of five plasmatrons in six experiments was over 32 minutes. Duration of one experiment was about 5 minutes.

Voltage and current variation in five plasmatrons in one of the experiments is shown in Figure 55. The current changed in a range from 240 to 300 A, and voltage varied in a range from 45 to 70 V. Variation of the plasmatrons power in the same experiment is given in Figure 56. Plasmatrons power is 14 ... 18 kW. The average power of five plasmatrons is 82 kW.

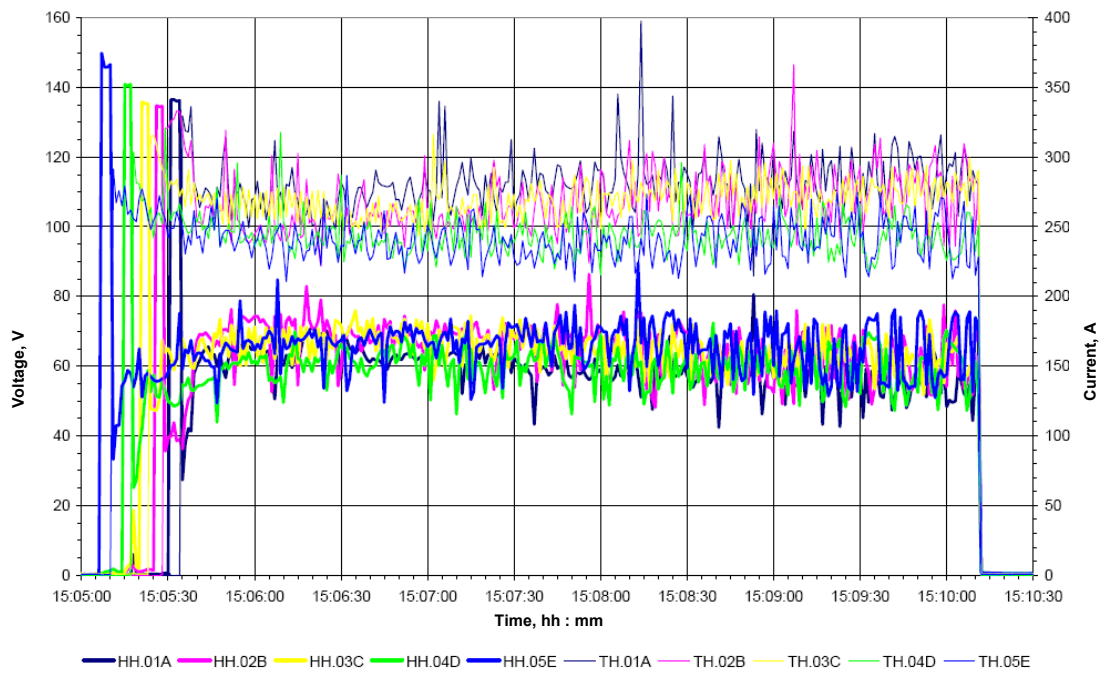


Figure 55 – Voltage and current of five plasmatrons in the Test 6

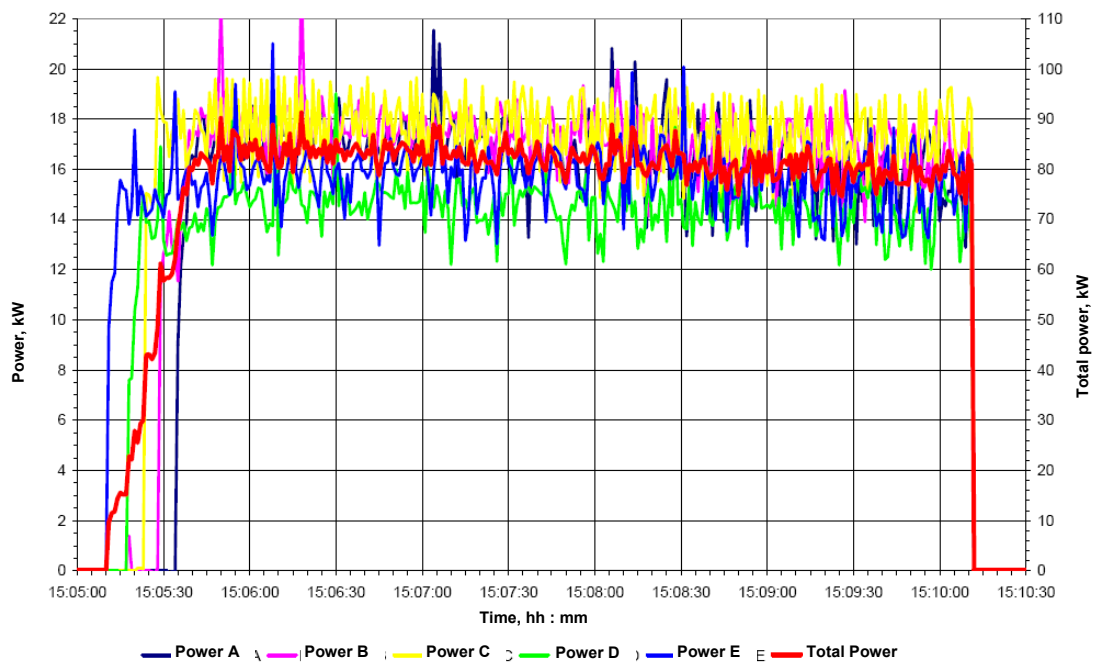


Figure 56 – Power of five plasmatrons in Test 6

The maximum heating of water in plasmatrons cooling paths was equal to 18 °C. Temperature curve of the graphite nozzle and wall of the RPV model in the six experiments is given in 57, 58. The maximum temperature of the graphite nozzle was equal to 1600 °C. The temperature of the RPV model wall in the sixth experiment exceeded 400 °C.

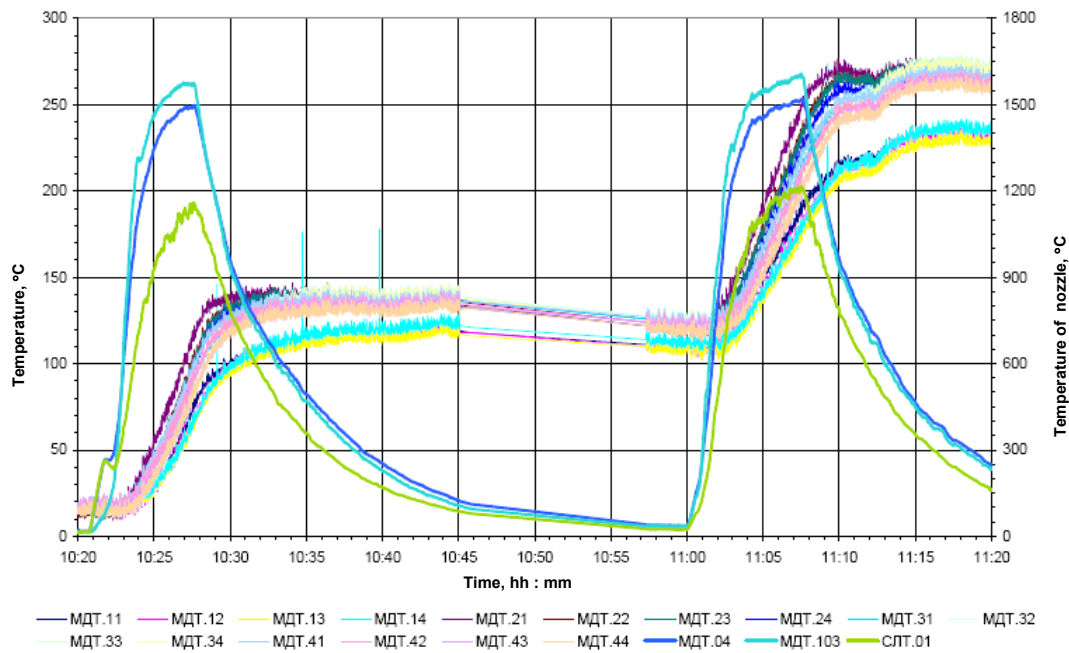


Figure 57 – The temperature of the nozzle and wall of the RPV model in the first and second tests

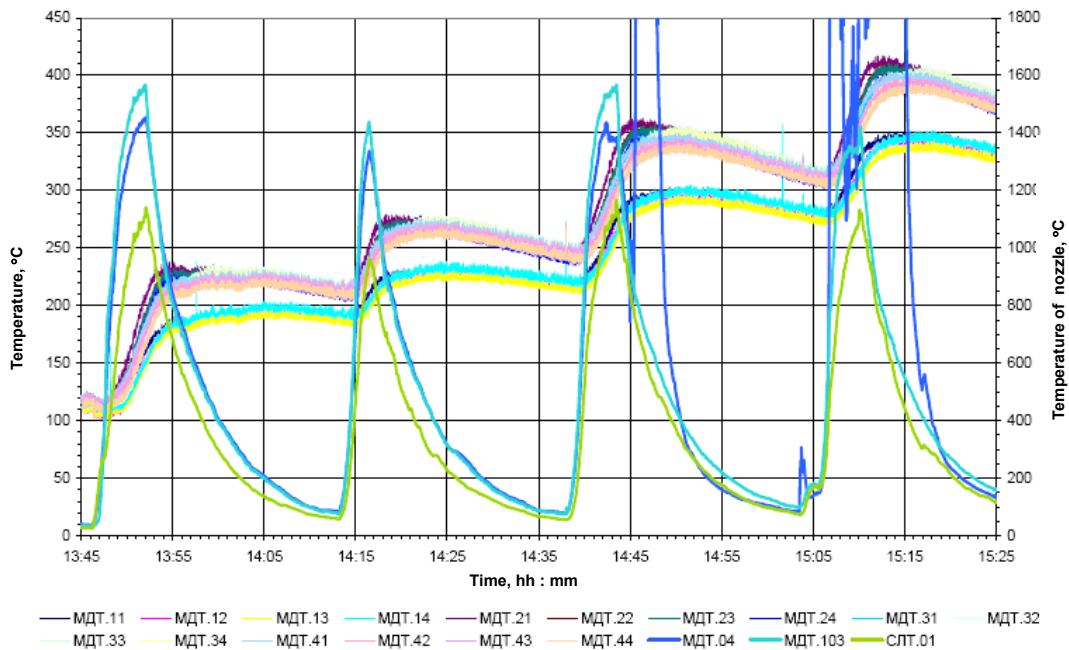


Figure 58 – The temperature of the nozzle and wall of the RPV model in the third, fourth, fifth and sixth tests

Variation of the plasmatrons total power and heat losses to the cooling water during experiments 1...6 are shown in Figures 59, 60. The figures give also the temperature curve of the graphite nozzle at distance 110 mm from its end face and changes of integral of power and integral of heat losses to the cooling water. In the last three experiments the plasmatrons total power sometimes exceeded 85 kW.

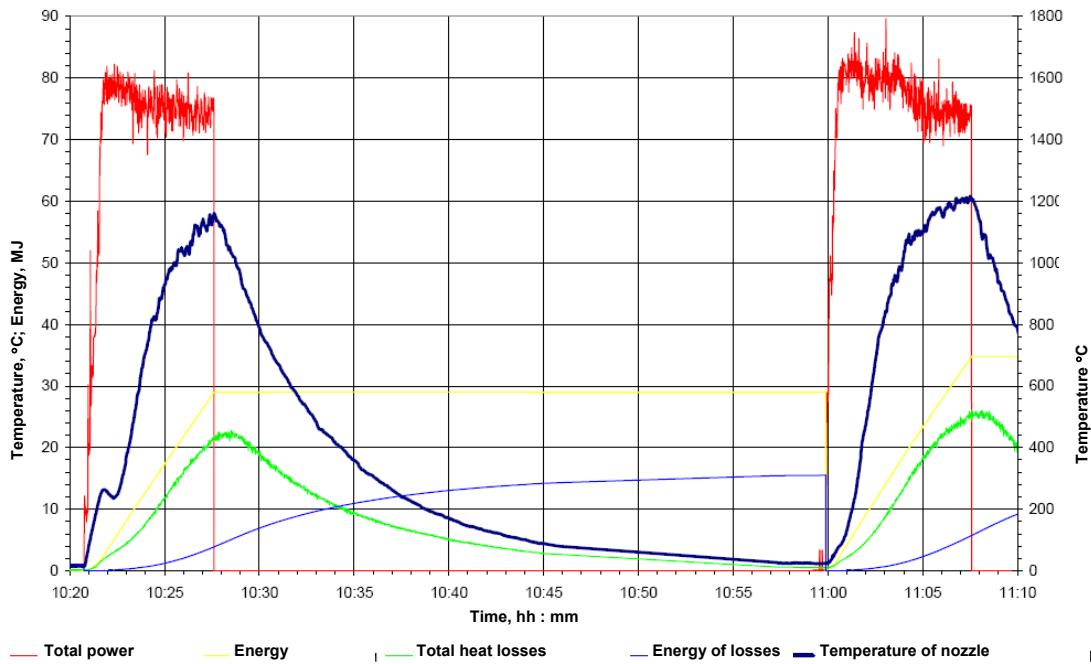


Figure 59 – Total power of plasmatrions in the 1st and 2nd tests

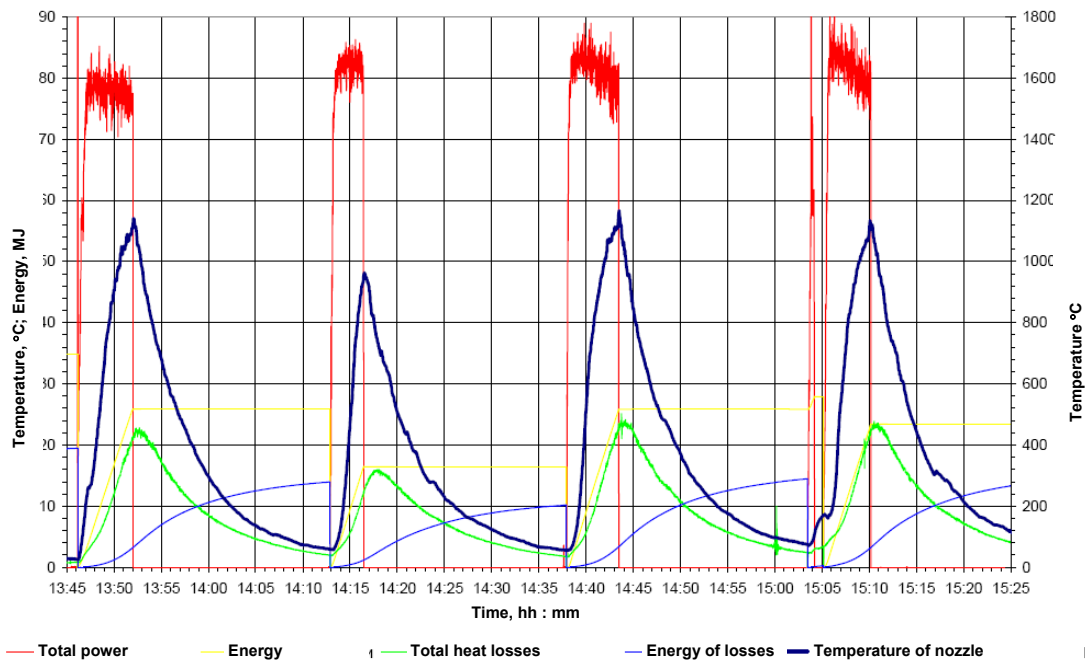


Figure 60 – Total power of plasmatrions in the 3rd, 4th, 5th and 6th tests

The thermocouples are placed in the RPV model by four groups in the location of RPV steel samples. The arrangement of thermocouples in each of samples is shown in Figure 61 - sections B and C-C. The first thermocouple of the group is located on depth 30 mm from the external surface of the RPV model. The second thermocouple is located on depth of 20 mm, the third - on depth of 12 mm, and the fourth - on depth of 2 mm from the external surface of the RPV model.

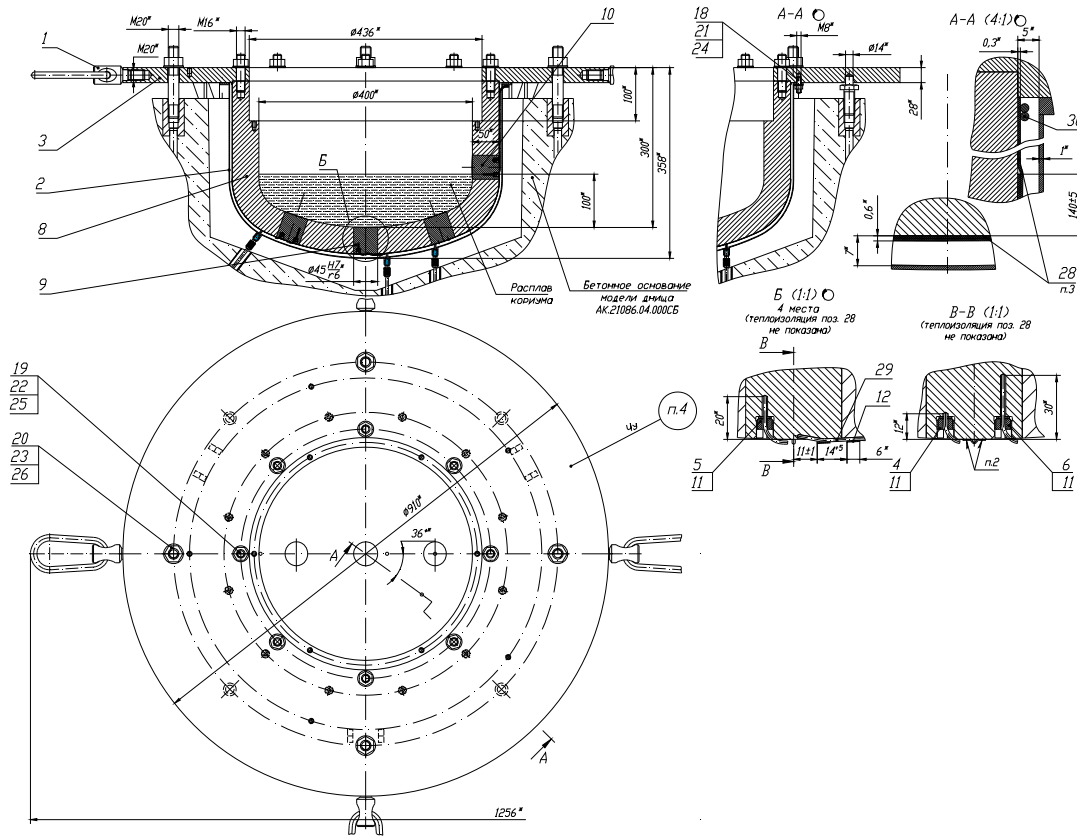


Figure 61 – Thermocouples arrangement in the RPV model

Conclusion

The comprehensive testing of the decay heat simulator in the corium for the integral tests demonstrated satisfactory operability of the device as a whole. Some faults in the plasmatrons electric supply system and instrumentation and measuring system were eliminated.

The device was running steady for 30 minutes. To avoid overheating of the RPV model wall, the duration of the test was not longer.

In the course of the testing maximum temperature of the vessel model wall did not exceed 100°C due to internal insulation of the RPV model wall.

3.2.3 Testing of single plasmatrons with immersion in the corium components

A group of 7 tests with a single plasmatrons (series TOP tests) immersed in the corium components mixture C-30 of mass up to 12 kg¹ were performed. The objective of the tests was to test the resistance of the graphite nozzle of the outer electrode of the plasmatrons made of graphite with the protective carbide zirconium layer against oxide medium attack at high temperature. In addition, in the course of the tests the possibility of temperature rise in the "corium/steel" interaction plane due to the use of the insulation on the external surface of the RPV model was estimated, as well as maximum possible parameters of the plasmatrons running on power and duration of testing was determined.

To perform the tests, a cell (see Fig. 62) consisting of two coaxial steel thin-wall vessels separated with the insulation layer (glass cloth) was designed. The external steel vessel was cooled with continuous water during the test. The corium components were loaded in the internal vessel, and the coaxial plasmatrons was fixed in alignment of the vessel the electrical circuit of which was included in the standard system of the "Lava-B" test facility.

¹ The given group of tests was not covered with the initial Project Working plan. The activity was performed in connection with the need for the experimental testing of the experimental section design in order to conduct the integral tests and to estimate the capability of the device for decay heat modeling

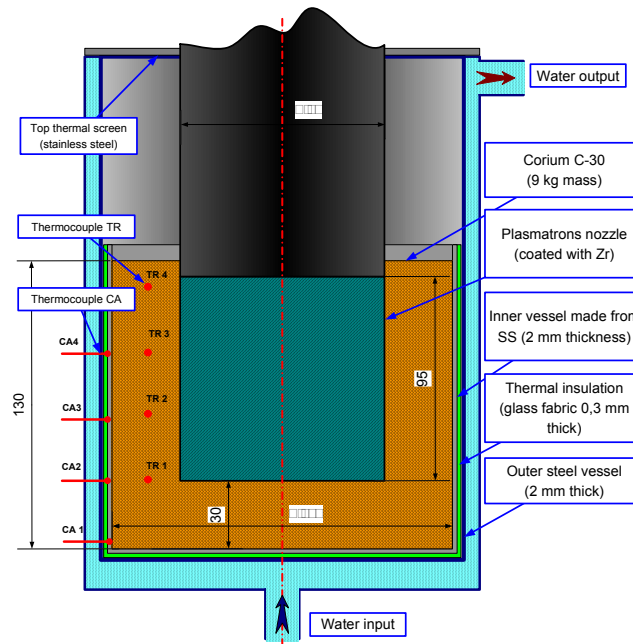


Figure 62 – Diagram of the cell for TOP tests

Для контроля параметров эксперимента ячейка оснащалась термодатчиками на наружной стенке внутреннего сосуда и в слое загрузки кориума.

Heating of water at the cooling jacket outlet of the external vessel, electrical parameters of the plasmatrons and temperature of the plasmatrons external nozzle over the burden level of the corium components were also controlled.

Table 7 includes the parameters reached in the course of the TOP series tests.

Table 7 – Parameters of TOP tests

Parameter	TOP-1	TOP-2	TOP-3	TOP-4	TOP-5	TOP-6	TOP-7
Time of operation, hh:mm	1 : 00	2 : 00	2 : 00	1 : 53	2 : 30	2 : 20	2 : 34
Gas composition in the inter-electrode space	N ₂	N ₂	N ₂	N ₂ ; 36%N ₂ +64%Ar	N ₂	15%N ₂ +85%Ar	N ₂ +Ar
Gas pressure in the inter-electrode space, atm	n.d.	n.d.	n.d.	1,5-1,8	1,35	2,6	1,5
Average pressure of gas in facility vessel, atm.	1,3	1,2	1,4	1,1-1,0	1,2	2,4	1,2
Average voltage value of electric arc, V	62	60	75	60,5	65	52	59
Average current value of electric arc, A	270	272	220	312	290,6	318	307
Average plasmatrons power, kW	16,8	16,3	16,5	18,3	18,7	15,9	18,1
Power input, MJ	60,7	119,2	119,0	125,3	170,7	138,4	167,0
Maximum temperature of outer electrode nozzle (148 mm from the bottom)	387	594	511	767	828	590	656
Maximum temperature of gas exhausted from the melt, deg.C	352	483	381	818	859	683	547
Maximum temperature of inner vessel wall, deg.C							
- 2 mm from the bottom	673	623	527	413	605	384	471
- 30 mm from the bottom	1107	693	764	856	777	869	755
- 60 mm from the bottom	1149	980	846	929	936	964	877
- 90 mm from the bottom	880	951	844	861	842	774	742
- on the bottom	n.d.	287	235	345	625	229	203
Maximum temperature of corium, deg.C							
- 30 mm from the bottom	1319*	2002*	1843*	1920*	1921*	1970*	2418
- 55 mm from the bottom	2133*	1985*	2215	1997*	2245*	2402*	2090
- 80 mm from the bottom	2230*	2190	1949	2176*	2469*	2573	2682
- 105 mm from the bottom	1429	2034	1576	2264	2113	1979	1975
Rate of graphite erosion, g/min	0,26	0,23	0,464	1,89	1,16	0,29	0,607
Graphite type	ARV	ARV	ARV	ARV	ARV	R4340	R4340

The detailed description of each test is represented in the Reports for the 1st and 2nd year of the Project implementation. The given report describes only TOP-6 test since it was performed using the electrode nozzles of the plasmatrons made of graphite R4340 which was provided for manufacturing all graphite components of the test facility in the integral large-scale tests.

Test TOP-6

The objective of the test was:

- to determine resistance of the graphite nozzle of the outer electrode of the plasmatrons made of graphite R4340 with protective carbide zirconium layer against oxide medium attack at high temperature;
- to produce melt from the loading consisting of zirconium dioxide powder (ZrO_2), uranium dioxide pellets (UO_2) and metal zirconium in the steel vessel;
- to compare the erosion rate of the graphite nozzle made of graphite R4340 with the experimental results of the nozzles made of graphite ARV-1.

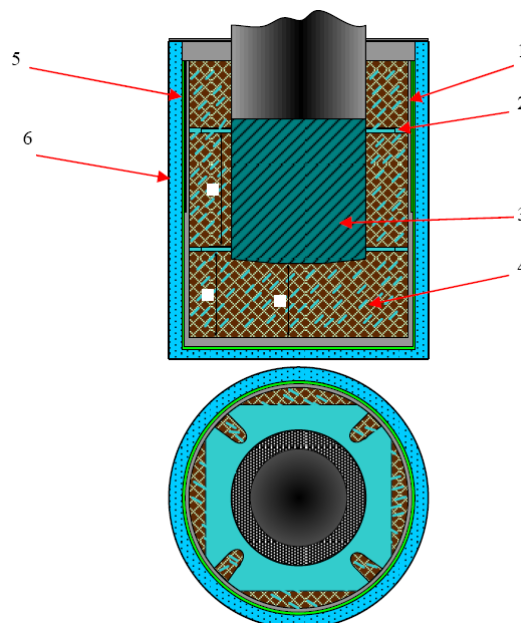
Nominal parameters of the melt heating system in the RPV model are as follows:

- maximum value of the plasmatrons working current, A – to 400;
- plasmatrons arc volts, V – to 70;
- open circuit volts on the plasmatrons, V – to 140;
- water flow rate through the plasmatrons cooling path, kg/s – to 0,08;
- consumption of argon supplied to inter-electrode space, kg/s – 0,001;
- consumption of nitrogen supplied to inter-electrode space, kg/s – 0,00008.

The external surface of the internal vessel was covered with two glass-cloth layers at a distance 100 mm from the upper end of the vessel and with one glass-cloth layer at a distance 90 mm from the vessel bottom (total vessel height – 190 mm) which was used as thermal and electrical insulation. Mass of the insulated vessel with the thermocouples was equal to 2,552 kg. In the experimental cell there was loaded the burden consisting of the following materials:

- uranium dioxide powder – total mass 1,116 kg,
- uranium dioxide pellets – 9,144 kg,
- metallic zirconium – 1,74 kg.

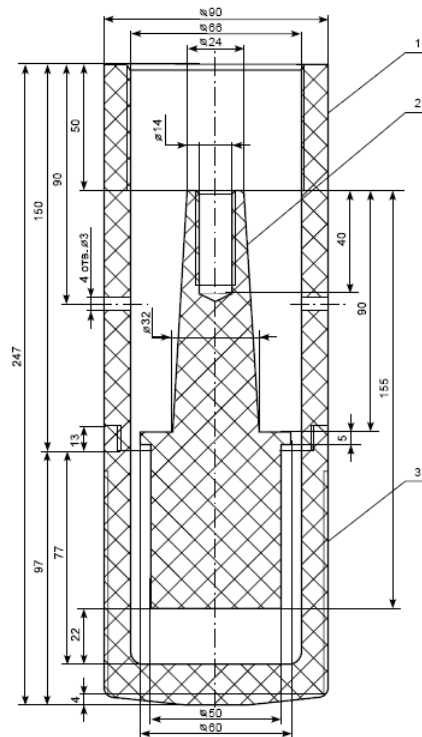
The metallic zirconium was used in the form of granules. The cell loading diagram is represented in Figure 63.



1 – glass cloth; 2 – center ring; 3 – nozzle coated; 4 – burden (UO_2 (pellets) ZrO_2 (powder) + Zr (granules));
5 – vessel; 6 – experimental cell

Figure 63 – Scheme of burden loading

A cylindrical nozzle of the internal electrode and lower part of the composite nozzle of the outer electrode made of graphite R4340 were installed on the plasmatrons. The upper composite nozzle part of the outer electrode was made of graphite ARV-1. Nozzles drawing are represented in Figure 64.

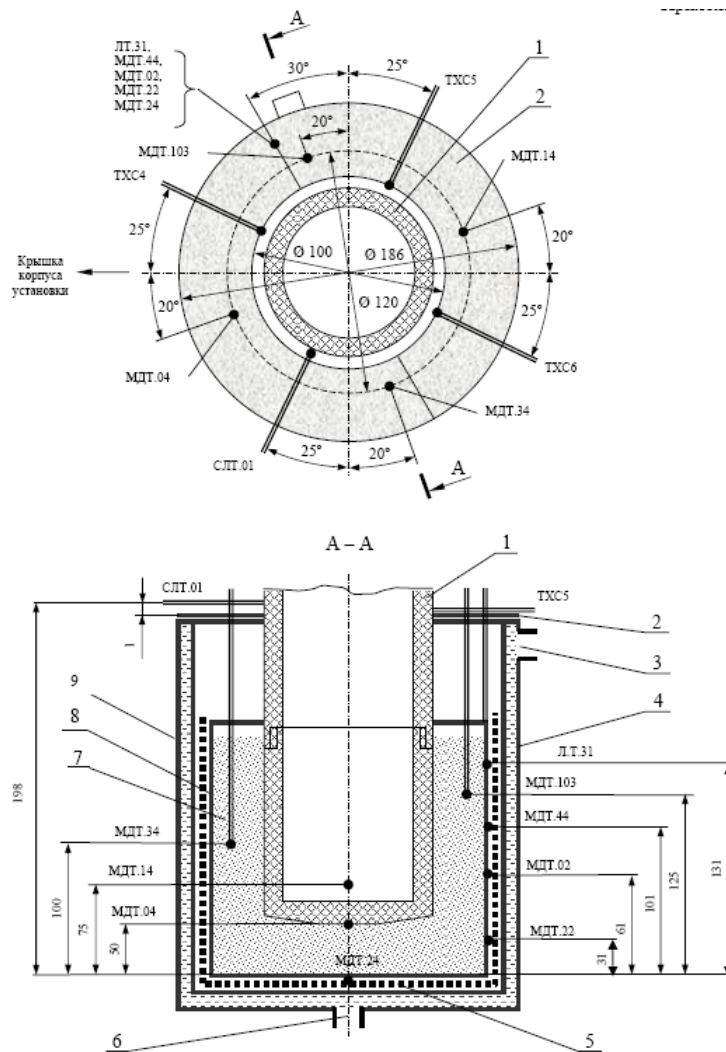


1 – upper part of the composite graphite nozzle; 2 – nozzle of the internal electrode; 3 – bottom part of the composite graphite nozzle

Figure 64 – Graphite plasmatrons nozzles

The external surface of the outer electrode nozzle bottom was coated with protective carbide zirconium layer. To improve zirconium spreading, from the outside the screw M90×1.5 was made on the lateral surface of the nozzle bottom, and on the end of the nozzle bottom the grooves of concentric-form rings were cut.

In the burden located in the experimental cell 4 thermocouples W-Re5/20: MDT.04, MDT.14, MDT.34, MDT.103 were installed. Five thermocouples CA, represented in Figure II.2.1.4, were installed on the outer surface of the vessel for the purpose of measuring temperature of the wall and vessel bottom. Their designations are as follows: c.p. L.T.31, MDT.44, MDT.02, MDT.22, MDT.24. On the protective shield, from the top, see Figure 65, item 2, three thermocouples CA c.p. TCJ4, TCJ 5, TCJ 6 for measuring temperature of gas released through the gap between the protective shield and outer electrode nozzle, were installed. On the outer electrode nozzle, a thermocouple CA c.p. CLT.01 was installed at a distance of 148 mm from the lower end of the outer electrode nozzle (1 mm over the screen). The thermocouples layout is given in Figure 65.



1 – composite graphite nozzle of outer electrode; 2 – protective shield; 3 – cooling water outlet; 4 – cooling water jacket; 5 – glass fiber cloth; 6 – cooling water inlet; 7 – uranium dioxide pellets, metal zirconium and zirconium dioxide powder mixture; 8 – internal vessel; 9 – experimental cell.

Figure 65 – Thermocouples layout in the experimental cell

Electric arc ignition was performed with supply of argon in the inter-electrode opening with further, after ignition, nitrogen supply to produce gas mixtures.

After the arc ignition and nitrogen supply to the inter-electrode space of the plasmatrons the maximum running current was established on the electric feed rectifier.

Total arc burning period was 2 hours 20 minutes. Changes for plasmatrons running parameters, such as voltage, current, power, argon and nitrogen pressure, as well as the outer electrode nozzle temperature are graphically represented in Figure 66².

² In the course of the test the parameter registration was interrupted. Before the test completion the registration process was restored.

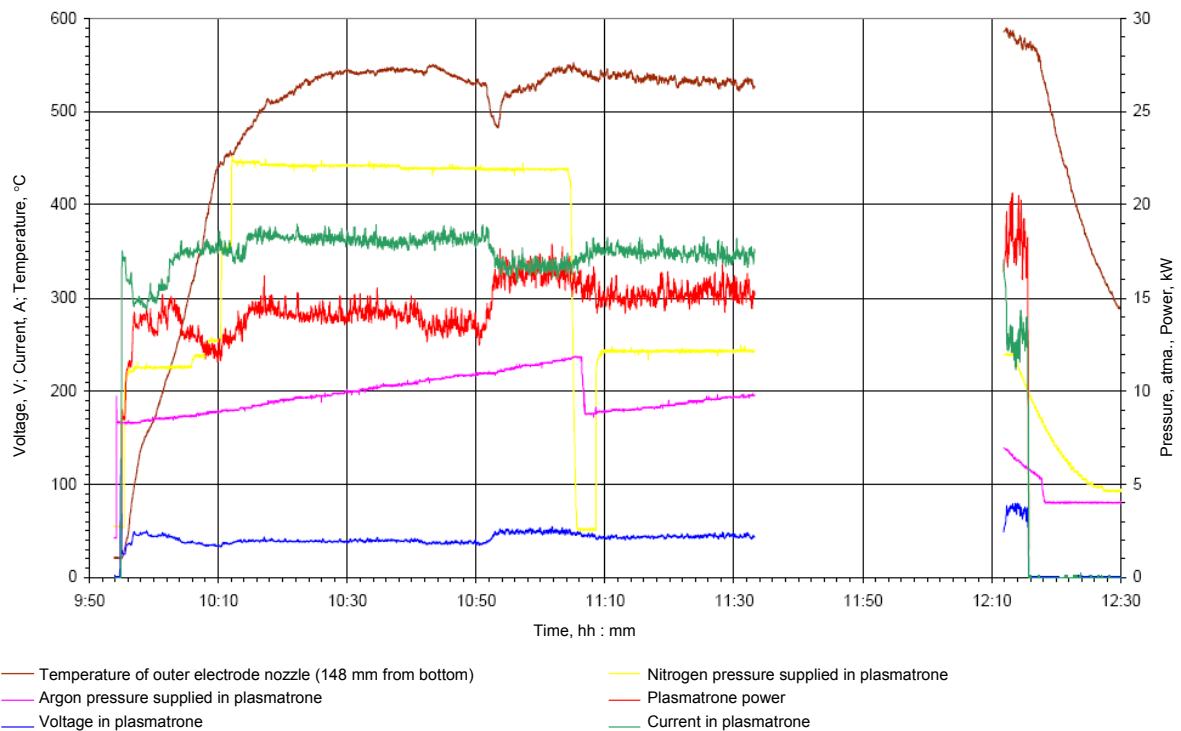


Figure 66 – Plasmatrons parameters change

Figures 67, 68 give the temperature curves of the loading and steel wall of the cell internal vessel during the test.

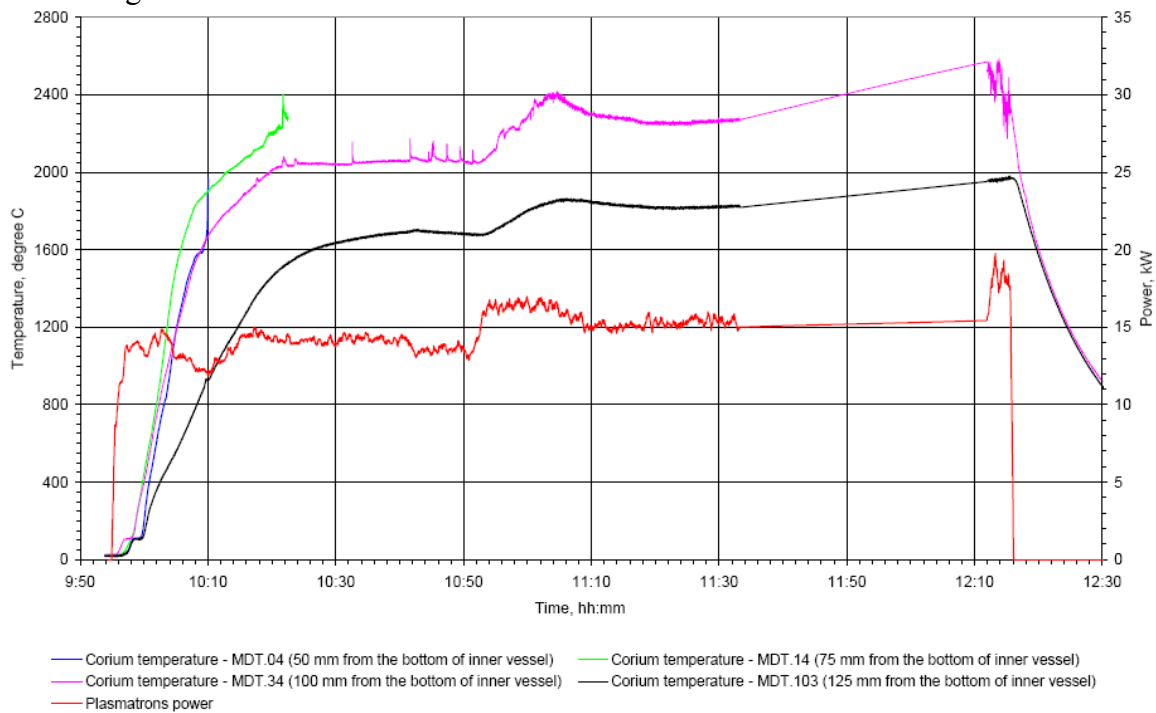


Figure 67 - Change of loading temperature

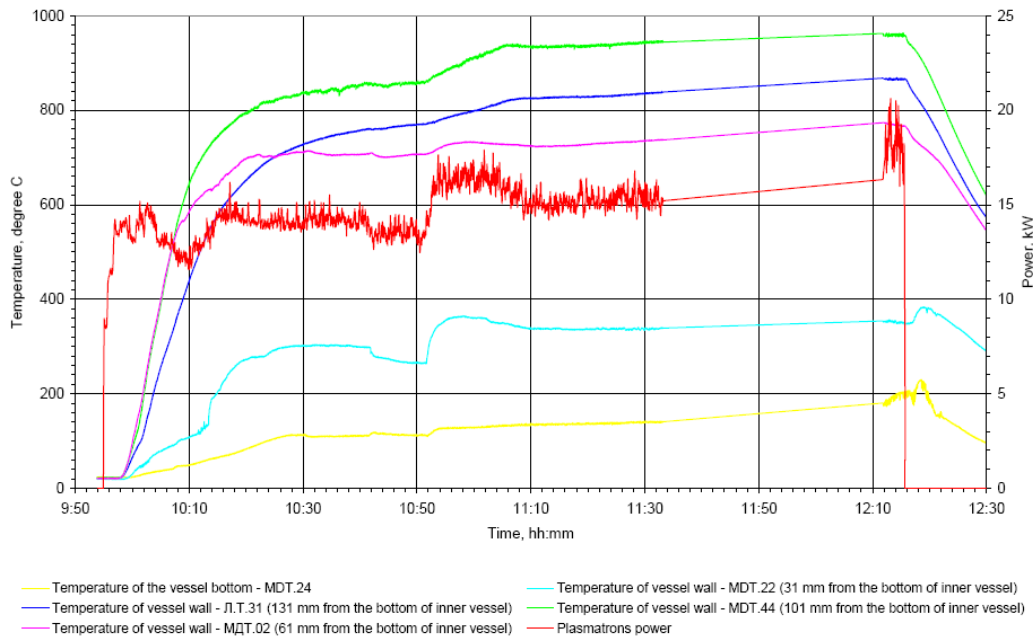


Figure 68 – Temperature curve of the vessel wall

After completion of the test the graphite nozzles of the outer and internal electrodes and burden in the experimental cell were examined. In the result of the examination and required measurement there was detected as follows:

a) the cylindrical part of the internal electrode graphite nozzle was burnt out by 12÷15 mm, maximum length of the remaining part was 48 mm. Total length of the remaining nozzle was equal to 143 mm (before the test the total nozzle length was 155 mm). Appearance of the internal electrode graphite nozzle after the test is represented in Figure69.



Figure 69 – Graphite nozzle of the internal electrode after the test

б) there were no visible damages on the internal surface of the composite graphite nozzle bottom of the outer electrode. The nozzle bottom had no burnout and traces of interaction with melt.

в) upper part of the outer graphite nozzle had also no visible damages.

Appearance of the outer electrode nozzle and the melt after cutting the experimental device vessel is represented Figure 70. In order to keep the melt location in the device the latter was filled with sulfur.

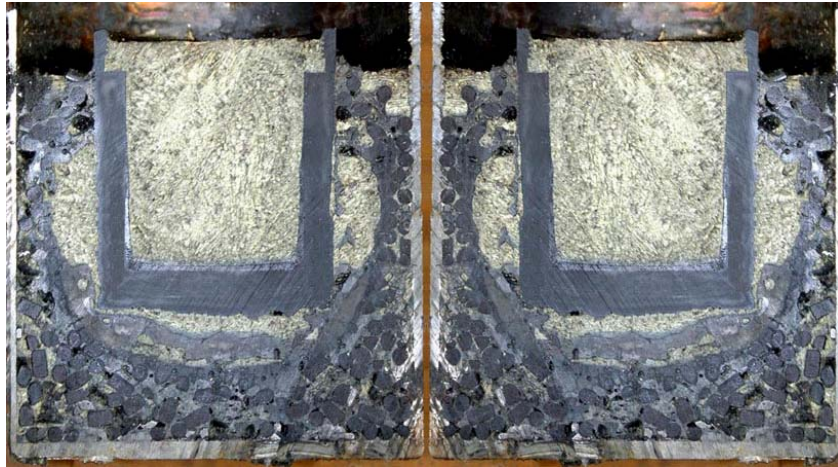


Figure 70 – Appearance of the vessel, composite graphite nozzle bottom of the outer electrode and caked burden after cutting of the vessel

Table 8 includes averaged voltage, current, plasmatrons power, water heating in the cooling paths, heat losses with cooling water, outer electrode nozzle temperature, obtained during the plasmatrons run, and also includes the temperature in different points of the burden heating vessel.

Table 8 – Parameter values resulted from the plasmatrons running

Parameter	Value
Time of the plasmatrons run, h : min : s.	2 : 20 : 40
Averaged voltage of the electric arc, V	38,8 – 45,4 – 72,2
Averaged current of the electric arc, A	354 – 344 – 256
Averaged plasmatrons power, kW	13,7 – 15,6 – 18,2
Maximum heating of water in the plasmatrons cooling path, °C	7,62
Heat losses with plasmatrons cooling water, %	13,2
Maximum water heating in the water cooling jacket of the burden heating device, °C	3,68
Heat losses with cooling water of the burden heating device, %	54,1
Maximum temperature of the outer electrode nozzle, °C (c.p. CLT.01)	590
Maximum temperature of gas released from the burden (melt), °C	611
- c.p. TCJ4	683
- c.p. TCJ5	530
- c.p. TCJ6	
Maximum temperature of vessel wall, °C	
- at a distance of 131 mm from the vessel bottom, c.p. L.T.31	869
- at a distance of 91 mm from the vessel bottom, c.p. MDT.44	963
- at a distance of 61 mm from the vessel bottom, c.p. MDT.02	774
- at a distance of 31 mm from the vessel bottom, c.p. MDT.22	384
- on the vessel bottom, c.p. MDT.24	229
Maximum temperature of melt, °C	1970*
- at a distance of 50 mm from the vessel bottom, c.p. MDT.04	2401*
- at a distance of 75 mm from the vessel bottom, c.p. MDT.14	2584
- at a distance of 100 mm from the vessel bottom, c.p. MDT.34	1979
- at a distance of 125 mm from the vessel bottom, c.p. MDT.103	
Distance from the lower end of the internal electrode nozzle to the outer electrode nozzle bottom, mm	22
- before the test	34
- after the test (minor distance)	
Mass of the internal electrode graphite nozzle, kg:	0,3157
- before the test	0,275
- after the test	

Note: * - indicated temperature at the moment of thermocouple failure

Conclusions on the testing results

As a consequence of the ~141-minute experiment performed the burden melt was produced but the burden was not molten completely. Maximum burden temperature registered by the thermocouples was equal to 2584 °C. The plasmatrons energy release was 138,4 MJ.

Within the experiment performance, ~20 % of consumable part of the internal electrode nozzle was used. Graphite burning out rate was 0,29 g/min.

During the experiment (or at the stage of the cell cooling) the protective coating on the most part of the outer electrode graphite nozzle surface was damaged.

3.2.4 Calculation of the experimental cell for testing a single plasmatrone with corium components loading

To estimate the temperature field in the experimental cell as well as to prepare the following test, heat calculation on the following model (Figure 71) in consideration of the experimental data, was carried out.

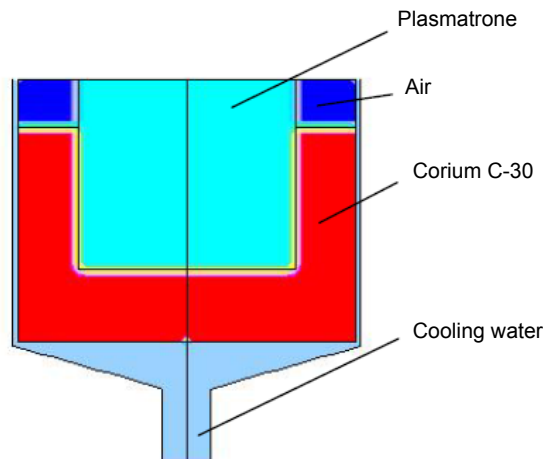
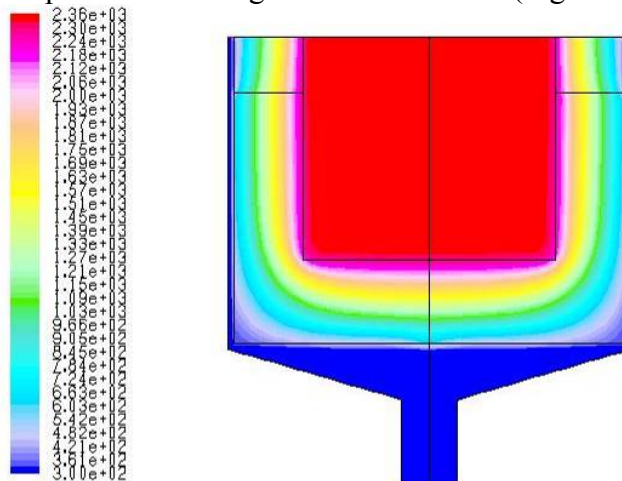


Figure 71 – The calculation diagram of the experimental cell

The calculations showed that at maximum plasmatrons power 18 kW (specified energy release in the plasmatrons material 36 MW/m³) the temperature of the plasmatrone surface and corium layers adjacent to the plasmatrons verges towards 2400 K (Figure 72).



Contours of Static Temperature (k) (Time=0.0000e+00)

Figure 72 – The stationary temperature field in the material at plasmatrone power 18 kW

The temperature field stabilization time in the cell materials since the time of heating start is about 10 minutes. Figure 73 illustrates the temperature curve of the plasmatrons surface and corium in the vicinity of the plasmatrons surface after its actuation as well as warming of the corium in the vicinity of the cooling path wall at cooling water rate 0.2 kg/s and 1 kg/s.

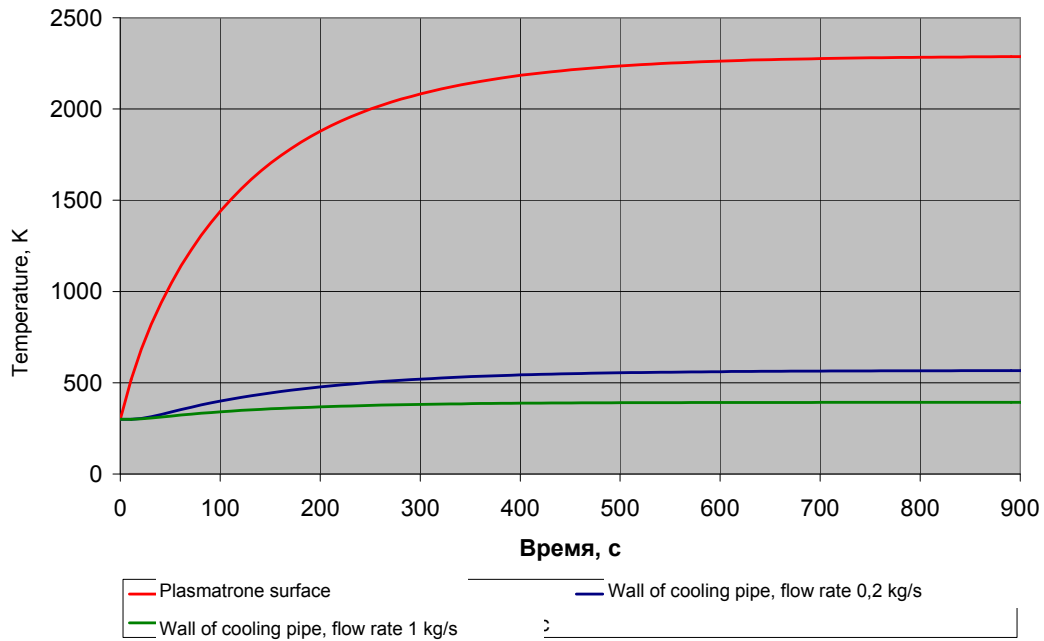


Figure 73 – Temperature curve of the materials on actuation of the plasmatrone

Copper current leads of the external and internal electrodes of the plasmatrons are cooled with distilled water. The objective of the thermo-hydraulic calculation of the plasmatrons is to determine minimally sufficient water flow rate supplied for plasmatrons cooling when copper elements of the structure remain their integrity and no boiling of water in the electrodes cooling path.

As initial data for the calculation there was assumed that the plasmatrone power is ~ 18 kW from which about 60 % is released in the internal electrode. The lower nozzle end of the external electrode is put at depth up to ~ 120 mm in the melt of temperature 3100 K. The temperature of water supplied to the cooling path of the device is 300 K.

For the calculation of the device the thermohydrodynamic mathematical model with two-dimensional ax symmetrical calculation diagram (Figure 74) describing the plasmatrone geometry is used.

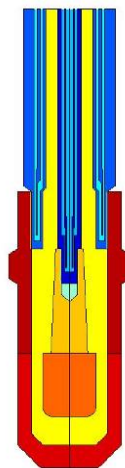


Figure 74 – Calculation diagram of the plasmatrons

The calculations showed that maximum temperature of the plasmatrone structure elements material, at power 18 kW, does not exceed 3400 K (on condition that the lower plasmatrone end is immersed in the corium with temperature not more than 3100 K). The temperature of the structure copper elements is lower 1350 K). Maximum temperature of copper falls to the lower end of the internal current lead. About 80% of the energy released in the internal electrode, by

means of the radiant heat exchange, is transferred to the wall of the external electrode. The temperature field in the plasmatrons structure elements material is given in Figure 75.

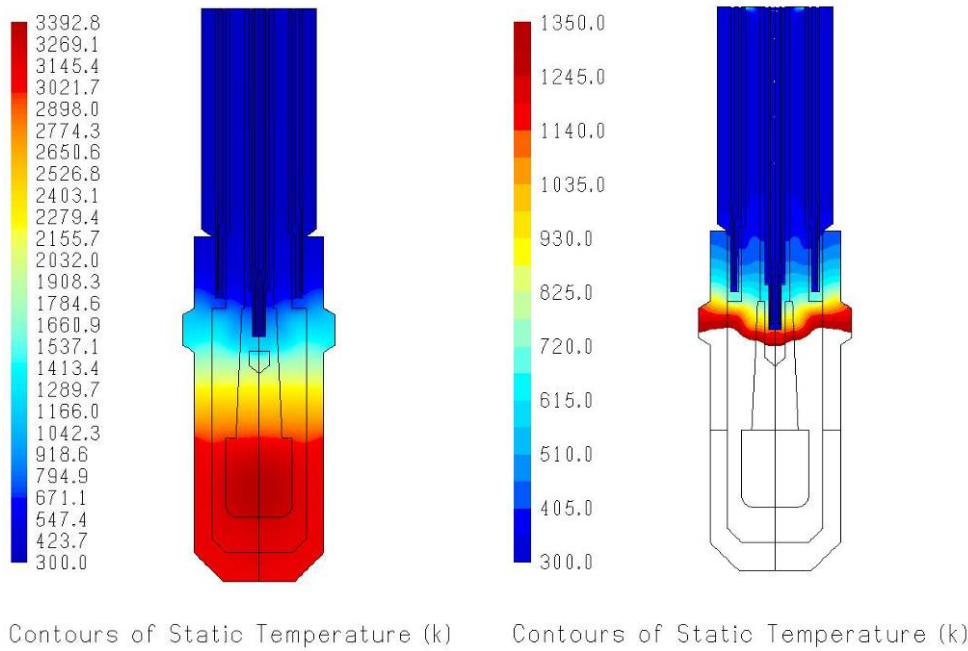


Figure 75 – Temperature field [K] in the materials of the plasmatrons structure elements

Dependence of net power released with the plasmatrons on the temperature of melt surrounding the external electrode is seen in Figure 76.

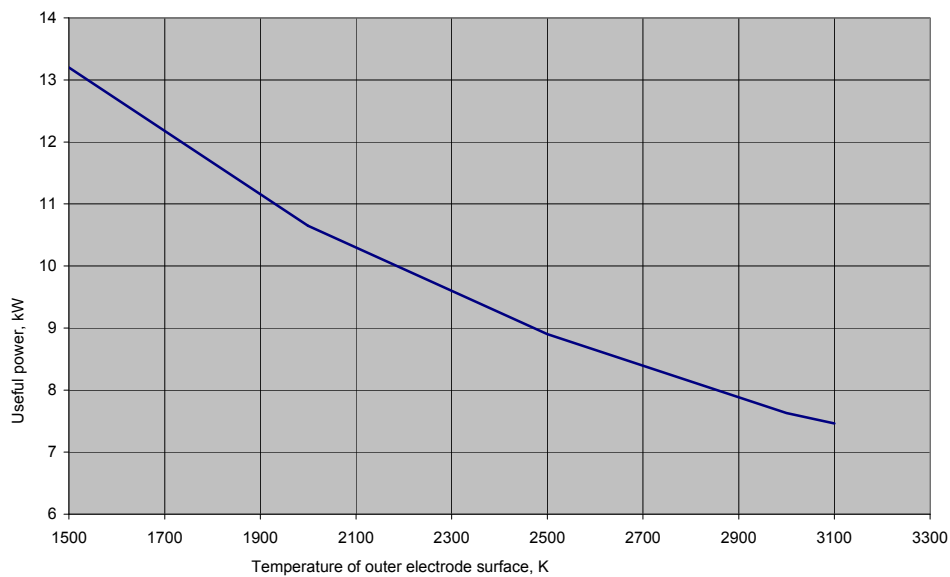


Figure 76 - Dependence of net power released with the plasmatrons on the temperature of the external electrode nozzle surface

The calculations resulted that in the electrode cooling paths the dead zones are formed (Figure 77a illustrates the water velocity field in the electrode cooling paths and convective current of argon in the inter-electrode space, the dead zones are marked with circles). Formation of the dead zones is possible in the vicinity of the lower end of the external electrode cooling path and in the regions of the exit branch widening of the internal and external electrode cooling paths. The calculations showed that when the corium temperature in the vicinity of the electrode exceeds its melting point (3100 K) and when cooling water flow

rate is less than 100 g/s in the external electrode cooling path, and when water flow rate is less than 50 g/s in the internal electrode cooling path, boiling of water is possible in the dead zones. Figure A.2.1.17b depicts the coolant temperature field in the plasmatrons cooling paths at water flow rate 100 g/s and 50 g/s in the internal and external electrode paths, respectively.

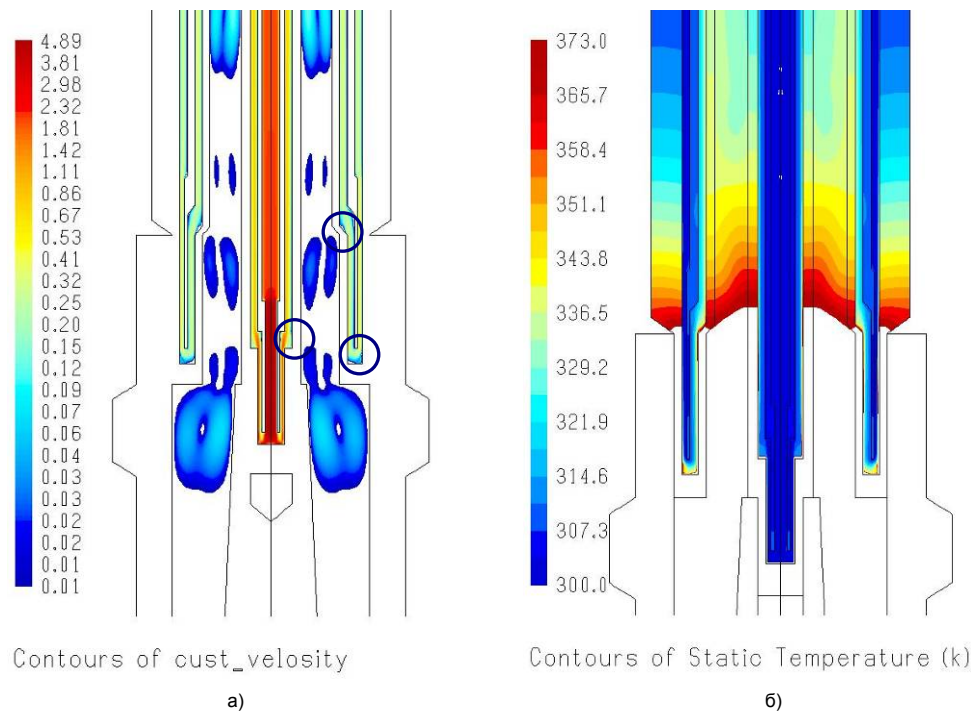


Figure 77 – Water velocity field [m/s] in the plasmatrone cooling paths (a) and temperature field [K] of the coolant (b) at water flow rate 100 g/s and 50 g/s in the cooling paths of the internal and external electrodes, respectively

3.2.5 Thermal calculation of TOP tests conditions

The device for heating up of the corium by means of the plasmatrons in the TOP tests is a cylindrical two-layer steel vessel filled with 12 kg corium mass. In the vessel center there is a plasmatrons sunken in the corium at a depth of 140 mm; the distance from the external plasmatrons surface to the vessel walls is 30 mm; the distance from the lower end of the plasmatrons to the vessel bottom is 50 mm. To reduce heat losses the upper end of the vessel is covered with the heat shield. Between the steel walls of the vessel there is glass cloth insulation. The insulation thickness in the upper part of the device is 0.6 mm, the thickness of the insulation in the lower part of the device and on the device bottom is 0.3 mm. The vessel is enclosed with steel housing. In the 2 mm clearance between the vessel and housing the water is supplied for the device cooling. The diagram of the device for heating up of the corium by means of the plasmatrons in the TOP-2 tests is seen in Figure 78.

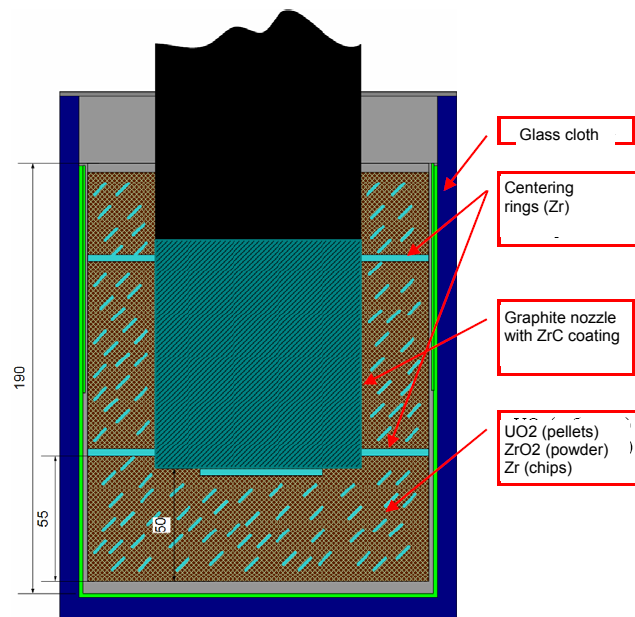


Figure 78 – The diagram of the experimental cell for TOP-2 tests

For estimating of the expected parameters there were conducted thermohydrodynamic calculations of the device. The geometry of the calculated model of the system includes a vessel filled with corium and the plasmatrons (Figure 79).

In calculations there were used the conditions and assumptions as follows:

- It is assumed that there was no heat sink from the upper plasmatrons end and from the device lid.
- Water flow rate in the plasmatrons cooling paths was assumed as equal to 100 g/s, in the vessel cooling path – 200 g/s.
- Coolant temperature at the cooling path inlet was specified as 300 K.
- Thermo-physical properties of the materials used in the calculations were taken the same as in the calculations of the TOP-1 and TOP-2 tests conditions.
- The irradiative heat transfer component that is of significant importance in the system was considered. To calculate the irradiative heat transfer in the inter-electrode space, between the plasmatrons nozzle surface, vessel walls and filling in the upper part of the device the “Surface-to-surface” method was used with consideration of emissivity and the angular coefficients of the system under consideration, the irradiative heat transfer in the clearance between the vessel walls was considered in the form of effective addition to thermal conduction of air filling the clearance.
- Emissivity of steel and graphite was assumed as equal to 0.6, emissivity of thermal insulation is 0.2.
- Plasmatrons power in the calculation of TOP-2 test conditions was assumed as equal to 17 kW, in predictive calculations – 18 kW.
- It was assumed that 2/3 energy release falls on the internal electrode of the plasmatrons; in the external electrode there is 1/3 total energy release.
- Energy release sources, elevation - ~ 5 mm, are on the level of the bottom end of the internal electrode.

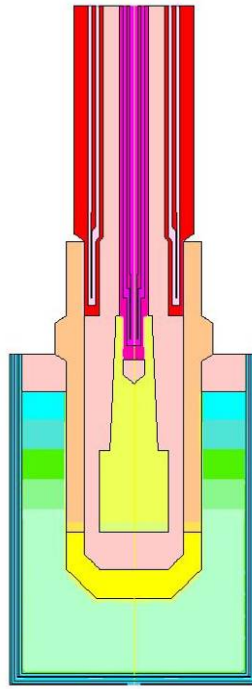


Figure 79 – Geometry of the calculation model

Considering the fact that the corium in the device is in the form of filling, the coefficient of the filling heat conductivity was calculated preceding from the assumption that filling porosity on corium was equal to 0.7.

In the calculations there was used the reduced coefficient of air heat conductivity enabling to consider the irradiative heat transfer in the gap between the vessel walls. The reduced coefficient of air heat conductivity was calculated on the following relation:

$$\lambda = \lambda_0 + 4 \cdot \sigma \cdot \varepsilon \cdot \delta \cdot T^3,$$

where:

λ_0 – air heat conductivity; σ – Stefan-Boltzmann constant; ε – reduced emissivity of the vessel walls; δ – size of the gap between the walls; T – average temperature of air in the gap.

In the course of the estimated calculation there was checked the value of possible heat expansion of the vessel wall materials. It was resulted that on heating of the internal wall of the vessel by 1000 K and negligible heating of the external wall of the vessel, the gap between the walls would reduce by ~ 0.2 mm. Consequently, at given heating of the internal wall the clearance between the walls in the bottom part of the device practically disappears, and in the upper part of the device – decreases halves.

The calculation results of the system with the clearance (that is uniform on the device elevation) between the walls equal to 0.3 mm with regard to the TOP-2 test conditions are represented in Figure 80.

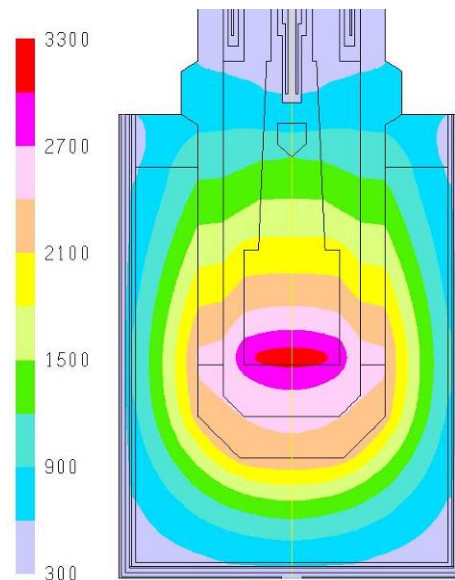


Figure 80 – Distribution of the temperature field in the system [K] with the clearance of 0.3 mm (that is uniform on the device elevation) between the walls

It is found that the results of the calculation agree with the results realized in the course of the TOP-2 test. Thus, the thermocouples MDT.02 and MDT.44 installed on the internal wall of the vessel at an altitude of the plasmatrone arc registered temperature ~ 1100 K, the indication of the thermocouple MDT.11 located on the vessel bottom was 600 K. We see from the results of the post-test investigation of the TOP-2 test that the temperature of the most filling part in the course of the test was lower than the melting point of zirconium, and only a small filling layer adjoining the plasmatrons nozzle, has temperature exceeding the zirconium melting point. Zirconium located in that layer transited to the liquid condition, the liquid migrated to the lower nozzle end – the area where the ingot was formed.

The calculated temperature of the device internal wall and bottom is close to the temperature registered during the experiment. The calculated temperature field in the device material is such that only the filling layer of about 5...6 mm thickness enclosing the plasmatrons nozzle exceeds the zirconium melting point.

The further calculations of the system with the use of the developed calculated model were targeted at optimization of the device structure; the objective was to rise the temperature of filling and the device internal wall. For that purpose it was considered the increasing of the insulation thickness between the vessel walls, organization of an air gap between the vessel walls and modification of the filling layer height in order to reduce the heat exchange surface area between the filling and the coolant cooling the device.

Figure 81 demonstrates the temperature field in the system material at thickness of the insulation layer between the vessel walls equals to 0.5 mm. We see from the results of the calculation that organization of such thickness of the insulation layer and preservation of the gap size during the experiment equal to 0,5 mm enables to increase the temperature of the internal wall of the device up to 1300...1350 K, in this case the thickness of the filling layer in the vicinity of the electrode nozzle, where the temperature exceeds the zirconium melt point, will be about 10 mm.

Figure 82 demonstrates the temperature field in system material at the insulation layer thickness on the internal wall of the vessel equal to 0.5 mm and air gap between the insulation and the external wall of the vessel equal to 0.5 mm. In this case the temperature of the internal wall of the device is possible up to 1500...1600 K with the filling layer thickness in the vicinity of the electrode nozzle in which the temperature exceeds the zirconium melting point, will be also about 10 mm.

We suppose that changing in the filling layer height enables to reduce the heat exchange surface area between the filling and the cooling (cooling the device), and thereby will increase the temperature of filling and the internal wall of the device, was not justified. The calculation of the system, when the electrode was put in the filling at a depth 60 mm (Figure 83), showed that in this case the efficiency of the plasmatrons running degrades. Heat losses to the plasmatrons cooling paths increase, the radiant outflow of energy from the nozzle surface to the internal wall of the vessel is taken place. Despite the fact that the temperature of the upper filling layer in the vicinity of the cell wall is close to 1500 K, the most filling part remains unheated.

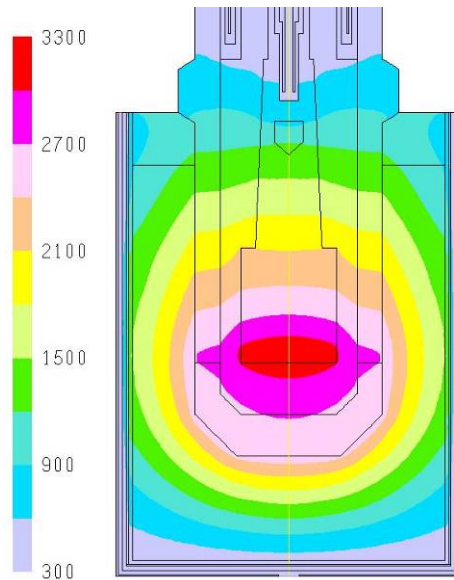


Figure 81 – Temperature field in the system material at thickness of the insulation between the vessel walls equal to 0.5 mm

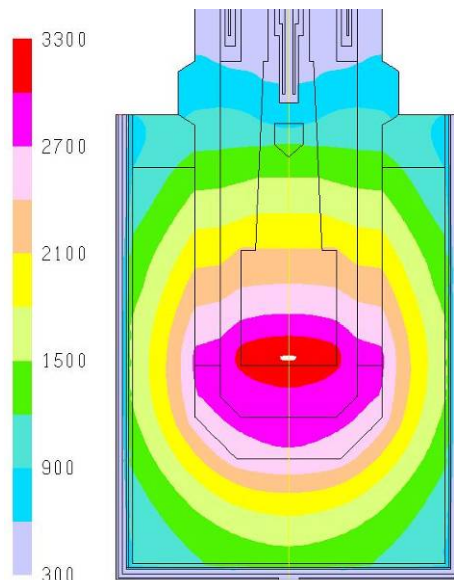


Figure 82 - Temperature field in the system material at thickness of the insulation on the internal wall of the vessel equal to 0.5 mm and air gap between the insulation and the external wall of the vessel equal to 0.5 mm

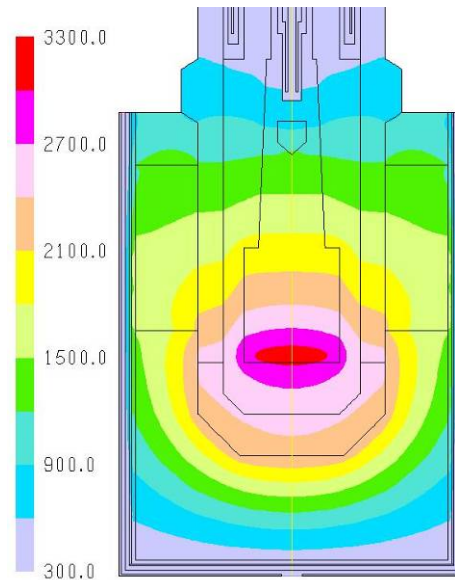


Figure 83 - Temperature field in the system material at putting the plasmatrons in the filling at a depth 60 mm (thickness of the insulation layer between the vessel walls 0.5 mm)

Based upon the performed calculations we may conclude as follows:

1. For the effective running of the plasmatrons the filling layer height should be as much as possible. That reduces heat losses to the heater cooling paths and the stray radiant energy outflow from the nozzle surface to the internal wall of the vessel.
2. On selecting gap sizes between the vessel walls, in the design of the device we have to consider that the diameter of the internal wall of the device may increase by ~ 0.2 mm on heating.
3. The insulation layer 0.5 mm enables to provide the temperature of the internal wall of the device at level 1300...1350 K, thereby the thickness of the filling layer in the vicinity of the electrode nozzle, where the temperature exceeds the zirconium melting point, will be about 10 mm.
4. The heat efficiency of the filling increases on organization of the air gap between the insulation and the external wall of the vessel. Thereby, the temperature rise of the external wall of the device up to 1500...1600 K is possible with the filling layer thickness in the vicinity of the electrode nozzle, where the temperature will exceed the zirconium melt point, will be about 10 mm.

3.2.6 Calculation of corium thermal conductivity on the results of TOP-2 tests

Based upon the results registered in the course of the TOP-2 test, the stationary calculation of the corium temperature field in ax symmetric statement using the ANSYS program was executed. The finite-element model with 11482 knots is presented in figure 84.

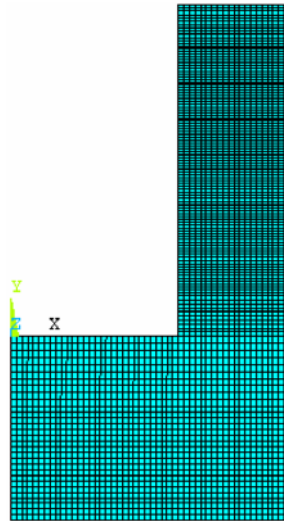


Figure 84 - The finite-element model of corium

The boundary conditions necessary for calculation, were defined on experimental data. On an external corium surface temperature in piecewise-linear interpolation has been set on the basis of 5 thermocouples indications which arrangement was shown in figure 85.

T1 = 603°C (h = 131 mm, r = 75 mm)

T2 = 733°C (h = 101 mm, r = 75 mm)

T3 = 771°C (h = 61 mm, r = 75 mm)

T4 = 576°C (h = 31 mm, r = 75 mm)

T5 = 207°C (h = 0 mm, r = 0 mm)

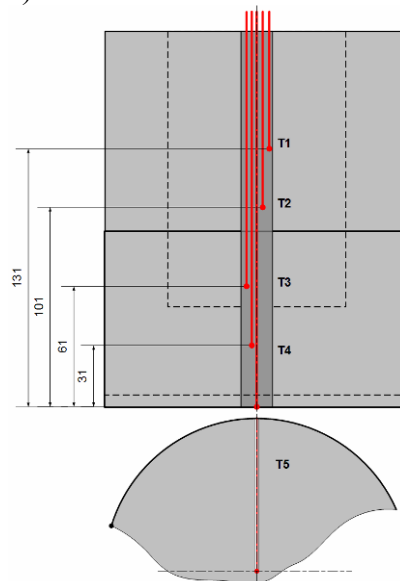


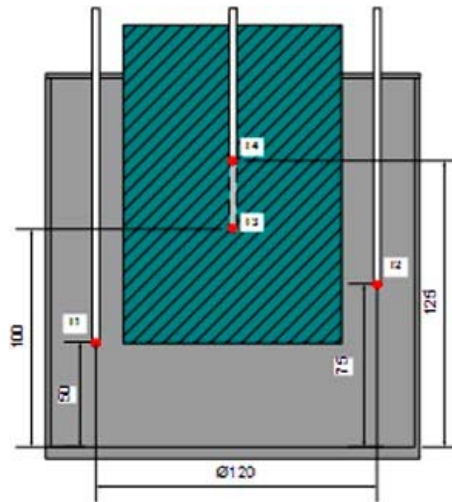
Figure 85 - Thermocouples layout on the surface of inner vessel

On an internal corium surface (along the external electrode surface) the uniform thermal flux is set that is calculated on total power defined by measurement of the flow rate and difference of temperature of the cooling water at the inlet and outlet. As a result $q = 0.48 \text{ MW/m}^2$.

The corium thermal conductivity was taken to minimize the difference of the calculated and experimental values of corium temperature, measured by the thermocouples - their location is seen in figure 86 (thermocouples T₁ and T₂ are failed).

T3_{exp} = 1546°C (h = 100 mm, r = 60 mm)

T4_{exp} = 1591°C (h = 125 mm, r = 60 mm)



T1 – MDT.04, T2– MDT.14, T3 – MDT.31, T4 – MDT.103.

Figure 86 – Layout of thermocouples in the corium

As a result, the thermal conductivity was equal to 5.35 W/(m·K), and the calculated temperature coincided practically with the measured one:

$$T_{3calc} = 1546^{\circ}\text{C}$$

$$T_{4calc} = 1593^{\circ}\text{C}$$

The temperature field is shown in Figure 87. Judging by the temperature a small layer of corium melt should adjoin to the electrode surface.

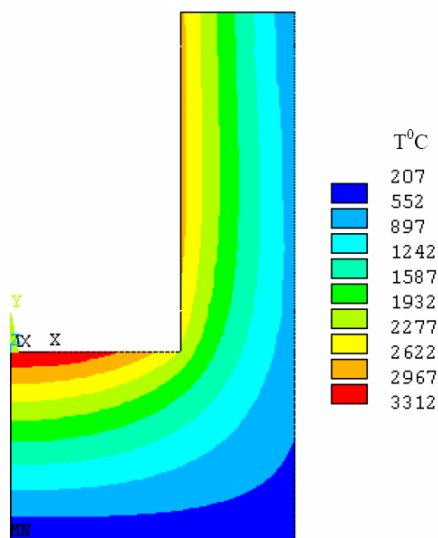


Figure 87 - Temperature field in the corium

Since the power fraction supplied to the corium from the electrode bottom is unknown actually, we may expect that at less value of this power, the power (and thermal flux) supplied to the melt along the lateral surface increases. This creates some (small) increase of the corium thermal conductivity.

We should note that calculations of the molten pool in the RPV model were carried out earlier for values of thermal conductivity 3.3 W/(m·K). If we use in the calculations the obtained value of thermal conductivity, the molten pool volume decreases essentially. In order to have the molten pool volume more essential in the tests with the RPV model, it is expedient to perform these tests with corium C-70 for which thermal conductivity should be much less than for corium C-30.

3.2.7 Calculation of corium thermal conductivity using the results from TOP-5 test

The calculation of test TOP-5 was executed in the following statement. From the pictures the boundary of the molten area around of the electrode was defined and we assumed that on that border there should be an equal temperature, which value is between liquidus and solidus of the melt. On the boundaries (on the vessel walls) the temperature was set according to the indications of the thermocouples. Then, varying the temperature on the boundary of the molten area, we found the temperature value at which the calculated temperature in the thermocouples location points in the "melt" were the most close to the measured values.

As a result the temperature on the boundary of the melted area was equal to 2300 °C (it is close to solidus-liquidus temperature). Thus in point MDT.103 measurement (approx.) – 1950°C, calculation 1980 °C, in point MDT.34 measurement - 1850 °C (approx.), calculation 1830°C, in point MDT.14 measurement - 1400 °C (approx.), calculation 1580 °C. Each measurement was taken from the time shelf not long before heating cut.

Measurement MDT.04 - was rejected, since the temperature is unfairly high, does not agree with other measurements.

Thermal conductivity of the solid corium was equal to 5 W/ (m·K). At this value the power supplied to the corium was 18,6 kW. The temperature field in the experimental cell TOP-5 is shown in Figure 88.

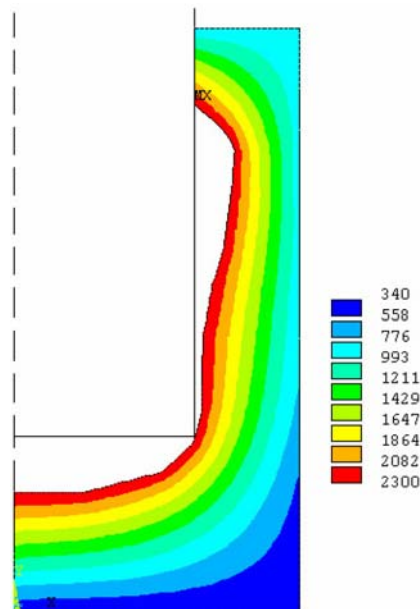


Figure 88 - Temperature field in experimental cell TOP-5

In addition to the activity described in chapter 3 of the given report the off-line and comprehensive testing of the gas feed/withdrawal system, water feed system, power supply system and DMS was performed. A large scope of the computational and experimental work on applying protective coating on the graphite components of the "Lava-B" test facility, contacting with corium during the integral tests, was completed. In the large group of tests there was tested the protective coating life against the corium components at high temperature (also for the corium with additive of stainless steel components).

The possibility of heating 60 kg corium components located in the model with the help of the plasmatrone heater (the calculations were conducted in connection with long delivery delay of the graphite materials for the EMF of the "Lava-B" test facility and long search of the alternatives for the performance of the integral tests) was estimated.

The detailed description of the experimental results is represented in the Project Annual Technical Reports for 1...3 years.

4 Integral tests

In implementing the Project there were performed 4 large-scale integral experiments instead of three tests scheduled. The fourth test was a repetition of the first one on corium composition. As opposed to other experiments, in the fourth test the heat insulation efficiency outside the vessel model was increased greatly and the second upper thermal shield was added. The corium loading data in all integral tests are included in Table 9.

Table 9 – Loading of the initial components in the melting volume

Test	Material in EMF				Add corium in RPV model	Total in test	Corium in RPV model after test
	UO ₂ , g	Zr, g	ZrO ₂ , g	Total, g	g	g	g
INECOR-1	45720	8815	5580	60115	-	60115	-
INECOR-1/2	45720	8430	4830	58980	-	58980	-
INECOR-1/3	46200	8530	5285	60015	10000	70015	47040
INECOR-2	46200	8485	5340	60025	9400	69425	68928
INECOR-3	46200	8491	5326	60017	-	60017	58445
INECOR-1/4	46200	8495	5340	60035	-	60035	55370

4.1 First integral test INVECOR-1.3

The first integral test was dedicated to modeling of the molten corium pool on the lower head of the reactor pressure vessel, when the main share of the oxide corium falls to the lower plenum in the form of the molten prototype corium C-30. After falling the melt on the lower head of the reactor vessel decay heat in the corium is simulated by means of an assembly of five coaxial plasmatrons. On preparation of the test, the ~60 kg core components were loaded in the "Lava-B" electric melting furnace. The approach of corium components location in the graphite crucible was similar to that used in the first calibration test (see Fig. 31). About 10 kg of oxide corium C-90 in the form of small particles of the ingot produced in the first calibration test was loaded additionally in the experimental section. Thereby, in case of complete drainage of the melt from the EMF, existence of 70 kg prototype corium is expected in the experimental section.

Figure 89 gives the experimental section diagram for the first integral test.

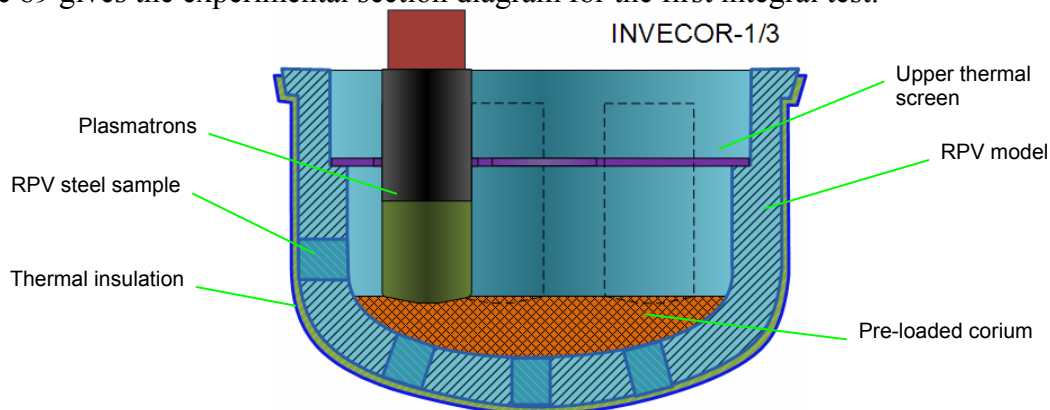


Figure 89 – Diagram of the experimental section for the first integral test

The experimental section was prepared as provided by the results and recommendations of the preliminary calculations and supporting tests (Fig. 26, 27). The lower parts of the outer nozzles of the coaxial plasmatrons were coated with the protective zirconium carbide layer (Fig. 90).



Figure 90 – Coaxial plasmatrons before their installation in the experimental section

The experimental section ready-assembled with the plasmatrons decay heat simulator was located in the "Lava-B" MR and connected to the electrical, gas, water and instrumentation communications of the test facility (Fig. 91). Before the test the cavities of the EMF and MR were leak tested, then air was exhausted from the cavities and argon was filled in the cavities.

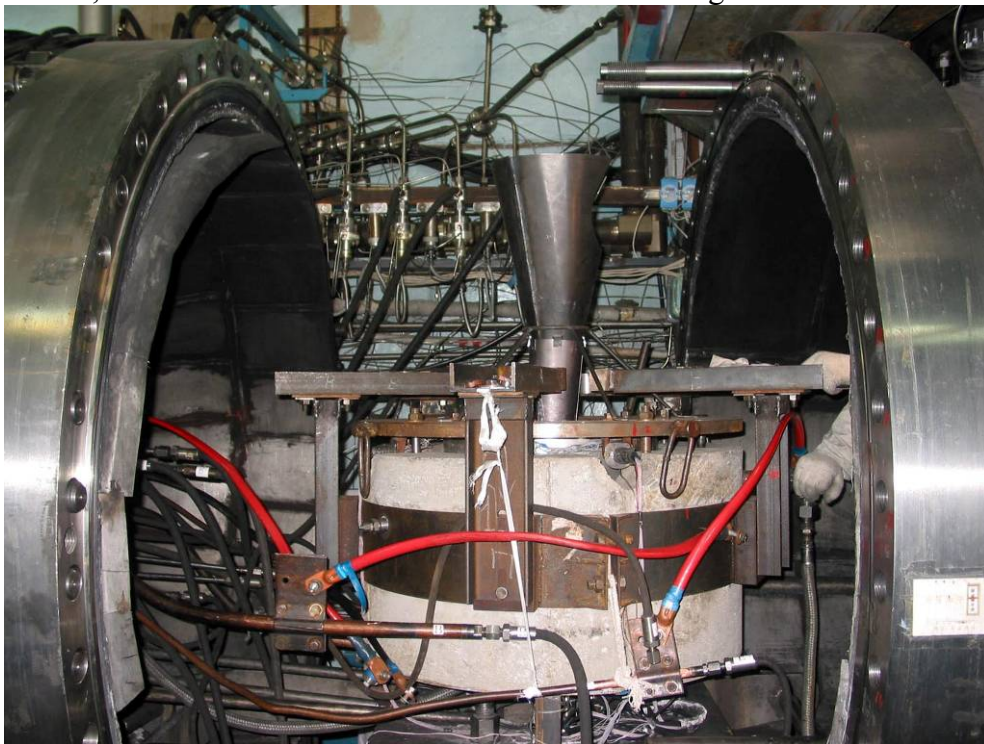


Figure 91 – Experimental section in the "Lava-B" MR

The diagram of the corium components warming/melting in the "Lava-B" EMF was prepared based upon the results from the large-scale calibration tests (Fig. 92). Stability of the plasmatrons running at the stage of preliminary warming up of the reactor pressure vessel model prior to the melt discharge was provided with the use of argon as a working gas of the plasmatrons, in spite of the fact that in such case the plasmatrons power is lower than on their running with nitrogen or gas mixture.

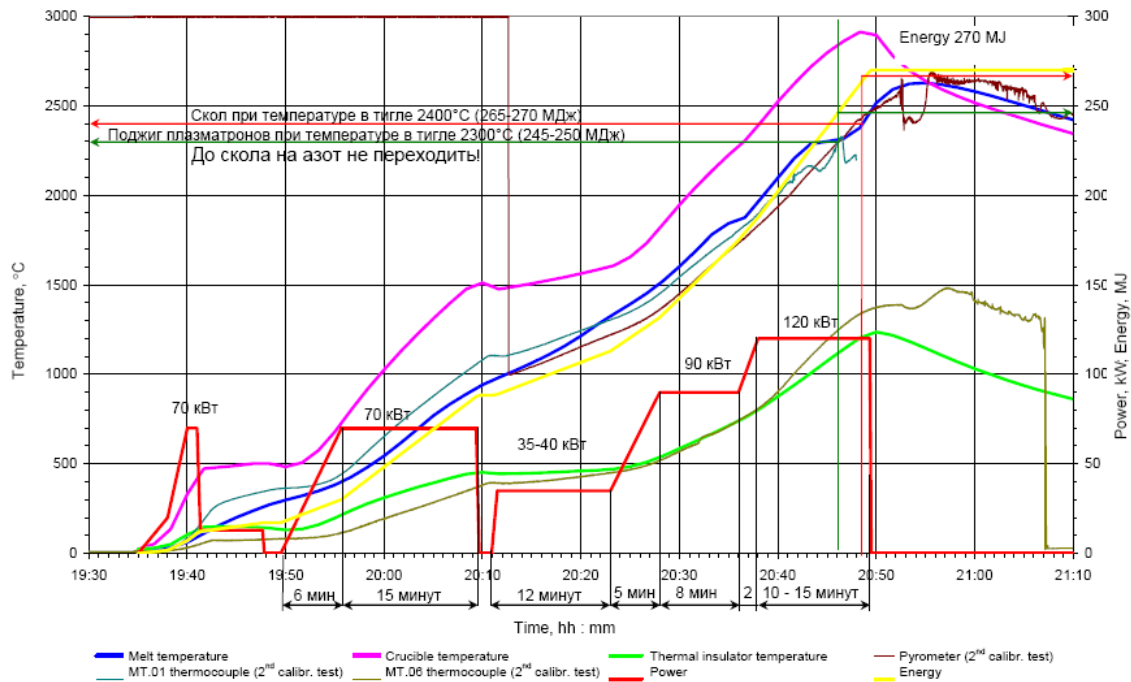


Figure 92 – Calculation diagram of corium components warming up in the "Lava-B" EMF

The electrical power of the EMF inductor increased stepwise to provide more uniform warming of the loading in the crucible and to prevent melt ejection upward from the lateral peripheral zone of the loading owing to local overheating of the melt and impact of electromagnetic field of the inductor (Fig. 93).

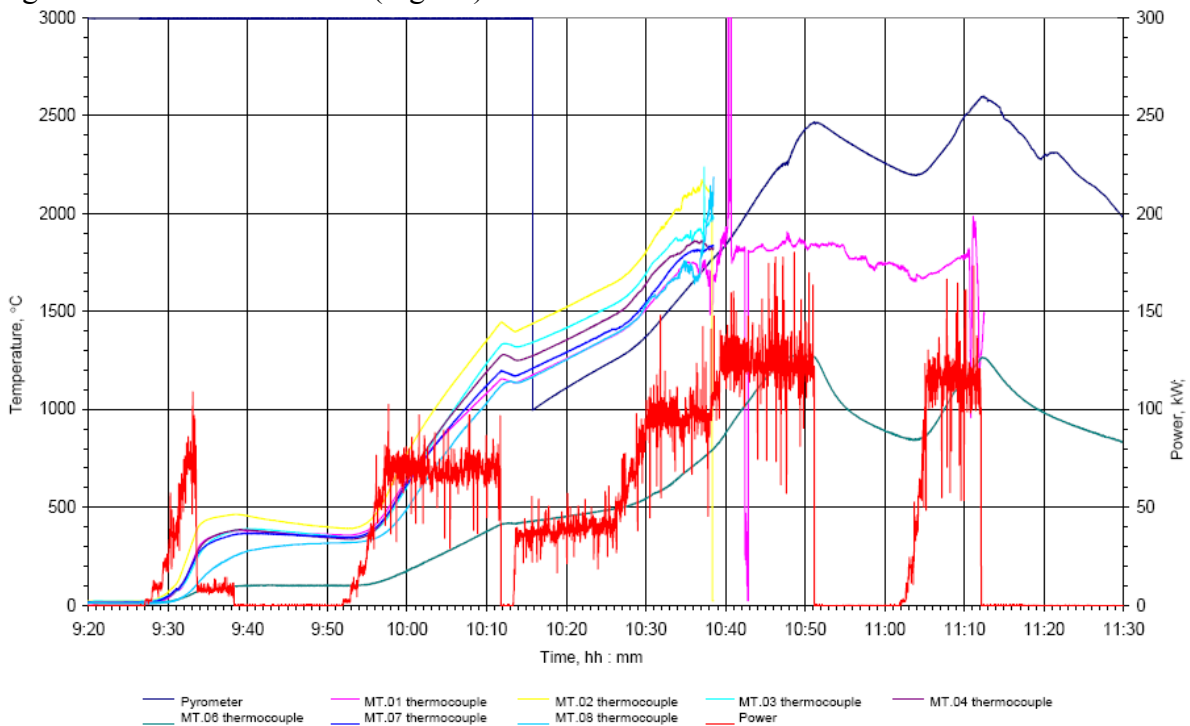
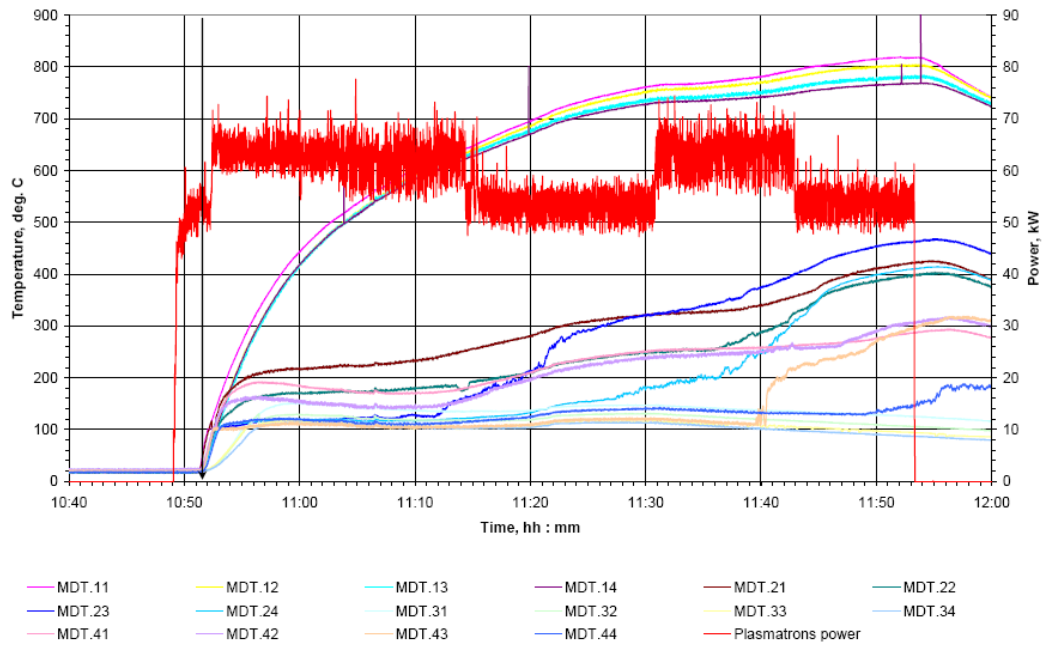


Figure 93 – Diagram of corium components heating in the "Lava-B" EMF

Approximately 10 minutes before reaching of the preset corium temperature, the plasmatrons of the device for simulating decay heat were activated to preheat the reactor vessel model. In achieving the corium temperature in the crucible (according to the pyrometer indications), the plug in the melting crucible bottom was broken and the melt was drained to the reactor vessel

model. The fact of the melt fall was registered by all thermocouples located in the reactor vessel model and in the "Lava-B" MR (Fig. 94).



INVECOR – 1.3

Figure 94 – Temperature of the reactor vessel model wall

The duration of the test (from the melt discharge to the moment of the plasmatrons disconnection) was approximately one hour. The plasmatrons were disconnected as a result of the arc interruption in one of the plasmatrons and impossibility of its repeated ignition. Maximum temperature was registered on the lateral wall of the reactor vessel model and was equal to about 820 °C. The average total power of the plasmatrons was 65 kW. After completion of the test and cooling of the main "Lava-B" units the EMF and MR were disassembled and primary examined. It was founded that near 10 kg corium components was left in the melting crucible. That fact was considered at planning the next test. In the experimental section there was discovered the solidified corium melt, thereby the upper layer represented a fine filling. The layer thickness was about 2 cm (Fig. 95).



Figure 95 – View of the experimental section after the experiment

After removing the layer of corium particles and withdrawal of the plasmatrons, the graphite nozzles of the plasmatrons contacting with corium during the experiment were examined. It was discovered that the protective coating prevented chemical interaction between the components of corium and carbon (Fig. 96).



Figure 96 – Condition of the plasmatrons electrode nozzles

The description of the post-test operations and the resultant data will be represented below in section 5.2 of the given report.

4.2 Second integral test INVECOR-2

In preparation of the experimental section for the second integral test, as per the working plan, it was necessary to add stainless steel in the corium located in the reactor vessel model. To avoid undesirable physical and chemical processes in the EMF melting crucible, there was decided to locate sheet stainless steel in the experimental section simulating the internal cladding of the VVER reactor vessel (Fig. 97).



Figure 97 – Stainless steel in the reactor vessel model

The steel sheet was fixed with dot welding to the internal surface of the reactor vessel model.

As it was in the first integral test, 9,4 kg corium oxide C-90 taken from the ingot produced in the first calibration test was located in the reactor vessel model (Fig. 98).

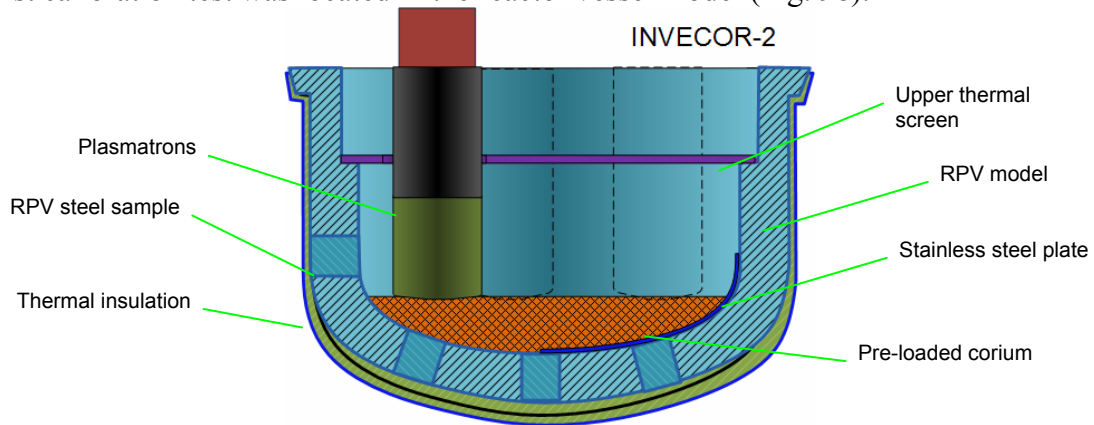


Figure 98 – Structure of the experimental section for the second test

The diagram of power supply to the EMF inductor was updated in consideration of the results from the first integral test, - heating rate of the corium components loading was decelerated in the area of the metallic zirconium melting in order to prevent undesirable moving of the melt inside the crucible before the plug break and melt discharge (Fig. 99). The diagram of corium heating in the EMF during the experiment is given in Fig. 100.

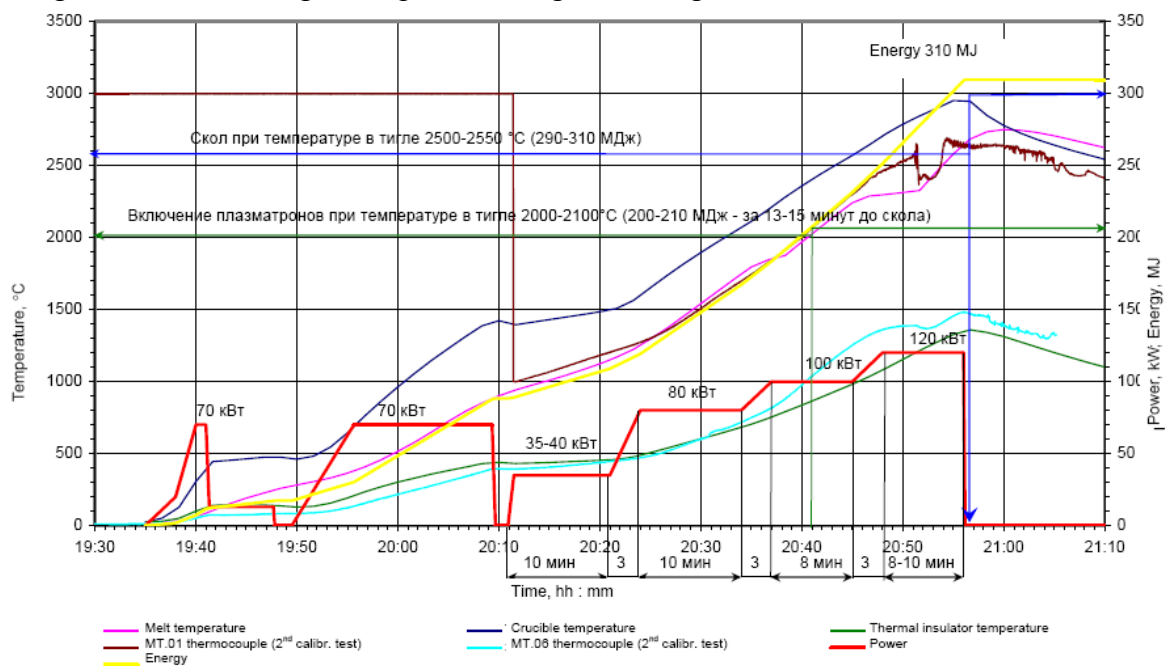


Figure 99 – Calculation diagram of corium components heating in the EMF

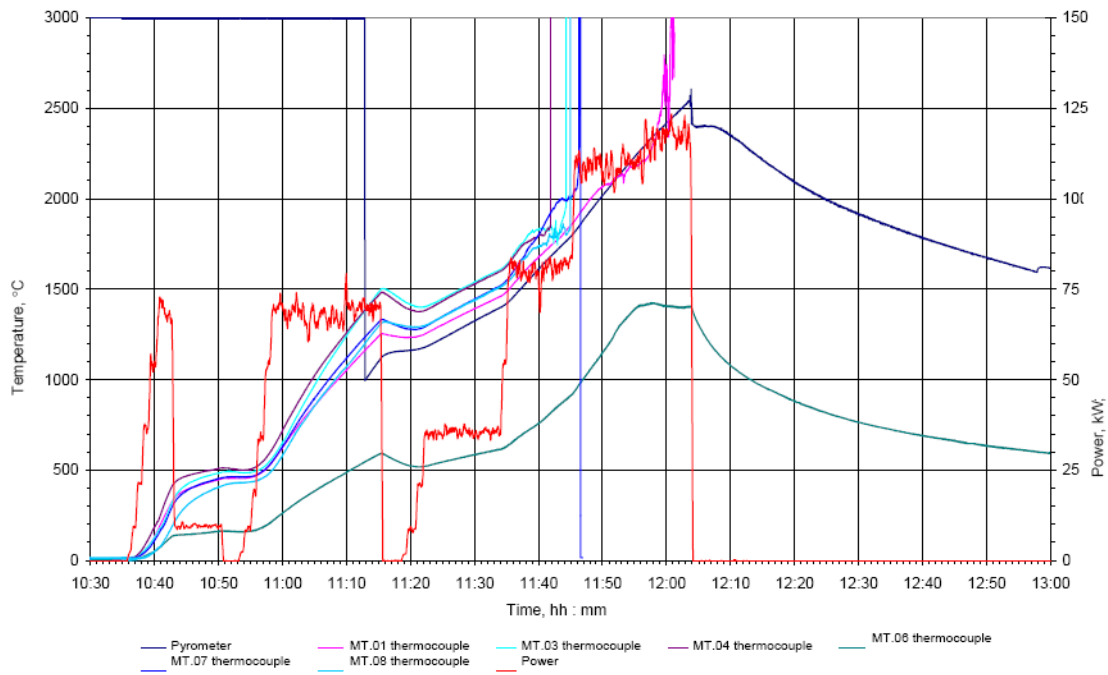
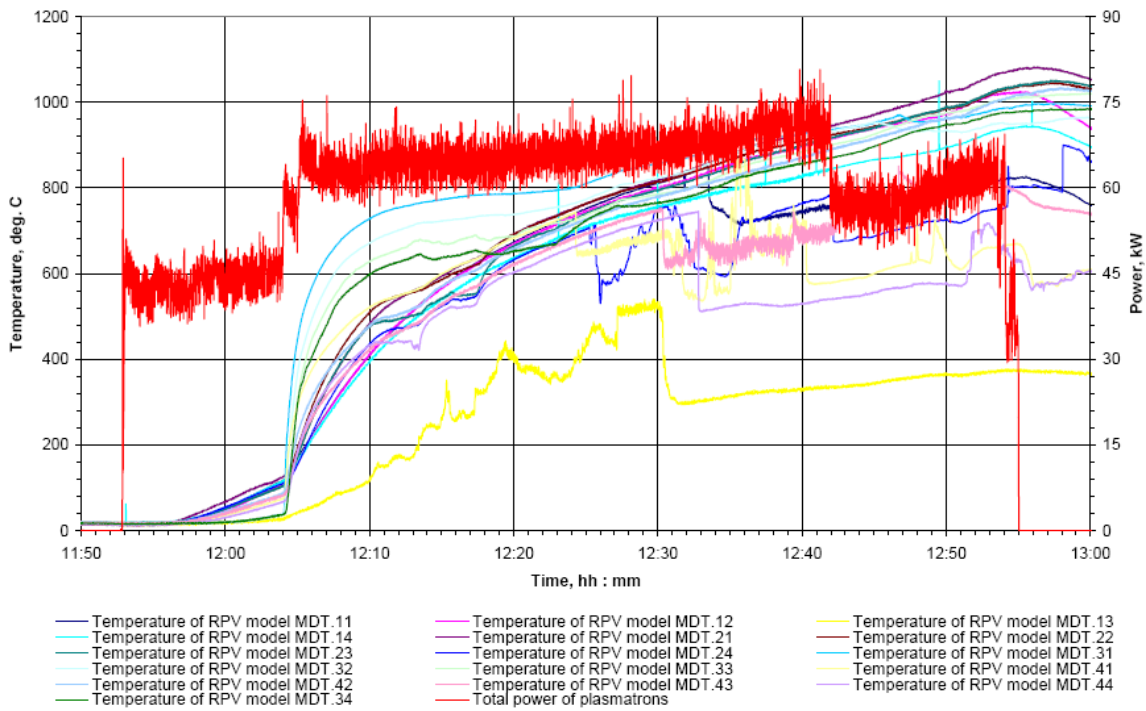


Figure 100 – Diagram of corium components heating in the EMF

The hole in the crucible bottom for discharge of the corium melt was opened when the temperature 2570 °C inside the crucible was reached. The plasmatrons heater was actuated 15 minutes before the melt discharge, that provided warming up of the reactor vessel model wall up to ~150 °C³.

Figure 101 represents the temperature curves in the wall of the reactor vessel model during the experiment. The total duration of the experiment (including the preheating stage) was about 1 hour. The average power of all plasmatrons during the experiment was about 75 kW. During the experiment the maximum heating temperature of the vessel model wall was observed in the central part of the model bottom and was equal to 1050°C. As it was in the previous case, the experiment was stopped due to the arc interruption in the plasmatrons.

³ We should remember that the moment of corium discharge is determined according to the readings of the pyrometer measuring the temperature inside the crucible. The cause for opening of the discharge hole may be not only reaching the preset temperature but also temperature fluctuation in the vicinity of the preset level. The fluctuations may be induced with the start of melt splashing upwards, to the side of the drainage holes. To avoid loss of the melt discharged to the experimental section the plug breaking instruction is given. In this connection, the time of the vessel model preheating with the plasmatrons would not be defined strongly in advance.



INVECOR – 2

Figure 101 – Temperature of the vessel model wall

The maximum temperature of the vessel wall reached in the experiment was 1100 °C. The hottest zone was on the vessel model bottom under the plasmatrons.

During the experiment the temperature of the upper heat shield was about 820 °C (Fig. 102), in the time of the melt discharge there was observed temperature excursion of the shield up to 1300 °C (probably, as a result of the contact between the shield and the director cone for the melt discharge).

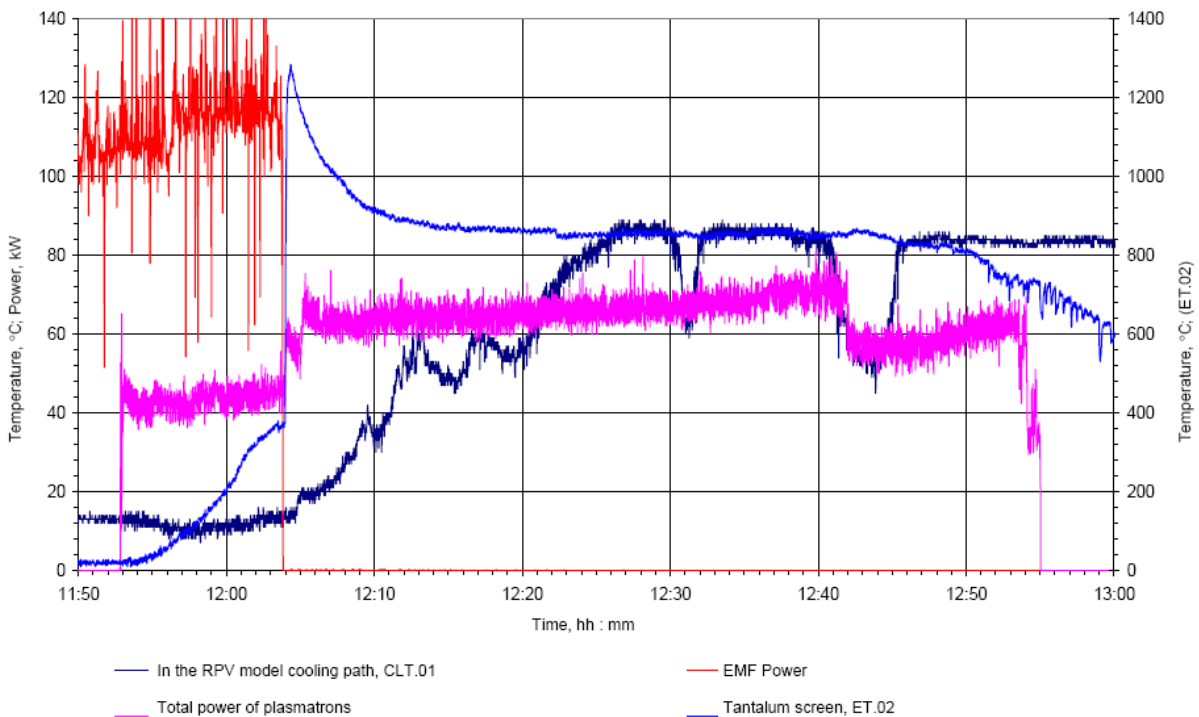
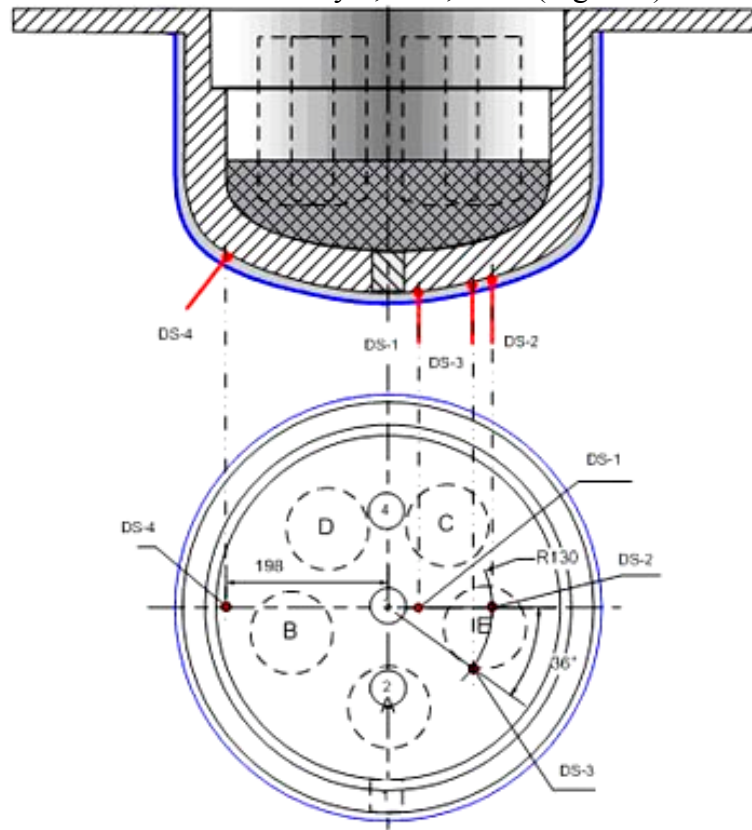


Figure 102 – Temperature of the upper heat shield during the experiment

The displacement/strain gages installed in the bottom part of the vessel model (Fig. 103) registered displacement of the model wall by 0,1...0,2 mm (Fig. 104).



Top view

Figure 103 – Placement of the displacement/strain gages of the model wall

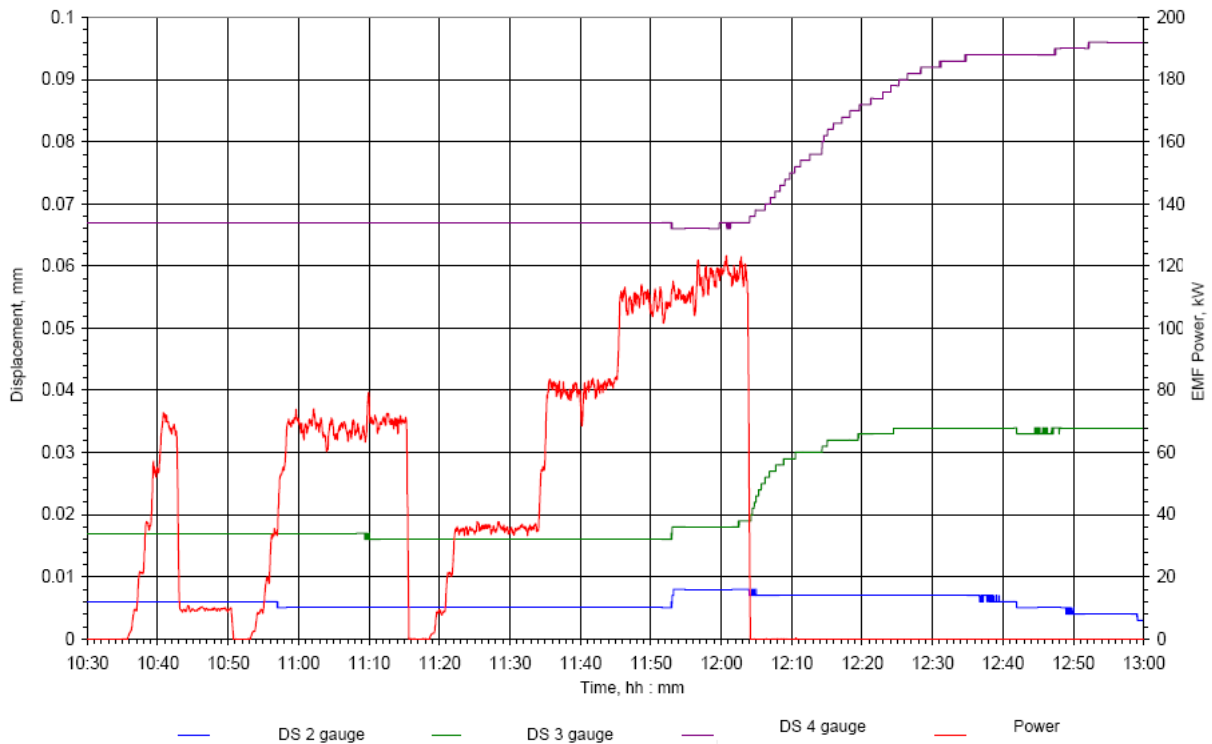


Figure 104 – Readings of the displacement/strain gages of the model wall

After completion of the test and cooling of the main "Lava-B" units the EMF and MR were disassembled and primary examined. It was founded that there were no practically corium components in the melting crucible. In the experimental section there was discovered the solidified corium melt, thereby the upper layer, as it was in the first test, represented a fine filling. The layer thickness was about 2 cm (Fig. 105).



Figure 105 – View of the experimental section after the experiment

After removing the layer of corium particles and withdrawal of the plasmatrons, the graphite nozzles of the plasmatrons contacting with corium during the experiment were examined. It was discovered that there was no erosion of the graphite on the nozzles surface that demonstrates reliability of the protective coating.

The description of the post-test operations and the resultant data will be represented below in section 5.3 of the given report.

4.3 Third integral test INVECOR-3

In preparation of the experimental section for the third integral test, as per the working plan, it was necessary to add stainless steel in the corium located in the reactor vessel model. In this test it was decided to simulate falling of the steel construction fragments from the top on the corium pool after its discharge and formation of the upper crust. Such configuration may serve the testing of the postulate scenario for severe accident progression as provided by that, in the corium pool located on the vessel bottom, a layer of metallic melt is formed over the oxide layer (so called "focus-effect"). The existence of such layer is considered as a dangerous event from the view point of penetration probability in the contact area of the molten metal and the reactor vessel wall.

The diagram of the material layout in the reactor vessel model is represented in Figure 106. The metal plate was hung lower the upper heat shield on the copper cramps. It was expected that after the melt drain and the plate heating with heat emission, the copper cramps would be molten or would lose stiffness getting free the hanged steel plate. The time of the plate heating before the copper cramps degradation is sufficient in order to have time to form a solid crust on the corium surface and to prevent the steel falling in the corium oxide melt directly.

As opposed to the previous experiments, the corium fragments were not added to the vessel model that would ensure higher temperature of the model heating before the melt drain.

In addition, to increase the temperature of the model wall, in the experiment there was specified the minimum possible flow rate of water cooling the external surface of the vessel model (thermal insulation).

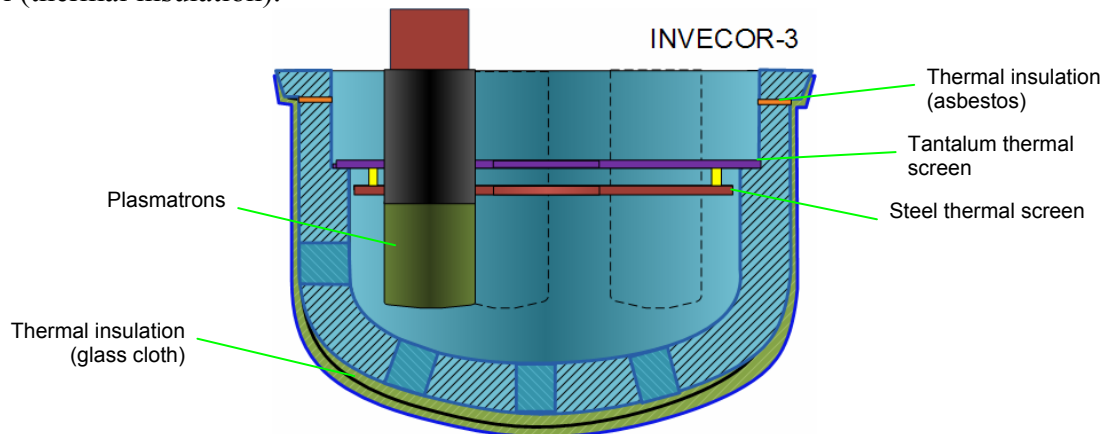


Figure 106 – Scheme of the reactor vessel model preparation for the test

Figures 107, 108 depict the calculation and experimental diagrams of the corium components heating in the EMF.

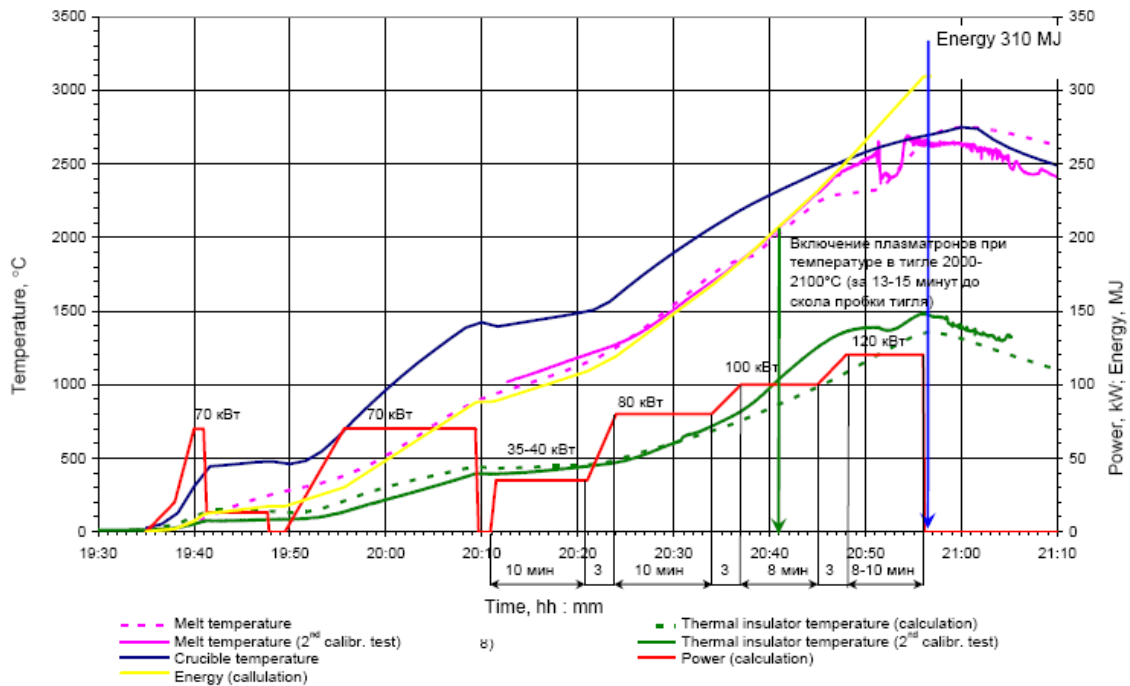


Figure 107 – Calculation diagram of the corium components heating in the EMF

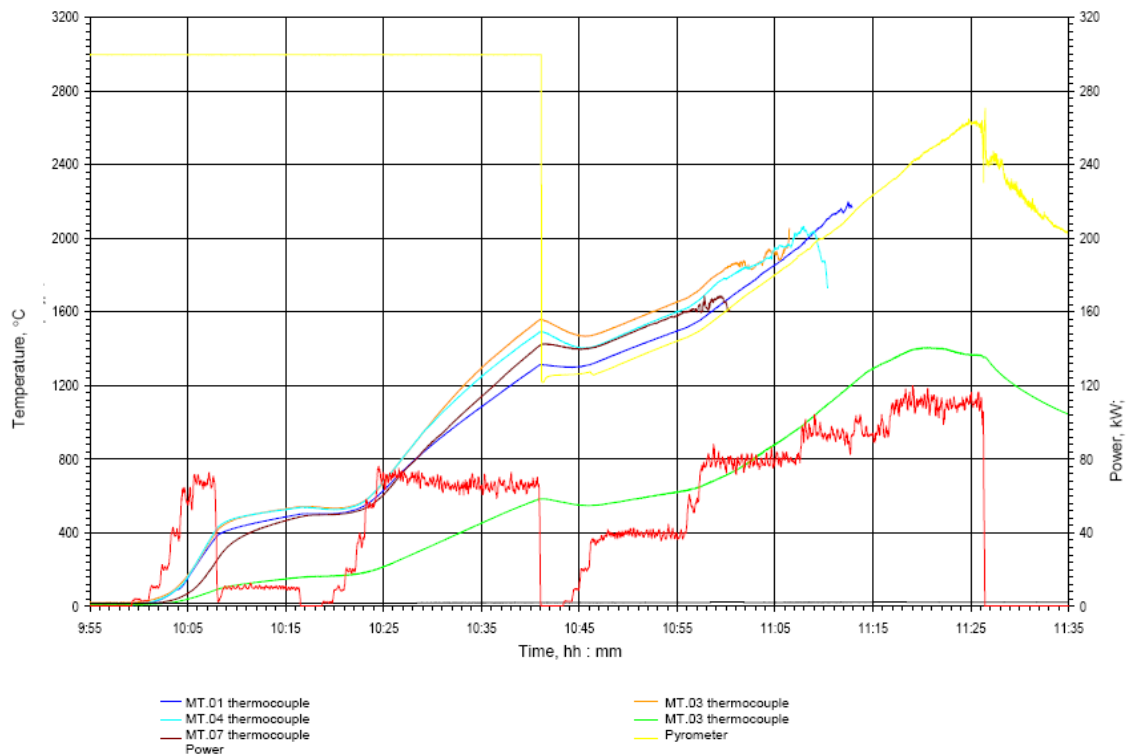
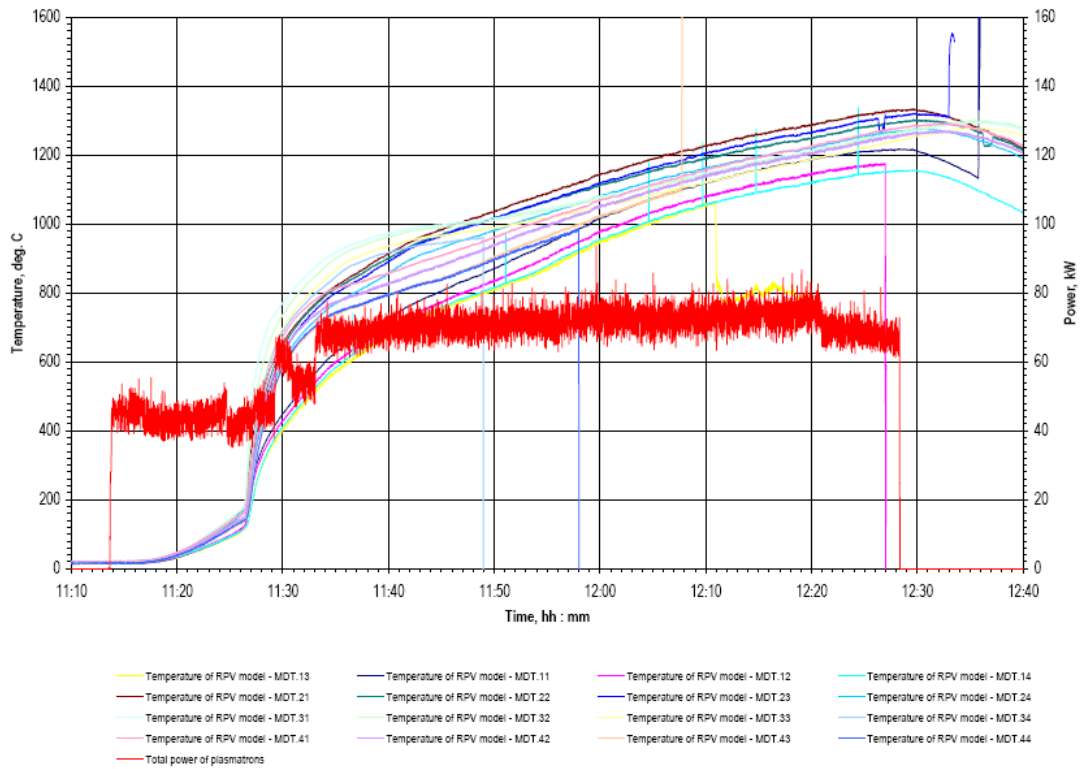


Figure 108 – Diagram of the corium components heating in the EMF

The hole in the crucible bottom for discharge of the corium melt was opened when the temperature 2630 °C inside the crucible was reached. The plasmatrons heater was actuated ~15 minutes before the melt discharge, that provided warming up of the reactor vessel model wall up to ~180°C (at the preheating stage of the cooling water flow rate on the external surface of the vessel model was switched off).

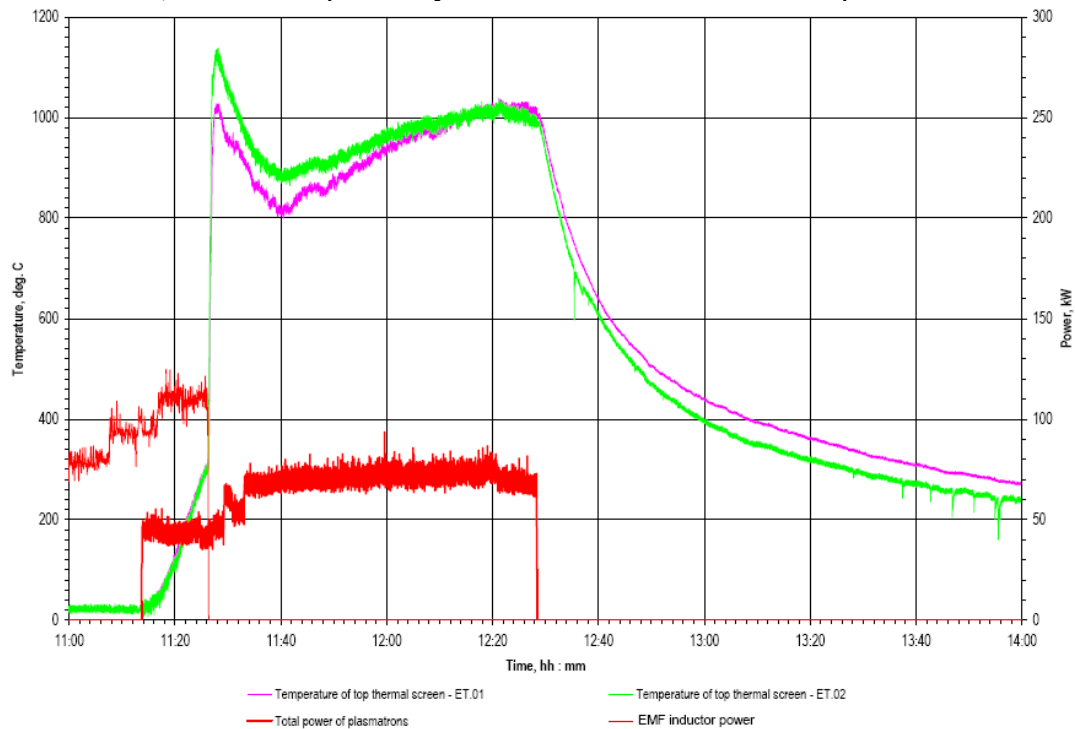
Figure 109 illustrates the temperature curves in the wall of the vessel model during the experiment. Total duration of the test (including the preheating stage) was over one hour. The average power of all plasmatrons during the experiment was about 78 kW. During the experiment the maximum heating temperature of the vessel model wall was observed in the central part of the model bottom and was equal to 1350°C.



INVECOR – 3

Figure 109 – Temperature of the vessel model wall

From the behavior of the temperature curve of the upper heat shield we may presume (Figure 110) that the upper steel plate fell on the corium surface 10...12 minutes later after the melt drain to the model, as it was expected by the initial conditions of the experiment.



INVECOR-3 (Thermal screen)

Figure 110 – Temperature of the upper heat shield during the experiment

The deformation gages demonstrate displacement of the vessel model wall by 0,1...0,3 mm, depending on the placement (Figure 111).

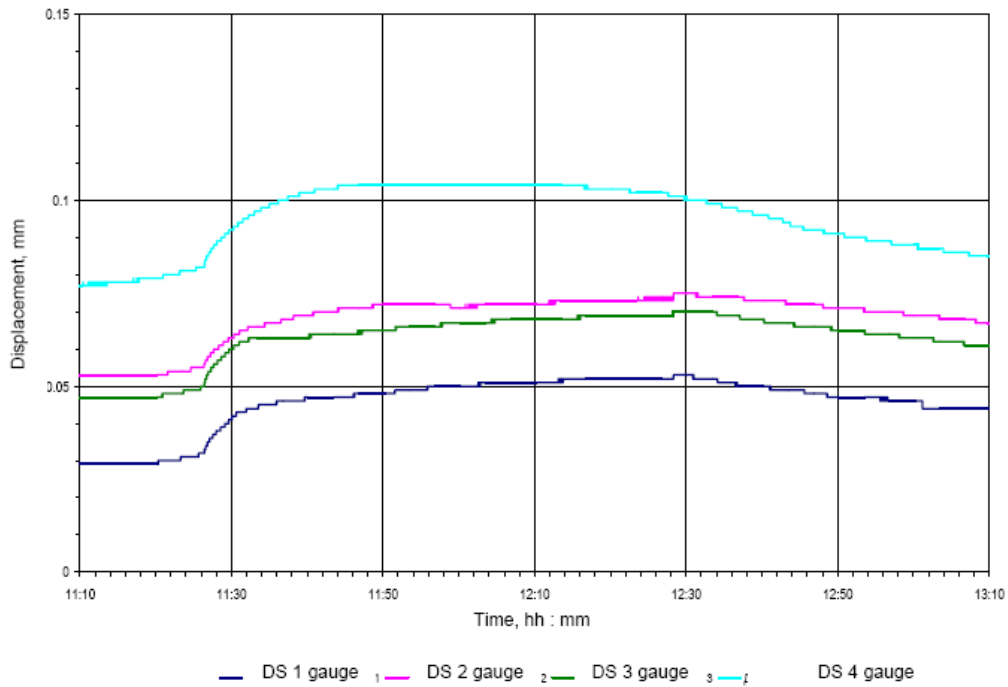


Figure 111 – Readings of the displacement/deformation gages of the vessel model wall

After completion of the test and cooling of the main "Lava-B" units the EMF and MR were disassembled and primary examined. It was founded that there were no practically corium components in the melting crucible. In the experimental section there was discovered the solidified corium melt, thereby the upper layer, as it was in the previous tests, represented a fine filling. The layer thickness was about 2,5...3 cm (Fig. 112). Steel plate remains were located over the corium particles layer. In some places there was discovered "welding" of the plate remains with the vessel model wall.



Figure 112 – View of the experimental section after the test

After removing the layer of corium particles and withdrawal of the plasmatrions, the graphite nozzles of the plasmatrions contacting with corium during the experiment were examined. It was discovered that there was no erosion of the graphite on the nozzles surface that demonstrates reliability of the protective coating.

The description of the post-test operations and the resultant data will be represented below in section 5.4 of the given report.

It is necessary to notice, that the internal surface of the concrete base strongly degraded in the course of experiment (Fig. 113), that is connected with a stop of the cooling water flow for rise in temperature in a zone of a corium/steel interaction. As it could affect safety of works performance, in following experiment other measures have been applied to rise of temperature in experimental section.



Figure 113 – Inner surface of concrete base after the test

4.4 Fourth integral test INVECOR-4

The fourth integral test was a repetition of the first integral experiment from the view point of corium composition. The main differences in the test execution conditions were provided with the following measures:

- lack of preliminary filling of corium oxide to the reactor vessel model;
- increase of the external insulation efficiency of the reactor vessel model owing to changing glass cloth for graphite felt (that decreases insulation thermal conductivity by 8...10 times);
- increase of the upper heat shield efficiency over the corium owing to location and positive clamping of the steel plate between the corium surface and the main tantalum shield;
- control of the external cooling water flow rate from the condition of maintenance of the outlet temperature at the level 90 °C.

The diagram of the experimental section preparation and its appearance are given in Figure 114. To evaluate heat fluxes along the vessel model wall, there were installed additional thermocouples between the 1st and 2nd groups of thermocouples (in the zone of maximum model curvature).

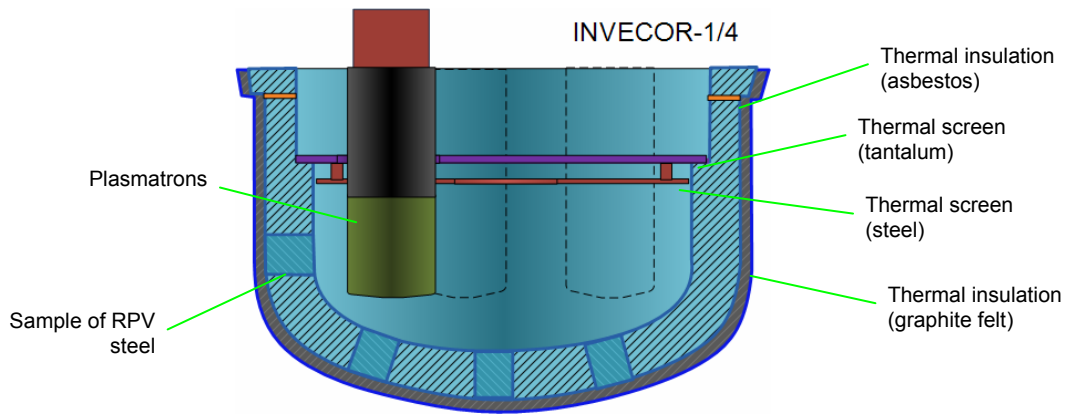


Figure 114 –Preparation of the reactor vessel model for testing

Figures 115, 116 depict the calculation and experimental diagrams of the corium components heating in the EMF.

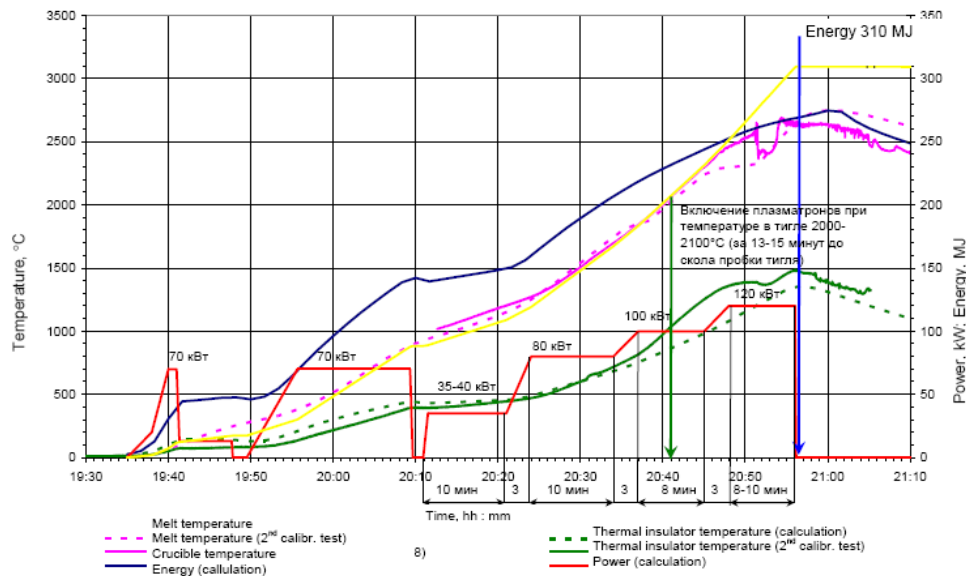


Figure 115 – Calculation diagram of the corium components heating in the EMF

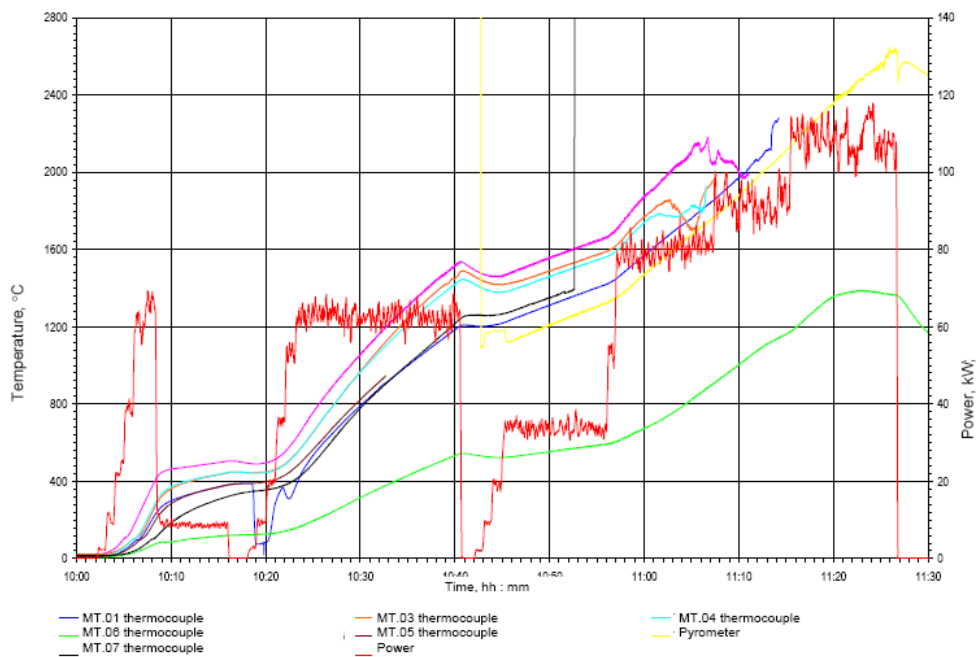


Figure 116 – Diagram of the corium components heating in the EMF

The hole in the crucible bottom for discharge of the corium melt was opened when the temperature 2630 °C inside the crucible was reached. The plasmatrons heater was actuated ~15 minutes before the melt discharge, that provided warming up of the reactor vessel model wall up to ~250°C (at the preheating stage of the cooling water flow rate on the external surface of the vessel model was switched off).

Figure 117 illustrates the temperature curves in the wall of the vessel model during the experiment. Total duration of the test (including the preheating stage) was over two hours. The average power of all plasmatrons during the experiment was about 75 kW. During the experiment the maximum heating temperature of the vessel model wall was observed in the central part of the model bottom and was equal to 1400°C.

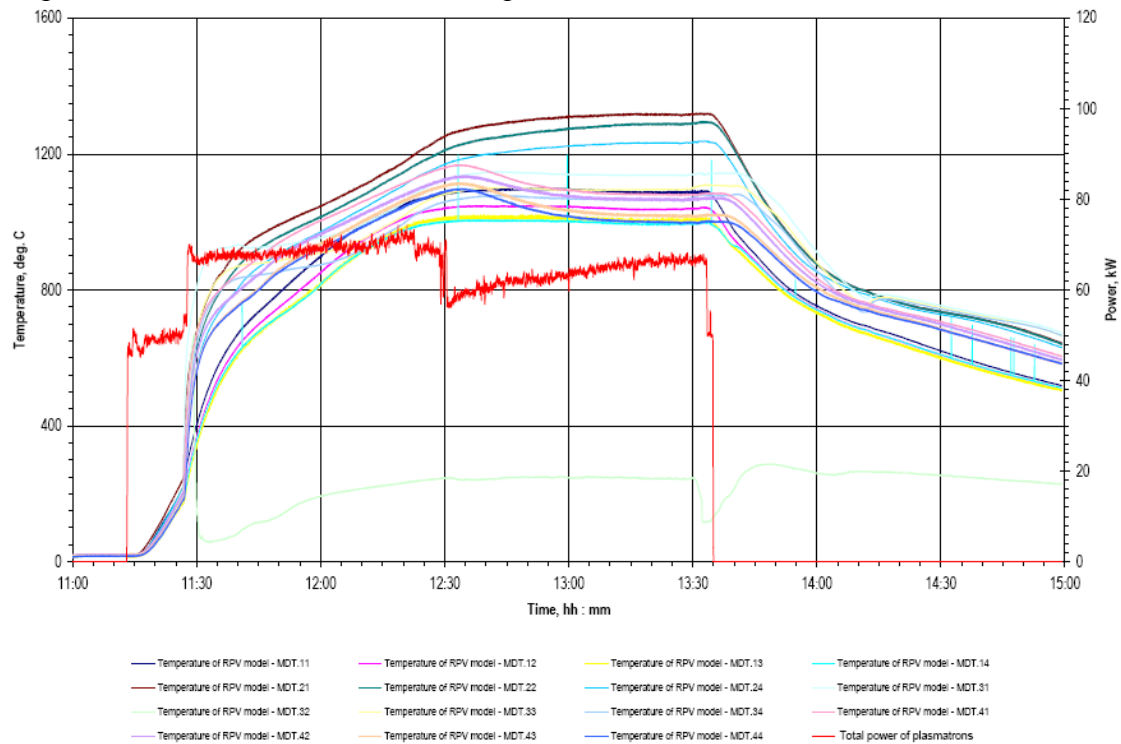
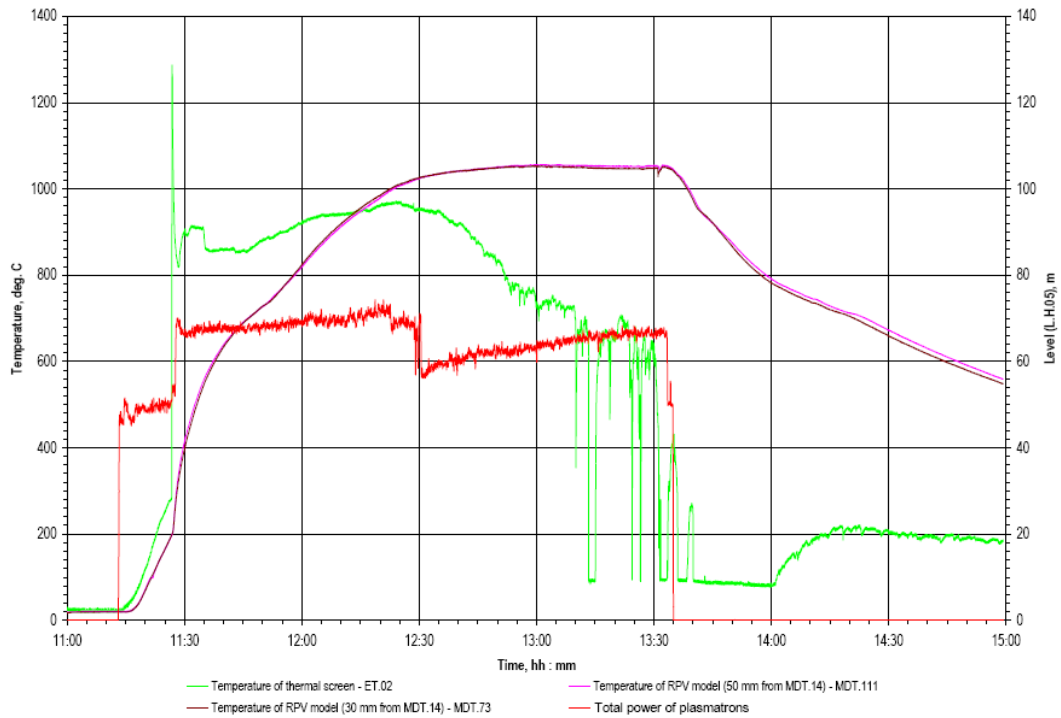


Figure 117 – Temperature of the reactor vessel model wall

The temperature of the upper tantalum screen was somewhat lower than in the previous tests (Figure 118), that confirms the effect of use of the intermediate steel screen.



INVECOR-1.4 (Thermal screen)

Figure 118 – Temperature of the upper heat screen during the experiment

The deformation gages demonstrate displacement of the vessel model wall by 0,1...0,3 mm, depending on the placement location (Figure 119).

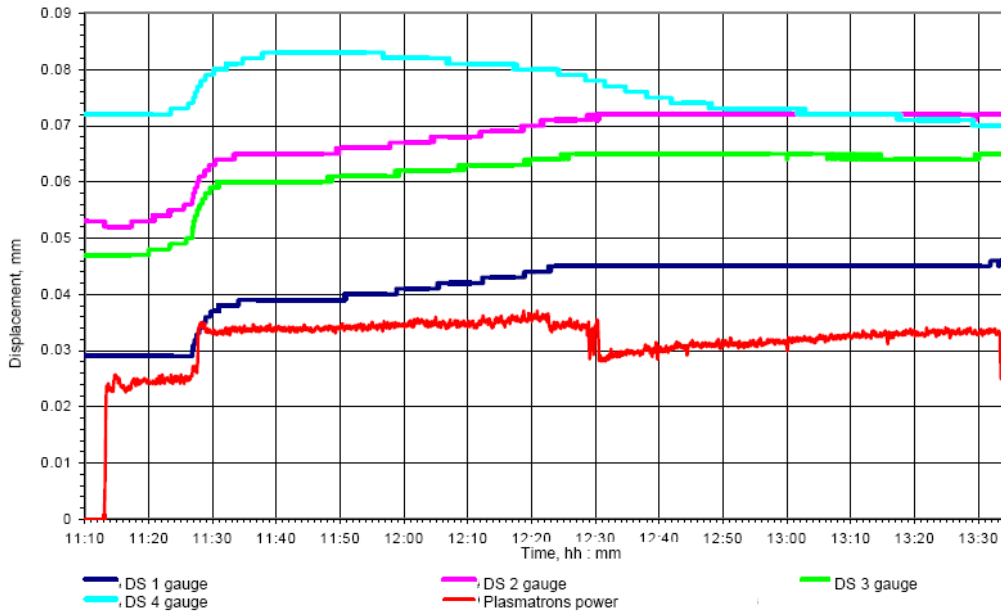


Figure 119 – Readings of the displacement/ deformation gages of the vessel model

After completion of the test and cooling of the main "Lava-B" units the EMF and MR were disassembled and primary examined. It was founded that there were no practically corium components in the melting crucible. In the experimental section there was discovered the solidified corium melt, thereby the upper layer, as it was in the previous tests, represented a fine filling. The layer thickness was about 2,5...3 cm (Fig. 120).



Figure 120 – View of the experimental section after the test

After removing the layer of corium particles and withdrawal of the plasmatoms, the graphite nozzles of the plasmatoms contacting with corium during the experiment were examined. It was discovered that there was no erosion of the graphite on the nozzles surface that demonstrates reliability of the protective coating.

The description of the post-test operations and the resultant data will be represented below in section 5.5 of the given report.

4.5 Post-test calculations

The estimated calculations of the temperature fields of the reactor vessel model filled with corium oxide with temperature 2460 °C in the performed integral tests were carried out. The decay heat was simulated by means of the plasmatoms heaters.

Main objectives of the calculation:

- estimation of the temperature field of the lower head of the reactor pressure vessel model and the corium loaded in the model;
- estimation of the heat flux through the wall of the lower head of the reactor pressure vessel model.

Table 10 – Initial data for the post-test calculations

	INVECOR-1.3	INVECOR -2	INVECOR -3	INVECOR -1.4
Mass of the discharged corium, kg	40	60	60	
Corium mass in the model before the melt discharge, kg	10	9,4	0	0
Power of one plasmatoms, kW	13		15	
Number of plasmatoms, piece	5	5	5	5
Temperature of the discharged corium, °C	2560	2570	2630	2630
Duration of heating, h	1	1	1	2
Porosity of the corium located in the model before the melt discharge	0,4	0,4	-	-
Flow rate of water cooling the vessel model, kg/s	0,21	0,03	0...0,03	0...0,03
Part of plasmatoms power released with the cooling water	0,2	0,2	0,3	0,3

In the calculations the values were used as follows:

Latent heat of zirconium melting, kJ/kg 210;
 Solution heat of uranium dioxide in the zirconium melt, kJ/kg 260;
 Calculated value of corium heat conductivity 8,3 W/(m·K).
 The diagram of the vessel model with main dimensions is represented in Figure 121.

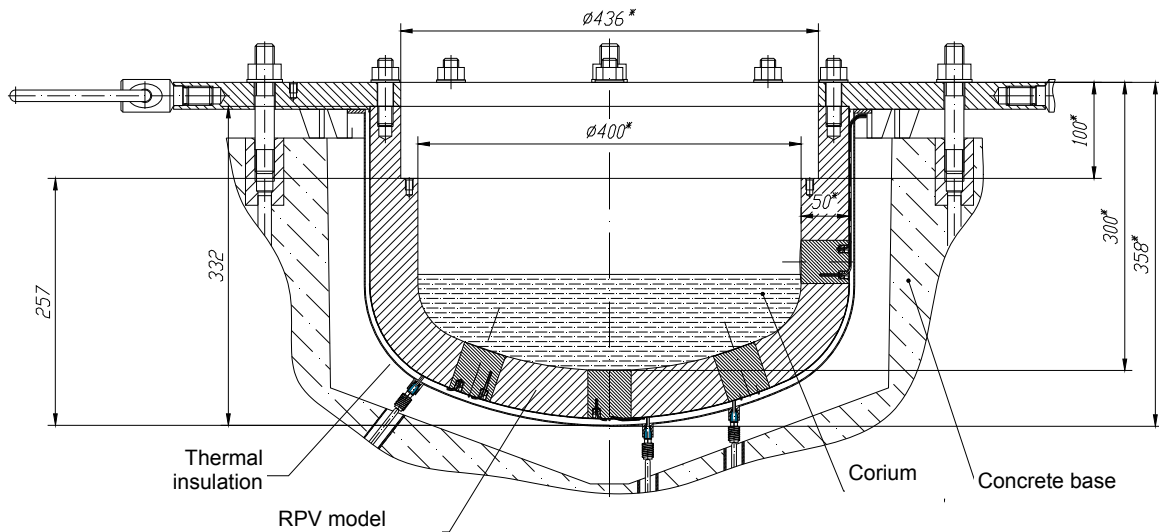


Figure 121 – Diagram of the lower head of the reactor pressure vessel model with main dimensions
 The diagram of the vessel model with plasmatrons is represented in Figure 122.

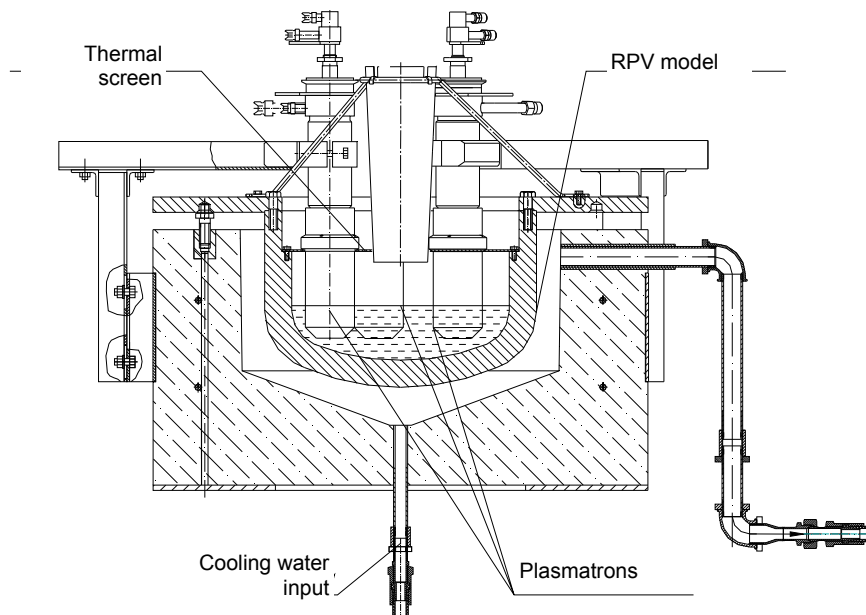


Figure 122 – Diagram of the vessel model with plasmatrons

The diagram of the plasmatrons graphite nozzles with main dimensions is given in Figure 123. In calculation of the experimental device temperature field a part of a plasmatrone of 220 mm length from the lower end of the graphite nozzle of the external electrode is used. It was accepted in the calculation that a part of the graphite nozzle surface is cooled with the water-cooled external electrode (see blue lines in Figure 123). Red lines – the surface through which the energy released in the plasmatrons transfers to the graphite nozzle and then to the melt enclosing the plasmatrons.

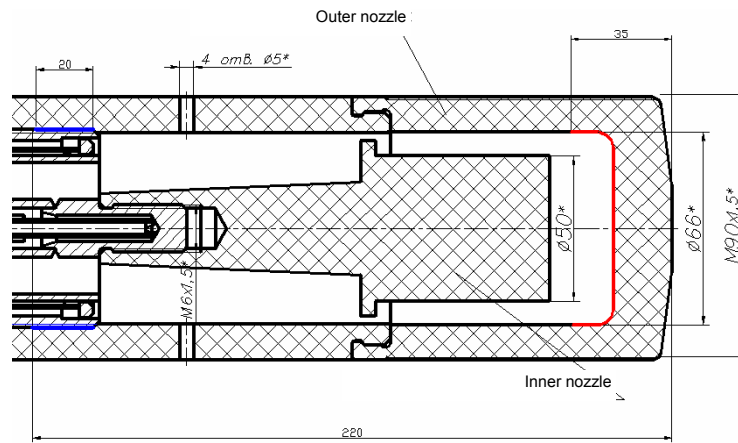


Figure 123 – Diagram of the lower part of the plasmatrons

Figure 124 depicts the layout of the thermocouples in the model wall.

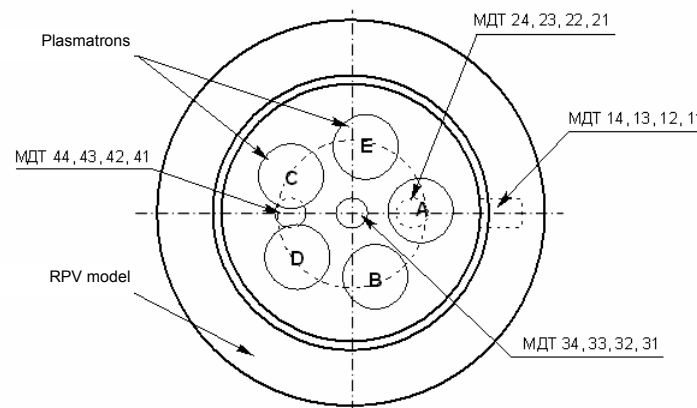


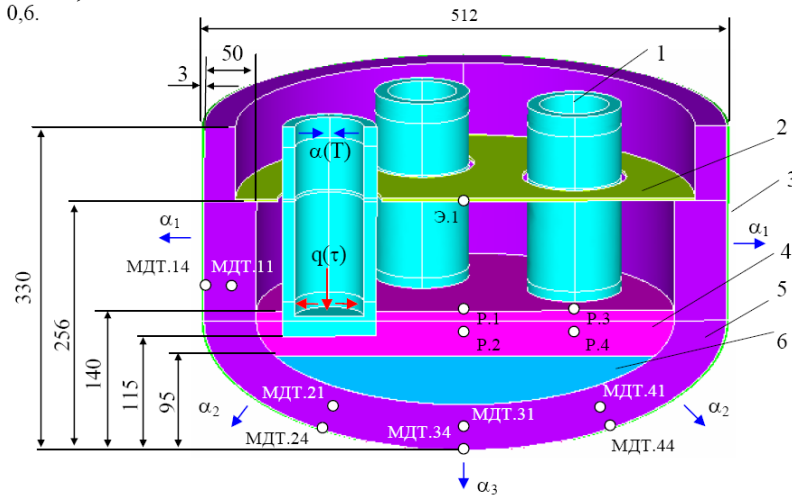
Figure 124 – Layout of the thermocouples in the model wall

Table 11 includes the thermocouples coordinates in the lower head of the reactor pressure vessel model.

Table 11 – Designation of thermocouples in the reactor vessel model

Check point	Depth from the external surface of the model, mm
Thermocouples of group 1, in the sample of the vessel steel on the lateral surface of the vessel model	
MDT.11	30
MDT.12	20
MDT.13	12
MDT.14	on the external surface of the vessel model
Thermocouples of group 2, in the sample of the vessel steel on the bottom part of the vessel model (under the plasmatrons)	
MDT.21	30
MDT.22	20
MDT.23	12
MDT.24	on the external surface of the vessel model
Thermocouples of group 3, in the sample of the vessel steel on the bottom part of the vessel mode (model center)	
MDT.31	30
MDT.32	20
MDT.33	12
MDT.34	on the external surface of the vessel model
Thermocouples of group 4, in the sample of the vessel steel on the bottom part of the vessel model (between the plasmatrons)	
MDT.41	30
MDT.42	20
MDT.43	12
MDT.44	on the external surface of the vessel model

The assigned task of the unsteady heat exchange was solved using the ANSYS code. In connection with the design model symmetry, for easy calculation there was used $1/2$ part of the vessel model with the plasmatrons. The calculated model with main dimensions is represented in Figure 125. Blue arrows are the surfaces involved in the convective heat exchange. Red arrows are the surfaces through which the energy transfers to the nozzle of the external electrode of the plasmatrons. Radiative heat exchange is taken place between the melt surface, nozzles, heat shield and internal wall of the vessel model. Emissivity of the above surfaces is accepted as equal to 0,6.



1 – graphite nozzle of the external electrode; 2 – thermal screen; 3 – thermal insulation; 4 – melt; 5 – vessel model; 6 – preloaded corium (for tests INVECOR-1.3 and INVECOR-2)

Figure 125 – Design model of the experimental section

Calculation results

The calculation error after the plasmatrons disconnection in the considered check points varies from 1 to 21 %.

Figures 126 and 127 represent the temperature fields of the vessel model wall and the whole model accordingly after the plasmatrons disconnection for the INVECOR-1.3 experiment. Maximum heating of the model wall as it is seen from the temperature field (Figure 123) is observed under the plasmatrons.

The plasmatrons make a major contribution to the melt heating. In existing active plasmatrons the calculated value of the lateral sample temperature in point MDT.11 is 770 °C in an hour after the melt drain. If the plasmatrons power equals to zero, the calculated value of the temperature in the same check point would not exceed 160 °C.

In compliance with the performed calculation, in an hour after the melt drain, the corium temperature in the model center would not exceed ~ 1480 °C, the corium temperature between the plasmatrons would be ~ 1860 °C, maximum temperature of the thermal screen would not exceed ~ 1200 °C.

Maximum density of the heat flux determined according to the temperature readings in the check points MDT.21, MDT.24 was ~ 110 kW/m², approximately in 35 minutes after the melt drain. At the end of the test the maximum density of the heat flux through the plugs did not exceed ~ 100 kW/m².

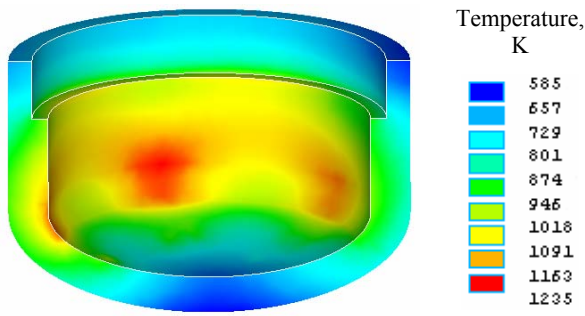


Figure 126 – Temperature field of the vessel model wall in an hour after the melt drain

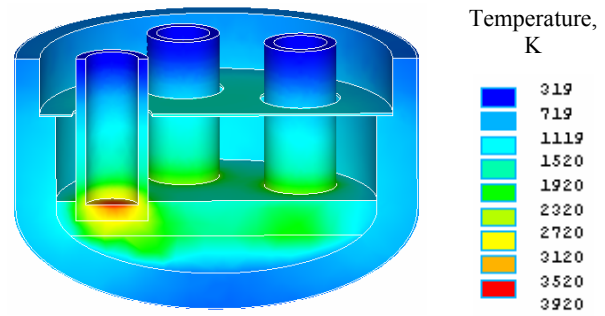


Figure 127 – Temperature field of the vessel model, corium, nozzles and heat shield in an hour after the melt drain

Figures 128 and 129 represent the temperature fields of the vessel model wall and the whole experimental section respectively after the plasmatrons disconnection for INVECOR-2 test. Maximum heating of the model wall as it is seen from the temperature field (Figure 125) is observed under the plasmatrons. Maximum temperature of the vessel model after the plasmatrons disconnection is 1046 °C (1319 K).

From the temperature field given in Figure 126 it is seen that the maximum temperature of the plasmatrons external nozzle equals to 3377 °C (3650 K).

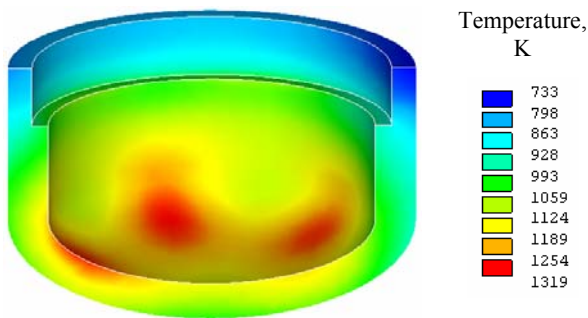


Figure 128 – Temperature field of the vessel model wall after the plasmatrons disconnection

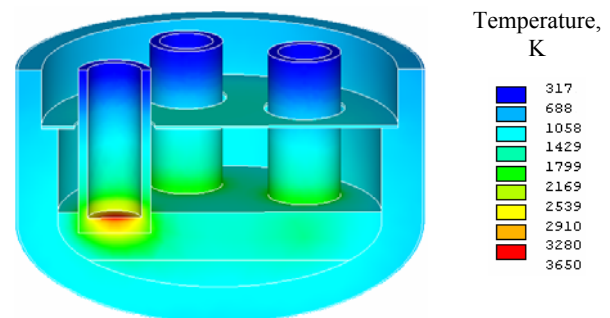


Figure 129 – Temperature field of the vessel model, corium, nozzles and heat shield after the plasmatrons disconnection

Figures 130 and 131 represent the temperature fields of the vessel model wall and the whole experimental section respectively after the plasmatrons disconnection for INVECOR-3 test. Maximum heating of the model wall as it is seen from Figure 127 is observed under the plasmatrons. Maximum calculated temperature of the model wall after the plasmatrons disconnection is 1434 °C (1707 K).

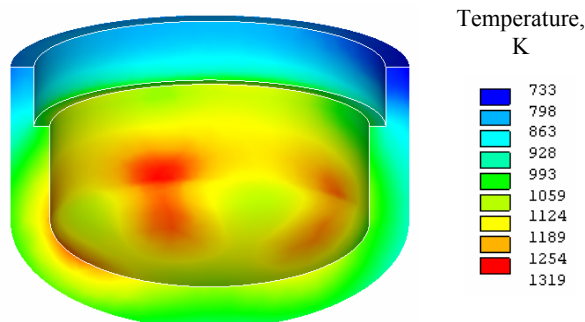


Figure 130 – Temperature field of the vessel model wall after the plasmatrons disconnection

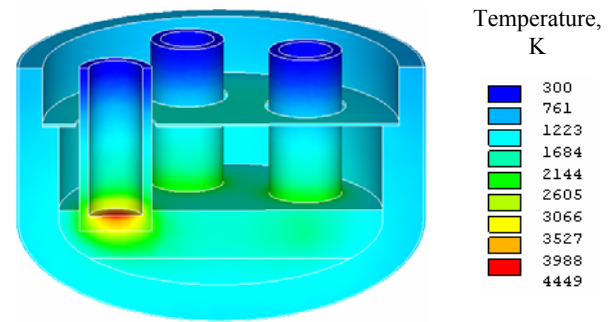


Figure 131 – Temperature field of the vessel model, corium, nozzles and heat shield after the plasmatrons disconnection

Figures 132 and 133 represent the temperature fields of the vessel model wall and the whole experimental section respectively after the plasmatrons disconnection. Maximum heating of the model wall as it is seen from Figure 129 is observed under the plasmatrons. Maximum calculated temperature of the lower head of the reactor pressure vessel model after disconnection of the plasmatrons is 1397 °C (1670 K).

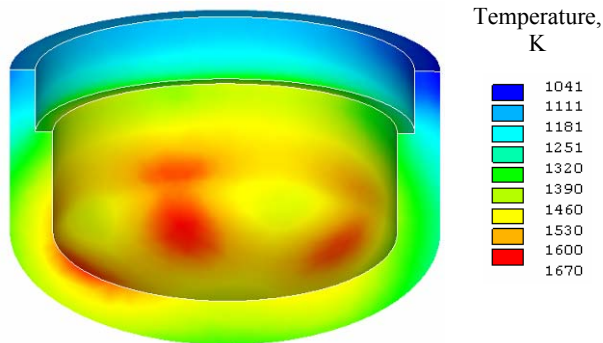


Figure 132 – Temperature field of the vessel model wall after the plasmatrons disconnection

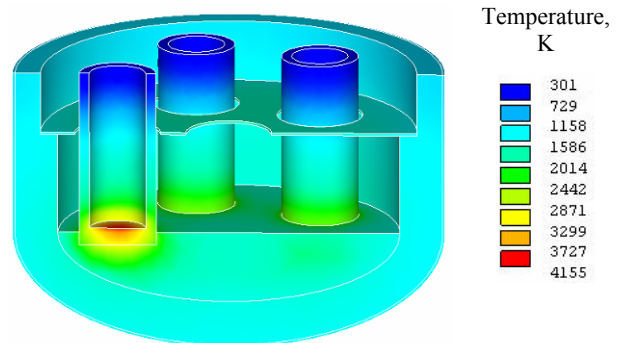


Figure 133 – Temperature field of the vessel model, corium, nozzles and heat shield after the plasmatrons disconnection

In the result of the calculations the calculated data were compared with the results of the integral tests INVECOR. Deviation of the calculated values from the temperature obtained after the processing of the experimental data varies in the considered check points from 5 to 21 %.

5 Results

The considerable amount of works has been executed in frameworks the post-test researches of details of experimental facilities and corium both after supporting and calibration experiments devoted to debugging of experimental techniques, and corium and a material of RPV model after large-scale integral experiments in "Lava-B" facility.

5.1 Investigations after the calibration tests

The results of the post-test study after the supporting experiments dedicated to the improvement of the experiment technique and reliability of the "Lava-B" main units are described in details in the reports for 1...3 year of the Project implementation. The results of the study were the foundation for the preparation of the large-scale tests in the "Lava-B" test facility with the use of 60 kg prototype corium, performed during the 4th year of the Project implementation. The most significant data were resulted from the investigation of the corium samples produced after conduction of the 1st calibration test, i.e. that corium was used for additional loading of the experimental section on preparation of the integral tests INVECOR-1.3 and INVECOR-2.

The corium samples to be investigated were taken from the ingot left in the melting crucible after completion of the test (Figure 134).

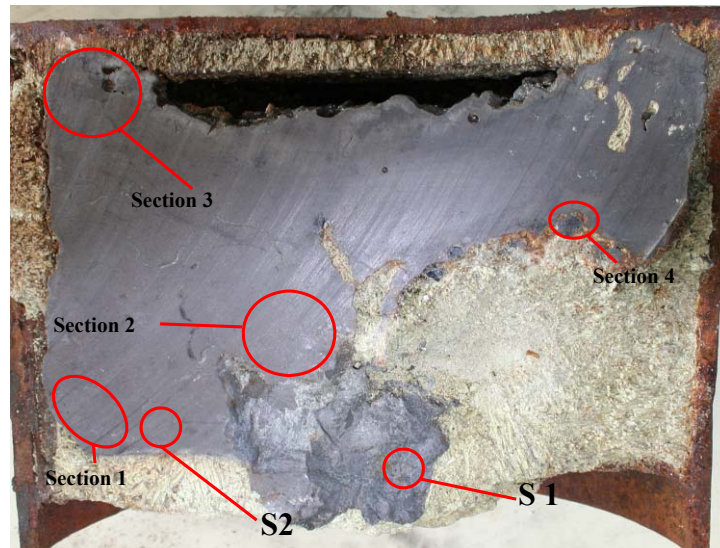


Figure 134 – Cut of the melt ingot with sampling points for investigation

The phase analysis was performed through the X-ray diffractometry method of polycrystals on powered samples prepared from the samples material taken for investigation. The results of the phase analysis are included in Table 12. The table includes the measured values of lattice spacing for the oxide and oxycarbide phases and their approximate component composition. The phase sequence in the table cells corresponds to the reduction of their volume content in the samples. The elements gradation in the formulation of the variable composition phases is also corresponds to the reduction of their relative atomic percentage.

Table 12 – The results of the qualitative analysis of the sample phase composition

Sample	Sample type and sampling point	Main phase	Other phases
A10.1	Fuel pellets from the ingot cavity	UO ₂ (0,5470(5) nm)	U _{0.8} Zr _{0.2} O ₂ (0,542 nm);
A10.2	Fragment of the melt ingot in the upper part (foam)	U _{0.95} Zr _{0.05} O ₂ (0,546(8) nm); (U,Zr)(C,O) _{1-x} (0,489 nm)	(U,Zr)(C,O) _{1-x} (0,470÷0.485 nm)
S1	Fragment of the melt ingot in the area of drain hole	U _{0.9} Zr _{0.1} O ₂ (0,544(7) nm)	Zr(C,O)(0,467(5) nm); α-(U,Zr)
S2	Fragment of the melt in the ingot bottom	U _{0.95} Zr _{0.05} O ₂ (0,545(6) nm)	Zr(C,O)(0,469(8) nm); α-(U,Zr)
S3.1	Fragment of the melt around the pellets	U _{0.9} Zr _{0.1} O ₂ (0,545(1) nm)	α-(U,Zr)
S3.2 (A10.1)	Fuel pellets at the stage of dissolution	UO ₂ (0,5470(5) nm)	U _{0.8} Zr _{0.2} O ₂ (0,542 nm);
S4	Fragment of the melt in the upper part of the ingot on the crucible axis	U _{0.95} Zr _{0.05} O ₂ (0,546(1) nm)	(Zr,U) (C,O) (0,472÷0.495 nm)
S5	Fragment of the melt in the upper part of the ingot at crucible walls	U _{0.95} Zr _{0.05} O ₂ (0,546 nm); (Zr,U) (C,O) _{1-x} (0,470(4) nm);	(U,Zr)(C,O) _{1-x} (0,472÷0.495 nm)
S6	Fragment of the melt in the ingot center	U _{0.95} Zr _{0.05} O ₂ (0,545(5) nm); Zr (C,O) _{1-x} (0,467(5) nm)	α-(U,Zr); Zr(C,O) _{1-x} (0,464 nm)

From the results of the X-ray phase analysis the main components of the solidified melt samples are oxide phases of variable composition (U, Zr)O₂ with fcc lattice – uranium dioxide lattice and carbide phases of variable composition with fcc lattice of zirconium carbide lattice, the general formula of which may represent as (U,Zr)(C,O)_{1-x}.

Oxide solid solutions (U, Zr)O₂ are characteristic for all samples. The phase composition was estimated from the lattice spacing value. The common trait of the phase composition of the samples is lack of solid solutions with high content of zirconium as well as lack of metal zirconium.

The element analysis demonstrates rather homogeneous distribution of uranium and zirconium in splitting of the solidified melt fragments.

Figure 135 depicts the microstructure of the corium ingot sample (designated as №1 in Figure 134).

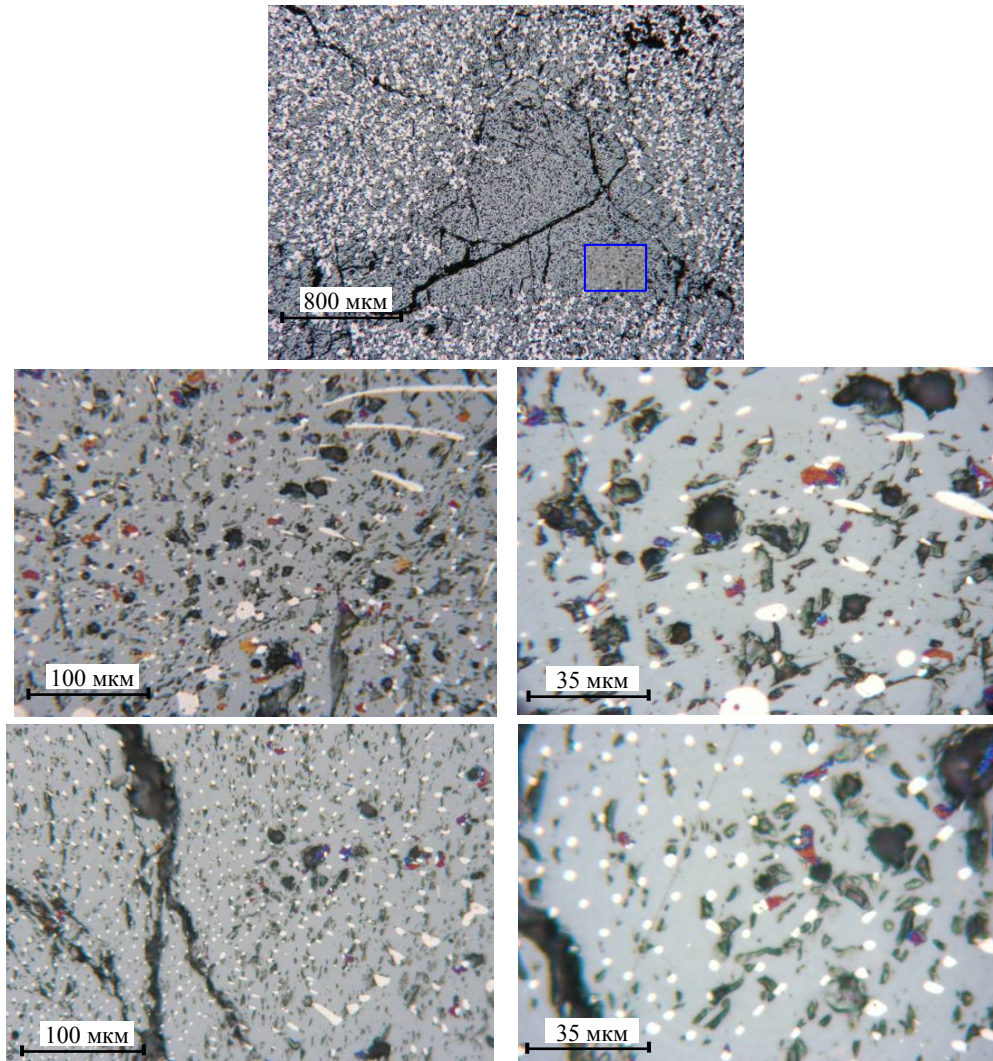


Figure 135 – Microstructure of areas of the microsection №1 material

The fragment material is mainly homogeneous. Dark constituent corresponds to solid solution $(U,Zr)O_2$, light – oxycarbide phase $Zr(C,O)_{1-x}$. Occasional color inclusions is the phase on the basis of metal α - uranium covered with oxide film.

The observed microstructure corresponds completely to the main phase composition of the ingot material determined from the results of the X-ray phase analysis (samples S1, S2, S3.2, S4÷S6).

After the second calibration test the phase composition of the solidified melt samples was not investigated, since the most melt, on splashing from the crucible, was in long contact with the crucible insulation (graphite felt), and that may result in formation of large quantity of carbide phases. After the second calibration test the melt was used no more.

5.2 Investigation after the integral test INVECOR-1.3

After the test INVECOR-1.3 completion, the vessel model was taken from the MR. The appearance of the vessel model with the melt after removing the upper heat shield is represented in Figure 136. Sampling of material from the vessel model was performed in two steps. At the first stage there was sampled fragmented corium located over the melt ingot as a layer of about 20 mm thickness of 5 zones on the sectors of plasmatrons location (Figure 136). The sixth zone was located in the model center (Figure 137).

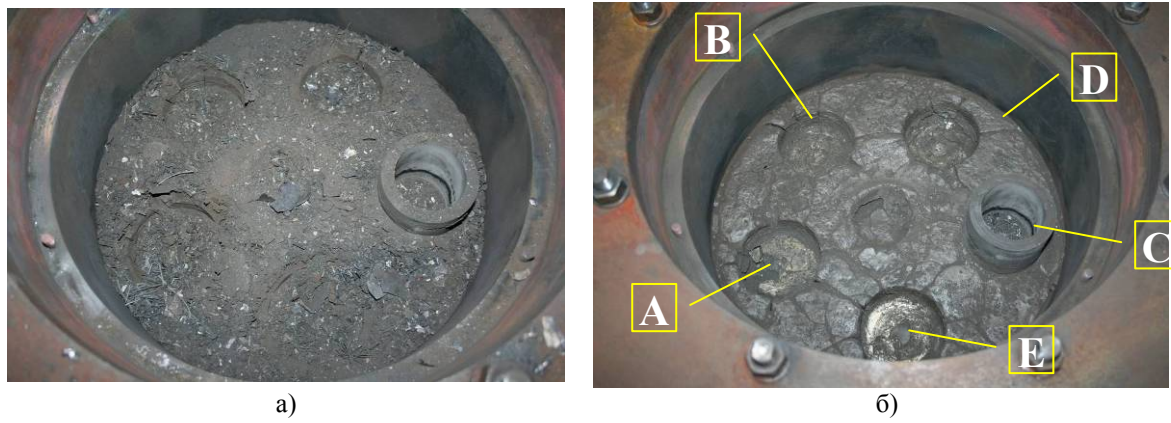


Figure 136 – View of the material in the vessel model: a) – initial state; б) – after fragments layer removal

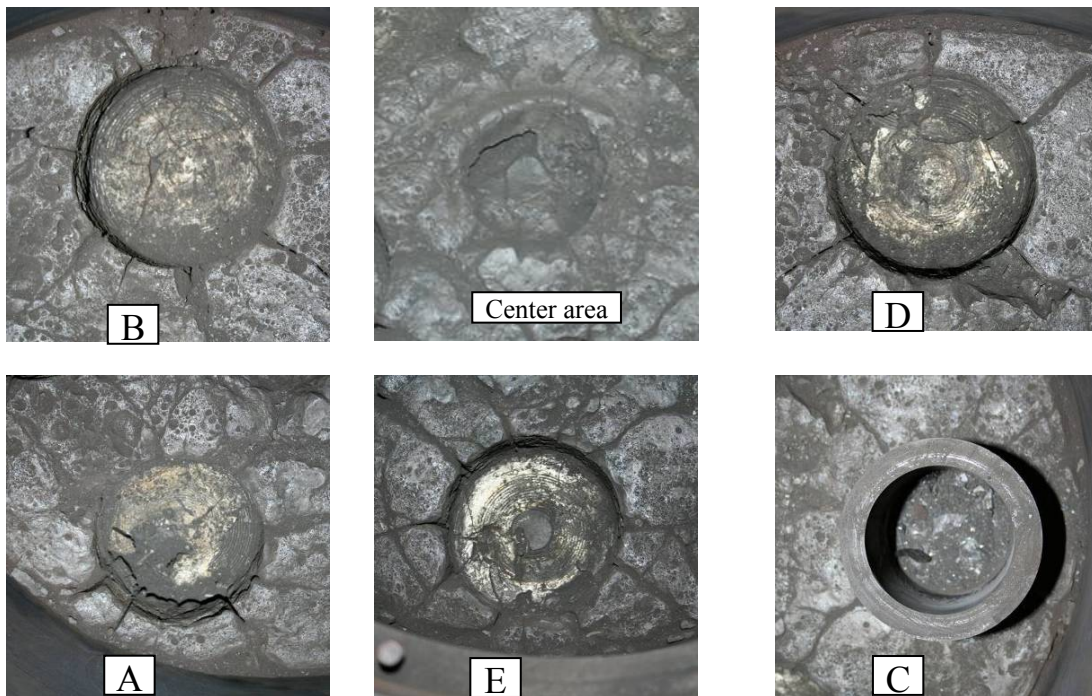


Figure 137 – The melt ingot zones in the vicinity the plasmatrons nozzles after fragmented layer removal

For the investigation there were sampled the material in the plasmatrons A region and in the model center. Each sampled material was fractionated according to the characteristic size of particles. From every fine fraction there were selected representative weighted portions for preparation of samples. Designation of samples and fraction mass are represented in Table 13.

Table 13 – Description of sampling and the samples of the fragmented corium

Designation	Description of sampling	Sampling mass, g	Sample mass, g
RPA-F0	Fraction of particles with size less than 200 microns	101,06	
RPA -F1	Fraction of particles with size from 200 microns to 800 microns	72,4	2,56
RPA -F2	Fraction of particles with size from 800 microns to 2,8 mm	121,57	7,36
RPA -F3	Fraction of particles with size from over 2,8 mm	55,81	-
RP0-F0	Fraction of particles with size less than 200 microns	157,73	
RP0-F1	Fraction of particles with size from 200 microns to 800 microns	107,81	4,21
RP0-F2	Fraction of particles with size from 800 microns to 2,8 mm	118,59	3,55
RP0-F3	Fraction of particles with size from over 2,8 mm	75,62	

The ingot material was fragmented, mainly along the cracks existing in the ingot. The ingot sector in the plasmatrone region and the ingot fragment from the central part were chosen for the study (Table 14).

Generally, the ingot is the solidified homogeneous melt on the support from corium fragments loaded in the vessel model before the experiment. A part of the melt penetrated between the corium debris of the loading and seen in the form of drops or stains with yellowy surface on the ingot breaks and from its bottom. Along with the yellowy stains the collection of melt with silver surface is also available under the ingot. The ingot has also coarse porosity, cavities and other inhomogeneity.

Table 14 – Description of ingot material sampling and samples

Designation	Description of sampling	Designation	Description of samples
SA1	Corium fragments of initial loading to the vessel model	OSA1	One of fragments
SA2	Solidified drop-stains of the melt that are, silver on breaks, are in the lowest part under the ingot and debris.	OSA2	Fragments of small ingot under the plasmatrone "A" nozzle end
SA3	Drop-stains of the melt between the debris of the initial loading with yellowy surface	OSA3	Several breaks of stains
SA4	Break of crucible fragment under the plasmatrone "A" end face with fritted edges	OSA4	The fragment included the contact surface with the plasmatrone edge, limited with the fritted surface from the opposite side
SA5	Break of the ingot fragment under the plasmatrone "E" end with unfritted edges and with sharp pattern of the thread	OSA5	The fragment included the surface of contact with plasmatrone end, from the opposite side is bounded with the contact with initial loading fragments
SA6	The ingot fragment area in the inter-electrode region (A-D) has a pore separated the top and bottom of the ingot	OSA6.1	The ingot material over the pore
		OSA6.2	The ingot material under the pore
SA7	Fragment of the ingot center (SO)	OSA7.1	Material on the ingot top, porous
		OSA7.2	Material of the ingot bottom is bounded with porous material and with boundary of the contact with initial loading
SA8	Area of the ingot fragment in the inter-electrode region (A-D), contains the pore bounding the ingot top and bottom	OSA8.1	The ingot material over the pore
		OSA8.2	The ingot material under the pore (middle)
		OSA8.3	The ingot material under the pore (bottom), is bounded with the boundary of contact with filling
SA9	Area of the ingot fragment in the inter-electrode region (A-E),	OSA9.1	Ingot top
		OSA9.2	Ingot bottom
SA10	Break of the ingot in the region of contact with the wall	OSA9.3	Break of the ingot in the region of contact with the wall

The diagram of the vessel model sampling is given in Figure 138.

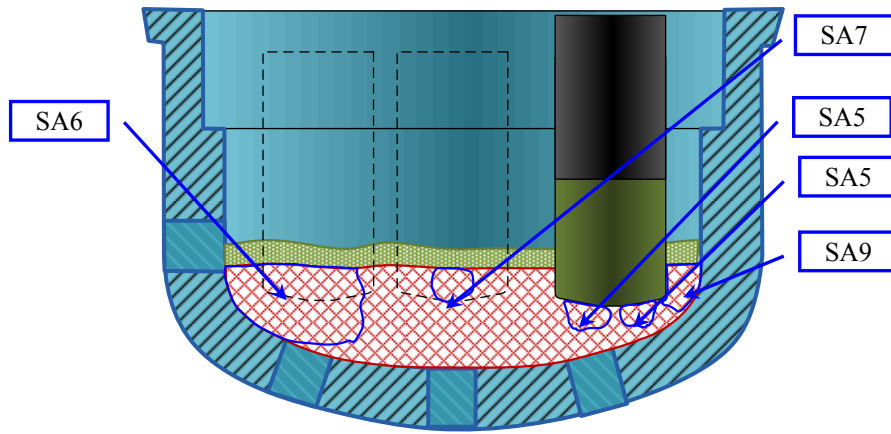


Figure 138 – Diagram of the material sampling for investigation

The appearance of the fragments taken for analysis and the sampling points are represented in Figure 139.

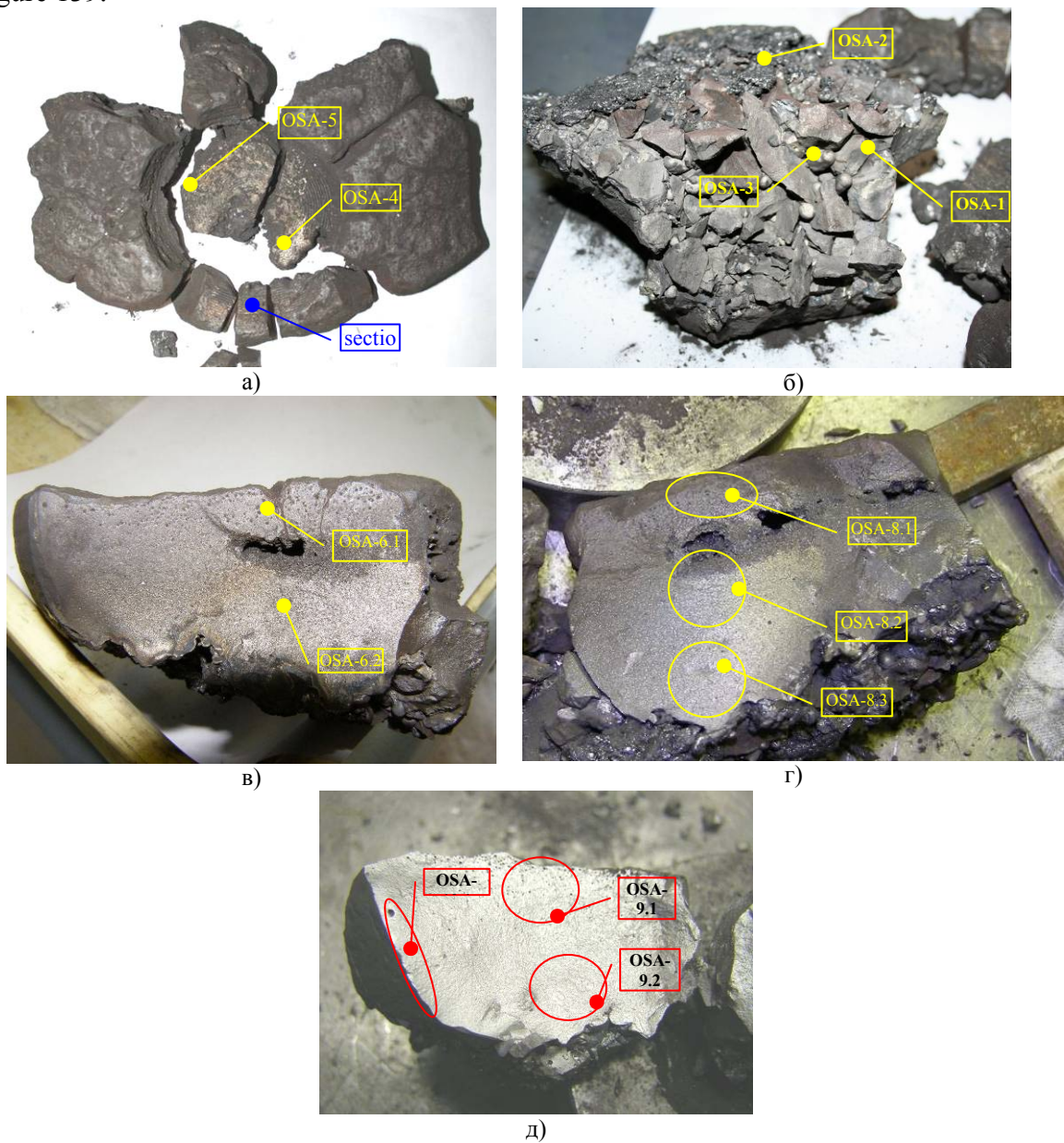


Figure 139 – Fragment of the ingot material

The results of the corium samples composition analysis.

The phase analysis data are included in Tables 4, 5. The tables represent the measured values of the lattice spacing a_0 and their approximate content for the oxide and oxycarbide phases. The phase sequence in the table cells corresponds to the reduction of their volume content in the samples. The tables include also the data from determination of the relative mass content of uranium and zirconium in the samples material.

According to the results of the X-ray phase analysis the main components of phase content of the melt ingot sample (sample series OSA) are oxide phases of variable content $(U,Zr)O_2$ with fcc lattice – uranium dioxide lattice, metallic zirconium phase, stabilized with oxygen $\alpha-Zr(O)$, and the phase $\alpha-(U,Zr)$ on the basis of α -uranium crystal lattice. The common feature of the samples is also low content of zirconium in the main solid solution $(U,Zr)O_2$ with estimated content $U_{\sim 0.9}Zr_{\sim 0.1}O_2$. The estimation of the phase content was conducted in terms of the lattice spacing value. From the totality of the ingot material samples, the samples taken from the central region (sample OSA7.1) are distinguished by the existence of iron-bearing phase that is the most reliably identified as Zr_2FeO_x or $\epsilon-Zr_6Fe_3O_{0.6}$ with the cubic lattice of the space groups Fm3m or Fd3m. The element analysis confirms the presence of iron in the sample.

According to the results of the X-ray phase analysis the main components of the fragmented corium samples (sample series RPA, RP0) are also oxide phases of variable content $(U,Zr)O_2$ with fcc lattice – uranium dioxide lattice. The metal zirconium phase stabilized with oxygen $\alpha-Zr(O)$ is rather less in this material than in the ingot material, and the phase $\alpha-(U,Zr)$ based upon the crystal lattice α -uranium is practically absent. The common feature of the samples is also low content of zirconium in the main solid solution $(U,Zr)O_2$ with estimated content from $U_{0.97}Zr_{\sim 0.03}O_2$ to $U_{0.93}Zr_{\sim 0.07}O_2$. The primary common feature of the fragmented corium samples content against the ingot is the existence of oxide phases with high zirconium content. This zirconium oxide with the monoclinic crystal lattice, the lines of which are somewhat diffused on the diffraction patterns, but are easily identified, and also the phases, the existence of which are identified on the diffraction patterns only by the increase of the background and by the lengthening of the reflections slope of the main solid solution to the side of wide angles, that corresponds to increasing of zirconium content in the solid solution $(U,Zr)O_2$ with any crystal lattice. The similar diffraction pattern may occur in the case of prompt crystallization of the phases (hardening), when the non-equilibrium stages with heavy distorted crystal lattices are generated.

The data from the determination of the relative mass content of uranium and zirconium in the samples are included in Tables 15, 16. The element analysis demonstrates the homogeneous distribution of uranium and zirconium in the corium fragment samples. The element composition of the fragmented corium is practically identical to the ingot material composition.

Table 15 - Results of the qualitative phase and quantitative element analysis of the corium ingot samples

Sample	Phase composition	Element composition, weight, %		U/Zr
		Zr	U	
OSA1	$U_{0,95}Zr_{0,05}O_2$ (0,546 nm); (Zr,U)(C,O) _{1-x} (0,470 nm); α -(U,Zr)	32,6	67,4	2,06
OSA2	UC_2 ; (Zr,U) (C,O) _{1-x} (0,474 nm); (U,Zr)(C,O) _{1-x} (0,474÷0.495 nm)	17,0	83,0	4,90
OSA3	$U_{0,9}Zr_{0,1}O_2$ (0,545 nm); α -Zr(O); α -(U,Zr)	30,5	69,5	2,28
OSA4	$U_{0,9}Zr_{0,1}O_2$ (0,544(5) nm); α -Zr(O); α -(U,Zr)	32,8	67,2	2,05
OSA5	$U_{0,9}Zr_{0,1}O_2$ (0,544(5) nm); α -Zr(O); α -(U,Zr)	31,9	68,1	2,13
OSA6.1	$U_{0,9}Zr_{0,1}O_2$ (0,545 nm); α -Zr(O); α -(U,Zr)	30,6	69,4	2,27
OSA6.2	$U_{0,9}Zr_{0,1}O_2$ (0,545 nm); α -Zr(O); α -(U,Zr)	29,7	70,3	2,37
OSA7.1	$U_{0,9}Zr_{0,1}O_2$ (0,545 nm); α -Zr(O); α -(U,Zr); Zr_2FeO_x	28,3	71,7	2,53
OSA7.2	$U_{0,9}Zr_{0,1}O_2$ (0,545 nm); α -Zr(O); α -(U,Zr); Zr_2FeO_x	32,6	67,4	2,07
OSA7.3	$U_{0,9}Zr_{0,1}O_2$ (0,545 nm); α -Zr(O); α -(U,Zr); Zr_2FeO_x	31,2	68,8	2,21
OSA8.1	$U_{0,95}Zr_{0,05}O_2$ (0,546 nm); α -Zr(O); α -(U,Zr)	31,6	68,4	2,16
OSA8.2	$U_{0,9}Zr_{0,1}O_2$ (0,545 nm); α -Zr(O); α -(U,Zr)	30,3	69,7	2,30
OSA8.3	$U_{0,9}Zr_{0,1}O_2$ (0,545 nm); α -Zr(O); α -(U,Zr)	31,7	68,3	2,16
OSA9.1	$U_{0,9}Zr_{0,1}O_2$ (0,545 nm); α -Zr(O); α -(U,Zr)	32,4	67,6	2,08
OSA9.2	$U_{0,9}Zr_{0,1}O_2$ (0,545 nm); α -Zr(O); α -(U,Zr)	31,2	68,8	2,21
OSA10.1	$U_{0,9}Zr_{0,1}O_2$ (0,545 nm); α -Zr(O); α -(U,Zr)	31,2	68,8	2,20

Table 16 – Results of the qualitative phase and quantitative element analysis of the fragmented corium samples

Sample	Phase composition	Element composition, weight, %		U/Zr
		Zr	U	
RPA-F0	$U_{0,95}Zr_{0,05}O_2$ (0,545 nm); (Zr,U)O ₂ ; α -Zr(O); ZrO_2^{MKL} ;	31,2	68,8	2,21
RPA-F1	$U_{0,95}Zr_{0,05}O_2$ (0,545 nm); α -Zr(O); (Zr,U)O ₂ ZrO_2^{MKL} ;	35,1	64,9%	1,85
RPA-F2	$U_{0,95}Zr_{0,05}O_2$ (0,545 nm); α -Zr(O); (Zr,U)O ₂ ZrO_2^{MKL} ;	34,0	66,0%	1,94
RP0-F0	$U_{0,95}Zr_{0,05}O_2$ (0,545 nm); (Zr,U)O ₂ ; α -Zr(O); ZrO_2^{MKL} ;	31,7	68,3%	2,15
RP0-F1	$U_{0,95}Zr_{0,05}O_2$ (0,545 nm); α -Zr(O); (Zr,U)O ₂ ; ZrO_2^{MKL} ;	31,1	68,9%	2,21
RP0-F2	$U_{0,95}Zr_{0,05}O_2$ (0,545 nm); α -Zr(O); ZrO_2^{MKL} ; (Zr,U)O ₂ ; α -(U,Zr)	31,6	68,4	2,17

For the metallographic investigation, the metallographic sample of the ingot vertical section containing the boundary of the vessel model wall/plasmatrone surface contact was produced (Figure 140). The pictures of the metallographic sample surface microstructure in 12 regions are depicted in Figure 141.

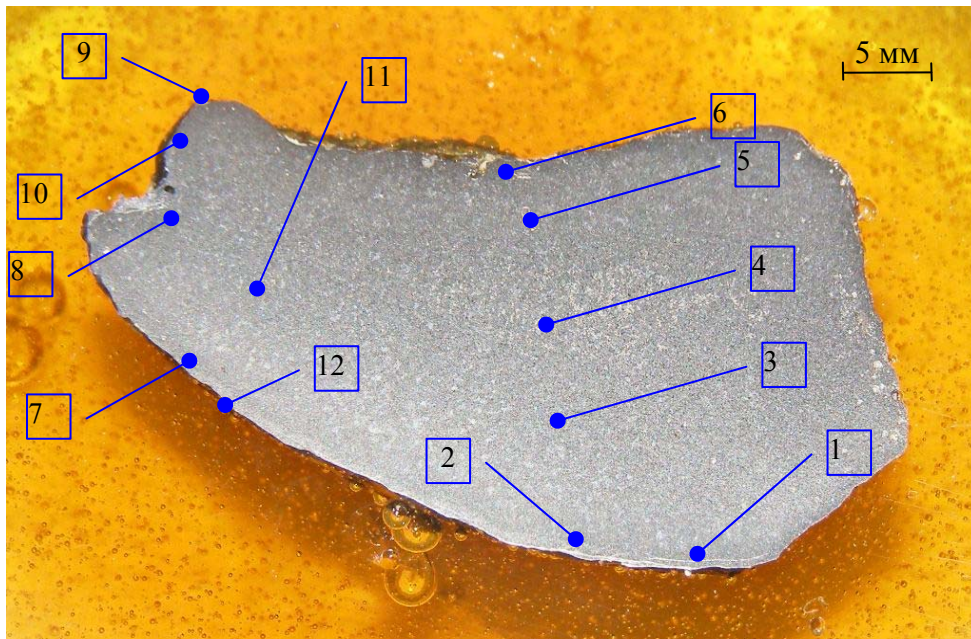


Figure 140 – Vertical section of the ingot fragment

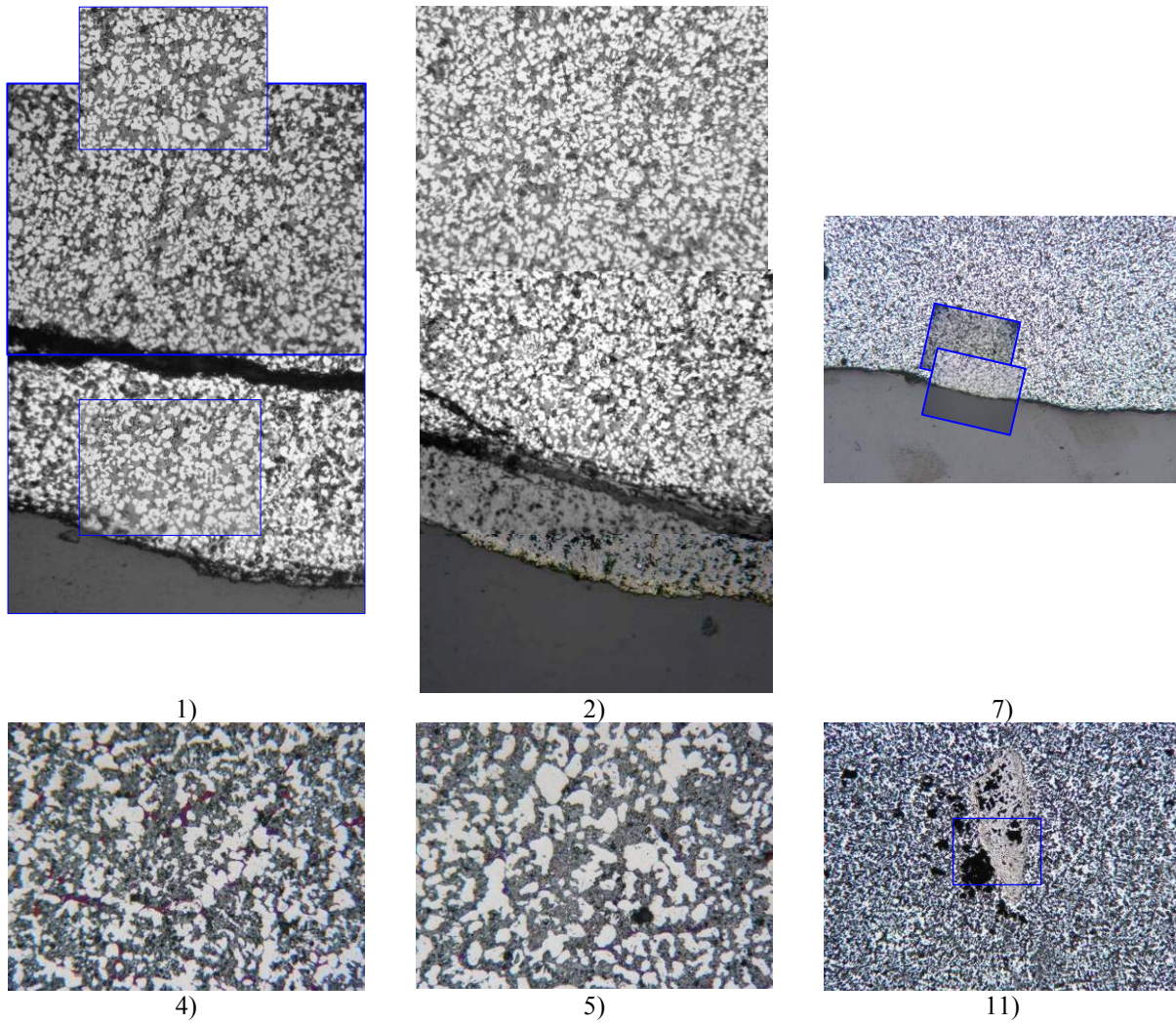


Figure 141 – Microstructure of the ingot in different regions

The data from the phase and element analysis of corium samples in the vessel model enable to conclude as follows:

1. The phase composition of all ingot material samples is practically identical, that is confirmed by the data from the element analysis and says about homogeneity of the melt both at the moment of solidification and at the melt drain moment. That confirms the identity of the phase and element composition of the melt crust sample on the drain cup (sample OA4), the melt ingot samples and fragmented corium in the vessel model.
2. Lack of the carbide phase characteristics in the ingot material demonstrates practically zero-content of carbon in the melt.

The microstructure patterns expose the homogeneous distribution of the melt phase components against the ingot section. Three main phase components are distinguished in the ingot material microstructure:

- dark pleated matrix material of grey color filling the space between the extractions of the light phase;
- solid precipitation of the light supposedly metallic phase with round shape and characteristic lateral dimensions about 20 microns; located in the form of fine inclusion in the grey phase or along the boundaries between the light and dark main structural components;
- in the areas of the light phase precipitation, on their boundaries, and also in the form of fine inclusions of irregular shape, in the matrix there are extractions of another metal phase, covered with oxide film giving them sharp colored paint of blue, violet and red colors.

Solid solution $(U,Zr)O_2$, based upon the FCC lattice of uranium dioxide, corresponds to the dark component of the structure. Then, on the basis of the phase analysis results, corresponds to white extractions of the metal phase – phase of metal α -zirconium stabilized with oxygen α -Zr(O). In addition the phase analysis data show likely presence of metal α -uranium or solid solution on its basis. In this case, the formation of oxide film on the surface of the metal uranium extractions is absolutely logical.

Some features have the microstructures along the ingot boundaries, they are as follows:

1. some reduction of characteristic dimensions of the light phase precipitation in the vicinity of the contact with the vessel model wall;
2. absence of precipitation with colored paint in the stripe with width 200÷500 microns on the boundary of the ingot/vessel model wall contact and, on the contrary, increased concentration of fine precipitation of colored paint in the vicinity of the upper ingot surface;
3. presence of thin (from 10 to 150 microns) material crust on the external ingot surface in the contact region with the vessel model wall, the microstructure of which is sharply different from the microstructure of the main material;
4. presence of the crust fragments of the material on the top ingot boundary with characteristic microstructure, and also occasional inclusions of these fragments at a distance of the upper boundary in the ingot depth.

5.3 Investigation after the integral test INVECOR-2

The appearance of the solidified melt location in the vessel model after removal of the plasmatrons and tantalum funnel is represented in Figure 142. Figure 143 depicts the diagram of the corium location in the vessel model.

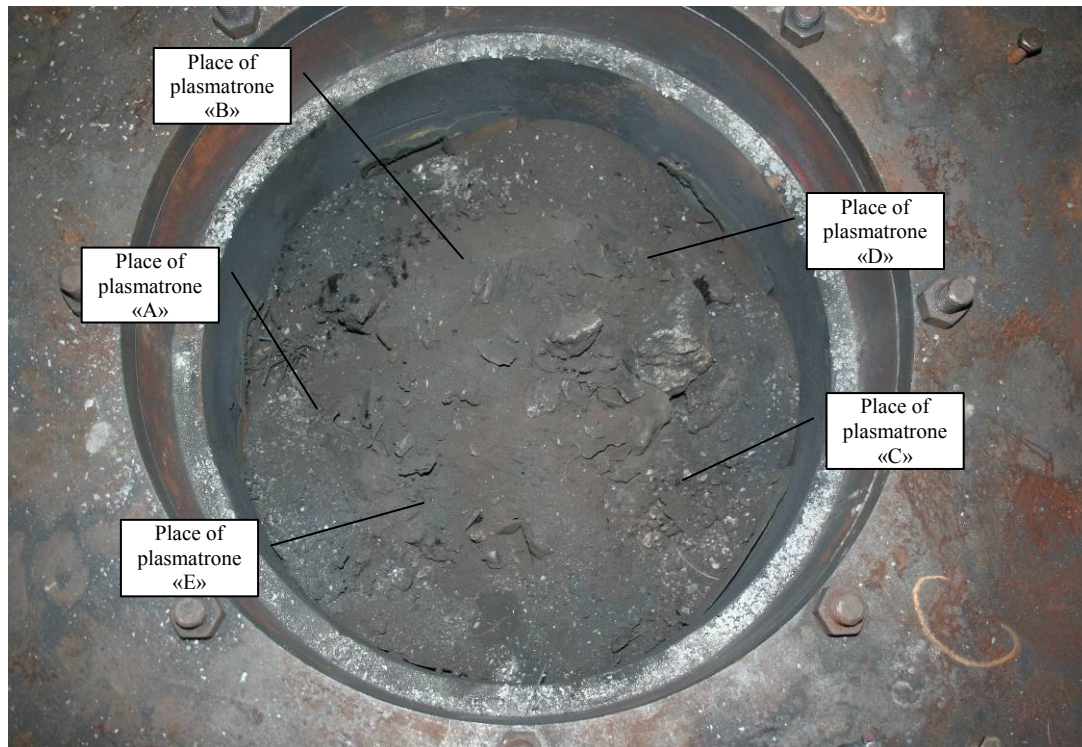


Figure 142 – Appearance of corium in the vessel model after removal of the plasmatrone nozzles

The model material was sampled in two stages. At the first stage the unbound material located over the melt ingot was removed. For the investigation the material over the central ingot area was sampled. For the analysis the material was fractioned according to the characteristic size of particles. From each fraction there were sampled representative weights for preparation of samples (samples of series LF, see Table 17).

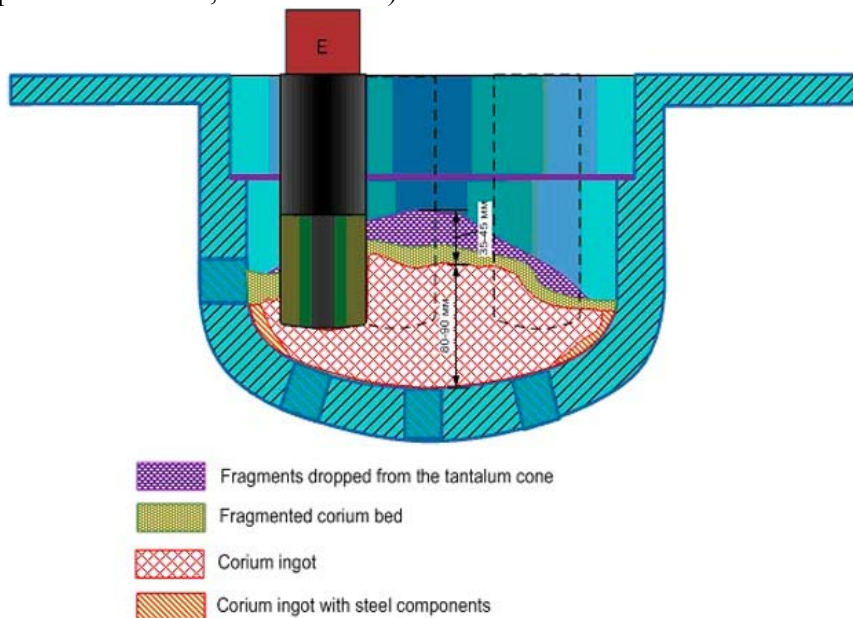


Figure 143 – The layout of corium in the vessel model

Table 17 – Grain-size composition of corium fragments over the ingot

Fraction No.	Particle size	Fraction mass, g	Designation of sampling
15	Less than 50 microns	1678	LF-15
14	from 50 microns to 100 мкм	353	LF-14
13	from 100 microns to 200 microns	341	LF-13
12	from 200 microns to 400 microns	396	LF-12
11	from 400 microns to 800 microns	469	LF-11
10	from 800 microns to 1,6 mm	617	LF-10
9	from 1,6 mm to 2,8 mm	588	LF-9
8	from 2,8 mm to 4 mm	410	LF-8
7	from 4 mm to 5,6 mm	434	
6	from 5,6 mm to 8 mm	309	
5	from 8 mm to 10 mm	138	
4	over 10	393	

The appearance of the melt ingot in the vessel model after removal of the fragments layer is represented in Figure 144.

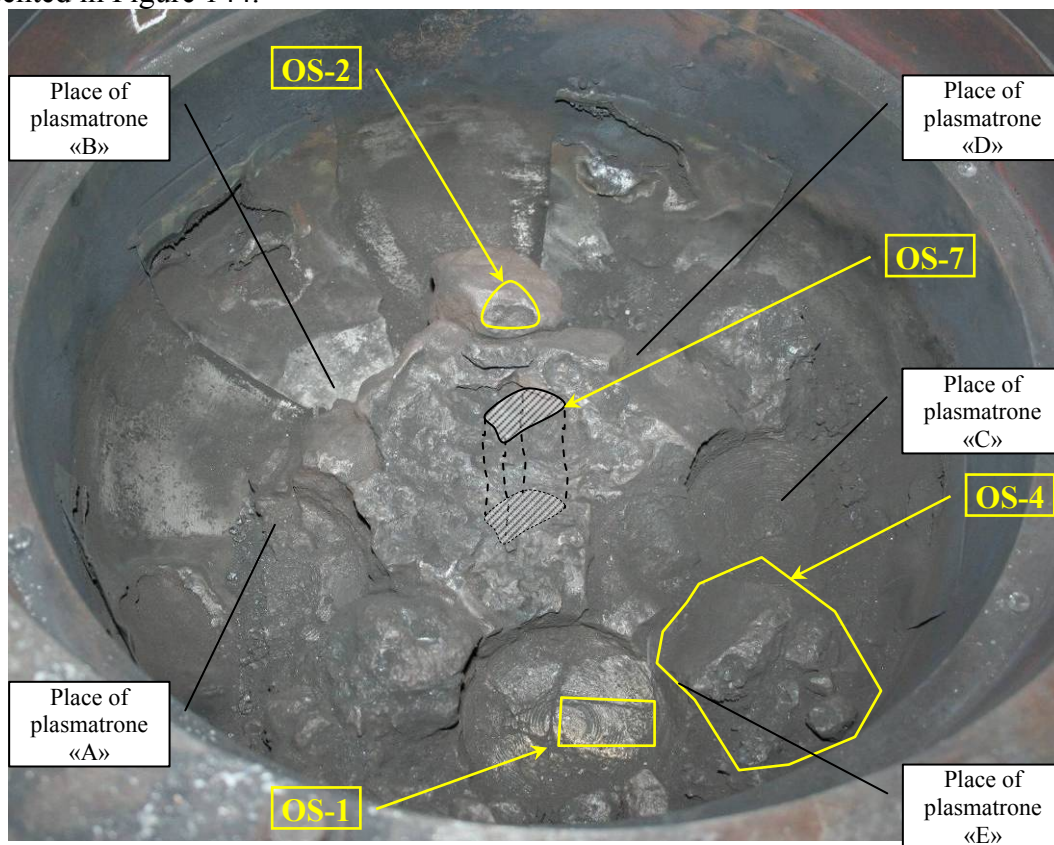


Figure 144 – Appearance the melt ingot in the vessel model after removal of the fragments layer

Stainless steel preliminary fastened on the internal surface of the vessel model in order to simulate the VVER design, partially maintains its integrity. Only the central part of the plate was eroded totally (Figure 145).



Figure 145 – The vessel model surface after corium removal

In the general case the ingot represents the homogeneous solid material with a pronounced dendrite structure. The dendrite arms are directed from the bottom to the top of the ingot. From the bottom the ingot surface is produced either with the solidified melt material or partially molten and caked material of the support from corium fragments loaded in the vessel model before the test. The shape of the ingot back surface replicates the vessel model shape. The picture of ingot back surface is represented in Figure 146.

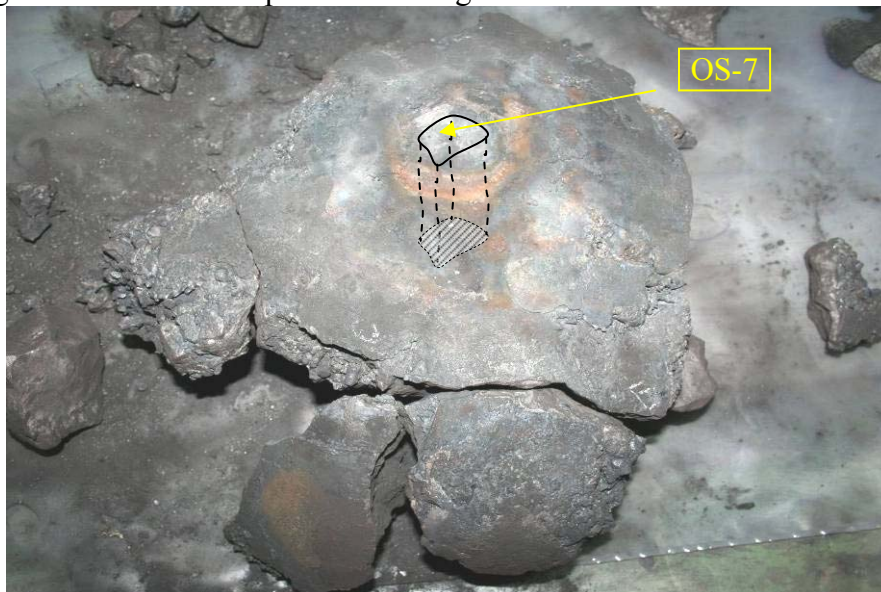


Figure 146 – The surface of the ingot central region from the side of the vessel model wall

The most homogeneous surface of the corium melt/vessel model wall contact is observed in the central region, where the ingot has maximum thickness. As moving away to the model periphery, the ingot surface share, produced with partially molten material, increases (initial loading residual).

The ingot was divided into fragments mainly along the existing cracks. For the investigation there were chosen as follows: the ingot fragment over the central sample of the vessel steel (OS-7, Figure 147); the ingot fragment between the plasmatrone E and C (OS-3, 4); material samples in the top (OS-2) and bottom (OS-5, 6) regions of the ingot; fragment of the ingot under the plasmatrone "E" (OS-1). Description of the ingot sampling is included in Table 18.

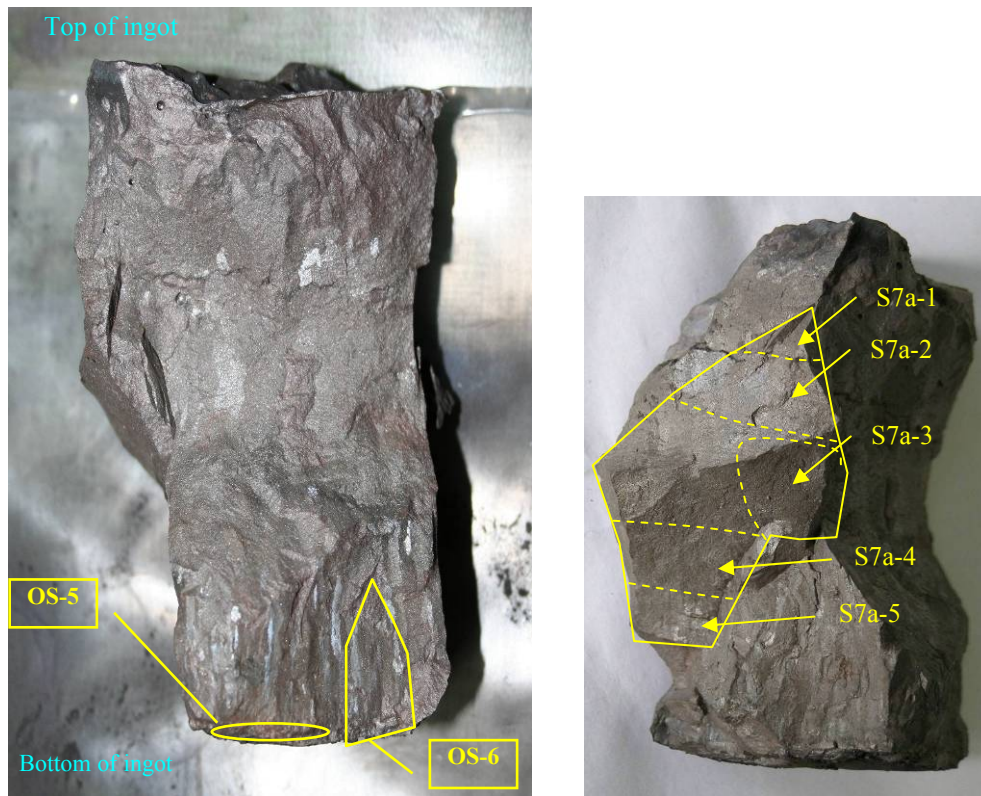


Figure 147 – The ingot fragment from the central area with sampling points

Table 18 – Description of material samples under investigation

Sample designation	Description of material and sampling point
LF-6÷15	Loose material in the central ingot area
Microsection -1	Ingot fragment under the plasmatrone "E"
OS-1	
OS-2	Spalling of the material from the ingot top with smooth surface in the plasmatrons "D" and "B" areas for characterization of this ingot region
OS-3	Large fragment of the top ingot part between electrodes "E" and "C"
OS-4	Large fragment of the bottom ingot part between electrodes "E" and "C"
OS-5	Spalling of the surface layer of the ingot material over the central insert made of reactor pressure vessel steel
OS-6	Fragments of spalling in the bottom ingot part over the central insert
Microsections 2.1, 2.2	Spalling of the corium ingot material over the insert made of reactor pressure vessel steel
OS-7.4, OS-7.a	

The data resulted from the phase analysis.

The data resulted from the phase analysis are included in Tables 19, 20. The tables for the phases with cubic crystal lattice represent the measured values of lattice spacing a_0 and their approximate content. The sequence of the elements location in the formulation of the variable content phases corresponds to the reduction of their relative atom concentration as well. The tables include also the results of determining relative mass content of uranium and zirconium in the sample material.

The phase composition of samples of the fragmented corium layer.

From the results of the X-ray phase analysis the main components of the fragment samples (sample series LF) are oxide phases of variable composition $(U,Zr)O_2$ based upon the FCC lattice of uranium dioxide.

Table 19 - Results of the qualitative phase and quantitative element analysis of sample composition of the fragmented corium

Sample	Phase composition	Element composition, weight %		U/Zr
		Zr	U	
LF-15	$U_{0.95}Zr_{0.05}O_2$ (0,545 nm); $ZrO_2^{tetr.}$; ZrO_2^{mcl}	20,4%	79,6%	3,89
LF-14	$U_{0.95}Zr_{0.05}O_2$ (0,545 nm); $ZrO_2^{tetr.}$; ZrO_2^{mcl} ;	19,8%	80,2%	4,05
LF-13	$U_{0.95}Zr_{0.05}O_2$ (0,545 nm); $ZrO_2^{tetr.}$; ZrO_2^{mcl}	16,8%	83,2%	4,96
LF-12	$U_{0.95}Zr_{0.05}O_2$ (0,545 nm); $ZrO_2^{tetr.}$; ZrO_2^{mcl}	18,1%	81,9%	4,52
LF-11	$U_{0.95}Zr_{0.05}O_2$ (0,545 nm); $ZrO_2^{tetr.}$; ZrO_2^{mcl} ;	19,5%	80,5%	4,13
LF-10	$U_{0.95}Zr_{0.05}O_2$ (0,545 nm); $ZrO_2^{tetr.}$; ZrO_2^{mcl}	19,4%	80,6%	4,15
LF-9	$U_{0.95}Zr_{0.05}O_2$ (0,545 nm); $ZrO_2^{tetr.}$; ZrO_2^{mcl}	18,2%	81,8%	4,48
LF-8	$U_{0.95}Zr_{0.05}O_2$ (0,545 nm); $ZrO_2^{tetr.}$; ZrO_2^{mcl} ;	17,6%	82,4%	4,69

The lattice parameters of the variable composition phases (U,Zr)O₂, determined from the maximum angles on the diffraction reflection profiles, enable to estimate their chemical composition and approximate proportion in the samples. In the large fraction material samples it is managed to identify definitely the existence of UO₂ pellets material as well as the whole set of phases within the composition range from UO₂ to U_{~0,8}Zr_{~0,2}O₂., the quantitative content of which reduces with increasing of zirconium content. As the fraction particles size changes, so the uranium dioxide/solid solutions ratio remains approximately equal, with the exception of the smallest fractions. In the diffraction patterns of sample LF-14 and, especially sample LF-15, uranium dioxide peaks were not discovered separately, and the chemical composition of the solid solutions lies within the range U_{0,97}Zr_{~0,03}O₂ to U_{0,93}Zr_{~0,07}O₂.

Along with the above phases, there are also phases the presence of which is determined only from the decreasing of intensity of the first two phases lines with simultaneous increasing of the background in the angles area, where the lines of uranium and zirconium oxides are located. In the table these phases are designated as ZrO₂^{tetr} and ZrO₂^{mcl} against the coincidence of the most identified peaks. The number of the phases increases as fraction particles size decreases and is at its maximum in fraction material #15 (sample LF-15).

The phase composition of the ingot material sample of the solidified melt.

From the results of the X-ray phase analysis the main components of the solidified melt samples are oxide phases of variable composition (U, Zr)O₂ with fcc lattice - uranium dioxide lattice.

The oxide solid solutions (U,Zr)O₂ are characteristic for all samples. The common trait of the phase chemical composition is low content of zirconium in the solution as well as lack of the metal zirconium phase. The estimating chemical composition of the oxide phase was determined from the lattice spacing value and was close to the composition U_{~0,95}Zr_{~0,05}O₂ (0,546 nm) in all samples.

In some ingot material samples it was revealed the presence of the phase on the basis of the crystal lattice α -uranium α -(U,Zr) and the iron-bearing phase the most easily identified as Zr₂FeO_x or (U,Zr)Fe₂ with cubic lattice of space groups Fm3m or Fd3m. The element analysis confirms the presence of iron in these samples.

Table 20 - Results of the qualitative phase and quantitative element analysis of the corium ingot samples composition

Sample	Phase composition	Element composition, weight %		U/Zr
		Zr	U	
OS-2	$U_{-0.95}Zr_{-0.05}O_2$ (0,5453 nm); α -(U,Zr)	24,2%	75,8%	3,13
OS-5	$U_{-0.97}Zr_{-0.03}O_2$ (0,546 nm); α -(U,Zr); (U,Zr)Fe ₂ (a ₀ =7,1 nm)	20,3%	79,7%	3,93
OS-6	$U_{-0.97}Zr_{-0.03}O_2$ (0,546 nm); α -(U,Zr)	21,6%	78,4%	3,64
OS7.4.1	$U_{-0.95}Zr_{-0.05}O_2$ (0,545(8) nm); α -(U,Zr)	24,3%	75,7%	3,12
OS7.4.2	$U_{-0.95}Zr_{-0.05}O_2$ (0,545(8) nm); α -(U,Zr)	20,8%	79,2%	3,81
OS7a.1	$U_{-0.95}Zr_{-0.05}O_2$ (0,545(8) nm); α -(U,Zr)	23,6%	76,4%	3,23
OS7a.2	$U_{-0.95}Zr_{-0.05}O_2$ (0,545(8) nm); α -(U,Zr)	25,0%	75,0%	3,00
OS7a.3	$U_{-0.95}Zr_{-0.05}O_2$ (0,545(9) nm); α -(U,Zr)	22,7%	77,3%	3,41
OS7a.4	$U_{-0.95}Zr_{-0.05}O_2$ (0,546(0) nm); α -(U,Zr)	24,9%	75,1%	3,02
OS7a.5	$U_{-0.95}Zr_{-0.05}O_2$ (0,546(0) nm); α -(U,Zr)	23,8%	76,2%	3,21

The element analysis demonstrates the homogeneous distribution of uranium and zirconium in the sampled material along the ingot section.

Relative content of zirconium in the fragments layer over the ingot is somewhat less than in the ingot itself.

The results of measuring samples density.

To measure the hydrostatic density, there were selected the ingot fragments the description of which is included in Table 21.

Table 21 – Description of sampling and material samples for measuring density

Designation	Description of material and sampling points
OS-2	Fragment of material from the ingot top with smooth surface in the plasmatrons D and B regions
OS-7a	Large fragment in the ingot middle part
OS-6p_1,2	Fragment of spalling in the bottom ingot part over the central insert with removed nearbottom crack
OS-7_s1-8	Region of OS-7 fragment material cut

The large fragment of the central part was divided into 8 parts along the existing cracks (Figure 148).



Figure 148 – Fragment of the central ingot

The results of density measurement in relation to average distance from the lower head of the reactor pressure vessel model are included in Table 22.

Table 22 – Hydrostatic density of the ingot samples

Sample	Average distance from the model bottom, mm	Density, g/cm ³
S7_S1	110	9,46
OS-2	105	9,54
S7_S2	100	9,47
S7_S3	95	9,59
S7_S4	70	9,59
S-7a	70	9,54
S7_S5	45	9,56
S7_S6	30	9,73
S7_S7	20	9,61
S7_S8	10	9,66
OS-6p	10	9,59

The results of the phase and element analysis of material and ingot samples in the vessel model enable to make a conclusion as follows:

3. The phase composition of all ingot material samples is practically identical, that is confirmed with the element analysis data and says about homogeneity of the melt both at the solidification and melt drain points. This also tells us about the identity of the phase and element composition of the melt crust sample on the tantalum funnel (sample OC-3), samples of the melt ingot material and corium fragments over the ingot in the vessel model.
4. In the samples with direct contact with steel elements of the facility there was found the presence of products of their chemical interaction with corium melt. In the rest of the ingot samples the content of iron-bearing phases was equal to zero in fact.

Metallography

To perform metallographic examination, the metallographic sections of the vertical ingot sections were produced from samplings OS-7 and OS-1 (Figure 149).

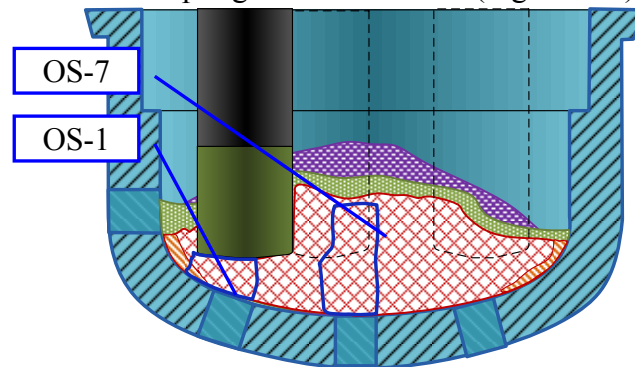


Figure 149 – Diagram of the ingot fragments sampling

The OS-1 fragment material is monolithic with non-uniform macrostructure where we may see several main structurally different regions (Figure 150):

1. The main ingot part in the *fragment* center is a relatively homogeneous material where we may define lighter colored areas (2a) in the main darker matrix of the ingot (2b);
2. The ingot bottom with thickness 5-7 mm containing finer and contrasting light inhomogeneities in the dark matrix;
3. A layer of dark homogeneous material with width to 1-2 mm (on the periphery from the nozzle axis) in the vicinity of the boundary with the vessel model;
4. A thin layer (to 0,5 mm) of light material on the boundary of the vessel model contact;

Region 1 – Main ingot part

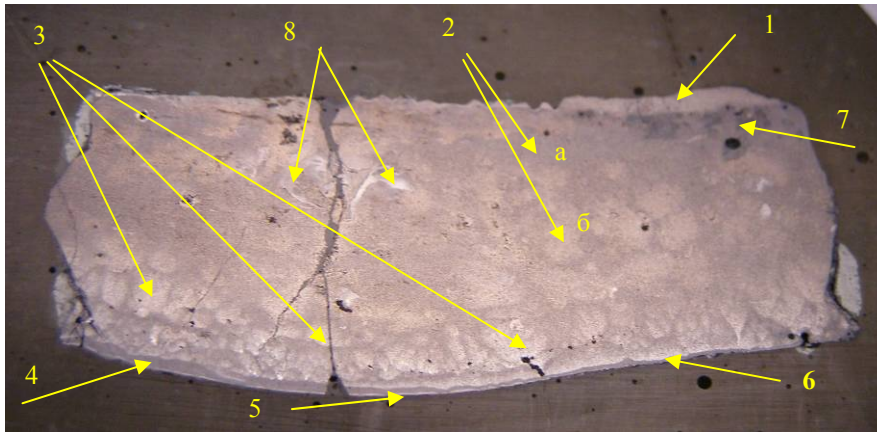


Figure 150 – Macrograph of the metallographic section surface in the reflected light that contains characteristic regions

The microstructure analysis in the main ingot area denotes the presence of macroscopic inhomogeneities of chemical and phase material composition of the ingot main part. The lighter colored areas have microstructure the formation of which may be connected with high content of the dissolved iron in these melt regions (Figures 151, 152).

The element analysis of the metallographic sections surface demonstrates the presence of iron about $0,4 \div 0,2\%$ in the central and upper ingot parts.

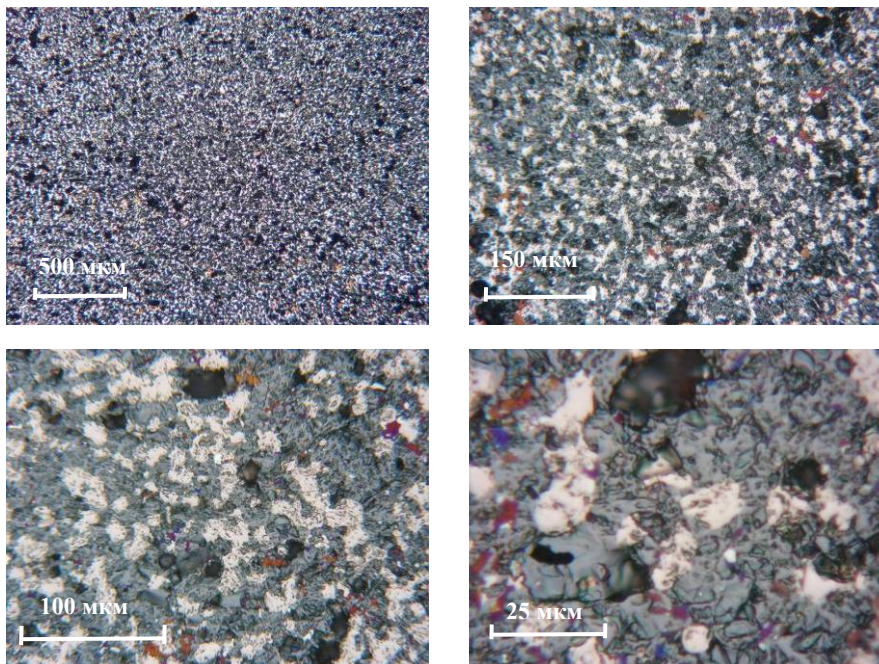


Figure 151 - Microstructure of the main dark material in the central ingot areas (region 2b)

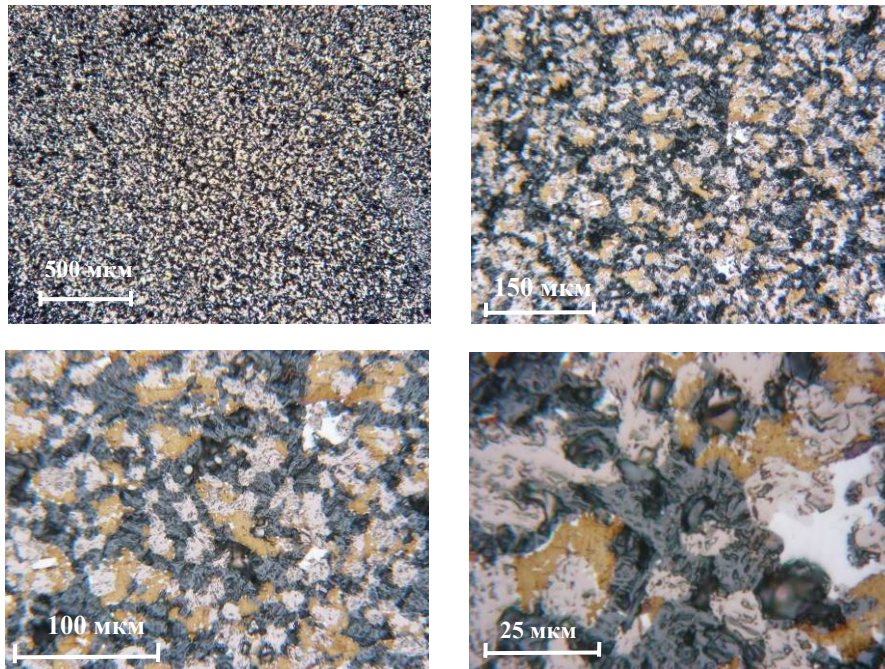


Figure 152 - Microstructure of the light material areas in the central ingot part (region 2a)

The element analysis of the metallographic section surface areas denotes the presence of iron at level $1 \div 2$ % weight in the region to 5 mm from the metallographic section bottom which decreases to the level $0,4 \div 0,2\%$ in the central and upper ingot areas. The phase analysis of the lower metallographic section region shows the presence of phases α -(U,Zr,(Fe)) based upon the lattice α -modification of metal uranium and the phases with the cubic lattice of space group Fd3m ($a_0=0,706 \div 0,710$ nm). Hypothetically, light-brown colored and white releases are formed with the phases α -(U,Zr,(Fe)) and (U,Zr)Fe₂ respectively.

Regions 4 and 5 – Material on the boundary with the vessel model

The characteristic microstructures of the regions material are represented in Figures 153 and 154.

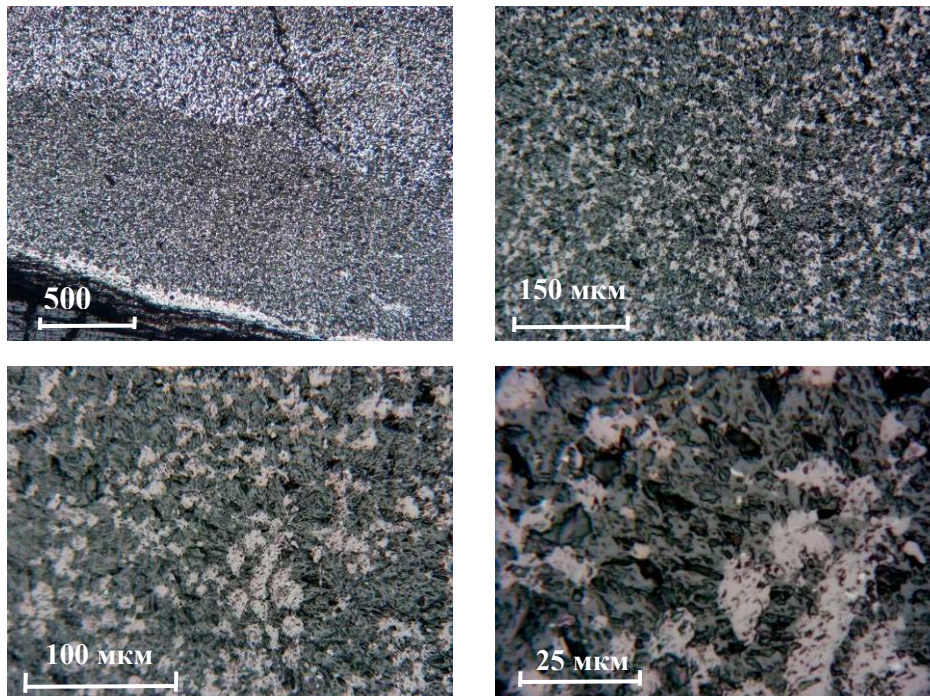


Figure 153 – Microstructure of the dark material layer in the vicinity of the lower ingot surface (region 4)

The presence of iron in the layer, defined from the element analysis results of its surface, does not exceed 0,1 %mass. The microstructure of the light boundary layer is given in Figure 154.

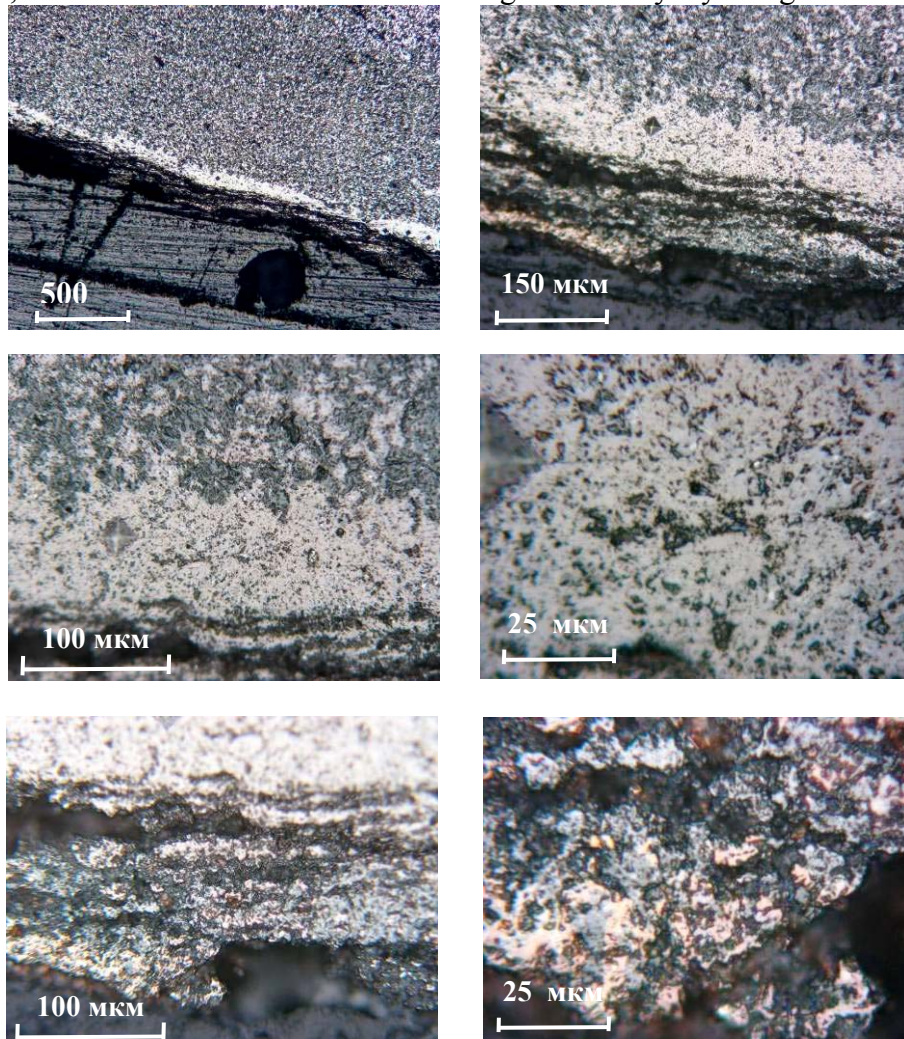


Figure 154 – Characteristic microstructure of the light material layer in the lower boundary ingot layers (region 5)

The fragment material from the central corium ingot part is monolith (Figure 155) with non-uniform macrostructure where we may see several main structurally different regions:

1. the main ingot part in the *fragment* center is a relatively homogeneous material with the pronounced dendrite structure;
2. the contrasting large dark irregular-shaped inclusions in the main ingot part;
3. the ingot bottom with thickness 5-7 mm, as the lighter part, where we may distinguish relatively fine and contrasting light inhomogeneities in the darker base.

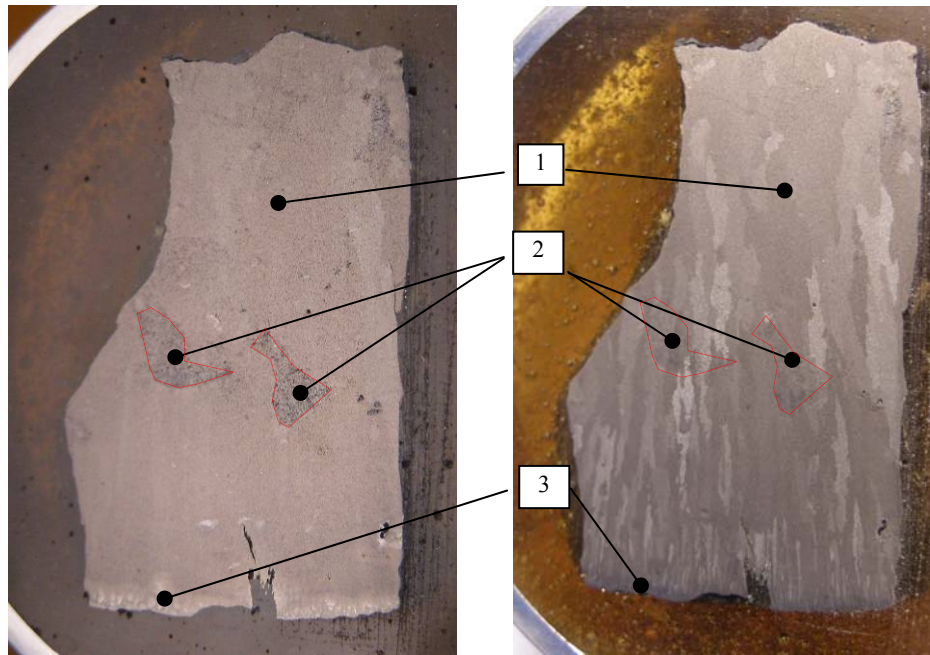


Figure 155 – Macrographs of the metallographic section surface at uniform (from the left) and directional (from the right) lighting with the characteristic structure regions

Region 1 – The main ingot region in the fragment center

The main ingot part in the fragment center is a relatively uniform material with the pronounced dendrite structure where we see dark large irregular-shaped inclusions. The dendrites' axes direct vertically, their size increases from the bottom to the top of the fragment. The microstructure of the given area material is shown in Figure 156.

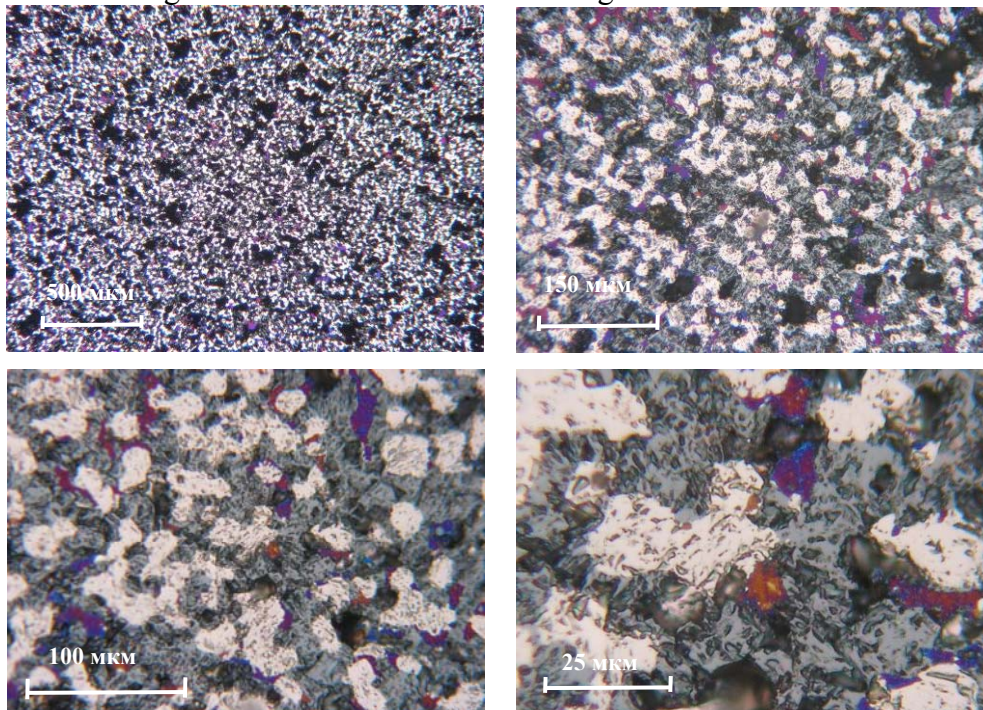


Figure 156 - Characteristic microstructure of the main ingot part in the fragment center (region 1)

Region 3 – Bottom ingot part

The darker areas in the bottom ingot part consist of the main dark and light structural constituents corresponding to the solid solution $(U,Zr)O_2$ and the transient phase with high content of zirconium oxide. Microhardness of the light brown-colored material releases ranges

3±5 GPa that enables to assume that it is also the phase on the basis of metal uranium α -(U,Zr(Fe)). Change in color of the oxide film demonstrates likely change of chemical composition of the given phase. In addition, in these regions there are releases of the light-colored phases that are not covered with the lapse of time with the oxide film, that are most probably belong to inter-metallic phase (U,Zr)Fe₂. The characteristic microstructures of the dark regions material of the lower metallographic section area are represented in Figure 157.

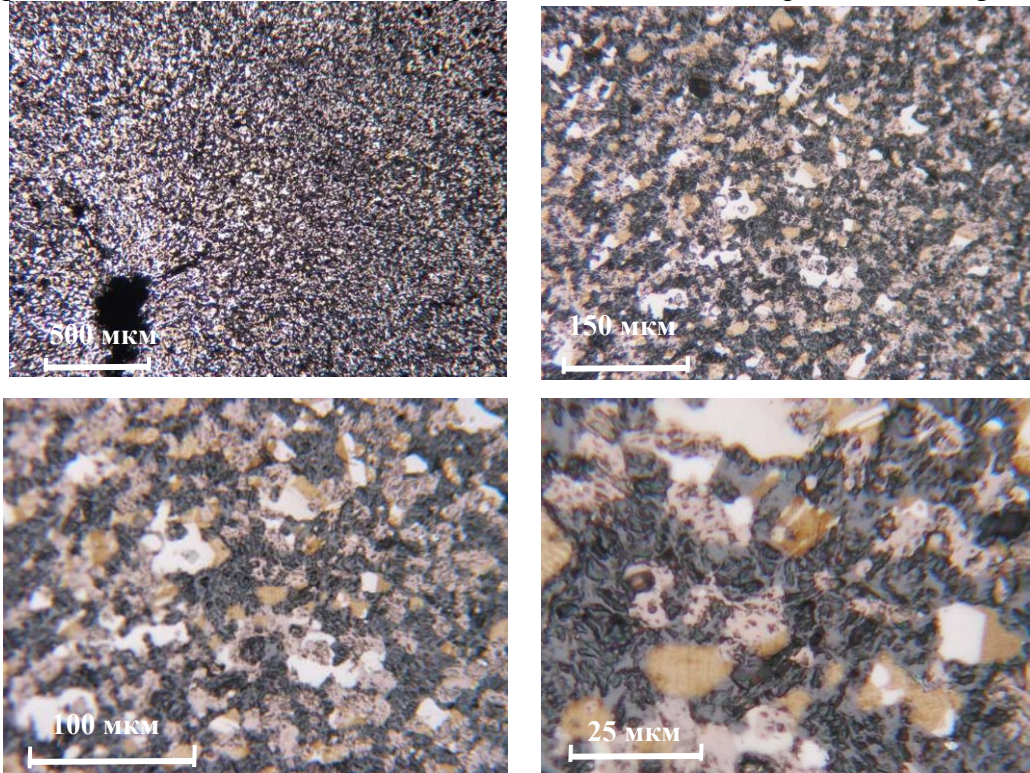


Figure 157 - Microstructure of main material in the lower ingot areas (region 3)

Conclusion

The results of the phase and element analysis of material samples from the EMF and ingot in the lower head reactor vessel model enable to conclude as follows:

1. The phase composition of all ingot material samples is practically identical, that is confirmed with the results of the element analysis as well and tells about the melt homogeneity both on its solidification and its draining moments. The latter is demonstrated with the identity of the phase and element composition of the melt crust sample on the tantalum funnel (sample OS-3), samples of the melt ingot material and the loose material over the ingot in the vessel model.
2. In the samples with direct contact with the test facility steel elements the presence of the steel/corium melt interaction products was detected.
3. The ingot fragments material is mainly homogeneous with the microstructure typical for oxide-metal corium. Inclusions of metal α -uranium is relatively rare and present both in the main ingot material and in the partially dissolved fragments of uranium dioxide pellets.
4. The presence of iron and iron-contained phases in the central and especially in the lower ingot parts is well harmonized with the experiment geometry and denotes dissolution of iron in the corium melt.

5.4 Investigation after the integral test INVECOR-3

After completion of the INVECOR-3 experiment, the vessel model was removed from the MR.

In disassembling the solidified melt fragments were taken from the walls of the steel and tantalum funnels (samples OS-1 and OS-3) for their study (Figure 158).

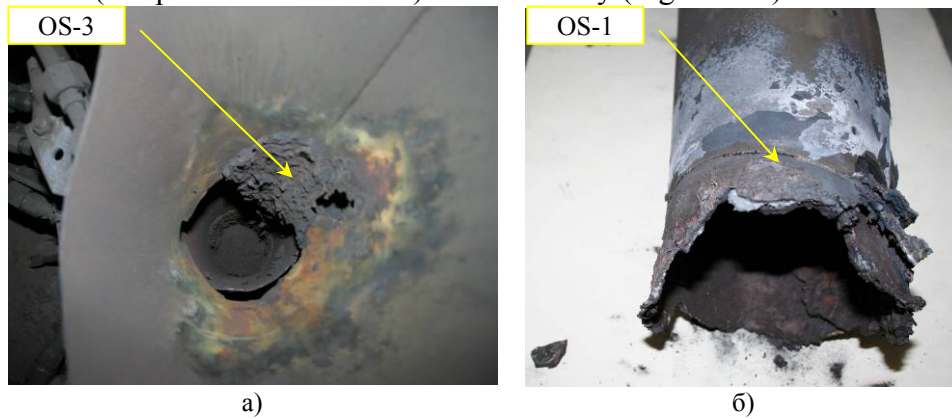


Figure 158 – Corium on the steel (a) and tantalum (b) funnels

The appearance of the solidified corium melt in the vessel model after disassembling of the plasmatron and tantalum funnel is represented in Figure 159.



Figure 159 – RPV model with solidified melt after plasmatrons dismantling

The vessel model material was sampled in two stages. At the first stage there was removed the fragments layer located in the form of a "hill" over the melt ingot center (sampling PIIO-1). That material, mainly, was run from the tantalum funnel during the disassembling. Then the disperse material residual over the ingot center (sampling PIIO-2) and the disperse material over the ingot in the plasmatrons peripheral areas (sampling PIIA÷PIIE) were removed. The material in the plasmatrons "A" region was sampled (sampling PIIA) for analysis. Afterwards the material was fractionated with consideration of the characteristic dimensions of particles. From each fraction there were selected representative weights for preparation of samples (samples of series LO1_F, LO2_F, LA_F). The fractionation results and the fragment samples are included in Tables 23-25.

Table 23 – The results of the material fractionation and designation of sampling PII0-1

Fraction No.	Particle size	Fraction mass, g	Designation of samples for analysis
15	Less than 50 microns	676,01	LO_1_F-15
14	from 50 microns to 100 microns	138,36	
13	from 100 microns to 200 microns	91,58	LO_1_F-13
12	from 200 microns to 400 microns	104,94	
11	from 400 microns to 800 microns	118,79	LO_1_F-11
10	from 800 microns to 1,6 mm	163,47	
9	from 1,6 mm to 2,8 mm	191,99	LO_1_F-9
8	from 2,8 mm to 4 mm	177,64	
7	from 4 mm to 5,6 mm	163,49	
6	from 5,6 mm to 8 mm	176,19	
5	from 8 mm to 10 mm	137,35	
4	from 10 mm to 12,5 mm	170,23	
3	from 12,5 mm to 16 mm	78,38	
2	from 16 mm to 20 mm	83,64	
1	over 20 mm	94,3	

Table 24 - The results of the material fractionation and designation of sampling PII0-2

Fraction No.	Particle size	Fraction mass, g	Designation of samples for analysis
15	Less than 50 microns	136,88	LO_2_F-15
14	from 50 microns to 100 microns	22,03	
13	from 100 microns to 200 microns	22,83	LO_2_F-13
12	from 200 microns to 400 microns	31,25	
11	from 400 microns to 800 microns	41,64	LO_2_F-11
10	from 800 microns to 1,6 mm	69,46	
9	from 1,6 mm to 2,8 mm	91,39	LO_2_F-9
8	from 2,8 mm to 4 mm	64,33	
7	from 4 mm to 5,6 mm	83,4	
6	from 5,6 mm to 8 mm	78,78	
5	from 8 mm to 10 mm	19,99	
4	from 10 mm to 12,5 mm	64,59	
3	from 12,5 mm to 16 mm	20,48	
2	from 16 mm to 20 mm	-	
1	over 20 mm	-	

Table 25 - The results of the material fractionation and designation of sampling PIIA

Fraction No.	Particle size	Fraction mass, g	Designation of samples for analysis
15	Less than 50 microns	366,15	LA_F-15
14	from 50 microns to 100 microns	53,11	
13	from 100 microns to 200 microns	48,25	LA_F-13
12	from 200 microns to 400 microns	59,17	
11	from 400 microns to 800 microns	80,47	LA_F-11
10	from 800 microns to 1,6 mm	116,03	
9	from 1,6 mm to 2,8 mm	209,75	LA_F-9
8	from 2,8 mm to 4 mm	178,19	
7	from 4 mm to 5,6 mm	204	
6	from 5,6 mm to 8 mm	312,66	
5	from 8 mm to 10 mm	246,87	
4	from 10 mm to 12,5 mm	162,04	
3	from 12,5 mm to 16 mm	85,82	
2	from 16 mm to 20 mm	92,32	
1	over 20 mm	-	

The appearance of the main melt ingot in the vessel model after removal of the corium fragments layer is represented in Figure 160.



Figure 160 – The vessel model with the melt after removal of the fragments layer

The ingot surface is uneven and contains debris fused with porous "foam"-solidified solution. In the ingot center there are hollows with small regular melt crystals formed on the hollows surface. As a rule, the main ingot material in this area has metallic luster. In the top region, the debris fragments, foam material and material in the hollow areas were sampled. In the bottom the ingot is solid. The material of this ingot part is characterized with samples OI-2_(4÷7).

Table 26 – The samples for analysis of the sampling material after INVECOT-3 test

Sampling designation	Description of material and sampling point	Sample designation
OS-1	The melt fragment from the steel funnel	OS-1
OS-3	The melt fragment from the tantalum funnel	OS-3
PIIO_1	Loose material ("hill") over the ingot center	LO_1F(15÷9)
PIIO_2	Loose material in the ingot central part	LO_2F(15÷9)
PIIA	Loose material in the electrode "A" region	LA_F(15÷9)
OS-5	The ingot fragments from the plasmatrone "A" area	OS-5_(1÷3)
OIA-1	The melt fragment on the plasmatrone A nozzle	OIA-1
OI-2_1	One of the debris fragments at the ingot top	OI-2_1
OI-2_2	"foam" material, porous in some areas, silver, connecting the debris material at the ingot top	OI-2_2
OI-2_3	Material of the ingot areas consisting of small regular crystals	OI-2_3
OI-2_4	Solid samples at the ingot bottom (sampling for determination of thermo-physical material properties)	OI-2_4
OI-2_5		OI-2_5
OI-2_6		OI-2_6
OI-2_7		OI-2_7

The points for sampling ingot fragments from the central area are illustrated in Figure 161.

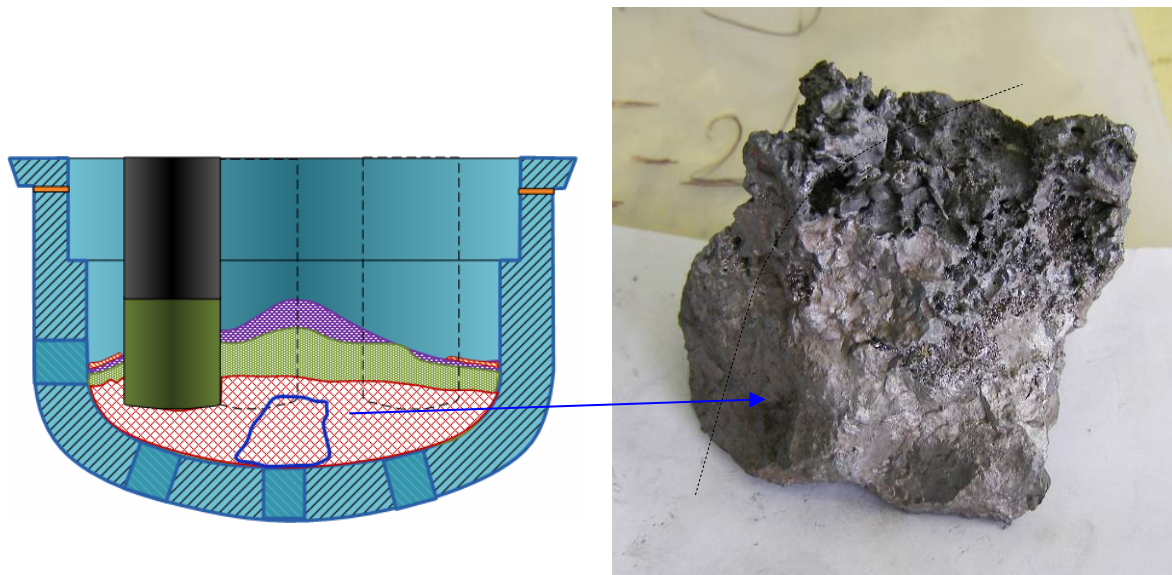


Figure 161 – Sampling point for the ingot fragment for investigation

To study the central ingot material, the samples from the ingot material fragments were produced (Figure 162). One half of the samples was used for the preparation of the sample in the form of a pellet for measuring thermo-physical properties, the second half – to perform X-ray phase and element analysis.

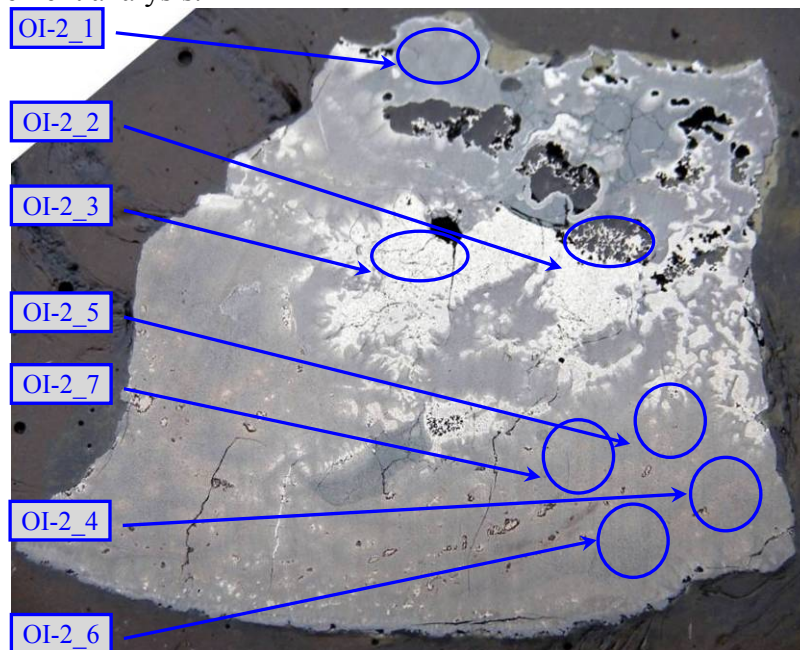


Figure 162 – The ingot fragment with the points of sampling for the study

The results of the phase analysis are included in Tables 27-30. The tables for the oxide phases represent the measured values of lattice spacing a_0 and their approximate component content. The phases sequence in the table cells corresponds to the reduction of their volume content in the samples. The sequence of the elements location in the formulation of the variable content phases corresponds to the reduction of their relative atom concentration as well. The tables include also the results of determining relative mass content of uranium and zirconium in the sample material.

Table 27 – The results of the qualitative phase and quantitative element composition of corium ingot samples

Sample	Phase composition	Relative mass content of elements, %			U/Zr
		Zr	U	Fe	
OE-1	$U_{-0.95}Zr_{-0.05}O_2$ (0,544 nm);	16,8	83,2	0,0	5,0
OS-1	$U_{-0.95}Zr_{-0.05}O_2$ (0,544 nm); α -(U,Zr); (U,Zr)Fe ₂ ($a_0=7,03\div 7,1$ nm);	21,3	77,4	1,4	3,6
OS-3	$U_{-0.95}Zr_{-0.05}O_2$ (0,544 nm); α -(U,Zr); (U,Zr)Fe ₂ ($a_0=7,03\div 7,1$ nm);	21,6	77,8	0,6	3,6
OS-5.1	$U_{-0.97}Zr_{-0.03}O_2$ (0,546 nm); (U,Zr)Fe ₂ ($a_0=0,705$ nm)	21,0	77,9	1,1	3,7
OS-5.2	$U_{-0.97}Zr_{-0.03}O_2$ (0,546 nm); (U,Zr)Fe ₂ ($a_0=0,704\div 0,706$ nm); $U_{-0.85}Zr_{-0.15}O_2$ (0,542 nm); α -Fe	23,5	69,3	7,1	2,9
OS-5.3	$U_{-0.95}Zr_{-0.05}O_2$ (0,545(8) nm); α -(U,Zr); (U,Zr)Fe ₂ ($a_0\approx 0,704\div 0,708$ nm)	21,4	77,3	1,3	3,6
OIA-1	$U_{-0.85}Zr_{-0.15}O_2$ (0,544 nm); UO ₂ (0,546(9) nm); (U,Fe)C ₂ (?)	25,0	72,4	2,6	2,9
OI-2_1	$U_{-0.95}Zr_{-0.05}O_2$ (0,544 nm); UO ₂ (0,546(9) nm); (U,Fe)C ₂ (?)	21,1	76,8	2,2	3,6
OI-2_2	$U_{-0.95}Zr_{-0.05}O_2$ (0,544 nm); UO ₂ (0,546(9) nm); (U,Fe)C ₂ (?)	22,2	71,4	6,4	3,2
OI-2_3	(U,Zr)Fe ₂ ($a_0=0,705$ nm); $U_{-0.75}Zr_{-0.25}O_2$ (0,539 nm); $U_{-0.95}Zr_{-0.05}O_2$ (0,544 nm); α -Fe; Fe ₃ Zr	26,9	59,0	14,1	2,2
OI-2_4	$U_{-0.97}Zr_{-0.03}O_2$ (0,5460±0,0002 nm; U ₆ Fe(?); α -(U,Zr(?)); (U,Zr)Fe ₂	24,6	75,1	0,3	3,0
OI-2_5	$U_{-0.98}Zr_{-0.02}O_2$ (0,5463±0,0002 nm; (U,Zr)Fe ₂ (0,708±0,002 nm); U ₆ Fe(?);	25,5	72,8	1,8	2,9
OI-2_6	$U_{-0.97}Zr_{-0.03}O_2$ (0,5460±0,0002 nm; U ₆ Fe(?); α -(U,Zr(?)); (U,Zr)Fe ₂	26,6	73,0	0,4	2,7
OI-2_7	$U_{-0.98}Zr_{-0.02}O_2$ (0,5463±0,0002 nm; (U,Zr)Fe ₂ (0,708±0,002 nm); U ₆ Fe(?);	25,9	73,6	0,5	2,8

From the results of the X-ray phase analysis the main components of the phase content of the solidified melt samples are oxide phases of variable composition (U,Zr)O₂ with FCC lattice – uranium dioxide lattice.

Oxide solid solutions (U,Zr)O₂ are characteristic for all samples. The common trait of this phase composition is low content of zirconium in the solution as well as lack of the metal zirconium phase. The evaluation chemical composition of the oxide phase was determined based on the lattice spacing value and was within the composition range $U_{-0.97}Zr_{-0.03}O_2\div U_{-0.85}Zr_{-0.15}O_2$ (0,546÷0,542 nm).

Table 28 - The results of the qualitative phase and quantitative element analysis of samples composition of the disperse material fractions of sampling PIIO_1

Sample	Phase composition	Relative weight content of elements, %			U/Zr
		Zr	U	Fe	
LO1_F15	$U_{0.95}Zr_{0.05}O_2$ (0,545 nm); ZrO ₂ ^{tetr.} ; ZrO ₂ ^{mcl.}	19,7	80,1	0,2	4,1
LO1_F13	$U_{0.95}Zr_{0.05}O_2$ (0,545 nm); ZrO ₂ ^{tetr.} ; ZrO ₂ ^{mcl.}	19,8	78,5	1,7	4,0
LO1_F11	$U_{0.95}Zr_{0.05}O_2$ (0,545 nm); ZrO ₂ ^{tetr.} ; ZrO ₂ ^{mcl.}	20,6	78,4	1,0	3,8
LO1_F9	$U_{0.95}Zr_{0.05}O_2$ (0,545 nm); ZrO ₂ ^{tetr.} ; ZrO ₂ ^{mcl.}	20,7	78,7	0,6	3,8

Table 29 - The results of the qualitative phase and quantitative element analysis of samples composition of fractions - sampling PIIO_2

Sample	Phase composition	Relative weight content of elements, %			U/Zr
		Zr	U	Fe	
LO2_F15	$U_{0.95}Zr_{0.05}O_2$ (0,545 nm); ZrO ₂ ^{tetr.} ; ZrO ₂ ^{mcl.} ;	24,4	75,0	0,6	3,1
LO2_F13	$U_{0.95}Zr_{0.05}O_2$ (0,545 nm); ZrO ₂ ^{tetr.} ; ZrO ₂ ^{mcl.} ; Ta ₂ O ₅ ; TaC	25,0	74,4	0,6	3,0
LO2_F11	$U_{0.95}Zr_{0.05}O_2$ (0,545 nm); ZrO ₂ ^{tetr.} ; ZrO ₂ ^{mcl.} ; Ta ₂ O ₅ ; TaC	24,8	74,8	0,5	3,0
LO2_F9	$U_{0.95}Zr_{0.05}O_2$ (0,545 nm); ZrO ₂ ^{tetr.} ; ZrO ₂ ^{mcl.} ; Ta ₂ O ₅ ; TaC	25,4	74,3	0,3	2,9

Table 30 - The results of the qualitative phase and quantitative element analysis of samples composition of the disperse material fractions of sampling PIIA

Sample	Phase composition	Relative weight content of elements, %			U/Zr, rel.unit
		Zr	U	Fe	
LA_F15	$U_{0,95}Zr_{0,05}O_2$ (0,545 nm); $ZrO_2^{tetr.}$, $ZrO_2^{mcl.}$, Ta_2O_5 ; TaC	22,4	77,4	0,2	3,4
LA_F13	$U_{0,95}Zr_{0,05}O_2$ (0,545 nm); $ZrO_2^{tetr.}$, $ZrO_2^{mcl.}$, Ta_2O_5 ; TaC	30,2	68,4	1,5	2,3
LA_F11	$U_{0,95}Zr_{0,05}O_2$ (0,545 nm); $ZrO_2^{tetr.}$, $ZrO_2^{mcl.}$, Ta_2O_5 ; TaC	27,9	71,5	0,6	2,6
LA_F9	$U_{0,95}Zr_{0,05}O_2$ (0,545 nm); $ZrO_2^{tetr.}$, $ZrO_2^{mcl.}$, Ta_2O_5 ; TaC	24,3	75,0	0,7	3,1

The data resulted from measuring thermo-physical properties of samples from the central ingot are included in Table 31.

Table 31 – Thermo-physical properties of the ingot samples

Sample	Specific heat, C_p , $J \cdot kg^{-1} \cdot K^{-1}$	Thermal conductivity, $a \times 10^{-6} \cdot m^2 \cdot s^{-1}$	Thermal diffusivity, λ , $W \cdot m^{-1} \cdot K^{-1}$	Density, ρ , g/cm^3
OI-2_4	271,0	2,60	6,93	9,85
OI-2_5	258,8	2,75	6,97	9,82
OI-2_6	283,9	2,36	6,62	9,80
OI-2_7	263,4	2,61	6,90	10,03

To perform the metallographic study, one of the response surfaces of the samples was used for measuring thermo-physical properties.

5.5 Investigations after integral test INVECOR-1.4

After completion of the integral test INVECOR-1.4 the vessel model was taken from the MR. The samples of the ingot and fragmented corium were chosen for the phase and element analysis of the melt composition.

The data from the phase analysis are included in Tables 34-35, 37-39. The measured values of the lattice spacing a_0 and their approximate component content are included in the tables for the phases with crystal lattices of the cubic symmetry. The phase sequence in the table cells corresponds to the reduction of their volume content in the samples. The elements gradation in the formulation of the variable composition phases is also corresponds to the reduction of their relative atomic percentage. Along with the data from the phase analysis the tables include also the data from determination of the relative mass content of uranium, zirconium and iron in the samples material.

Sampling of material from the vessel model was performed in two steps. At the first stage the fragmented material located over the melt ingot was removed (sampling PIIO).

The view of the corium in the vessel model after removal of the fragmented material, poured out from the tantalum funnel, disassembling of the tantalum and steel (fragments) shields is represented in Figure 163.

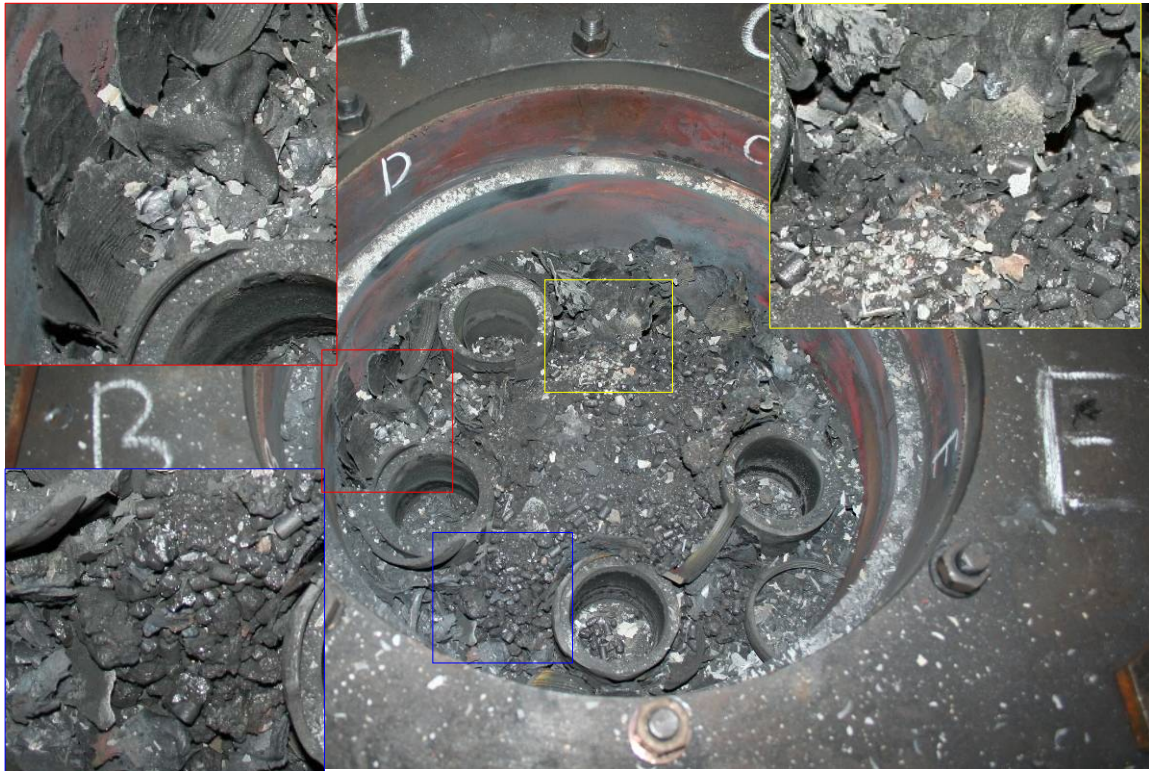


Figure 163 – Location of corium in the trap after removal of the shields

Investigation of the fragmented corium.

Large fragments and a layer of fine fragments of the material (sampling PIIS, PIIO-2) were removed from the ingot surface.

The PIIO-1 and PIIO-2 samplings material was fractionated according to the characteristic size of particles. The material was sampled from the fractions for analysis (samples of series LO1_F, LO2_F). Distribution of particles on fractions and designation of samples for analysis are included in Tables 32, 33.

Table 32 - Grain-size distribution of the first fragments layer over the ingot

Particle size	Mass, g	Mass fraction, %	Sample designation
below 400 mcm	698	16,2%	L1_F12
from 400 mcm to 1,6 mm	686	16,0%	L1_F10
from 1,6 mm to 4,0 mm	810	18,9%	L1_F8
from 4,0 mm to 8,0 mm	1430	33,3%	
from 8,0 mm to 12,5 mm	481	11,2%	
from 12,5 mm to 20,0 mm	192	4,5%	

Table 33 - Grain-size distribution of the second fragments layer over the ingot

Particle size	Mass, g	Mass fraction, %	Sample designation
below 400 mcm	699	38,7%	L2_F12
400 mcm to 1,6 mm	441	24,4%	L2_F10
from 1,6 mm to 4,0 mm	367	20,3%	L2_F8
from 4,0 mm to 8,0 mm	209	11,6%	
from 8,0 mm to 12,5 mm	77	4,3%	
12,5 mm to 20,0 mm	13	0,7%	

The appearance of the fragmented corium is given in Figure 164.

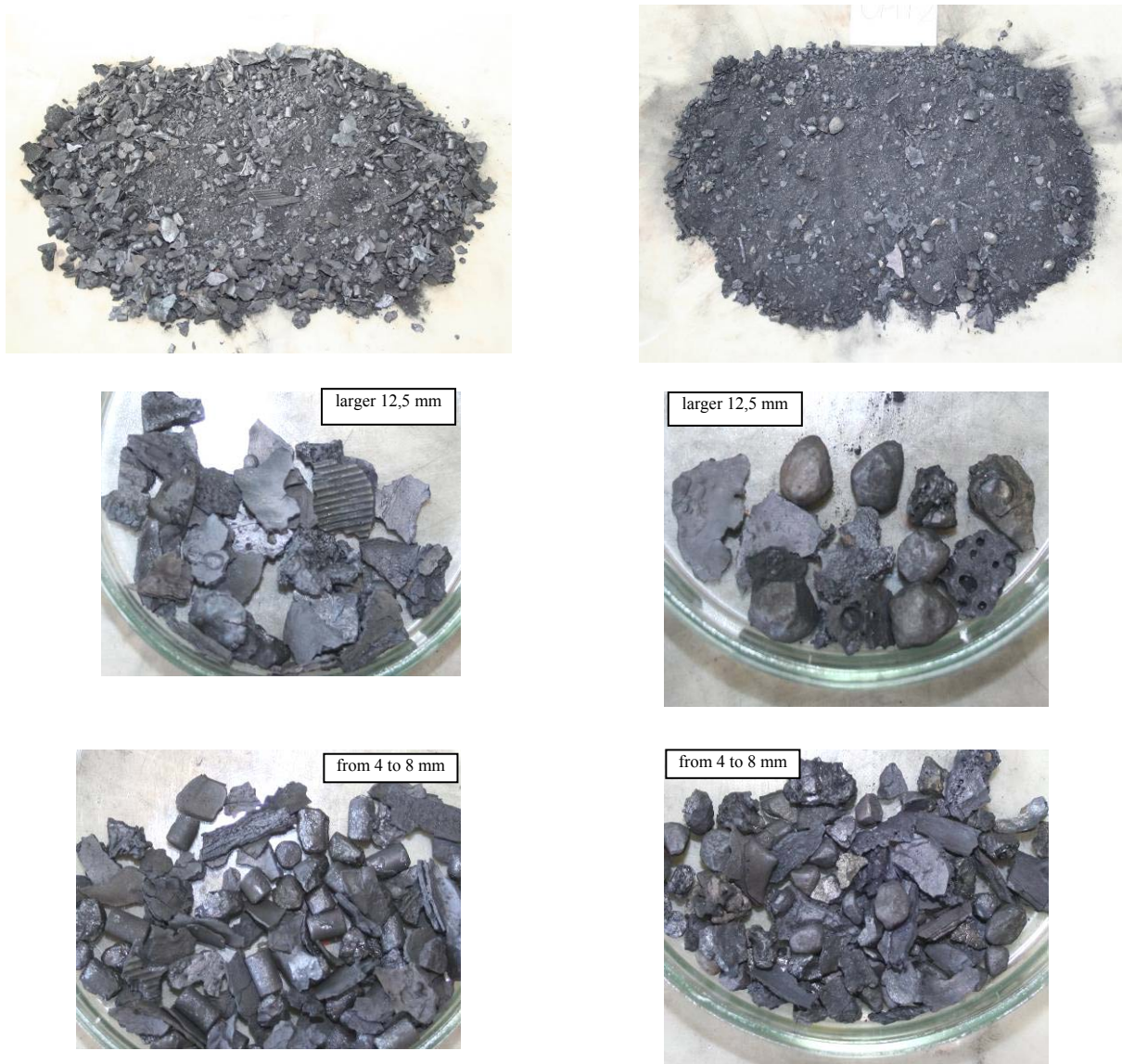


Figure 164 – The appearance of the material of the first (on the left) and the second (on the right) corium fragments layers over the ingot

From the X-ray phase analysis the main sample components of the upper fragments layer (sample series L1) are uranium dioxide UO_2 , and also oxide phases of the variable composition $(\text{U,Zr})\text{O}_2$ with FCC lattice of uranium dioxide and on the basis of the tetragonal and monoclinic lattices of zirconium dioxide (in Table 34 these phases are designated as $\text{ZrO}_2^{\text{tet}}$ and $\text{ZrO}_2^{\text{mnc}}$). The lattice parameters of the variable composition phases $(\text{U,Zr})\text{O}_2$, determined from the maximum angles on the diffraction reflection profiles, enable to estimate their chemical composition and approximate proportion in the samples. In the large fraction material samples it is managed to identify definitely the existence of UO_2 pellets material as well as the whole set of phases within the composition range from UO_2 to $\text{U}_{-0,8}\text{Zr}_{-0,2}\text{O}_2$.

The phase fraction composition of the second fragments layer (sample series L2) is differed with the lack of uranium dioxide. Their composition base are oxide phases $(\text{U,Zr})\text{O}_2$ with FCC lattice of uranium dioxide, the phase $(\text{Zr,Ur})\text{O}_2$ based upon the tetragonal and monoclinic modification of zirconium dioxide and $\alpha\text{-Zr(O)}$.

We should note the presence in the material a considerable number of fine fractions of the variable composition $\text{U}_{-0,5}\text{Zr}_{-0,5}\text{O}_2$ with FCC lattice spacing 0,533 nm. In the samples of the finest fractions, the lines of the higher uranium oxide U_3O_{8-x} are determined.

Table 34 –The results of the qualitative phase and quantitative element analysis of the fragmented corium samples

Sample	Phase composition	Relative weight content of elements, %			U/Zr
		Zr	U	Fe	
L1_F12	UO ₂ (0,547 nm); U _{0.85} Zr _{0.15} O ₂ (0,546÷0.540 nm); U _{0.5} Zr _{0.5} O ₂ (0,533 nm); U ₃ O ₈ ; ZrO ₂ ^{MCL} ; ZrO ₂ ^T	20,9	78,7	0,4	3,8
L1_F10	UO ₂ (0,547 nm); U _{0.85} Zr _{0.15} O ₂ (0,546÷0.540 nm); ZrO ₂ ^{MCL} ; ZrO ₂ ^T	25,5	73,9	0,6	2,9
L1_F8	UO ₂ (0,547 nm); U _{0.85} Zr _{0.15} O ₂ (0,546÷0.540 nm); ZrO ₂ ^{MCL} ; ZrO ₂ ^T	19,4	80,1	0,5	4,1
Average L1	UO ₂ (0,547 nm); U _{0.85} Zr _{0.15} O ₂ (0,546÷0.540 nm); ZrO ₂ ^{MCL} ; ZrO ₂ ^T ; U _{0.5} Zr _{0.5} O ₂ (0,533 nm); U ₃ O ₈	21,9	77,6	0,5	3,6
L2_F12	U _{0.95} Zr _{0.05} O ₂ (0,545 nm); U _{0.8} Zr _{0.2} O ₂ (0,544÷0.535 nm); U _{0.5} Zr _{0.5} O ₂ (0,533 nm); ; ZrO ₂ ^{MCL} ; ZrO ₂ ^T ; U ₃ O ₈ ; α-Zr(O)	30,7	68,6	0,7	2,2
L2_F10	U _{0.95} Zr _{0.05} O ₂ (0,545 nm); U _{0.8} Zr _{0.2} O ₂ (0,546÷0.540 nm); ZrO ₂ ^{MCL} ; ZrO ₂ ^T ; α-Zr(O); U _{0.5} Zr _{0.5} O ₂ (0,533 nm);	31,0	68,1	0,9	2,2
L2_F8	U _{0.94} Zr _{0.06} O ₂ (0,545 nm); U _{0.8} Zr _{0.2} O ₂ (0,545÷0.535 nm); α-Zr(O); ZrO ₂ ^{MCL} ; ZrO ₂ ^T ; U _{0.5} Zr _{0.5} O ₂ (0,533 nm)	31,9	67,2	0,9	2,1
Average L2	U _{0.94} Zr _{0.06} O ₂ (0,545 nm); U _{0.8} Zr _{0.2} O ₂ (0,546÷0.540 nm); ZrO ₂ ^{MCL} ; ZrO ₂ ^T ; α-Zr(O); U _{0.5} Zr _{0.5} O ₂ (0,533 nm); U ₃ O ₈	31,2	68,0	0,8	2,2

To describe the plate large fragments located over the ingot, there were selected the characteristic corium samples. Their appearance and designation are given in Figure 165.

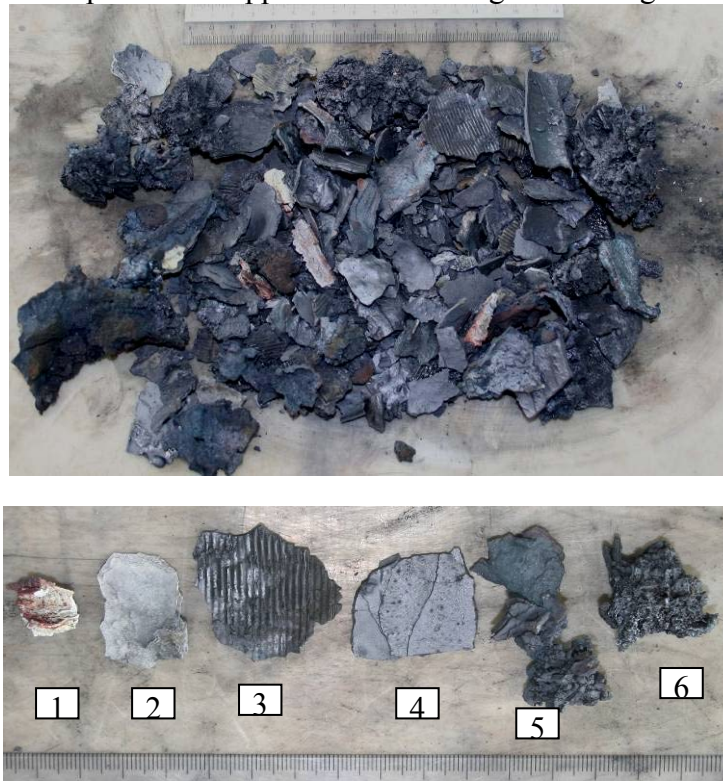


Figure 165 – Appearance of the large unbound corium fragments material over the ingot (on the top) and the samples for analysis (bottom)

The quantitative element sample composition of the large fragments material (sample series LS) over the ingot, in whole, corresponds to the material composition of the large particle fractions of the lower fragments layer. The phase composition of the fragments is represented mainly with solid solutions (U,Zr)O₂ with FCC lattice of uranium dioxide and (Zr,Ur)O₂ on the

basis of the cubic or tetragonal modifications of zirconium dioxide. Table 35 includes the estimated composition of solutions with high content of zirconium in approximation of the cubic crystal lattice. We should note the lack of the metallic zirconium phase.

Table 35 – The data from the qualitative phase and quantitative element analysis of fraction samples of the disperse material

Sample	Phase composition	Element content, %wt.			
		Zr	U	Fe	U/Zr
LS-1	TaO, Ta ₂ O ₅	0,3	0,2	0,4	1,3
LS-2	ZrO ₂ ^{MCL} , ZrO ₂ ^T	97,5	2,3	0,2	0,0
LS-3	U _{-0,7} Zr _{-0,3} O ₂ (0,538 nm); ZrO ₂ ^T ; ZrO ₂ ^{MCL}	30,6	69,0	0,4	2,3
LS-4	U _{-0,9} Zr _{-0,1} O ₂ (0,544 nm); ZrO ₂ ^{MCL} ; ZrO ₂ ^T	29,7	70,2	0,1	2,4
LS-5	U _{-0,3} Zr _{-0,7} O ₂ (0,525 nm); U _{-0,7} Zr _{-0,3} O ₂ (0,538 nm)	31,3	68,0	0,7	2,2
LS-6	U _{-0,9} Zr _{-0,1} O ₂ (0,544 nm); ZrO ₂ ^T ; ZrO ₂ ^{MCL} ; U _{-0,3} Zr _{-0,7} O ₂ (0,525 nm)	26,0	63,1	10,9	2,4

Investigation of the corium ingot material

The appearance of the corium ingot after removal of the fragments layer is represented in Figure 166. The corium ingot was relatively easy divided into large pieces along the natural cracks.



Figure 166 – The appearance of the corium ingot surface after removal of the disconnected fragments
The diagram of the ingot fragments sampling is represented in Figure 167.

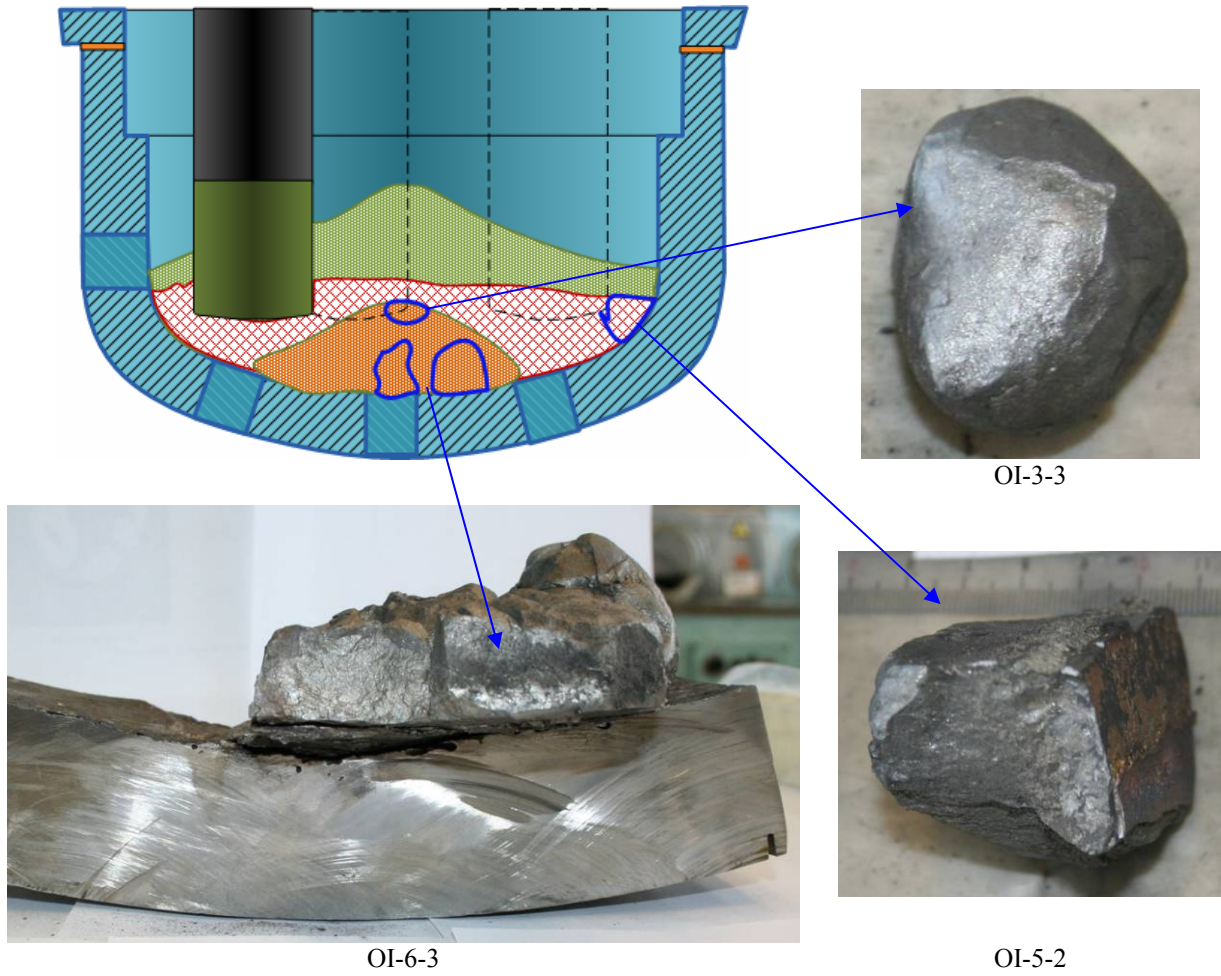


Figure 167 – Diagram of some sampling from the vessel model

Figures 168, 169 illustrate the appearance of the ingot samples taken for the analysis, the samples description is included in Table 36.



Figure 168 – Appearance and designation of samples from the large ingot material fragments



Figure 169 – Appearance of the crust surface (samples OI-5-2) from the vessel model side (on the left) and the break surface from the ingot side (on the right)

Table 36 – Description of the material samples from the upper ingot layer

Sample	Description of sample material
OS-2-1	The melt ingot fragment in the upper material layer
OS-2-2	Platy material from the ingot bottom surface
OI-1-A1	Platy material from the ingot bottom surface
OI-3-1	Ingot fragment
OI-3-2	Ingot fragment
OI-3-3	Ingot fragment
OI-5-2	Break of the platy material layer from the ingot bottom
OI-6-3	One of the fragments in the ingot center
OI-6-4	Crust in the ingot center

The data from the qualitative phase and quantitative element analysis of the material samples composition from the vessel model are included in Table 37.

Table 37 - Data from the qualitative phase and quantitative element analysis of the material samples composition from the vessel model

Sample	Phase composition	Element content, %wt.			
		Zr	U	Fe	U/Zr
OS-2_1	$U_{-0.95}Zr_{-0.05}O_2$ (0,545 nm); $\alpha-Zr(O)$; $\alpha-(U,Zr)$	30,4	69,1	0,5	2,3
OS-2_2	$U_{-0.95}Zr_{-0.05}O_2$ (0,545 nm); $(Zr,U)O_2^T$; $(Zr,U)O_2^{MCL}$; $\alpha-Zr(O)$	29,5	70,4	0,1	2,4
OI-1_A1	$U_{-0.85}Zr_{-0.15}O_2$ (0,542 nm); $(Zr,U)O_2^T$; $(Zr,U)O_2^{MCL}$; Zr_2FeO_x	30,3	69,3	0,4	2,3
OI-3_1(1)	$U_{-0.95}Zr_{-0.05}O_2$ (0,545 nm); Zr_2FeO_x (1,218 nm); $\alpha-Zr(O)$; $\alpha-(U,Zr)$				
OI-3_1(2)	$U_{-0.95}Zr_{-0.05}O_2$ (0,545 nm); $\alpha-Zr(O)$; $\alpha-(U,Zr)$; Zr_2FeO_x				
OI-3_2(1)	$U_{-0.95}Zr_{-0.05}O_2$ (0,544 nm); $U_{-0.7}Zr_{-0.3}O_2$ (0,539 nm); $(Zr,U)O_2^T$; $\alpha-Fe$ (~10% weight); $\alpha-(U,Zr)$				
OI-3_2(2)	$U_{-0.75}Zr_{-0.2}O_2$ (0,538÷0,540 nm); $U_{-0.5}Zr_{-0.5}O_2$ (0,533 nm); $(U,Zr)Fe_2$ ($a_0 \approx 0,704$; $a_0 \approx 0,708$ nm); $(Zr,U)O_2^T$; $\alpha-Fe$ (~10% weight); $\alpha-(U,Zr)$; $U_{-0.95}Zr_{-0.05}O_2$ (0,544 nm);				
OI-3_3	$U_{-0.95}Zr_{-0.05}O_2$ (0,545 nm); $\alpha-Zr(O)$; $\alpha-(U,Zr)$; Zr_2FeO_x	30,6	68,9	0,5	2,3
OI-5_2	$(U,Zr)Fe_2$ ($a_0 \approx 0,704 \div 0,708$ nm); $U_{-0.95}Zr_{-0.05}O_2$ (0,545 nm); $ZrFe_3$; $\alpha-Fe$ (~10% weight); $\alpha-Zr(O)$; $\alpha-(U,Zr)$; Zr_2FeO_x	23,2	60,4	16,4	2,7
OI-6_3	$U_{-0.95}Zr_{-0.05}O_2$ (0,545 nm); $\alpha-Zr(O)$; $\alpha-(U,Zr)$; Zr_2FeO_x	29,0	70,6	0,4	2,4
OI-6_4	$U_{-0.95}Zr_{-0.05}O_2$ (0,545 nm); $(U,Zr)Fe_2$ ($a_0 \approx 0,704 \div 0,708$ nm); $ZrFe_3$; $\alpha-Fe$; $\alpha-Zr(O)$; $\alpha-(U,Zr)$; Zr_2FeO_x	20,5	61,1	18,4	3,1

According to the results of the X-ray phase analysis the main components of phase content of the melt ingot sample (OI-3_1, OI-3_2, OI-3_3; OS-2_1, OI-6-3) is a solid solution $(U,Zr)O_2$ with FCC lattice – uranium dioxide lattice and α -phase of metallic zirconium, stabilized with oxygen $\alpha-Zr(O)$. The phase on the basis of α -uranium crystal lattice $\alpha-(U,Zr)$ exists insignificantly in the samples as well. The common feature of the sample phase composition is low content of zirconium in the main solid solution $(U,Zr)O_2$ with estimated content

$U_{-0.9}Zr_{-0.1}O_2$. The estimation of the phase content was conducted in terms of the lattice spacing value.

The iron-bearing phases $(U,Zr)Fe_2$, Zr_2FeO_x with the cubic lattice of the space groups $Fm3m$ or $Fd3m$ are also met in the corium sample OI-3_2(1,2) where the presence of α -iron is also discovered. In the porous part of the fragment OI-3_1 (sample OI-3_1(1)) the phase Zr_2FeO_x is identified most correctly.

The samples of the bottom crust of the peripheral ingot regions (samples OS-2_2, OI-1_A1) have a close phase composition similar to the phase composition of samples LS-4 and LS-5, and represent a hardening ingot layer in the zones where there were no melting of the vessel model material.

On the contrary, the crust samples OI-5_2, OI-6_4 are taken in the regions where melting of the vessel model material is taken place, and involve the products of corium/steel melt interaction. The most important from the iron-bearing phases, the presence of which is great in the samples of the near-bottom crust (OI-5_2, OI-6_4), are the intermetallide phases $ZrFe_3$ (close-packed fcc structure), $(Zr,U)Fe_2$ (ferromagnetic, laves phase with the cubic lattice $MgCu_2$) and metallic phase α -Fe.

Analysis of samples from the separate regions of the corium ingot

At the last stage of the experimental section disassembling, there were removed easy-separated fragments of the corium ingot, following which a monolith "central" ingot, the material of which was melted with the model wall, left in the central region of the vessel model. The metallographic sections characterizing the ingot structure in the vertical section, were produced from a number of large fragments in the central and peripheral regions of the ingot. The cylinder samples were taken from the mating one-halves of the fragments sections for the phase analysis and measuring of thermo-physical properties.

The appearances of the metallographic sections with the sampling points are represented in Figure 170.

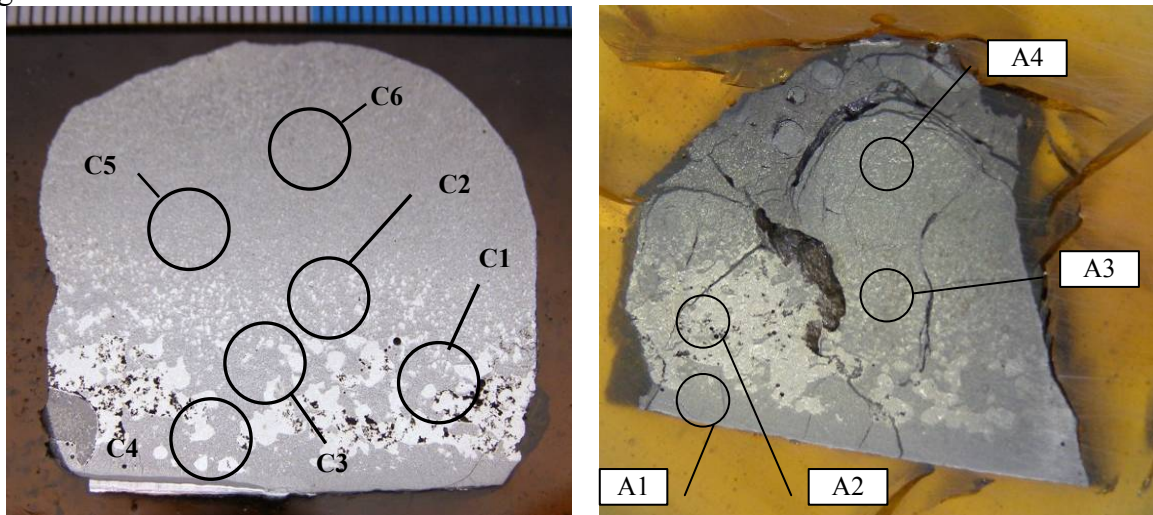


Figure 170 – Appearances of the ingot metallographic sections I-1_1C (on the left) and the ingot I-1_A (on the right) with sampling points

The results of the qualitative phase and quantitative element analysis of the sample material composition from the vessel model are included in Tables 38, 39.

Table 38 – Results of the qualitative phase and quantitative element analysis of the sample material composition of the ingot I-1_C

Sample	Phase composition	Element composition, %			U/Zr
		Zr	U	Fe	
C0	$U_{-0.95}Zr_{-0.05}O_2$ (0,545 nm); α -Zr(O); α -(U,Zr); Zr_2FeO_x	28,8	70,7	0,6	2,5
C1	$U_{-0.95}Zr_{-0.05}O_2$ (0,545 nm); α -Zr(O); α -(U,Zr); Zr_2FeO_x	31,3	67,7	1,0	2,2
C2	$U_{-0.95}Zr_{-0.05}O_2$ (0,545 nm); α -Zr(O); α -(U,Zr); Zr_2FeO_x ; α -Fe(?); (U,Zr)Fe ₂ ($a_0 \approx 0,704 \div 0,708$ nm)	32,4	64,1	3,5	2,0
C3	$U_{-0.95}Zr_{-0.05}O_2$ (0,545 nm); α -Zr(O); α -(U,Zr); Zr_2FeO_x	32,1	66,5	1,4	2,1
C4	α -Zr(O); $U_{-0.95}Zr_{-0.05}O_2$ (0,545 nm); α -(U,Zr); Zr_2FeO_x	34,7	63,6	1,7	1,8
C5	$U_{-0.95}Zr_{-0.05}O_2$ (0,545 nm); α -Zr(O); α -(U,Zr); Zr_2FeO_x	33,8	65,4	0,7	1,9
C6	$U_{-0.95}Zr_{-0.05}O_2$ (0,545 nm); α -Zr(O); α -(U,Zr); Zr_2FeO_x	31,5	68,1	0,4	2,2

Table 39 - Results of the qualitative phase and quantitative element analysis of the sample material composition of the ingot I-1_A2

Sample	Phase composition	Element composition, %			U/Zr
		Zr	U	Fe	
A1	$U_{-0.95}Zr_{-0.05}O_2$ (0,545 nm); α -Zr(O); α -(U,Zr); Zr_2FeO_x	31,6	67,9	0,5	2,1
A2	α -Zr(O); $U_{-0.95}Zr_{-0.05}O_2$ (0,545 nm); α -(U,Zr); Zr_2FeO_x ; ($a_0 \approx 0,704 \div 0,708$ nm); α -Fe; (U,Zr)Fe ₂	40,1	58,8	1,2	1,5
A3	$U_{-0.95}Zr_{-0.05}O_2$ (0,545 nm); α -Zr(O); α -(U,Zr); Zr_2FeO_x	31,8	67,7	0,5	2,1
A4	$U_{-0.95}Zr_{-0.05}O_2$ (0,545 nm); α -Zr(O); α -(U,Zr); Zr_2FeO_x	28,9	70,3	0,8	2,4

According to the results of the X-ray phase analysis the main components of samples taken from the upper ingot regions with homogeneous microstructure (C5, C6, C0, A3, A4) is the solid solution (U,Zr)O₂ with uranium dioxide FCC lattice and α -phase of metallic zirconium stabilized with oxygen α -Zr(O). In addition the samples have, not much, the phase on the basis of lattice spacing α -uranium α -(U,Zr) and iron-bearing phase Zr_2FeO_x with cubic lattice of spacing groups Fd3m or Fm3m. The common feature of the samples phase composition is low content of zirconium in the main solid solution (U,Zr)O₂ with estimated content $U_{-0.9}Zr_{-0.1}O_2$. The estimation of the phase content was conducted in terms of the lattice spacing value.

The samples of the material from the lower ingot area, containing light metal inclusions (A2, C4, C3), differ with high content of the metal phases set α -Zr(O) and α -(U,Zr), and iron-bearing phase Zr_2FeO_x .

The thermo-physical properties of the ingot samples were studied through the flashing method at room temperature. The results from determination of thermo-physical properties of corium samples from ingot I-1_C are included in Table 40.

Table 40 – Thermo-physical properties of corium samples (ingot I-1_C)

Sample	Specific heat, C_p , J·kg ⁻¹ ·K ⁻¹	Thermal conductivity, λ , W·m ⁻¹ ·K ⁻¹	Thermal diffusivity, λ , W·m ⁻¹ ·K ⁻¹	Density, ρ , g/cm ³
C-1	299,5	1,86	5,4	9,75
C-2	286,4	1,94	5,4	9,80
C-3	292,9	1,94	5,6	9,78
C-4	296,3	1,91	5,6	10,10
C-5	268,6	2,30	5,9	9,53
C-6	297,0	2,30	6,4	9,53

A special consideration was given to the investigation of the bottom ingot part OI-1_1C, where the material layer of about 1 mm thickness containing the corium/vessel model steel interaction products, was detected. Enlarged view of this region before and after etching is represented in Figure 171. Some of the constituents that are lower the thin light layer, located under the wider dark layer of the material, was subjected to appreciable impact of acid etchant. In the rest of the ingot part the etchant did impact appreciably on none constituents.

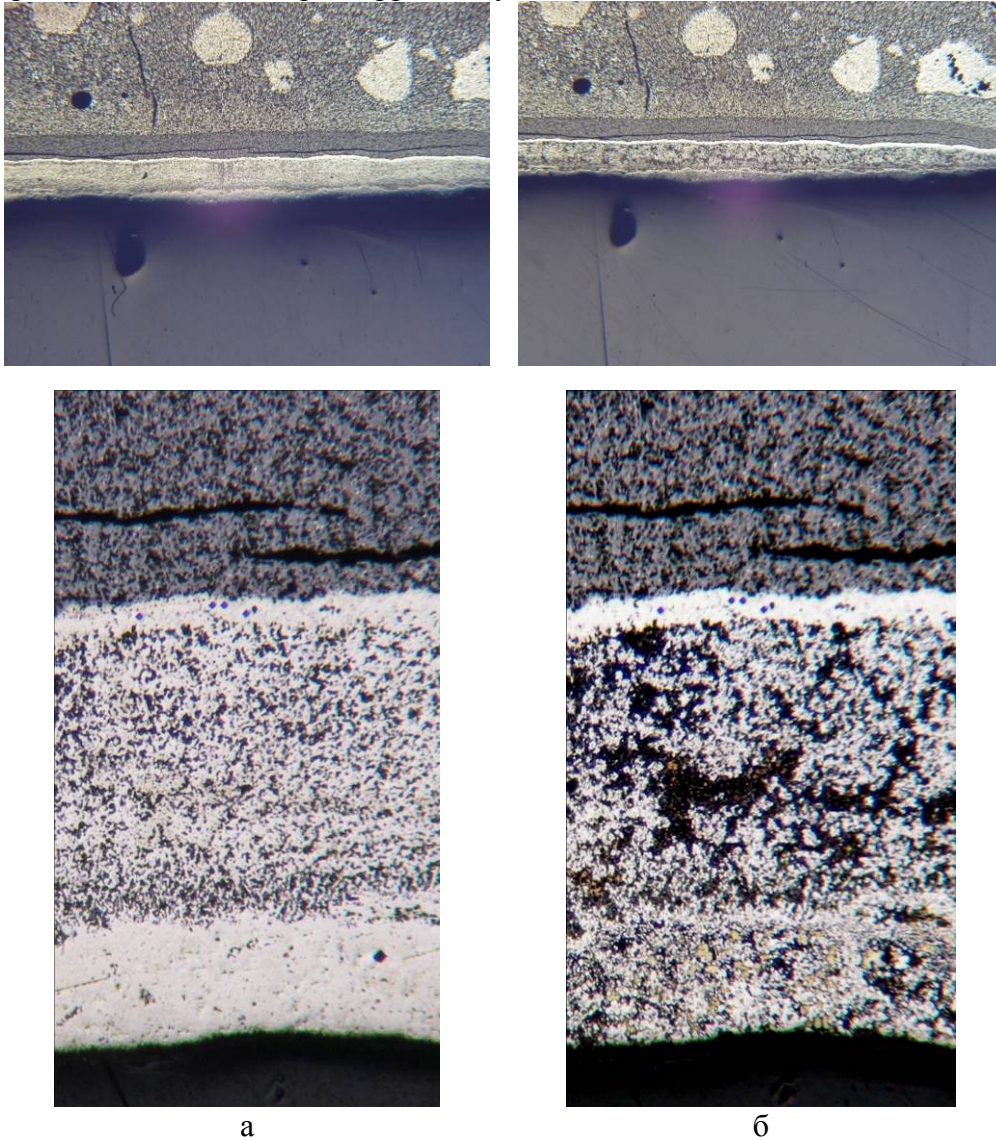


Figure 171 - Metallographic section of corium interaction area with steel before (a) and after etching (b)

Of the samples that are the most correspond to this metallographic section region we may designate the crust samples OI-5_2 and OI-6_4. The main distinctive feature of phase composition of the samples is presence of great number of iron-bearing intermetallic phases $ZrFe_3$, $(Zr,U)Fe_2$ and metallic phase α -Fe. Supposedly, just these phases were subjected to acid etchant impact.

The results from the phase and element analysis of the ingot samples in the reactor vessel model enable to conclude as follows:

5. The main phase composition of the ingot material samples is practically identical, that says about melt homogeneity both at the melt discharge and at its solidification.
6. In the samples contacting directly with steel elements there was detected the presence of the products of their chemical interaction with corium melt. In the rest of ingot samples the content of iron-bearing phases was equal to zero in fact.

5.6 Analysis of the data resulted from the integral tests INVECOR

In the result of the activity performed on realization of 4 large-scale integral experiments, there were discharged from 40 to 60 kg prototype corium melt C-30 from the 1,7 m height into the experimental sections representing the VVER reactor pressure vessel models on a scale of ~1:12 and involving the devices for decay heat simulation on the basis of 5 co-axial plasmotrons. The initial loading of the melting crucible of the induction electric melting furnace involved dioxide of depleted uranium in the form of BN-350 blanket pellets, metal zirconium in the form of plates and rods, and also zirconium oxide in the form of fine-disperse powder.

The result of the solidified corium study after the calibration test showed that at the chosen condition of initial components heat/melting there was no complete dissolution of uranium dioxide in the molten zirconium. Increase of the corium heating duration in the electric melting furnace resulted in undesired melt travels inside the furnace and its emission to the furnace gas drain system, as it was in the second calibration test. In addition, long holding of the corium melt in the graphite crucible may result in the interaction of oxide and metal components of corium with carbon, even if there is protective coating on the graphite surface⁴. In this connection it was decided to drain the melt of metal components with fragments of not complete dissolved fuel pellets⁵. Thereby, it was supposed that uranium dioxide dissolution in the zirconium melt will continue in the experimental section due to its heating with the decay heat simulator⁶.

The duration of the large-scale integral experiments was from 1 to 2 hours, thereby the “volume” energy release in the corium, due to the decay heat simulator running, was from 6 to 10 W/cm³ that corresponds to the postulated values for phenomenological description of severe accidents.

The corium melt temperature in its discharge into the experimental section was from 2570 to 2630 °C. Maximum temperature of the reactor vessel model wall was 850...1400 °C. Corium mass in the reactor vessel model was from 47 to 69 kg⁷. Maximum erosion depth of the vessel model steel wall was about 6 mm and was detected in the model center in the zone of the initial contact of corium jet melt with vessel in the INVECOR-1.4 test (the model wall temperature reaches 1400 °C).

The heat flux through the vessel model wall was not high (under 150...180 kW/m²), that is explained with the use of the insulation on the external water-cooled surface of the model. The existence of heat insulation and large thickness of the steel wall (as well as relatively large mass of the vessel model to the corium mass) resulted in redistribution of heat fluxes, i.e. the most heat of the corium was distributed along the model wall to the upper flange fastening the model in the test facility.

The other reason of the radial heat flux reduction is the gap between the external corium crust and the vessel model wall formed due to heat expansion of the model on corium/steel heat exchange. In one of the tests (INVECOR-1.4) there was discovered a layer crust with additional gas clearances that was additional thermal resistance on the way of radial heat flux distribution. In the experimental section disassembling it was discovered that in all tests the solidified corium represented a solid ingot and a layer of fine fragments over the ingot. Mass fraction of the fragmented corium came to 30% of the total corium mass in the vessel model.

⁴ We should remember that in applying the protective coating on the graphite crucible some surfaces are not covered, - these are the crucible cover and the top zone of the internal crucible surface.

⁵ The duration of the corium components heating/melt in the electric melting furnace is about 1 hour that is identical to the processes taken place in the TMI-2 reactor core (on the version of IAEA).

⁶ In dissolution of uranium dioxide in the zirconium melt it is absorbed near 265 kW per 1 kg of uranium dioxide.

⁷ In two tests the corium mass in the vessel model was increased due to pre-location of about 10 kg oxide corium (additionally to the drained melt) in the vessel model.

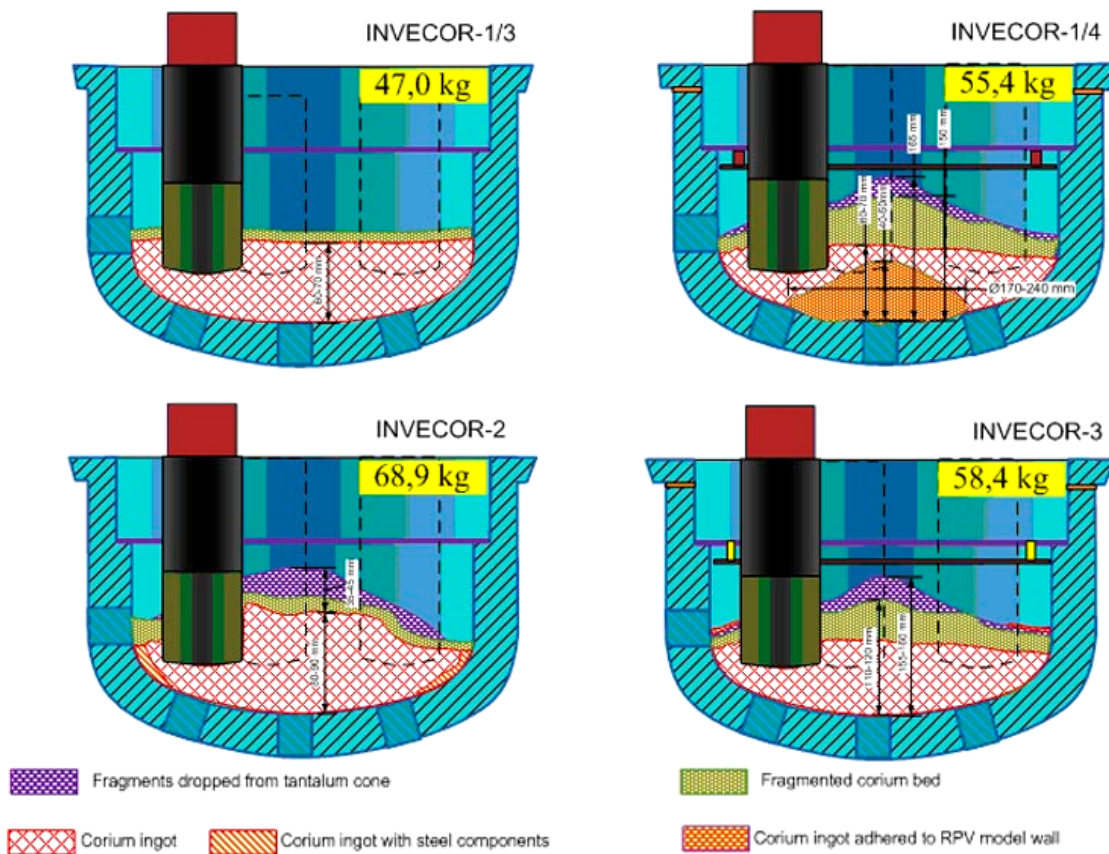


Figure 172 – Diagram of corium location in the experimental section after the tests

The phase composition of the fragmented corium was similar to the corium ingot content, but it contained more oxide components. The upper layer of the fragments, representing the products of the upper heat shield degradation and the director cone was removed and then was not considered in further analysis.

The ingot structure analysis especially in the vicinity of the plasmatrons surfaces did not reveal marked influence of local overheating corium near the plasmatrons on the process of likely formation of corium fragments with their further surfacing.

Based upon the results available, we may be confident in the supposition that corium fragments are formed due to the melt jet spray on its falling into the experimental section under low corium viscosity at high temperature (Figures 173, 174).

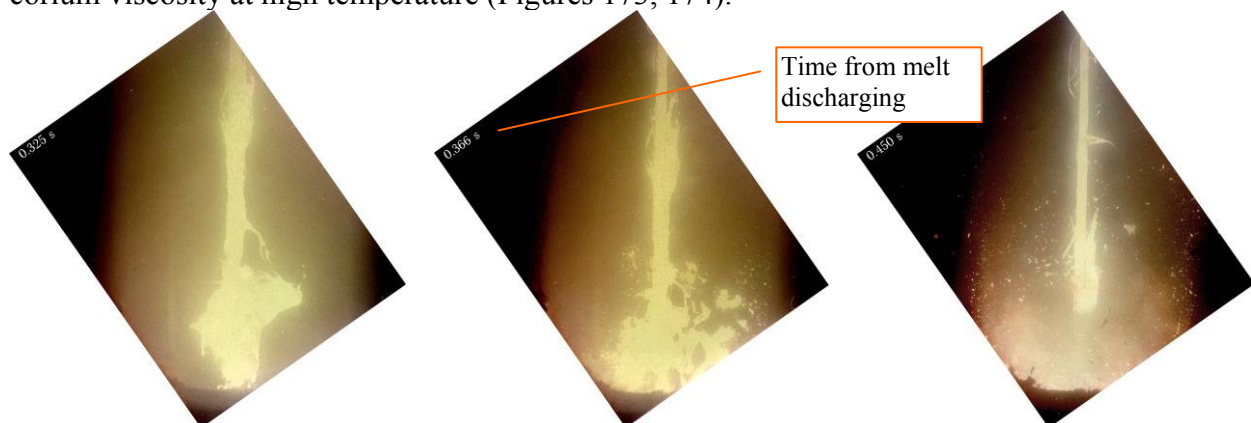


Figure 173 – Pictures of corium melt jet C-22 on its drain into the dry experimental section (Project COTELS)

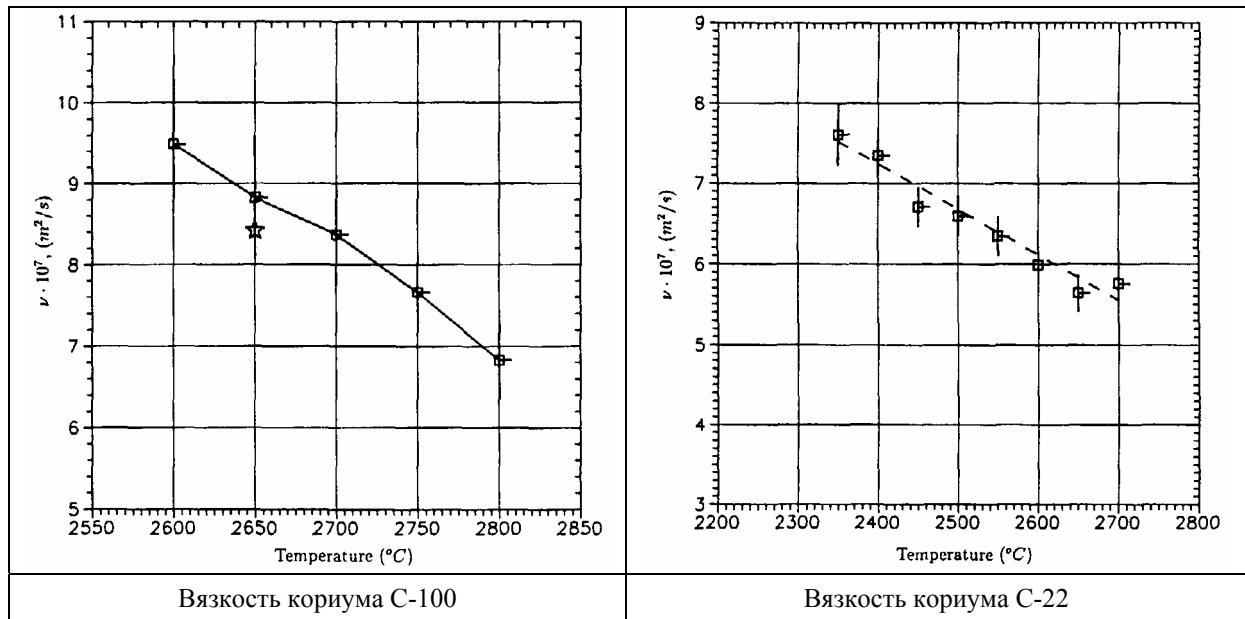


Figure 174 – Corium viscosity data (Project RASPLAV)

In the result of the earlier experiments on in-vessel "fuel/coolant" interaction (in-vessel FCI) the similar corium configuration (Figure 175) was obtained, but corium particles were larger greatly as compared with the INVECOR tests.

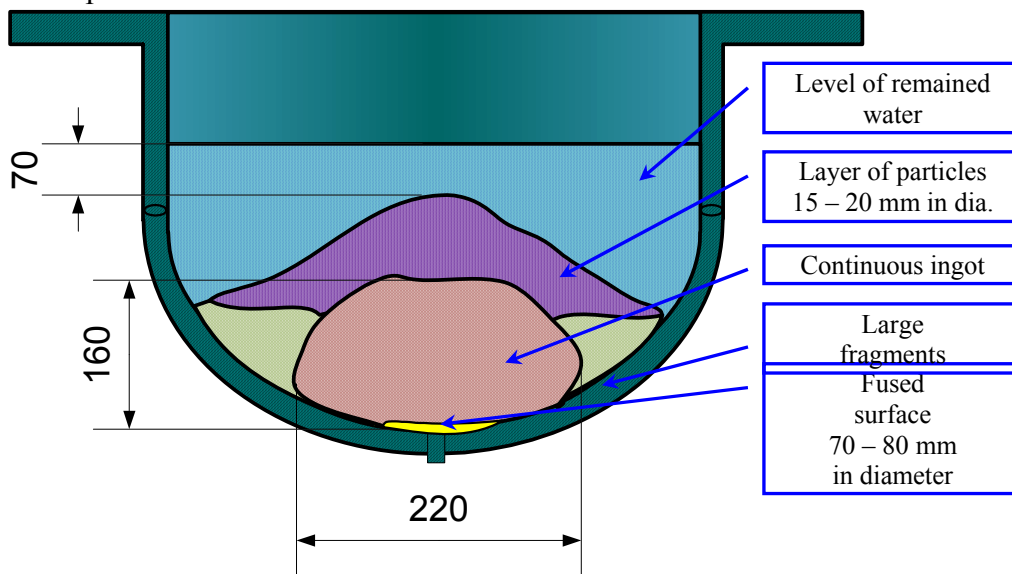


Figure 175 – Configuration of corium in the vessel model on melt draining to the residual water (Project COTELS)

It is safe to assume that on draining the corium melt in tests INVECOR the sprayed melt is solidified promptly on relatively cold surfaces of the vessel model, on the upper heat shield and on the water-cooled parts of the plasmatrons in the form of fine particles and thin crusts (Figure 176). Then the solidified particles fall from the upper experimental section elements on the top crust over the corium and/or are removed with the corium melt from the vessel model bottom at the final (relatively smooth) falling of the jet.

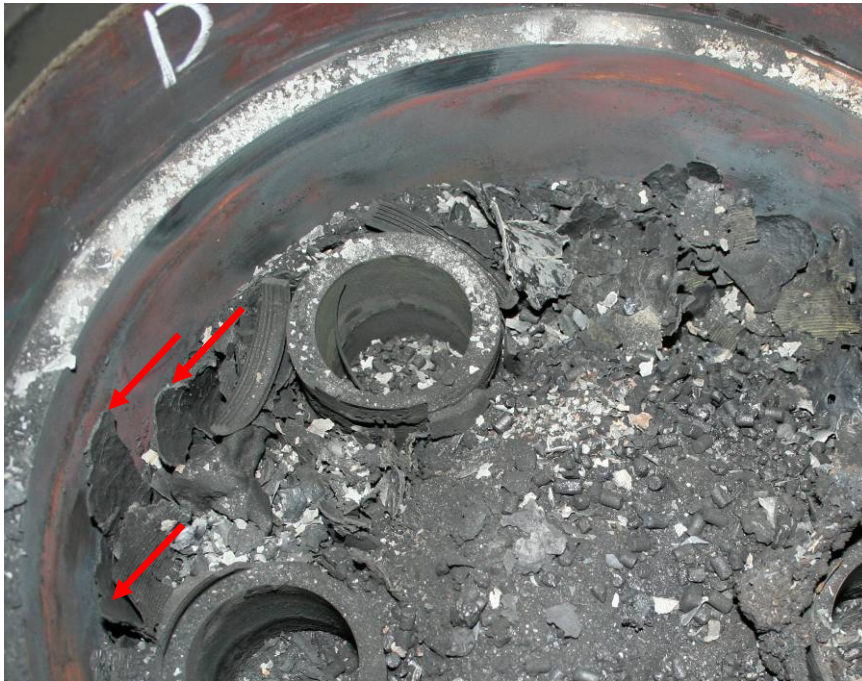


Figure 176 – The fragment of the thin corium crust on the lateral surface of the vessel model (INVECOR-1.4)

The most fragmented corium part was discovered in the experiments with higher temperature in the "corium/steel" interaction zone and at longer duration of the in-vessel melt retention modeling (INVECOR-3, INVECOR-1.4). Close study of the lower fragments layer showed that it was formed, mainly, with the plate-like debris. Most probably, these fragments are from the initial corium crust that was broken at heating of the internal corium volume with the plasmatrons heater in decay heat simulating. The initial crust cracking may be caused with increasing of corium volume on its reheating as well with gas pressure increase in the close pores inside the corium volume.

Taking into consideration the fact that the corium/steel relation may be changed due to the reduction of the vessel model wall thickness (Figure 177), the conditions and/or regularities of the fragmented layer formation may be studied in new tests, i.e. in the framework of the second milestone of the INVECOR Project.

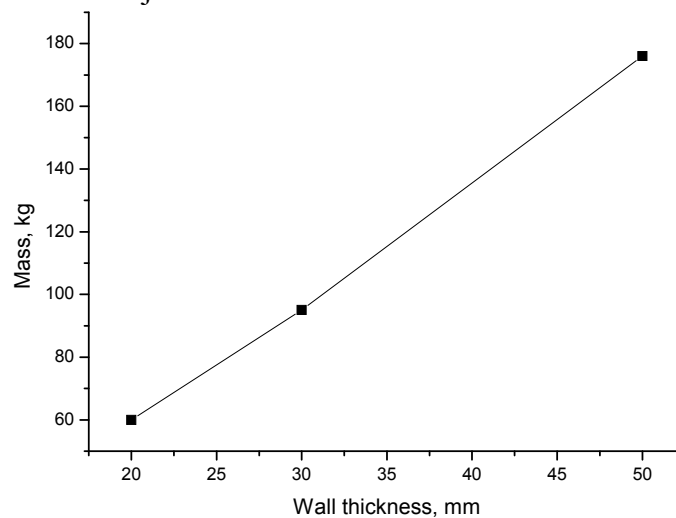


Figure 177 – Mass of the vessel model depending on the steel wall thickness

Reduction of the model wall thickness up to 25 mm may ensure "corium/steel" relation at nearly 1:1 and that has considerable influence on corium fragmentation degree at initial melt/steel contact.

6 Conclusion

As a consequence of the project implementation, there were performed four large-scale integral tests on simulation of the final stage processes of the second severe accident stage with water-cooled reactor core melting, involving 60 kg prototype corium melting, melt travel on the lower head reactor vessel and in-vessel melt retention with decay heat simulation.

The performance of the integral tests was made possible thanks to availability of the Institute's test facility designed for the large-scale experiments with the use of UO₂-containing corium as well as due to the performance of a large scope of the design and calculation activities and many supporting tests to justify working efficiency of the selected technical solutions.

In the experiments conducted it was succeeded in modeling the reactor situation on development of the in-vessel severe accident phase with simulation of real processes that may occur on serious degradation of the water-cooled reactor core. The configuration of corium, discovered in the experiments, located on the lower-head reactor vessel, gives the cause for supposing that the in-vessel corium retention prediction may be optimistic, i.e. the presence of the fragmented corium layer over the melt pool facilitates essentially its coolability through the internal filling of the vessel with water.

Low radial heat fluxes from the corium to the external cooling water may be explained as follows:

- presence of thermal insulation on the external surface of the vessel model, resulting in redistribution of heat fluxes from radial to longitudinal along the model wall to the upper massive flange of the vessel model;
- not complete dissolution of uranium dioxide in zirconium melt in the upper electric melting furnace and continuation of endothermal dissolution of uranium dioxide in the in-vessel corium retention process;
- formation of the gap between the external crust, enclosing corium, and the vessel model wall in the result of thermal steel expansion in the initial time of corium/steel heat interaction;
- stratification of corium crust at corium/steel boundary resulting in great decreasing of effective crust heat conductivity.

Stationary phenomena in the in-vessel corium retention process depend essentially on the following:

- preceding transitional processes connected with the corium pool formation and behavior in the reactor core;
- duration of corium pool existence in the core center;
- character and speed of corium melt falling on the lower head reactor vessel.

The activity was performed in compliance with the Project Working Plan considering the corrections agreed with the ISTC and foreign collaborators in the course of the Project implementation.

The interim data and new engineering solutions were discussed with the Project foreign collaborators through correspondence using a specially established Web-site as well as in the course of the regular meetings with the contact expert group of the European Committee on severe accidents management (CEG-SAM).

As a consequence of the tests performed there were produced over 200 kg corium, the further study of which may ensure important data for the use in the severe accidents codes.

Investigation of the fragmented corium formation conditions may be the subject for new programs with variation of the vessel model dimensions and tests performance conditions, i.e. in the form of the INVECOR Project second phase.

7 Comments

During realization of the procurement plan of the materials necessary for manufacturing of details of the electro-melting furnace and the device for decay heat imitation there were the problems connected with necessity of licensing of import/export of graphite materials of German firm SGL Carbon Group (due to most correspondence to experiments conditions). In this connection the work plan was twice corrected in connection with prolongation of time of performance of the project without additional financing.

Nevertheless, additional time has been devoted to performance of supporting experiments and the analysis of results that has allowed to execute large-scale integral experiments in the shortest terms.

Because the main part of work (large-scale integral experiments) has been executed in rather deadlines, the post-test research has not been executed in sufficient volume. At discussion of a situation with foreign collaborators of the project the arrangement has been reached, that the participants of the project responsible for this part of work will continue researches of corium samples and RPV steel after the actual termination of the project. It will allow more well-grounded prepare proposal for the second phase of INVECOR project.

Acknowledgments

The INVECOR Project was performed under financial support of the European Committee. The Project members express their thanks to the foreign collaborators:

- CEA, Saclay and Cadarache;
- IRSN;
- KIT (former FZK) and JRC-ITU, Karlsruhe;
- FZR, Dresden;
- Pisa University;

for the support of the Project at large, for the useful discussions and recommendations on the experiments conditions, for involvement in the analysis of the obtained data.

The Project members appreciate sincerely the experts of NITI by Alexsandrov for their active participation in the experiments computation justification as well as the experts of IBRAE for the useful discussions of the results.

The Project participants express their gratitude to all members of the contact expert group and the ISTC staff for the organization and sponsorship in the Project implementation.

Attachment 1: List of published papers and reports with abstracts

Attachment 2: List of presentations at conferences and meetings with abstracts

Attachment 3: Database INVECOR